A new Computational Method for the Fluid-structure Interaction in Random Nonlinear Ocean Waves

Vom Promotionsausschuss der
Technischen Universität Hamburg

zur Erlangung des akademischen Grades

Doktor der Naturwissenschaften (Dr. rer. nat.)

genehmigte Dissertation (Monografie)

von
Marten Hollm

aus
Itzehoe

2025

1. Gutachter: Prof. Dr.-Ing. Robert Seifried
2. Gutachter: Prof. Dr. rer. nat. Daniel Ruprecht

Tag der mündlichen Prüfung: 03. 12. 2024

MuM Notes in Mechanics and Dynamics

Editor: Prof. Dr.-Ing. Robert Seifried
Hamburg University of Technology
Institute of Mechanics and Ocean Engineering (MuM)
www.tuhh.de/mum

Volume 11
Marten Hollm
"A new Computational Method for the Fluid-structure Interaction in Random Nonlinear Ocean Waves"
Hamburg, 2025

DOI: https://doi.org/10.15480/882.14990
ORCID: https://orcid.org/0000-0001-5139-8918

Acknowledgments

This work is the result of my research during my time at the Institute of Mechanics and Ocean Engineering (MuM) at Hamburg University of Technology. I would like to deeply thank everyone who has contributed to this work in one way or another.

First of all, I would like to thank my supervisor and the head of our institute, Prof. Robert Seifried, for his continuous trust and support during my entire time at the MuM. I am deeply thankful for his guidance and help throughout all stages of my research, but also for the freedom to follow my own ideas. Furthermore, I would like to thank Prof. Daniel Ruprecht for acting as the second reviewer of this work and Prof. Gerhard Bauch for chairing the examination committee.

My next thanks go to our senior engineer, Marc-André Pick, who supported me throughout my studies and motivated me to become a Ph.D. student at the MuM. Also during my time at the MuM, he was always there for me with valuable advice and continuing support. For this, I am deeply grateful.

Special thanks go to Leo Dostal, who not only co-supervised my Master's thesis, but was also a dear colleague and office mate. He taught me a lot about the work as a Ph.D. student and introduced me to the fascinating world of nonlinear water waves. Without his initial guidance and patience, this work would definitely be a different one.

I would also like to thank all of my colleagues for a wonderful time at the MuM. Social and research life was always enjoyable. I am grateful for the mutual support, countless coffee breaks, discussions, barbecue events, and cake Mondays. I learned so much during this unforgettable time.

Furthermore, I am deeply grateful for the unconditional support and encouragement of my family, especially my parents. They have given me the freedom to follow my own path, while always standing by me and supporting me wherever possible. Without them, I would not be where I am today. They are an important part of my life and I am grateful for everything they have done for me.

Finally, I would like to thank Antonia for her love and unwavering support. She taught me to appreciate and enjoy the small things in life, offering a refreshing balance to my work and a source of strength and inspiration in challenging times. For this and for her immense patience, especially during the final stages of this dissertation, I am deeply grateful.

Hamburg, April 2025 Marten Hollm

To my family.

Abstract

An efficient computation of the fluid-structure interaction (FSI) between mechanical structures and ocean waves is an important topic in many ocean engineering and naval architecture applications. For example, the form and parameters of wave energy converters (WECs) should be optimized to harvest a large amount of energy in ocean waves. To this end, the corresponding hydrodynamic forces acting on the WECs must be computed for many designs. In addition, nonlinear wave effects must be considered to model the temporal behavior of larger or faster waves. This is, for example, interesting when ships are excited by rogue waves and the corresponding hydrodynamic forces acting on the hull of a ship should be calculated.

For many applications, it is often sufficient to consider the FSI within the potential flow theory instead of using the Navier-Stokes equations. However, the numerical solution of the governing equations of the potential flow theory is still computationally expensive. This thesis contributes to the improvement of the currently available numerical schemes, which compute the FSI in random nonlinear ocean waves. The approach used in this thesis is based on the nonlinear Schrödinger equation (NLS). Compared to the governing equations of potential flow theory, solutions of the NLS can be computed much more efficiently. This efficiency is used to develop a method that allows a fast computation of the FSI in nonlinear water waves.

In addition, an approach is proposed that enables the computation of random nonlinear water waves by perturbing analytical solutions of the NLS using irregular sea surfaces. This leads to the proposed approach, where random nonlinear water waves are computed using the NLS. This makes it possible to describe a method that employs the NLS to compute the FSI between a structure and random nonlinear water waves.

The new method is investigated with regard to its application areas, accuracy, stability, and computational efficiency. Here, numerical results for the water wave dynamics, the hydrodynamic forces acting on mechanical structures, the resulting motion of the structures, and the effect of the presence of the structures on the surrounding water waves are analyzed. All these results are compared with those obtained using classical random nonlinear water waves, in which the computation of corresponding wave-wave interactions is time-consuming. It is found that the NLS offers an interesting possibility to efficiently investigate the behavior of structures excited by random nonlinear ocean waves.

Contents

List of Figures

List of Tables

Abbreviations and Symbols

In the following, the most important abbreviations and symbols are defined.

Abbreviations

BC	boundary condition
CFB	cylindrical floating body
FSI	fluid-structure interaction
FFT	fast Fourier transform
IC	initial condition
JONSWAP	Joint North Sea Wave Project
NLS	nonlinear Schrödinger equation
PDE	partial differential equation
PM	Pierson-Moskowitz
RAO	response amplitude operator
ReSP	relaxation pseudo-spectral
WEC	wave energy converter

Functions and Scalars

c_{ph}	phase velocity
c_{gr}	group velocity
d	draft of CFB
d_{elec}	electrical damping
d_i	mechanical damping
d_{lin}	mechanical damping in linear case
g	gravitational acceleration
h	water depth
k	wave number
k_0	wave number of carrier wave
k_{pw}	wave number parameter of plane-wave solution
p	hydrodynamic water pressure
r	cylindrical coordinate
sgn	signum function
t	time coordinate
x, y, z	Cartesian coordinates
A	wave amplitude
D	spread function
C_0	cross-section of CFB and still water level
F	nonlinear function for 2nd order BC at $z = 0$
H	wave height
H_{s}	significant wave height
L	length of damping zone
LPE	lower peak envelope
M	mass of CFB and guidance
M_ω	number of wave components on long-crested random water wave
N_{F}	number of Fourier modes
Q	nonlinear function for 3rd order BC at $z = 0$
R	radius of CFB
RAO	response amplitude operator
$\mathrm{RAO_v}$	response amplitude operator of velocity
R_{i}	radius of inner layer of computational water domain
R_{S}	radius of spherical segment
R_Ω	radius of computational water domain
S	sea spectrum
S_{B0}	surface of body below the still water level
S_{B}	wetted surface of body
T	slow temporal coordinate
UPE	upper peak envelope
X, Z	slow spatial coordinates
X_{s}	shift in space
α	inclination angle of CFB
β	phase shift
δ	coefficient in NLS
ε	wave steepness
ζ	moving spatial coordinate
η	sea surface displacement
$\eta^{(i)}$	i-th Stokes component of η
θ	cylindrical coordinate
λ	wave length
$\lambda_{i,j}$	hydrodynamic damping
$\mu_{i,j}$	added mass
λ_{vis}	viscous damping
μ	damping function of absorbing BC

ν	coefficient in NLS
ξ	displacement of CFB
ρ	water density
τ	wave period
ϕ	velocity potential
ϕ_0	incident velocity potential
ϕ_j	radiation velocity potential, $j = 1, \ldots, 6$
ϕ_7	scattering velocity potential
ϕ_B	velocity potential of body disturbance
χ	wave direction
χ_0	main wave direction of progress
ψ	wave envelope
ψ_0	amplitude parameter for ψ
ω	wave frequency
ω_0	wave frequency of carrier wave
ω_p	peak frequency
Δt	time stepsize in t
ΔT	time stepsize in T
Δr	spatial stepsize in r
ΔX	spatial stepsize in X
Δz	spatial stepsize in z
ΔZ	spatial stepsize in Z
Ω	angular frequency

Matrices and Vectors

$\boldsymbol{n}$	normal vector
$\boldsymbol{r}$	position vector
$\boldsymbol{u}$	velocity vector
$\boldsymbol{F}$	hydrodynamic forces

Indices

min	minimum
max	maximum
K	Cartesian coordinates
Z	Cylindrical coordinates
(i)	i-th Stokes component

Points and Sets

C	set of points inside CFB
Ω	computational water domain
$\bar{\Omega}$	domain Ω for CFB in its resting position
$\mathring{\Omega}$	interior of Ω
$\partial\Omega$	boundary of Ω

Operators and Other Symbols

$()^*$	complex conjugate
$()^\mathrm{T}$	transpose
$\bar{()}$	mean

$\widehat{()}$	Fourier coefficient
$\lvert() \rvert$	absolute value
$\lvert() \rvert_{\mathrm{H}}$	height
$\lvert\lvert() \rvert\rvert_2$	euclidean norm
$\boldsymbol{\nabla}$	gradient
$\boldsymbol{\nabla}^2$	Laplace operator
$\mathcal{F}()$	Fourier transform
$\mathcal{H}()$	Hilbert transform

Introduction

Ships and offshore structures in the ocean differ widely in their geometric shape and submersed depth. When designing these structures, it is important that appropriate safety limits are taken into account. This can be done by knowing the hydrodynamic loads acting on the different mechanical structures. Here, the fluid-structure interaction (FSI) between the various mechanical structures and the incoming water waves must be analyzed.
In addition, the system response of mechanical structures to ocean waves can be of interest. This is the case, for example, when wave energy converters (WECs) are considered. These mechanical systems are placed in the ocean, and electrical energy is harvested from their motion. To increase the amount of harvested energy, the mechanical system has to be designed in such a way that the system shows large and fast motions in ocean waves. Again, this can be done by computing and analyzing the FSI between the corresponding mechanical structures and incoming water waves.
These are only two scenarios in which the FSI between waves and mechanical structures is of great importance. Since real ocean seas are nonlinear and random, an efficient analysis of the FSI between mechanical structures and random nonlinear water waves is of great interest in many areas of application.

1.1 Background and Motivation

In general, the behavior of fluids can be modeled using the Navier-Stokes equations. However, the numerical solution of these equations is computationally expensive. For many applications, however, it is often sufficient to consider the FSI within the potential flow theory [GreavesIglesias18, Lin08]. The nonlinear governing equations of the potential flow theory can be used to model the behavior of homogeneous, non-viscous, incompressible, and irrotational fluids, where surface tension effects are neglected.
The nonlinear governing equations of the potential flow theory contain boundary conditions at the unknown free water sea surface, which makes the computation of

solutions very difficult. Therefore, the nonlinear governing equations are simplified in many ocean engineering applications by applying Taylor series expansions, see e.g. [Mei83, MalenicaMolin95]. If only the corresponding first-order terms are considered, the linearized equations can be obtained, which can be solved with lower computational effort than the nonlinear governing equations.
The corresponding linearized wave theory can very well model the dynamics of water waves with small wave heights H and low wave velocities [Newman18]. However, a nonlinear wave theory must be used to model the behavior of larger and faster waves accurately. Corresponding nonlinear wave theories can be derived by considering the i-th order terms in the Taylor series expansions of the nonlinear governing equations, see e.g. [HollmSeifried23, MalenicaMolin95]. Figure 1.1 shows the limits of validity of the linear wave theory and the nonlinear wave theories of different orders according to [Le Méhauté76]. Here, g describes the acceleration due to gravity, h the water depth, τ the wave period, and λ the wavelength. It has to be noted that water waves cannot be assumed to be arbitrarily high, as they start to break at certain wave heights H and potential flow theory cannot be used to simulate wave breaking [Lin08]. It can also be seen that the limits of validity of the various wave theories depend on the water depth h.
Compared to the linear theory, nonlinear wave theories include additional wave effects that significantly influence the dynamics of waves. For example, the group velocity of waves is independent of the wave amplitude in linear wave theory. However, this changes when nonlinear wave theories of third order are used. Here, waves with a larger wave amplitude move faster than waves with a smaller wave amplitude [Newman18].
Also, within the linear theory, the sum of two solutions is also a solution. In this way, irregular seas can be calculated within the linear wave theory by the superposition of many regular waves, see e.g. [Faltinsen93]. However, the sum of two solutions is not a solution within nonlinear wave theories. Here, interactions between the different solutions must be calculated. Concerning the linear spectrum, this results in waves with the sums and differences of the frequencies, see e.g. [SharmaDean79]. If these frequencies coincide with the eigenfrequency of a given mechanical system, this can lead to relatively large movements of the system. For example, this could also have a positive effect on the performance of a WEC, as more energy can be harvested from a faster motion of a WEC.
Ocean waves have on average a wave steepness H/λ of $H/\lambda \approx 0.03 - 0.04$ [OnoratoEtAl13, TrulsenEtAl00]. Using the normalizations from Fig. 1.1, this means $H/(g\tau^2) \approx 0.005 - 0.006$ for deep water waves. Such a wave steepness of an average ocean wave can approximately be observed also by considering data of water waves, which have been measured at different positions in the North Sea and Baltic Sea. Data from corresponding real sea states are made publicly available in [BSH]. In addition to time series, monthly and annual statistics are provided in [BSH]. Figure 1.2 shows the locations of the buoys in the North Sea and Baltic

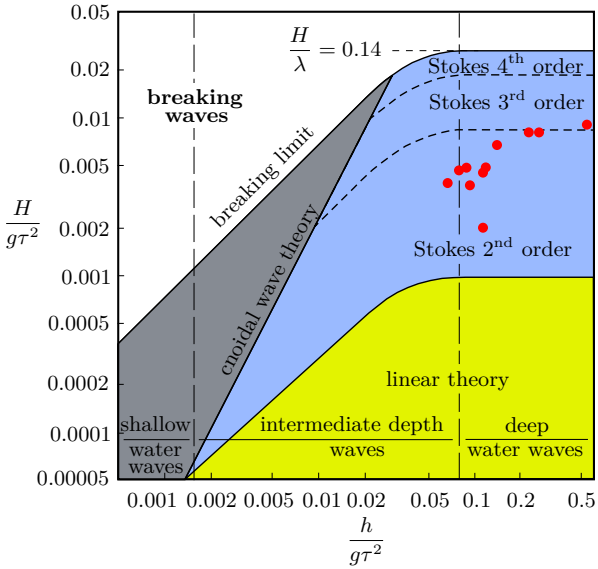

Figure 1.1: Limits of validity of different wave theories according to [Le Méhauté76]. The red dots illustrate how the data points from Tab. 1.1 are classified in the different wave theories.

Figure 1.2: Positions of the buoys listed in Tab. 1.1 taken from [BSH]. Map data is taken from [OpenStreetMap].

Sea, which have measured the data. The corresponding measured average sea state parameters are summarized in Tab. 1.1. Here, the significant wave height describes the mean value of the highest third of all measured waves. The peak period is defined as the wave period corresponding to the wave frequency, at

Table 1.1: Annual average real sea state parameters measured by buoys in the North Sea and Baltic Sea, taken from [BSH].

Name of buoy (year of measurement)	Water depth h [m]	Significant wave height [m]	Peak period [s]	$h/(g\tau^2)$ [-]	$H/(g\tau^2)$ [-]
Arkona (2021)	46	0.84	3	0.5210	0.0095
Elbe (2020)	25	1.05	4	0.1593	0.0067
FINO 1 (2021)	30	1.30	6	0.0849	0.0037
FINO 2 (2021)	24	0.76	3	0.2718	0.0086
FINO 3 (2021)	25	1.43	6	0.0708	0.0040
Helgoland Nord (2021)	30	1.15	5	0.1223	0.0047
Helgoland Süd (2021)	20	1.16	5	0.0815	0.0047
NSB-2 (2009)	42	1.55	6	0.1189	0.0044
NSB-3 (2012)	40	0.70	6	0.1133	0.0020
Westerland (2021)	13	1.04	5	0.0530	0.0042
Zingst (2019)	21	0.76	3	0.2379	0.0086

which the highest energy waves occur in the entire wave spectrum [ClaussEtAl88]. While the values of the significant wave height are given in [BSH], the values of the peak period were read from plots provided in [BSH]. The normalizations according to Fig. 1.1 are given to classify the measured values in a better way. The respective data from Tab. 1.1 are visualized as red dots in Fig. 1.1. It can be seen that an average sea state has been measured at all locations, which requires a nonlinear wave theory for accurate modeling according to the classification of [Le Méhauté76]. Thus, nonlinear random sea states should be used to analyze the behavior of mechanical systems in real ocean waves.

Various free and commercial codes are available to calculate the FSI with moving structures. Many codes, like OpenFOAM, STAR-CCM+ and REEF3D, solve the fully nonlinear Navier-Stokes equations with the inclusion of appropriate turbulence closure models. In theory, this set of equations can handle very complex phenomena with almost no limitations [Lin08]. However, solving this set of equations needs a large computational effort, which often requires high-performance computer facilities and well-trained staff [GreavesIglesias18]. This is a particular problem with stochastic sea states, as many simulations with long simulation times must be performed to describe the dynamics of a structure in random waves representatively.

Models using potential flow theory are the second most capable of simulating complex flows after those, which are based on the Navier-Stokes equations [GreavesIglesias18]. The nonlinear governing equations of potential flow theory can be solved, for example, using the Quasi Arbitrary Lagrangian-Eulerian Finite Element Method, which was first developed in [MaYan06]. Simulations using potential flow theory are faster than those using the Navier-Stokes equations in combination with an appropriate turbulence closure model, but their computational costs are still high [GreavesIglesias18, Lin08]. Even for the case that the nonlinear governing equations of potential flow theory are simplified applying the Taylor series expansions mentioned above, the calculation of the FSI in nonlinear water waves still requires long computation times. This is because

wave-wave interactions must be calculated for random nonlinear water waves, which can be very time-consuming [SlunyaevEtAl14].
However, there are other ways to describe nonlinear water waves. One is offered by using the nonlinear Schrödinger equation (NLS), which is a partial differential equation for the wave envelope of the water waves. The NLS can be used to accurately model nonlinear water waves in deep water with a narrow spectral bandwidth and moderate wave steepness H/λ of $H/\lambda \leq 0.05$ [Dysthe79, Witt19, Osborne10]. Using the normalizations from Fig. 1.1, this means $H/(g\tau^2) \leq 0.008$. It has to be noted that, on average, real ocean waves have a wave steepness H/λ of $H/\lambda \approx 0.03 - 0.04$ [OnoratoEtAl13, TrulsenEtAl00]. Furthermore, the ocean waves measured by buoys in [BSH] show such values for the wave steepness, see Tab. 1.1. Therefore, if the corresponding waves show a narrow spectral bandwidth, water waves presented in Tab. 1.1 can be modeled using the NLS.
The NLS has several advantages compared to the nonlinear governing equation of the potential flow theory. For example, a variety of analytical solutions of the NLS have been presented, see e.g. [CarterEtAl20, Peregrine83, SlunyaevEtAl13a]. Moreover, numerical solutions of the NLS can be computed much more efficiently than solutions of the nonlinear governing equation of the potential flow theory. These advantages make it interesting to use the NLS to compute the FSI between structures and nonlinear water waves.

1.2 Aim of the Work

An efficient calculation of the FSI between structures and real ocean waves is an important topic in many ocean engineering and naval architecture applications. The aim of this work is to establish a method, which can be used to calculate the FSI between a mechanical structure and random nonlinear water waves efficiently. The corresponding approach is based on the NLS. Compared to the nonlinear governing equations of potential flow theory, solutions of the NLS can be computed much more efficiently. The aim of this work is to use this efficiency to develop a method that allows the fast computation of the FSI between a mechanical structure and nonlinear water waves.
In contrast to the nonlinear governing equations of potential flow theory, several analytical solutions of the NLS are known. However, these analytical solutions of the NLS do not allow a description of irregular seas. To this end, an approach is proposed that enables the computation of random nonlinear water waves by perturbing analytical solutions of the NLS using irregular sea surfaces. This leads to the proposed approach, where random nonlinear water waves are computed using the NLS. This makes it possible to describe a method that employs the NLS

to compute the FSI between a structure and random nonlinear water waves. The new method is investigated with regard to its application areas, accuracy, stability, and computational efficiency. Regarding the computational efficiency, the aim of this work is to show that the NLS can be used to compute the FSI in random nonlinear water waves more efficiently than the use of classical random nonlinear water waves, in which the computation of corresponding wave-wave interactions is time-consuming.

1.3 Structure of the Work

Chapter 2 introduces the nonlinear governing equations, which can be used to describe the fluid motion within the potential flow theory. Furthermore, the corresponding linearized equations are introduced. Various solutions of the linearized equations are presented in the absence of any structure. Afterward, the effects of the presence and motion of a structure on the dynamics of the surrounding water waves are discussed.
The dynamics of a WEC for harvesting wave energy is investigated in the framework of linear wave theory in Chap. 3. The equations of motions of the WEC are presented for regular and random incoming water waves. The change in dynamics of a wave energy converter for different wave and system parameters is investigated. A control strategy for increasing the amount of harvested energy is presented.
Chapter 4 deals with nonlinear approximations of the nonlinear governing equations of fluid motion. Using Taylor series expansions and Stokes perturbation expansions, the nonlinear governing equations of fluid motion are transformed into a sequence of linear equations. Solutions of this sequence of linear equations are presented for incoming regular and random water waves. Based on this sequence of linear equations, it is presented how the FSI between a structure and nonlinear water waves can be calculated.
The NLS is introduced and investigated in Chap. 5. Based on the method described in Chap. 4, it is presented how the NLS can be used to compute the FSI in nonlinear water waves. The accuracy and stability of the developed method is investigated. Conclusions are drawn about the computational efficiency of the described scheme. Furthermore, an approach is proposed, which allows the consideration of random nonlinear water waves by perturbing analytical solutions of the NLS through irregular sea states. The effects of the corresponding perturbations on the dynamics of the water waves are shown by investigating the trajectories of water particles.
Chapter 4 and Chap. 5 presents the theoretical fundamentals and equations to

compute the FSI using the NLS. Afterward, a scheme is presented in Chap. 6 to compute the FSI numerically. The developed numerical scheme is verified and validated by comparing exemplary results of the presented scheme with corresponding results found in literature. Furthermore, the order of convergence of the presented numerical scheme is estimated.
In Chap. 7, the developed methods and numerical schemes are used to simulate the FSI between the WEC and nonlinear water waves using the NLS. Corresponding numerical results for the FSI are analyzed by studying the acting hydrodynamic forces and the motion of the WEC. Furthermore, effects of the presence of the WEC on the surrounding water waves are investigated. All results are presented using a linear and nonlinear wave theory, respectively. Furthermore, the effects of a perturbation of the analytical solutions of the NLS on the FSI are analyzed. Finally, the FSI is investigated in nonlinear water waves calculated using the classical approach where wave-wave interactions must be considered for computing random nonlinear water waves. In this way, the areas of application and computational efficiency of the developed scheme, which computes the FSI using the NLS, are investigated. Finally, Chap. 8 summarizes the results achieved in this work.

Fundamentals of Water Waves

In marine hydrodynamics, the effects of the wave environment on floating or fixed structures are studied. Of particular interest are the hydrodynamic loads acting on the various structures and the resulting motion of floating structures. Here, the motion of the bodies is purely resulting from the excitation of the waves. In addition, of engineering importance are the waves, which are generated by the presence and motion of structures [Newman18]. These problems are solved by describing and computing the fluid-structure interaction (FSI) between water waves and a floating or fixed structure. Depending on the underlying assumptions about the fluid, which has to be modeled, different descriptions can be used.

In this thesis, the behavior of homogeneous, incompressible, and non-viscous fluids is considered, where surface tension effects are neglected. Here, the fluid behavior is modeled using potential flow theory. Details about the potential flow theory can be found, for example, in [Newman18]. In general, water is viscous, and viscosity effects affect the motion of floating mechanical structures. However, they can be neglected if both the water amplitude and the wavelength of the incoming waves are small compared to the characteristic length of the mechanical structure [Faltinsen93]. Furthermore, surface tension effects are negligible if the wavelength of the water waves is substantially longer than 1.7 cm, at which point gravitational and surface tension effects are equal [YuenLake80].

This chapter introduces all fundamental equations to model the FSI between ocean waves and floating mechanical structures. The fully nonlinear governing equations of fluid motion are presented to model the dynamics of an inviscid, incompressible, and irrotational fluid. Furthermore, the boundary condition (BC) at the wetted surface of the structure is formulated. Here, it is assumed that the structure is impermeable to water. Knowing the temporal behavior of the water waves as well as the dynamics of the water beyond the sea surface, the hydrodynamic pressure acting on mechanical systems is computed using Bernoulli's equation. This allows the calculation of the corresponding hydrodynamic loads and the motion of structures floating in the real sea.

The content of this chapter is as follows: In Sect. 2.1, all fundamental equations are introduced to describe the nonlinear FSI. Then, the corresponding linearized governing equations are presented in Sect. 2.2, which are used to model linear regular and random waves. Finally, it is shown in Sect. 2.3 how the disturbance of a fixed or floating mechanical structure on the wave dynamics can be modeled using the linearized governing equations.

2.1 General Theory

The behavior of homogeneous, non-viscous, incompressible fluids, where surface tension effects are neglected, is considered. Let t denote the time and K: $\{O, x, y, z\}$ be a Cartesian coordinate system, whereby $z = 0$ describes the plane of the undisturbed free sea surface and the z-axis is positive upwards, see Fig. 2.1. The vertical displacement of any point on the free sea surface may be defined by the function $z = \eta = \eta(x, y, t)$. Here, it is assumed that the water waves are not breaking such that the value of $\eta(x, y, t)$ is uniquely defined everywhere.
Furthermore, it is assumed that the fluid is irrotational. This means that the curl of the flow velocity $\boldsymbol{v} \in \mathbb{R}^3$ vanishes everywhere in the fluid, i. e. it holds

$$\boldsymbol{\nabla} \times \boldsymbol{v} = 0. \tag{2.1}$$

Here, $\boldsymbol{\nabla}$ is the gradient operator. It can be shown that a fluid, which is not viscous and in which the fluid motion starts from an initial rest state, remains irrotational for all times [Stoker57]. Then there exists a velocity potential $\phi = \phi(x, y, z, t)$ such that the gradient of the velocity potential $\boldsymbol{\nabla}\phi$ is the velocity vector $\boldsymbol{v}$ of the fluid flow, i. e. $\boldsymbol{\nabla}\phi = \boldsymbol{v}$. Using this notation, the governing equations of fluid motion are given by, see e.g. [Newman18],

$$\boldsymbol{\nabla}^2\phi = \phi_{xx} + \phi_{yy} + \phi_{zz} = 0, \qquad \text{for} \quad -h \le z \le \eta(x, y, t), \tag{2.2a}$$

$$\eta_t + \phi_x\eta_x + \phi_y\eta_y = \phi_z, \qquad \text{for} \quad z = \eta(x, y, t), \tag{2.2b}$$

$$\phi_t + \frac{1}{2}\boldsymbol{\nabla}\phi \cdot \boldsymbol{\nabla}\phi + g\eta = 0, \qquad \text{for} \quad z = \eta(x, y, t), \tag{2.2c}$$

$$\phi_z = 0, \qquad \text{for} \quad z = -h. \tag{2.2d}$$

Here and in the rest of this work, f_s denotes the partial derivative of a function f with respect to the coordinate $s \in \{x, y, z, t\}$, i. e. $f_s := \dfrac{\partial f}{\partial s}$. Furthermore, $\boldsymbol{\nabla}^2$ denotes the Laplace operator in space, g is the gravitational acceleration, and h is the constant water depth. The sea bottom is assumed to be a rigid plane that is impermeable to water. Here, Eq. (2.2a) is the conservation of mass, Eq. (2.2b) is the kinematic BC at the free sea surface, Eq. (2.2c) is the conservation of momentum at the free sea surface, and Eq. (2.2d) is the kinematic BC at the bottom. The governing Eqs. (2.2a)-(2.2d) are diagrammed in Fig. 2.1. It has to be noted that the external pressure exerted on the sea surface η is assumed to be zero.
The dynamics of water waves on the open sea can be computed by solving Eq. (2.2). However, if there are additional boundaries like the surface of walls or mechanical structures like ships and offshore structures, additional equations have to be formulated to model the corresponding FSI. In this section, general floating and submerged bodies are considered, which are rigid and impermeable to water. They can be fixed or freely floating structures, as well as the intermediate category

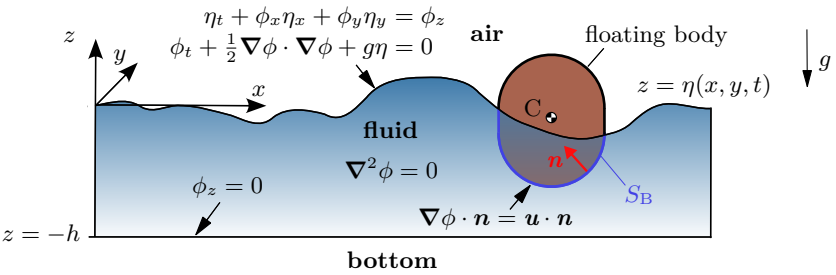

Figure 2.1: Governing equations of the nonlinear water wave problem and the FSI with a floating body of arbitrary shape.

of moored structures. In order to obtain water impermeability, the fluid at a point next to the moving structure must have the same velocity in the normal direction as the body itself at that point. Let S_B be the wetted surface of the mechanical body and $\boldsymbol{u}$ the velocity of a point on S_B. Then the kinematic BC at the surface of the body is given by

$$\nabla\phi\cdot\boldsymbol{n} = \boldsymbol{u}\cdot\boldsymbol{n}, \quad \text{for } (x,y,z)\in S_\mathrm{B}, \tag{2.3}$$

whereby $\boldsymbol{n}$ denotes the normal vector at S_B pointing out of the fluid and hence into the body. Equation (2.3) as well as the wetted surface S_B of a floating body of arbitrary shape is also shown in Fig. 2.1. The velocity vector $\boldsymbol{u}$ at any point on S_B can be described using the velocity $\dot{\boldsymbol{x}}_\mathrm{C}$ of the geometric center C of the body, the vector of angular velocity $\boldsymbol{\omega}$, and the position vector $\boldsymbol{r}$ from C to the corresponding point on S_B. Then the kinematic BC at the surface of the body reads accordingly, see e.g. [Newman18],

$$\nabla\phi\cdot\boldsymbol{n} = (\dot{\boldsymbol{x}}_\mathrm{C} + \boldsymbol{\omega}\times\boldsymbol{r})\cdot\boldsymbol{n}, \quad \text{for } (x,y,z)\in S_\mathrm{B}. \tag{2.4}$$

It has to be noted that in the presence of the body, Eq. (2.2) only holds for all points inside the fluid and outside the rigid body. However, in order to simplify the notation, these restrictions are neglected in the notation of Eq. (2.2). This simplified notation is also applied to the simplified and linearized equations, which are presented in the further course of this thesis.
After computing the velocity potential ϕ and the surface displacement η, the hydrodynamic pressure p can be calculated by means of Bernoulli's equation as

$$p(x,y,z,t) = -\rho\left(\phi_t + \frac{1}{2}\nabla\phi\cdot\nabla\phi + gz\right). \tag{2.5}$$

Here, ρ denotes the density of the fluid.

Finally, integrating the pressure over S_B, the hydrodynamic force $\boldsymbol{F}$ and torque $\boldsymbol{M}$ with respect to C acting on the body are given by

$$\boldsymbol{F} = \iint\limits_{S_\mathrm{B}} p\boldsymbol{n}\,\mathrm{d}S, \quad \boldsymbol{M} = \iint\limits_{S_\mathrm{B}} p(\boldsymbol{r}\times\boldsymbol{n})\,\mathrm{d}S. \tag{2.6}$$

2.2 Linearized Theory

The nonlinear BCs (2.2b) and (2.2c) at the unknown location of the free sea surface make the computation of a solution of the nonlinear governing equations of fluid motion (2.2) very difficult. Therefore, the corresponding linearized equations, which can be solved with lower computational effort, are considered in many fluid dynamics applications.
If the sea surface displacement η is sufficiently small, the slopes η_x and η_y are small quantities and of the same order of magnitude as η_t. Similarly, if the fluid velocity is a small quantity that is proportional to the wave motion, the derivatives ϕ_x, ϕ_y, and ϕ_z are also small [Newman18]. Then the nonlinear terms in Eqs. (2.2b) and (2.2c) become quadratically small and the corresponding BCs reduce to

$$\eta_t = \phi_z, \qquad \text{for} \quad z = 0, \tag{2.7a}$$

$$\phi_t + g\eta = 0, \qquad \text{for} \quad z = 0. \tag{2.7b}$$

It has to be noted that these BCs should be applied on the free sea surface $z = \eta$. However, under the assumption of small sea surface displacements η, it is common to apply these linearized BCs on the undisturbed free sea surface at $z = 0$. Taking the derivative of Eq. (2.7b) with respect to time, the two linearized BCs at $z = 0$ can be combined to

$$\phi_{tt} + g\phi_z = 0, \qquad \text{for} \quad z = 0. \tag{2.8}$$

Using Eq. (2.8) as BC at $z = 0$, the velocity potential ϕ can be computed below the still water level at $z = 0$.
It has to be noted that Eq. (2.8) does not apply when a floating structure, like a ship, has a steady forward velocity or a current is present around the structure [Faltinsen93]. Extended versions of Eqs. (2.7) and (2.8), which include the effects of a steady forward velocity of a floating structure or a current, are derived and discussed in [Faltinsen93, SkourupEtAl00, ShaoFaltinsen13]. To make the scope of this thesis not too extensive, the effects of a steady forward velocity of a floating structure or a current on the FSI are not discussed. In the following,

it is assumed that the floating structure has no steady forward velocity and no current is present around it.
The BC at the wetted surface of the structure S_B, which is time-dependent, is given by Eq. (2.4). However, computing the velocity potential ϕ only below the still water level at $z = 0$, it is sufficient to satisfy the BC (2.4) only on the surface of the body $S_{\mathrm{B}0}$, which is located below the still water level at $z = 0$, i. e.

$$S_{\mathrm{B}0} := \{(x, y, z) \in \text{surface of body} \mid z \leq 0\}. \tag{2.9}$$

Then Eq. (2.4) becomes

$$\boldsymbol{\nabla}\phi \cdot \boldsymbol{n} = (\dot{\boldsymbol{x}}_\mathrm{C} + \boldsymbol{\omega} \times \boldsymbol{r}) \cdot \boldsymbol{n}, \quad \text{at } (x, y, z) \in S_{\mathrm{B}0}. \tag{2.10}$$

Therefore, using Eqs. (2.2a), (2.2d), (2.8), and (2.10), the linearized governing equations of fluid motion are given by

$$\boldsymbol{\nabla}^2\phi = \phi_{xx} + \phi_{yy} + \phi_{zz} = 0, \qquad \text{for} \quad -h \leq z \leq 0, \tag{2.11a}$$
$$\phi_{tt} + g\phi_z = 0, \qquad \text{for} \quad z = 0, \tag{2.11b}$$
$$\phi_z = 0, \qquad \text{for} \quad z = -h, \tag{2.11c}$$
$$\boldsymbol{\nabla}\phi \cdot \boldsymbol{n} = (\dot{\boldsymbol{x}}_\mathrm{C} + \boldsymbol{\omega} \times \boldsymbol{r}) \cdot \boldsymbol{n}, \quad \text{at} \quad (x, y, z) \in S_{\mathrm{B}0}. \tag{2.11d}$$

After solving these equations to obtain the velocity potential ϕ, the corresponding sea surface displacement η can be computed by rearranging Eq. (2.7b). It holds

$$\eta = -\frac{1}{g}\phi_t, \qquad \text{for} \quad z = 0. \tag{2.12}$$

The total pressure inside the fluid can be obtained using the linearized Bernoulli equation, which can be obtained by retaining only the first-order linear terms of Eq. (2.5). Then, the total linearized pressure is given by

$$p(x, y, z, t) = -\rho\left(\frac{\partial\phi}{\partial t} + gz\right). \tag{2.13}$$

In the following, different solutions of the linearized governing equations of fluid motion from Eq. (2.11) are presented.

2.2.1 Regular Waves

In the absence of a structure, regular waves are the simplest waves, which satisfy the linear wave equations (2.11a)-(2.11c). For incoming regular waves with wave amplitude A and angular frequency ω, which is referred to in the following as the wave frequency, the sea surface displacement η is given by

$$\eta(x, y, t) = A\cos\left(k\left[\cos(\chi)x + \sin(\chi)y\right] - \omega t + \beta\right). \tag{2.14}$$

Here, k is the wave number, χ is the angle between the wave direction and the x-axis, and β is a phase shift. As presented, for example, in [SharmaDean79, MalenicaMolin95], the corresponding velocity potential ϕ is given by

$$\phi(x,y,z,t) = \frac{gA}{\omega}\frac{\cosh(k(z+h))}{\cosh(kh)}\sin\left(k\left[\cos(\chi)x+\sin(\chi)y\right]-\omega t+\beta\right). \quad (2.15)$$

Substituting Eq. (2.15) into Eq. (2.8), it results that the upper BC (2.8) is satisfied only if the wave frequency ω and wave number k are related by

$$\omega^2 = kg\tanh(kh). \quad (2.16)$$

This relation, which is the so-called dispersion relation, can be used to implicitly compute the wave number k for a given wave frequency ω and water depth h. Having calculated k and ω, the wave period τ and wavelength λ of the regular wave from Eq. (2.14) are given by

$$\tau = \frac{2\pi}{\omega}, \quad \lambda = \frac{2\pi}{k}. \quad (2.17)$$

Conversely, for a given wavelength λ and water depth h, Eq. (2.16) can be used to calculate the wave frequency ω.
Let $w_{\mathrm{pd}}(x,y) := \cos(\chi)x + \sin(\chi)y$ be the propagation direction of the wave described by Eq. (2.14). For an observer moving with the water wave, the shape of the wave does not change if the velocity of the observer is chosen in such a way that the phase $\vartheta(w_{\mathrm{pd}},t) := kw_{\mathrm{pd}} - \omega t + \beta$ remains constant [ClaussEtAl88]. It has to hold $\vartheta(w_{\mathrm{pd}},t) = \vartheta(w_{\mathrm{pd}} + \mathrm{d}w_{\mathrm{pd}}, t + \mathrm{d}t)$, whereby $\mathrm{d}w_{\mathrm{pd}}$ and $\mathrm{d}t$ are infinitesimally small shifts in space and time. This is true if the observer moves with the velocity

$$c_{\mathrm{ph}} = \frac{\mathrm{d}w_{\mathrm{pd}}}{\mathrm{d}t} = \frac{\omega}{k} = \frac{\lambda}{T}. \quad (2.18)$$

This is the so-called phase velocity of the water wave. Using Eq. (2.16), it follows

$$c_{\mathrm{ph}} = \sqrt{\frac{g}{k}\tanh(kh)}. \quad (2.19)$$

It can be seen that the phase velocity c_{ph} depends on the wave number k and the water depth h. It results that water waves with a longer wavelength $\lambda = 2\pi/k$ propagate faster than waves with a shorter wavelength. This phenomenon is generally known as dispersion. For this reason, Eq. (2.16) is called the dispersion relation. For very long waves resulting, for example, from a seaquake or a volcanic eruption, propagation speeds of over 500 km/h have already been observed on the open sea [ClaussEtAl88].
For very large water depths, the dispersion relation from Eq. (2.16), as well as the expressions for the velocity potential ϕ from Eq. (2.15) and the phase velocity c_{ph} from Eq. (2.19), can be simplified. In the field of fluid dynamics, it is common to define deep water conditions when the water depth is larger than half the

wavelength of the present water waves, i. e. $h \geq \frac{1}{2}\lambda$, see e.g. [ClaussEtAl88]. In this case, the velocity potential corresponding to the sea surface displacement from Eq. (2.14) is given by

$$\phi(x, y, z, t) = \frac{gA}{\omega} \mathrm{e}^{kz} \sin\left(k\left[\cos(\chi)x + \sin(\chi)y\right] - \omega t + \beta\right). \tag{2.20}$$

Here, the wave number k and frequency ω have to fulfill the dispersion relation

$$\omega^2 = kg. \tag{2.21}$$

In the same way, the expression for the phase velocity c_{ph} from Eq. (2.19) simplifies to

$$c_{\mathrm{ph}} = \sqrt{\frac{g}{k}}. \tag{2.22}$$

2.2.2 Irregular Seas

The sea surface displacement η from Eq. (2.14) as well as the corresponding velocity potential ϕ from Eqs. (2.15) and (2.20) only describe regular water waves. In general, a realistic sea surface is not regular but irregular or random. In order to model a realistic irregular sea surface, a superposition of many regular waves can be used. In the linear theory described by the linearized Eqs. (2.11), the sum of regular solutions is also a solution. Interactions between regular waves are not considered.

In this section, irregular seas are modeled by superposing regular waves with frequencies ω, corresponding wave numbers k, amplitudes A, propagation directions χ and phase angles β. Here, the amplitudes are obtained from the corresponding one-sided spectral density $S(\omega)$ [Faltinsen93, ClaussEtAl88], which can be found by measurements of the free sea surface displacements. Common sea spectral densities $S(\omega)$ are the Pierson-Moskowitz (PM) spectrum for deep water and the Joint North Sea Wave Project (JONSWAP) spectrum for shallow water waves. Both spectra can be expressed as a function of peak frequency ω_{p} and significant wave height H_{s}, see e.g. [ClaussEtAl88]. The peak frequency is defined as the wave frequency at which the highest energy waves occur in the entire wave spectrum. The significant wave height describes the average value of the highest third of the waves. Using these two parameters, the PM-spectrum and JONSWAP-spectrum are given by, see e.g. [Sichermann09],

$$S_{\mathrm{PM}}(\omega) = 0.3125 H_{\mathrm{s}}^2 \frac{\omega_{\mathrm{p}}^4}{\omega^5} \exp\left[-1.25\left(\frac{\omega_{\mathrm{p}}}{\omega}\right)^4\right] \tag{2.23}$$

and

$$S_{\mathrm{JON}}(\omega) = 0.2059 H_{\mathrm{s}}^2 \frac{\omega_{\mathrm{p}}^4}{\omega^5} \exp\left[-1.25\left(\frac{\omega_{\mathrm{p}}}{\omega}\right)^4\right] \gamma_{\mathrm{PEF}}^{\exp\left[-0.5\left(\omega-\omega_{\mathrm{p}}\right)^2/\left(b\omega_{\mathrm{p}}\right)^2\right]}, \tag{2.24}$$

with the peak enhancement factor $\gamma_{\mathrm{PEF}} = 3.3$ and $b = 0.07$ for $\omega < \omega_{\mathrm{p}}$ and $b = 0.09$ for $\omega > \omega_{\mathrm{p}}$. Similar to S_{JON}, there are other spectra with different peak enhancement factors γ_{PEF}, see e.g. [LeeEtAl22, GraingerEtAl21]. A review about the common models of the wind wave spectrum can be found in [RyabkovaEtAl19]. Figure 2.2a shows the spectra S_{PM} and S_{JON} for $\omega_{\mathrm{P}} = 1\,\mathrm{rad/s}$ and $H_{\mathrm{s}} = 2$. It can be seen that the JONSWAP-spectrum contains most of its energy in a narrower frequency band than the PM-spectrum.
The angle χ describes the propagation direction of the individual regular waves. The distribution of the propagation directions is given by the spread function $D(\chi)$, which causes a scattering in the propagation directions of the regular waves. The spread function $D(\chi)$ has to be normalized in such a way that

$$\int_{-\pi}^{\pi} D(\chi)\,\mathrm{d}\chi = 1 \tag{2.25}$$

is fulfilled.
One of the simplest used spread functions is the Cosine-squared distribution [Hughes85, CorbellaStretch14]. An example of such a spread function with an adjustable spreading width is given by

$$D(\chi) = \frac{2}{\chi_{\mathrm{R}}} \cos^2\left(\frac{\pi}{\chi_{\mathrm{R}}}\left(\chi - \chi_0\right)\right), \quad \text{for } |\chi - \chi_0| \leq \frac{\chi_{\mathrm{R}}}{2}, \tag{2.26}$$

see [DostalEtAl23, Lloyd89]. Here, the propagation directions of the regular waves are distributed around the main direction of progress of the waves χ_0 by means of a quadratic cosine function. The coefficient χ_{R} indicates the range of propagation directions from which regular waves can come. Figure 2.2b shows the spread function $D(\chi)$ for $\chi_0 = 0$ and $\chi_{\mathrm{R}} = \pi$. Alternative propagation functions can be found in [MitsuyasuEtAl75].
Given a sea spectrum $S(\omega)$ and spread function $D(\chi)$, an irregular sea surface displacement can be determined by, see e.g. [Faltinsen93, SharmaDean79].

$$\begin{aligned}\eta(x,y,t) = \sum_{m=1}^{M_\omega}\sum_{n=1}^{N_\chi} &\cos(k(\omega_m)\left[\cos(\chi_n)x + \sin(\chi_n)y\right] - \omega_m t + \beta(\omega_m,\chi_n)) \\ &\times \sqrt{2S(\omega_m)D(\chi_n)\Delta\omega_m\Delta\chi_n}.\end{aligned} \tag{2.27}$$

Here, the spectrum $S(\omega)$ is discretized in M_ω parts with respective widths $\Delta\omega_m$ and frequencies $\omega_m \in [\omega_{\min}, \omega_{\max}]$, which do not need to be equidistant. In the same way, the propagation directions are discretized in N_χ parts with respective widths $\Delta\chi_n$ and directions $\chi_n \in [-\pi, \pi]$. Furthermore, $\beta(\omega_m, \chi_n)$ is a random phase shift, which is uniformly distributed in the interval $[0, 2\pi)$. Since the phase shifts are randomly distributed, waves of the form as in Eq. (2.27) are so-called random waves.

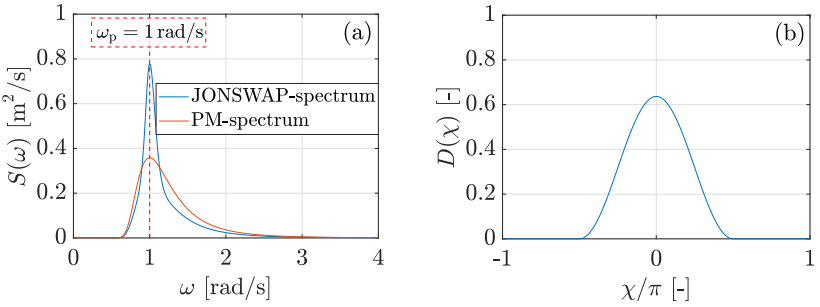

Figure 2.2: (a): PM-spectrum and JONSWAP-spectrum with the parameters $\omega_P = 1\,\text{rad/s}$ and $H_s = 2$. (b): Spread function $D(\chi)$ for $\chi_0 = 0$ and $\chi_R = \pi$.

Waves calculated using Eq. (2.27), whose components propagate in different directions, are so-called short-crested waves [Newman18]. As a simpler alternative, all wave components can be assumed to be unidirectional with propagation direction χ_0. Irregular seas of this form are so-called long-crested seas because the wave crests are parallel and the fluid motion is two-dimensional [Newman18]. The sea surface displacement η of long-crested water waves can be determined by, see e.g. [Faltinsen93],

$$\eta(x,y,t) = \sum_{m=1}^{M_\omega} \cos(k(\omega_m)\,[\cos(\chi_0)x + \sin(\chi_0)y] - \omega_m t + \beta(\omega_m))\sqrt{2S(\omega_m)\Delta\omega_m}. \tag{2.28}$$

Figure 2.3 depicts a short-crested as well as a long-crested sea using $H_s = 2\,\text{m}$ and $\omega_p = 1\,\text{rad/s}$. The wave surfaces of both seas have been calculated using $M_\omega = 50$ components of the spectrum and $\chi_0 = 0$. For the short-crested sea, regular waves propagating in $N_\chi = 41$ different directions are used, ranging from $-\chi_R/2$ to $\chi_R/2$ with $\chi_R = \pi$.
Comparing the Eq. (2.27) with Eq. (2.28), it can be seen that the calculation of the long-crested seas requires much lower computational effort. While a short-crested sea consists of $M_\omega \times N_\chi$ regular wave components, a long-crested sea consists only of M_ω regular wave components. Therefore, the number of regular function evaluations and the computation time is reduced significantly going from short-crested to long-crested waves.
After calculating the sea surface displacement of a random wave, which is obtained from the superposition of various regular wave components, the corresponding velocity potential ϕ can be calculated by superimposing the potentials of the related regular wave components. The velocity potential of a regular wave is given by Eq. (2.15).

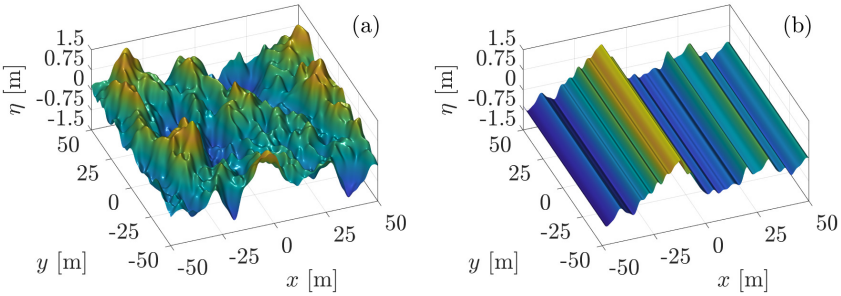

Figure 2.3: Example of a (a) short-crested and (b) long-crested sea.

2.3 Influence of the Body

In the previous section, various solutions of the linearized governing equations of fluid motion from Eq. (2.11) have been presented in the absence of any body. However, in the presence of a body, the fluid dynamics are disturbed by the body. The effects of the disturbance is discussed in the following.
From a physical point of view, the incoming water waves are diffracted on the wetted surface of the body and scattered in all directions. Furthermore, the incoming water waves set the body into motion. This motion generates additional waves, which move out in all directions. In mathematical terms, the linearity of the problem allows the velocity potential of the fluid to be decomposed into a sum of different velocity potentials of the form

$$\phi = \phi_0 + \phi_7 + \sum_{j=1}^{6} \phi_j, \tag{2.29}$$

see e.g. [Newman18, ClaussEtAl88, Mei83]. The different velocity potentials are defined as follows:

- ϕ_0: This is the incident potential of the incoming water waves, which are not disturbed by the presence of the body. The potential ϕ_0 is given by Eq. (2.15) for incoming regular water waves.
- ϕ_7: This is the scattering potential representing the reflections of the incoming waves at the surface of a non-moving body.
- ϕ_j for $j = 1, \ldots, 6$: These are the radiation potential caused by the motion of the body in direction j. Here, $j = 1, 2, 3$ represent the translational motion of the body in the x-, y- and z-direction and $j = 4, 5, 6$ the rotational motion about the x-, y-, and z-axis, respectively.

It is also convenient to define two combinations of the velocity potentials mentioned above, see e.g. [Newman18]:

- $\phi_\mathrm{D} = \phi_0 + \phi_7$: This is known as the diffraction potential.
- $\phi_\mathrm{B} = \phi_7 + \sum_{j=1}^{6} \phi_j$: This is known as the potential corresponding to the body disturbance.

While the incident velocity potential ϕ_0 can be written in closed-form expressions, the scattering and radiation potentials can generally only be computed numerically. The governing equations to calculate these potentials are presented in the following.
In the linear case, the interaction between the fluid and the body is described by Eq. (2.10). Substituting Eq. (2.29) into Eq. (2.10) yields

$$\boldsymbol{\nabla}\phi_0 \cdot \boldsymbol{n} + \boldsymbol{\nabla}\phi_7 \cdot \boldsymbol{n} + \sum_{j=1}^{6} \boldsymbol{\nabla}\phi_j \cdot \boldsymbol{n} = (\dot{\boldsymbol{x}}_\mathrm{C} + \boldsymbol{\omega} \times \boldsymbol{r}) \cdot \boldsymbol{n} \quad \text{at } (x, y, z) \in S_{\mathrm{B}0}. \tag{2.30}$$

Algebraic calculations show that this equation is fulfilled for

$$\boldsymbol{\nabla}\phi_j \cdot \boldsymbol{n} = (\dot{\boldsymbol{x}}_\mathrm{C} \cdot \boldsymbol{n})_j\,, \qquad \text{for } (x, y, z) \in S_{\mathrm{B}0},\ j \in \{1, 2, 3\}, \tag{2.31a}$$

$$\boldsymbol{\nabla}\phi_j \cdot \boldsymbol{n} = ((\boldsymbol{\omega} \times \boldsymbol{r}) \cdot \boldsymbol{n})_{j-3}\,, \qquad \text{for } (x, y, z) \in S_{\mathrm{B}0},\ j \in \{4, 5, 6\}, \tag{2.31b}$$

$$\boldsymbol{\nabla}\phi_7 \cdot \boldsymbol{n} = -\boldsymbol{\nabla}\phi_0 \cdot \boldsymbol{n}, \qquad \text{for } (x, y, z) \in S_{\mathrm{B}0}. \tag{2.31c}$$

Here, $(\boldsymbol{x})_j$ describes the j-th component of the vector $\boldsymbol{x} \in \mathbb{R}^3$. Equation (2.31) describes the BCs at the interface between the fluid and the body.
It has to be noted that the linearized governing equations of fluid motion from Eqs. (2.11a)-(2.11c) are satisfied by the incident velocity potential ϕ_0. Therefore, substituting Eq. (2.29) into Eqs. (2.11a)-(2.11c) shows that the scattering and radiation potentials have to fulfill the Eqs. (2.11a)-(2.11c) as well. Together with the BC (2.31), the velocity potentials ϕ_j, $j = 1, \ldots, 7$, have to satisfy

$$\boldsymbol{\nabla}^2\phi_j = 0, \qquad \text{for } -h \le z \le 0, \tag{2.32a}$$

$$\phi_{j,tt} + g\phi_{j,z} = 0, \qquad \text{for } z = 0, \tag{2.32b}$$

$$\phi_{j,z} = 0, \qquad \text{for } z = -h, \tag{2.32c}$$

$$\boldsymbol{\nabla}\phi_j \cdot \boldsymbol{n} = (\dot{\boldsymbol{x}}_\mathrm{C} \cdot \boldsymbol{n})_j\,, \qquad \text{for } (x, y, z) \in S_{\mathrm{B}0},\ j \in \{1, 2, 3\}, \tag{2.32d}$$

$$\boldsymbol{\nabla}\phi_j \cdot \boldsymbol{n} = ((\boldsymbol{\omega} \times \boldsymbol{r}) \cdot \boldsymbol{n})_{j-3}\,, \qquad \text{for } (x, y, z) \in S_{\mathrm{B}0},\ j \in \{4, 5, 6\}, \tag{2.32e}$$

$$\boldsymbol{\nabla}\phi_7 \cdot \boldsymbol{n} = -\boldsymbol{\nabla}\phi_0 \cdot \boldsymbol{n}, \qquad \text{for } (x, y, z) \in S_{\mathrm{B}0}. \tag{2.32f}$$

However, the boundary-value problem described by Eq. (2.32) does not offer a unique solution. In particular, if ϕ_j, $j = 1, \ldots, 7$, is a solution of Eq. (2.32), then $\phi_j + c\,(\phi_0 + \phi_7)$ is also a solution of Eq. (2.32) for any constant $c \in \mathbb{R}$. In order to overcome this problem, a radiation condition at infinity has to be imposed. This condition has to state that the waves on the free sea surface, other

than those due to the incident velocity potential ϕ_0 itself, are resulting from the presence of the body [Newman18]. Therefore, the waves corresponding to the velocity potentials ϕ_j, $j = 1, \ldots, 7$, have to propagate away from the body. For time-harmonic motion excited by waves of the form from Eq. (2.14) with wave number k, the radiation condition to be satisfied is given by [Wehausen71] as

$$\lim_{r\to\infty} \sqrt{r}\,(\varphi_{j,r} - \mathrm{i}k\varphi_j) = 0, \qquad \text{for } j = 1, \ldots, 7, \quad r = \sqrt{x^2 + y^2}. \tag{2.33}$$

Here, it has been assumed that the velocity potentials ϕ_j are harmonic in time and can be expressed in the form $\phi_j = \mathrm{Re}\{A\varphi_j \mathrm{e}^{-\mathrm{i}\omega t}\}$ for some function $\varphi_j = \varphi_j(x, y, z)$, $j = 1, \ldots, 7$. It has to be noted that the incident velocity potential ϕ_0 is excluded from the radiation condition.
After calculating the scattering and radiation potentials ϕ_j, $j = 1, \ldots, 7$, using Eqs. (2.32) and (2.33), the corresponding hydrodynamic pressure can be computed by substituting Eq. (2.29) into the linearized Bernoulli equation (2.13). Finally, the hydrodynamic forces and torques acting on the body can be computed using Eq. (2.6). Since only small sea surface displacements η are considered in the linearized wave theory, the forces and torques will be computed by integrating the pressure over S_{B0} instead of S_{B}. It results

$$\boldsymbol{F} = \underbrace{-\rho \iint\limits_{S_{\mathrm{B0}}} (\phi_{0,t} + \phi_{7,t})\, \boldsymbol{n}\, \mathrm{d}S}_{\boldsymbol{F}_1} \underbrace{-\rho \iint\limits_{S_{\mathrm{B0}}} \left(\sum_{j=1}^{6} \phi_{j,t}\right) \boldsymbol{n}\, \mathrm{d}S}_{\boldsymbol{F}_2} \underbrace{-\rho g \iint\limits_{S_{\mathrm{B0}}} z\boldsymbol{n}\, \mathrm{d}S}_{\boldsymbol{F}_3} \tag{2.34}$$

and

$$\begin{aligned} \boldsymbol{M} = &\underbrace{-\rho \iint\limits_{S_{\mathrm{B0}}} (\phi_{0,t} + \phi_{7,t})\, (\boldsymbol{r} \times \boldsymbol{n})\, \mathrm{d}S}_{\boldsymbol{M}_1} \underbrace{-\rho \iint\limits_{S_{\mathrm{B0}}} \left(\sum_{j=1}^{6} \phi_{j,t}\right) (\boldsymbol{r} \times \boldsymbol{n})\, \mathrm{d}S}_{\boldsymbol{M}_2} \\ &\underbrace{-\rho g \iint\limits_{S_{\mathrm{B0}}} z(\boldsymbol{r} \times \boldsymbol{n})\, \mathrm{d}S}_{\boldsymbol{M}_3}. \end{aligned} \tag{2.35}$$

The related terms in Eqs. (2.34) and (2.35) represent distinctly different contributions to the total force and torque acting on the body, respectively. The first components, $\boldsymbol{F}_1$ and $\boldsymbol{M}_1$, are the excitation force and torque, which are proportional to the amplitude of the incoming wave. The second components, $\boldsymbol{F}_2$ and $\boldsymbol{M}_2$, result from the motion of the body. They are dependent on the velocity and acceleration of the structure. The third components, $\boldsymbol{F}_3$ and $\boldsymbol{M}_3$, are the hydrostatic components representing the buoyancy force and the corresponding torque acting on the body. These three contributions are discussed separately in the next chapter, where the FSI between a given mechanical body and linear water waves is investigated.

Chapter 3

Analysis of a Wave Energy Converter using Linear Wave Theory

In the previous chapter, fundamental equations have been introduced to model the dynamics of a fluid without and with the presence of a mechanical structure. Analyzing the linearized equations (2.11), it has been shown that the velocity potential of the fluid, which is disturbed by the presence of a structure, can be computed by a sum of components ϕ_j. The different components ϕ_j lead to different load components acting on the structure, see Eqs. (2.34) and (2.35). In this chapter, the FSI between a linearized sea and a prescribed floating mechanical structure is analyzed. Here, the effects of the introduced load components on the motion of the structure are investigated. In addition, the effects of various system and fluid parameters on the dynamics of the structure are investigated. Relevant parameters could be, for example, the mass and size of the mechanical system or the amplitude and frequency of the incoming water waves.

As a given mechanical system, a wave energy converter (WEC) is considered. These systems are placed in the real sea, and electrical energy is harvested from their motion. Because of its high power density compared to solar and wind energy, wave energy is promising for future power generation [McCormick13]. Therefore, several new concepts for WECs have been investigated in the last years, see e.g. [VaziriEtAl14, YurchenkoAlevras18, DostalPick19]. Moreover, many ways to harvest energy from water waves are summarized in [DrewEtAl09]. However, there are still big challenges in wave energy harvesting, since up to now only a very small amount of energy is harvested from ocean waves. This is because ocean waves are highly irregular and produce only low-frequency forcing, which makes it difficult to use standard generators for electrical energy production.

A well-known WEC type is the so-called point absorber. Examples of points absorbers are shown in Figs. 3.1a and 3.1b. Generally, point absorbers are devices that possess small dimensions relative to the wavelength of the incoming waves. Compared to other types of WECs like attenuators or terminators, point absorbers have the advantage that, due to their small size, the wave direction is not important [DrewEtAl09]. Point absorbers can be of floating structure type which heaves up and down at the wave surface, see e.g. [WatersEtAl07]. Other designs are submerged below the water surface and excited by pressure differences. One example is the Archimedes Wave Swing, see [PolinderEtAl04].

Moreover, point absorbers differ in the number of moving components from which energy can be extracted. In the first generation, point absorbers have been constructed using a single body oscillating in heave. Examples of this

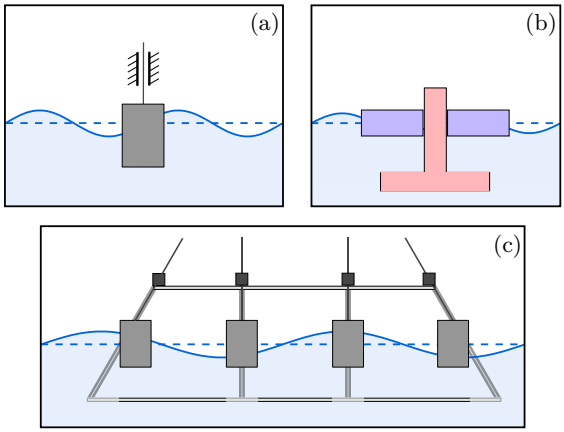

Figure 3.1: Sketch about different WECs. (a), (b): Two examples of classical point absorbers. (c): Multi-body WEC consisting of a combination of several point absorbers.

type can be found in [HollmEtAl22c, WatersEtAl07, LejerskogEtAl15] or in Fig. 3.1a. However, point absorbers only harvest the maximal amount of energy if the eigenfrequency of the oscillating body corresponds to the frequency of the incoming waves, see e.g. [BudarFalnes75, DrewEtAl09, PrudellEtAl10]. This is a serious disadvantage. Since the typical frequencies of water waves are usually very low ($0.1\,\mathrm{Hz} - 0.2\,\mathrm{Hz}$), the dimensions of the mechanical system have to be impractically large [LiangZuo17]. Therefore, two-body WECs have been constructed, whereby an additional body is designed beneath a floating body. Examples of such WECs can be found in [HarmsEtAl22, BeattyEtAl15, HadiEtAl20] or in Fig. 3.1b. Energy can then be harvested from the relative heave motion of the two bodies. The second body can be used to improve the performance of the whole system. Nevertheless, [WuEtAl14] have found that the performance of a two-body wave energy converter highly depends on the parameters of the system and the incoming waves. Therefore, finding suitable system parameters that allow the associated system to harvest a large amount of wave energy is challenging. This becomes even more challenging for WECs, which consist of more than two movable components. An example of such WECs can be found in [HollmEtAl22a] or in Fig. 3.1c.

In order to find suitable system parameters in the early design phase, the motion behavior of a WEC has to be modeled and simulated in the presence of different water waves. This simulation model forms the virtual prototype, which is the basis for a later possible system optimization. In this chapter, a WEC floating on the sea surface is presented, and its dynamic behavior in regular and random water waves is studied. To limit the scope of this work, a single-body point absorber WEC is presented and analyzed in the following.

Further results for the two-body and multi-body WEC from Figs. 3.1b and 3.1c can be found in [HarmsEtAl22, HollmEtAl22a].
In this chapter, possible improvements of the resulting dynamics and the averaged energy harvesting output of a single-body point absorber WEC are analyzed. The content of this chapter is as follows: First, the WEC is introduced in Sect. 3.1. The derivation of the equation of motion of the WEC excited by regular and random waves is presented Sect. 3.2 and Sect. 3.3, respectively. Then, experimental results of the point absorber in a wave flume are shown for different setups in Sect. 3.4. Based on the experimental results and parameters, simulation results are presented in Sect. 3.5 for different setups of the considered point absorber to analyze the motion of the WEC and the corresponding energy harvesting performance. Finally, a simple control strategy for increasing the averaged energy harvesting output is proposed in Sect. 3.6. The following results have been published in [HollmEtAl22c] and this chapter follows this publication in an extended version.

3.1 System Setup

A wave energy converter, which consists of a single cylindrical floating body (CFB) moving along a guidance, is considered. Figures 3.2a and 3.2b show a corresponding experimental rig in the wave flume of the Institute of Mechanics and Ocean Engineering at Hamburg University of Technology from two different angles. The WEC mainly consists of the CFB and an electrical generator. The CFB moves along the guidance rods with the generalized coordinate ξ. The guidance is inclined by the adjustable angle α. The CFB has a radius of R and a draft of d. A sketch of the mechanical system is shown in Fig. 3.2c. A large dynamic response of the CFB due to incoming waves is desirable. From this guided linear motion, electrical energy can be harvested using the electrical generator. There are various power take-off systems that convert linear motion into electrical energy, see [VermaakKamper12]. Some of them convert the linear motion of a point absorber to rotary motion, which is, for example, described in [ChandrasekaranRaghavi15].
A mechanical system similar to the one shown in Fig. 3.2 has been investigated by [YeungEtAl12]. However, [YeungEtAl12] have studied the system behavior only for an inclination angle of $\alpha = 90°$, which results in a WEC that only performs heave motion. It has to be noted that a point absorber oscillating only in heave motion has a eigenfrequency higher than common frequencies of the incoming water waves. Using the WEC depicted in Fig. 3.2 with an inclination angle $\alpha \neq 90°$, forces in the traveling direction of the water waves can also excite

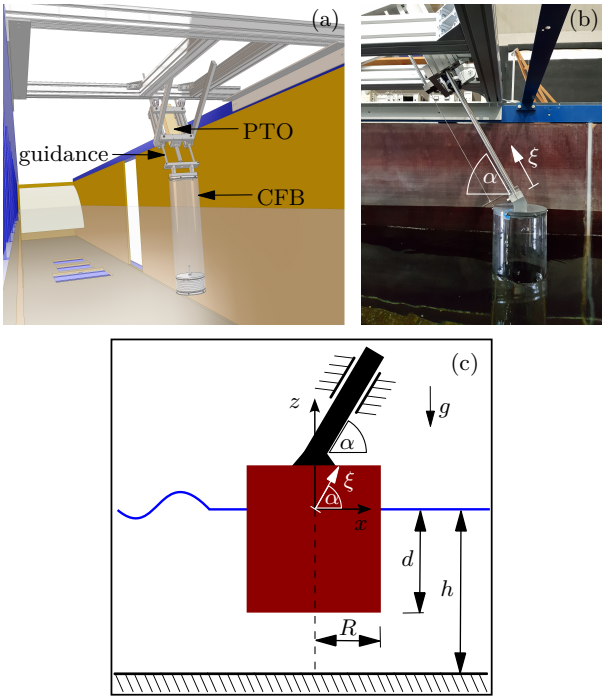

Figure 3.2: (a), (b): Experimental rig in the wave flume of the Institute of Mechanics and Ocean Engineering from two different perspectives. (c): Sketch of the WEC.

the WEC. In the further course of this chapter, it is investigated whether the introduction of an inclination angle α leads to higher displacements ξ of the CFB compared to the case $\alpha = 90°$.

3.2 System Response in Regular Waves

In this section, the system response of the considered WEC in regular water waves is described. To this end, the corresponding equation of motion is derived and the dynamic behavior of the CFB is described by the response amplitude operator.

3.2.1 Equation of Motion of the Wave Energy Converter

Let $\boldsymbol{F}$ be the vector of hydrodynamic forces given by Eq. (2.34). In the following, the components of $\boldsymbol{F}$ in x-, y-, and z-direction are denoted by F_1, F_2, and F_3, respectively. The components of the normal vector $\boldsymbol{n}$, which points inside the WEC and is shown in Fig. 2.1, are denoted similarly. It holds

$$\boldsymbol{F} = \begin{bmatrix} F_1 \\ F_2 \\ F_3 \end{bmatrix}, \quad \boldsymbol{n} = \begin{bmatrix} n_1 \\ n_2 \\ n_3 \end{bmatrix}. \tag{3.1}$$

Applying the balance of linear momentum in the direction ξ yields

$$M\ddot{\xi} = \cos(\alpha)F_1 + \sin(\alpha)\Big\{F_3 - Mg - \sin(\alpha)\lambda_{\mathrm{vis},z}\dot{\xi}\Big\} - F_{\mathrm{damp}}(\dot{\xi}). \tag{3.2}$$

Here, M is the mass of the CFB and the guiding rods, F_{damp} is the velocity-dependent damping force accounting for mechanical friction effects and damping due to the harvested energy, and $\lambda_{\mathrm{vis},z}$ is the viscous damping in the z-direction resulting from the fluid, as described in [YeungEtAl12]. Here, it is assumed that in the horizontal direction, the water flows around the hull of the cylinder without any viscous damping, such that no viscous damping forces act in the x-direction. In the following, incoming regular water waves with a sea surface displacement of the form

$$\eta(x,t) = A\cos\left(kx - \omega t\right) \tag{3.3}$$

are considered. Therefore, compared to the regular water waves from Eq. (2.14), incoming water waves are considered in the following that propagate in the x-direction and have a vanishing phase shift, i. e. $\chi = \beta = 0$.
For further calculations, it is advantageous to describe the incoming water waves using a complex notation. Equation (3.3) becomes

$$\eta(x,t) = \mathrm{Re}\{A\mathrm{e}^{\mathrm{i}(kx-\omega t)}\}. \tag{3.4}$$

Next, it is assumed that the body has been oscillating in these regular waves for such a long time that the transient motion has decayed. Then the displacement ξ of the CFB becomes harmonic with frequency ω and complex amplitude $\mathcal{A}$, i. e.

$$\xi(t) = \mathrm{Re}\{\mathcal{A}\mathrm{e}^{-\mathrm{i}\omega t}\}. \tag{3.5}$$

The corresponding velocity and acceleration of the CFB can be calculated by taking the derivative of ξ in time. The respective amplitude of the displacement in x- and z-direction is given by

$$\mathcal{A}_1 = \cos(\alpha)\mathcal{A}, \quad \mathcal{A}_3 = \sin(\alpha)\mathcal{A}. \tag{3.6}$$

Next, the velocity potential of the fluid disturbed by the CFB is investigated. In the linearized case, the velocity potential is given by Eq. (2.29). Since the WEC

only shows translational motion in x- and z-direction, ϕ is given by the sum of ϕ_0, ϕ_1, ϕ_3 and ϕ_7. For regular water waves with frequency ω, these velocity potentials ϕ_i are also regular with the same frequency. In the definition of these components ϕ_i, it can be seen that ϕ_0 and ϕ_7 depend on the incoming water wave. In contrast, ϕ_1 and ϕ_3 depend on the velocity of the body, which can also be deduced from the BC (2.32d). Therefore, the velocity potential disturbed by the CFB can be written as

$$\begin{aligned}\phi(x,y,z,t) &= \phi_0(x,y,z,t) + \phi_7(x,y,z,t) + \phi_1(x,y,z,t) + \phi_3(x,y,z,t) \\ &= \underbrace{\mathrm{Re}\{A[\varphi_0(x,y,z) + \varphi_7(x,y,z)]\mathrm{e}^{-\mathrm{i}\omega t}\}}_{=\phi_0+\phi_7} \\ &\quad + \underbrace{\mathrm{Re}\{(-\mathrm{i}\omega)(\mathcal{A}_1\varphi_1(x,y,z) + \mathcal{A}_3\varphi_3(x,y,z))\mathrm{e}^{-\mathrm{i}\omega t}\}}_{=\phi_1+\phi_3}.\end{aligned} \tag{3.7}$$

The values of φ_1, φ_3 and φ_7 can be computed numerically solving Eq. (2.32). For incoming regular water waves, the value of φ_0 can be computed from the corresponding velocity potential given by Eq. (2.15).
Having computed the different velocity potentials, the hydrodynamic forces F_1 and F_3 can be computed substituting Eq. (3.7) into Eq. (2.34). The force F_1 results in

$$F_1 = -\rho \iint\limits_{S_{\mathrm{B0}}} (\phi_{0,t} + \phi_{7,t})\, n_1 \,\mathrm{d}S - \rho \iint\limits_{S_{\mathrm{B0}}} (\phi_{1,t} + \phi_{3,t})\, n_1 \,\mathrm{d}S - \rho g \underbrace{\iint\limits_{S_{\mathrm{B0}}} z n_1 \,\mathrm{d}S}_{\overset{(*)}{=}0}. \tag{3.8}$$

Here, equation $(*)$ holds since the cylinder is rotational symmetric and the hydrostatic pressure is equal at each side of the cylinder.
Next, the representation for ϕ_0, ϕ_1, ϕ_3, and ϕ_7 from Eq. (3.7) and the representation for ξ from Eq. (3.5) are substituted into Eq. (3.8). It results

$$F_1 = \mathrm{Re}\{A f_1 \mathrm{e}^{-\mathrm{i}\omega t}\} - \mu_{1,1}\cos(\alpha)\ddot{\xi} - \mu_{1,3}\sin(\alpha)\ddot{\xi} - \lambda_{1,1}\cos(\alpha)\dot{\xi} - \lambda_{1,3}\sin(\alpha)\dot{\xi}, \tag{3.9}$$

whereby f_j, $\mu_{j,k}$, and $\lambda_{j,k}$, are given by

$$f_j = \mathrm{i}\omega\rho \iint\limits_{S_{\mathrm{B0}}} [\varphi_0 + \varphi_7] n_j \mathrm{d}S, \quad \text{for } j \in \{1,3\}, \tag{3.10}$$

$$\mu_{j,k} + \mathrm{i}\frac{\lambda_{j,k}}{\omega} = \rho \iint\limits_{S_{\mathrm{B0}}} \varphi_k n_j \mathrm{d}S, \quad \text{with } \mu_{j,k}, \lambda_{j,k} \in \mathbb{R} \;\text{ for } j,k \in \{1,3\}. \tag{3.11}$$

Here, f_j is the complex amplitude of the exciting force in the j-direction for an incoming wave of unit amplitude. Furthermore, $\mu_{j,k}$ is the added mass coefficient

and $\lambda_{j,k}$ is the hydrodynamic damping coefficient in the j-direction, which result from the motion of the body in k-direction [Newman18]. It has to be noted that for the considered CFB, a motion of the CFB in the z-direction does not result in a force in the x-direction. Therefore, it holds $\mu_{1,3} = \lambda_{1,3} = 0$.
The force F_3 can be computed in a similar way. The only difference is that the integral $\rho g \iint_{S_{\mathrm{B0}}} z n_3 \, \mathrm{d}S$ does not vanish but becomes the buoyancy force of the body. Therefore, the forces F_1 and F_3 result in

$$F_1 = \mathrm{Re}\{A f_1 \mathrm{e}^{-\mathrm{i}\omega t}\} - \cos(\alpha)\mu_{1,1}\ddot{\xi} - \cos(\alpha)\lambda_{1,1}\dot{\xi}, \tag{3.12a}$$

$$F_3 = \mathrm{Re}\{A f_3 \mathrm{e}^{-\mathrm{i}\omega t}\} - \sin(\alpha)\mu_{3,3}\ddot{\xi} - \sin(\alpha)\lambda_{3,3}\dot{\xi} + \rho g \pi R^2 \left(d - \sin(\alpha)\xi\right). \tag{3.12b}$$

It has to be noted that the hydrodynamic force acting in the y-direction, F_2, can be computed similarly. However, since the considered CFB is only moving in the $x-z$-plane, the force F_2 does not affect the motion of the CFB.
If the mechanical system is in its equilibrium position in still water at $\xi = 0$, the balance of forces in z-direction results in

$$\rho g \pi R^2 d = M g. \tag{3.13}$$

Substituting Eqs. (3.12) and (3.13) into Eq. (3.2), the equation of motion of the CFB, which is excited by regular water waves of amplitude A and frequency ω, is given by

$$\begin{aligned}(M + c_\alpha^2\mu_{1,1} + s_\alpha^2\mu_{3,3})\ddot{\xi} + (c_\alpha^2\lambda_{1,1} + s_\alpha^2\lambda_{3,3} + s_\alpha^2\lambda_{\mathrm{vis},z})\dot{\xi} \\ + F_{\mathrm{damp}}(\dot{\xi}) + s_\alpha^2\rho g\pi R^2\xi = \mathrm{Re}\{A(c_\alpha f_1 + s_\alpha f_3)\mathrm{e}^{-\mathrm{i}\omega t)}\}.\end{aligned} \tag{3.14}$$

Here, the abbreviations

$$s_\alpha := \sin(\alpha), \;\; c_\alpha := \cos(\alpha) \tag{3.15}$$

are used. In order to compute the values of f_1, f_3, $\mu_{j,j}$, and $\lambda_{j,j}$, the velocity potentials ϕ_j, $j = 1, \ldots, 7$, have to be computed, see Eqs. (3.7), (3.10), and (3.11). These potentials have to satisfy Eq. (2.32). For a cylindrical body, the potentials ϕ_j and corresponding hydrodynamic coefficients f_1, f_3, $\mu_{j,j}$, and $\lambda_{j,j}$ have been computed by [Yeung81] and [Garrett71]. Here, [Yeung81] and [Garrett71] have separated the water domain into an interior domain below the cylinder and an exterior domain beside the cylinder. Solutions for the different velocity potentials are obtained by matching eigenfunctions of the interior and exterior problems, whereby the eigenfunctions fulfill the different boundary conditions summarized in Eq. (2.32). In this way, [Yeung81] and [Garrett71] have determined analytical expressions for the hydrodynamic coefficients f_1, f_3, $\mu_{j,j}$, and $\lambda_{j,j}$. It has to be noted that f_1, f_3, $\mu_{j,j}$, and $\lambda_{j,j}$ depend on the radius R and draft d of the cylinder, the wave frequency ω, and the water depth h.

3.2.2 Modeling of Damping Force and Harvested Energy

In Eq. (3.14), the damping force F_{damp} considers all energy extracted from the motion of the system, which occur due to mechanical friction and the energy harvesting of the electrical generator. The damping due to mechanical friction is modeled using the damping force F_{mech}. In this work, a general nonlinear mechanical damping force F_{mech} of the form

$$F_{\text{mech}}(\dot{\xi}) = d_1\dot{\xi} + d_2|\dot{\xi}|\dot{\xi} + d_3\dot{\xi}^3 \tag{3.16}$$

is used. The damping coefficients d_1, d_2, and d_3 are determined by means of free decay tests.
Furthermore, the electrical generator converts kinetic energy from the motion of the CFB into electrical energy. The conversion of kinetic energy introduces a damping force in Eq. (3.14), which is also contained in the general damping force F_{damp}. Let η_{eff} be the energy conversion efficiency of the electrical generator. Additionally, let P_{elec} the amount of harvested electrical power and let P_{convert} the corresponding mechanical power converted from the motion of the CFB. Then it holds

$$P_{\text{elec}} = \eta_{\text{eff}} P_{\text{convert}}. \tag{3.17}$$

The converted mechanical power P_{convert} can be computed by the product of the velocity $\dot{\xi}$ of the CFB and some force F_{convert}, i. e. $P_{\text{convert}} = F_{\text{convert}}\dot{\xi}$. The force F_{convert} affects the motion of the CFB when the electrical generator harvests electrical energy.
Since electrical energy can only be harvested from the motion of the CFB, the force F_{convert} depends on the velocity $\dot{\xi}$ of the CFB. In this thesis, the force F_{convert} is assumed to be linearly dependent on the velocity of the CFB with some damping constant d_{elec}, i. e.

$$F_{\text{convert}} = d_{\text{elec}}\dot{\xi}. \tag{3.18}$$

Such a modeling approach for the force F_{convert} has also been used, for example, in [ErikssonEtAl05, OlayaEtAl14]. In order to indicate that the damping force F_{convert} results from energy harvesting, the damping constant d_{elec} is called the electrical damping constant in this thesis.
It can be summarized that energy harvesting introduces the damping force F_{convert} in the equation of motion (3.14). This force is considered in Eq. (3.14) in the damping force F_{damp}. Furthermore, the corresponding amount of converted electrical power, P_{elec}, is given by

$$P_{\text{elec}} = \eta_{\text{eff}} P_{\text{convert}} = \eta_{\text{eff}} F_{\text{convert}}\dot{\xi} = \eta_{\text{eff}} d_{\text{elec}}\dot{\xi}^2. \tag{3.19}$$

Considering the mechanical friction effects and the effects of energy harvesting, the damping force F_{damp} in Eq. (3.14) is given by

$$F_{\text{damp}}(\dot{\xi}) = F_{\text{mech}}(\dot{\xi}) + F_{\text{convert}}(\dot{\xi}). \tag{3.20}$$

In the further course of this chapter, the electrical power P_{elec} is investigated by simulating the dynamics of the CFB over a prescribed time domain. Afterward, the electrical power P_{elec} is integrated over this time domain to obtain the corresponding amount of harvested electrical energy.

3.2.3 Response Amplitude Operator

After the transient motion has decayed, the dynamic behavior of a linear mechanical system excited by regular forces becomes periodic, see Eq. (3.5). In order to harvest as much energy as possible, the velocity of the CFB has to be high. Therefore, the behavior of the amplitude of the CFB motion for different frequencies is of interest. The amplitude of the CFB can be analyzed by introducing the response amplitude operator (RAO), see e.g. [Newman18, YeungEtAl12]. For regular water waves, the RAO is defined by the quotient of the amplitude of the incoming water waves A and the response amplitude of the CFB $\mathcal{A}$.
In the following, it is assumed that the mechanical damping force F_{mech} is only linearly dependent on the velocity of the CFB, i. e.

$$F_{\text{mech}}(\dot{\xi}) = d_{\text{lin}}\dot{\xi} \tag{3.21}$$

with corresponding damping constant d_{lin}. Furthermore, all hydrodynamic coefficients are assumed to be constant. Substituting Eq. (3.5) into the equation of motion (3.14), the RAO results in

$$\text{RAO}(\omega) = \frac{\mathcal{A}}{A} = \frac{c_\alpha f_1 + s_\alpha f_3}{s_\alpha^2 \rho g \pi R^2 - \omega^2 C_{\text{mass}} - \mathrm{i}\omega C_{\text{damp}}} \tag{3.22}$$

with

$$\begin{aligned} C_{\text{mass}} &= M + c_\alpha^2 \mu_{1,1} + s_\alpha^2 \mu_{3,3}, \\ C_{\text{damp}} &= d_{\text{lin}} + d_{\text{elec}} + c_\alpha^2 \lambda_{1,1} + s_\alpha^2 \lambda_{3,3} + s_\alpha^2 \lambda_{\text{vis},z}. \end{aligned} \tag{3.23}$$

If the mechanical damping force F_{mech} is of the general nonlinear form shown in Eq. (3.16) and if the hydrodynamic coefficients are not assumed to be constant, the RAO can only be calculated numerically. This can be done by computing ξ numerically and dividing the amplitude of ξ by the wave amplitude A.
For energy harvesting, it is important that the velocity of the WEC is high, see Eq. (3.19). So the question is, with which parameters of the system and the fluid does the WEC move at high velocities. This question can be answered by investigating the response amplitude operator of the velocity of the WEC, which is given by $\dot{\xi}$. Since in regular waves the amplitude of $\dot{\xi}$ is given by $-\mathrm{i}\omega\mathcal{A}$, the corresponding response amplitude operator of the velocity, RAO_{v}, is given by

$$\text{RAO}_{\text{v}}(\omega) = \frac{-\mathrm{i}\omega\mathcal{A}}{A} = -\mathrm{i}\omega\text{RAO}(\omega) = \frac{-\mathrm{i}\omega(c_\alpha f_1 + s_\alpha f_3)}{s_\alpha^2 \rho g \pi R^2 - \omega^2 C_{\text{mass}} - \mathrm{i}\omega C_{\text{damp}}}. \tag{3.24}$$

3.3 System Response in Random Waves

After investigating the system response of the WEC excited by regular waves, the system response of the WEC due to incoming random waves is investigated. Equation (3.14) describes the motion of the CFB in regular waves. In order to extend this model to irregular seas consisting of many regular waves as presented in Sect. 2.2.2, the equation of motion (3.14) has to be modified.
An ansatz of computing the motion of a floating system in an irregular sea is to use average values for the added mass and hydrodynamic damping coefficients and include the excitation forces of each regular wave component in the right-hand side of Eq. (3.14), see [Wehausen71]. Hence, in this work, this ansatz is followed, and constant frequency independent values for $\mu_{j,j}$, $\lambda_{j,j}$, $j \in \{1,3\}$ are used. The excitation forces f_1 and f_3 are computed individually for each incoming regular wave component. For a given sea spectrum with prescribed peak frequency ω_p, the coefficients $\mu_{j,j}$ and $\lambda_{j,j}$ are computed at $\omega = \omega_\mathrm{p}$. In this way, the response of water waves with frequency ω_p, which have the highest amplitude in the irregular sea, can be computed.
In the following, long-crested random water waves propagating in the x-direction are considered. Based on Eq. (2.28) with $\chi_0 = 0$, the corresponding sea surface displacement is given by

$$\eta(x,t) = \sum_{m=1}^{M_\omega} \cos(k(\omega_m)x - \omega_m t + \beta(\omega_m))\sqrt{2S(\omega_m)\Delta\omega_m}. \tag{3.25}$$

Defining

$$\bar{\mu}_{j,j} := \mu_{j,j}(\omega_\mathrm{p}), \quad \bar{\lambda}_{j,j} := \lambda_{j,j}(\omega_\mathrm{p}), \quad \text{for } j \in \{1,3\}, \tag{3.26}$$

the equation of motion (3.14) of the CFB can be written as

$$\begin{aligned}(M + c_\alpha^2\bar{\mu}_{1,1} + s_\alpha^2\bar{\mu}_{3,3})\ddot{\xi} + (c_\alpha^2\bar{\lambda}_{1,1} + s_\alpha^2\bar{\lambda}_{3,3} + s_\alpha^2\lambda_{\mathrm{vis},z})\dot{\xi} + F_\mathrm{damp}(\dot{\xi}) \\ + s_\alpha^2\rho g\pi R^2\xi = \sum_{m=1}^{M_\omega} \mathrm{Re}\{\sqrt{2S(\omega_m)\Delta\omega_m}(c_\alpha f_1(\omega_m) + s_\alpha f_3(\omega_m))\mathrm{e}^{-\mathrm{i}\omega_m t + \mathrm{i}\beta(\omega_m)}\}.\end{aligned} \tag{3.27}$$

It has to be noted that solving Eq. (3.27) needs the computation of the values of $\bar{\mu}_{j,j}$, $\bar{\lambda}_{j,j}$, $f_1(\omega_m)$ and $f_3(\omega_m)$. Since all these values depend on the actual position of the CFB, this can get time-consuming for large M_ω. In order to reduce the computational effort, the values of $\bar{\mu}_{j,j}$, $\bar{\lambda}_{j,j}$, $f_1(\omega_m)$ and $f_3(\omega_m)$ are determined only once for the equilibrium position of the CFB in still water. These values are then used for the entire simulation. Here, it is assumed that the CFB does not make large amplitude motions and is always in the vicinity of this equilibrium. Due to the small displacements of the CFB, the exact values of the hydrodynamic coefficients, which continuously depend on the position of

the CFB, are then close to the corresponding values in the equilibrium position. This approach has also been proposed by [Wehausen71].
In the following, the hydrodynamic coefficients $\mu_{j,j}$, $\lambda_{j,j}$, f_1 and f_3 are always computed for the equilibrium position of the CFB. This means that these coefficients are kept constant over the entire simulation time when computing the motion of the CFB in regular and random waves solving Eq. (3.14) and Eq. (3.27), respectively.

3.4 Experimental Results

In order to validate the influence of the inclination angle α, corresponding experimental tests have been executed. The facility used to undertake the experiments is the wave flume of the Institute of Mechanics and Ocean Engineering at the Hamburg University of Technology. A sketch of the wave flume is shown in Fig. 3.3, and details of the wave flume are given in Tab. 3.1. The waves are generated by a back-and-forth motion of a spindle actuated wave flap with flap angle γ_{wf}. The type of movement of the flap generates different water waves, such as regular and random waves. A beach is installed at the end of the wave flume to reduce the reflection of water waves.
The dimensions of the floating system, which is shown in Fig. 3.2, are given in Tab. 3.2. The displacement of the CFB has been measured using a linear variable differential transformer, which is mounted on the guidance. The resolution of the position measurement is about a tenth of a millimeter. The corresponding velocity is obtained by differentiation of the numerical displacement.
In the following, it is described how the mechanical damping coefficients d_1, d_2, d_3,

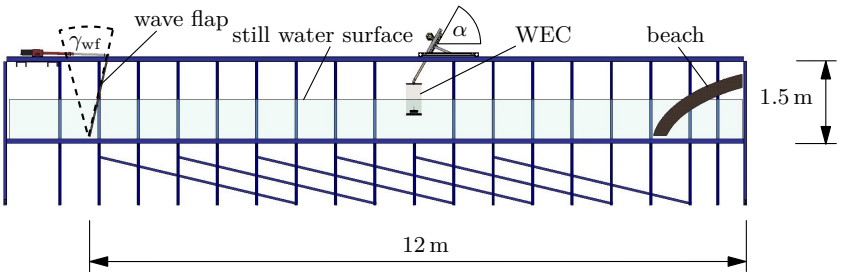

Figure 3.3: Sketch of wave flume at the Institute of Mechanics and Ocean Engineering at Hamburg University of Technology.

Table 3.1: Parameter values of the wave flume.

Length [m]	Width [m]	Depth [m]	Maximum wave height [m]	Maximum wave frequency [Hz]
12	1.50	1.50	0.6	2

Table 3.2: Parameter values of the floating system.

R [m]	d [m]	h [m]	$d_1 \left[\frac{\text{kg}}{\text{s}}\right]$	$d_2 \left[\frac{\text{kg}}{\text{m}}\right]$	$d_3 \left[\frac{\text{kg}\cdot\text{s}}{\text{m}^2}\right]$	$d_{\text{lin}} \left[\frac{\text{kg}}{\text{s}}\right]$
0.09	0.45	1.06	44.42	−99.23	73.00	18.00

and d_{lin} are determined using free decay tests. Afterward, measurements for the displacement ξ are presented for different inclination angles α and wave frequencies ω.

3.4.1 Estimation of Mechanical Damping Coefficients

The damping coefficients d_1, d_2, d_3, and d_{lin}, which are used to approximate the influence of mechanical friction, can be determined by means of free decay tests. The CFB is moving outside the water and is not connected to the electrical generator. However, in the direction of coordinate ξ, the CFB is connected to an additional spring with stiffness constant k_{sp}. The equation of motion of this system is given by

$$M\ddot{\xi} + F_{\text{mech}}(\dot{\xi}) + k_{\text{sp}}\xi = 0. \tag{3.28}$$

Here, F_{mech} is given by Eq. (3.16) for the nonlinear case and by Eq. (3.21) for the linear case, respectively. For an inclination angle of $\alpha = 60°$, Fig. 3.4a shows the displacement of the CFB measured in the experiment in blue. The values of the damping constants d_1, d_2, d_3, and d_{lin} have to be determined such that the difference between the experimentally measured displacement ξ_{meas} and the simulated displacement ξ_{sim} becomes small for all times. These values have been obtained by mathematical optimization with respect to the objective function

$$\text{minimize } G = \sum_{i=1}^{I} |\xi_{\text{meas}}(t_i) - \xi_{\text{sim}}(t_i)|. \tag{3.29}$$

Here, $t_1, \ldots, t_I$ are discrete time points for which measured data are available. For the computation of this optimization problem, a gradient-based optimization method has been used.
The damping coefficients d_1, d_2, d_3, and d_{lin} depend on the inclination angle α. For an inclination angle of $\alpha = 60°$, the resulting values of d_1, d_2, d_3 and d_{lin} are presented in Tab. 3.2. The corresponding simulated displacements ξ_{sim} are presented in Fig. 3.4a. It can be seen that using a linear model for the damping

force F_{mech} from Eq. (3.21), the displacement ξ_{sim} decays not as fast as the measured data ξ_{meas}. In contrast, using nonlinear modeling of the damping force F_{mech} from Eq. (3.16), the simulated data ξ_{sim} approximates the temporal behavior of the measured data ξ_{meas} for all times very well.
Furthermore, Fig. 3.4b shows the damping force F_{mech} against the velocity $\dot{\xi}$ using the values of d_1, d_2, d_3 and d_{lin} presented in Tab. 3.2. It can be seen that for $0.36\,\mathrm{m/s} \leq \dot{\xi} \leq 1\,\mathrm{m/s}$ the linear modeling approach of the damping force leads to larger values of F_{mech} than the nonlinear approach. The nonlinear damping force exceeds the linear one for all other velocities $\dot{\xi}$. In Sect. 3.5, the effects of the different modeling approaches of F_{mech} on the behavior of the WEC is analyzed. There, the dynamic behavior of the WEC is investigated using simulation results. However, before coming to simulation results, corresponding experimental results about the motion of the CFB are presented.

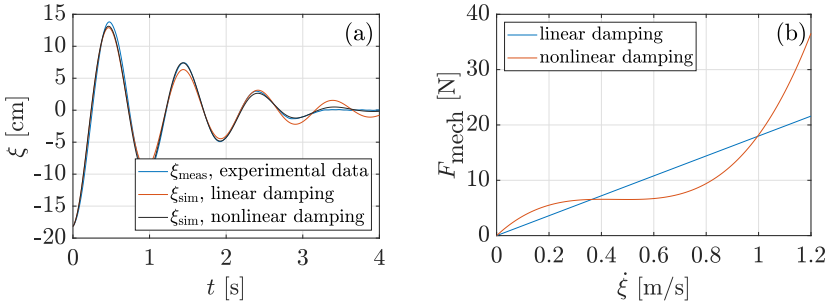

Figure 3.4: (a): Comparison between measured and simulated data for displacement ξ resulting from free decay tests. (b): Comparison of linear and nonlinear mechanical damping force F_{mech}.

3.4.2 Experimental Investigation of the Motion of the Wave Energy Converter

In the following, experimental result are shown, which present the motion of the WEC in regular waves for different inclination angles without the presence of an electrical generator. Figure 3.5 shows for the wave frequency $\omega = 2.57$ rad/s the measured temporal behavior of the displacement in the direction of the coordinate ξ. It is depicted that the displacement increases if the inclination angle α is changed from $\alpha = 90°$ to $\alpha = 45°$. Since higher displacements are reached in the same time domains, the velocities also get higher, from which more electrical energy can be harvested.
In order to illustrate the influence of a changing inclination angle for different wave frequencies ω, various RAOs can be computed. Here, the RAOs are related

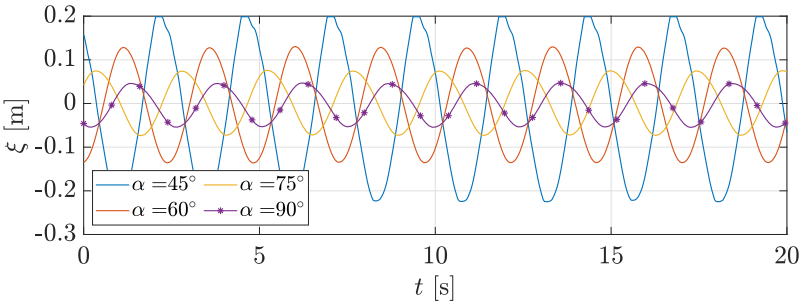

Figure 3.5: Experimental results for the response of the CFB for water waves of frequency $\omega = 2.57$ rad/s and for different inclination angles α.

to the measured amplitude of the incoming water waves and the displacements of the CFB. In Fig. 3.6, the RAOs of the displacement and velocity are depicted for different inclination angles α and frequencies $\omega \in [2\,\text{rad/s}, 4\,\text{rad/s}]$. It is shown that the displacement and the velocity of the CFB increases if the inclination angle α is changed from $\alpha = 90°$ to $\alpha = 60°$ and $\alpha = 45°$, respectively. From Eq. (3.19), it follows that more electrical power can be harvested from the increased velocity $\dot{\xi}$.

It has to be noted that the finite length of the wave flume leads to wave reflections at the end of the wave flume. The amplitudes of the wave reflections depend on the wave frequencies of the incoming waves. Consequently, the amplitudes of the waves exciting the WEC also depend on the corresponding wave frequencies. However, due to the nonlinear mechanical damping, the motion of the CFB does not depend linearly on the amplitude of the water waves. Therefore, experimental results in a wave flume of finite length represent the dynamic behavior of the

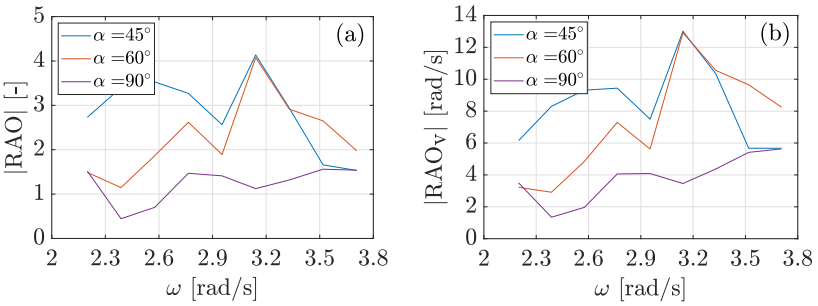

Figure 3.6: Experimentally determined RAOs for the (a) displacement and (b) velocity of the CFB for different inclination angles α.

mechanical system in an open sea only in a limited way.
Moreover, it should be noted that a realistic irregular sea mainly contains regular wave components in the frequency range $\omega \in [0.5, 1.5]\,\mathrm{rad/s}$. Since the wave flume has only a limited length, only waves with small wavelengths fit into the wave flume. Therefore, waves with frequencies in the range of $\omega \in [2\,\mathrm{rad/s}, 4\,\mathrm{rad/s}]$ have been chosen in the experiments to show the angular dependency on the dynamics of the WEC and on energy harvesting.

3.5 Simulation Results

In the following, simulations of the mechanical system are studied to obtain more details about the influence of the inclination angle on the motion of the mechanical system. Here, the simulated dynamic behavior of the WEC is computed by solving the equations of motion (3.14) and (3.27) in regular and random waves. In order to relate the simulation results to the results from the experiment, the geometric and damping parameters from the experiment given in Tab. 3.2 are used in the following. It has to be noted that the mechanical damping coefficients depend on the inclination angle α. However, the damping coefficients given in Tab. 3.2 are used for all considered values of α. In this way, only the effect of different inclination angles and incoming water waves on the dynamic behavior of the WEC is investigated. The effects of the change in damping coefficients at different inclination angles are not considered.
Simulation results are presented for a water density of $\rho = 1023\,\mathrm{kg/m^3}$ and without considering an electrical generator, i. e. $d_{\mathrm{elec}} = 0$. Moreover, a viscous damping coefficient of $\lambda_{\mathrm{vis,z}} = 13.69\,\mathrm{kg/s}$ is chosen, which represents the force due to viscous drag. The value of $\lambda_{\mathrm{vis,z}}$ appears in Eqs. (3.14) and (3.27) and has been taken from the work of [YeungEtAl12]. It has to be noted that [YeungEtAl12] use a cylinder of different size than described by the parameters stated in Tab. 3.2. In order to study the effect of the inclination angle at the motion of the cylinder, the stated value for $\lambda_{\mathrm{vis,z}}$ is used in this study.
In Fig. 3.7, the RAOs of the displacement and velocity are shown for different inclination angles α using linear and nonlinear mechanical damping, respectively. For the case of linear mechanical damping, the Eqs. (3.22) and (3.24) are used to calculate the value of RAO and $\mathrm{RAO_v}$, respectively. For the case of nonlinear mechanical damping, the values of RAO and $\mathrm{RAO_v}$ are computed using simulation results. For this, Eq. (3.14) is solved for waves of amplitude $A = 0.1\,\mathrm{m}$. Comparing Figs. 3.6 and 3.7, it can be seen that simulations and experiments lead to the same general dynamic behavior of the WEC. This means that a reduction of the inclination angle from $\alpha = 90°$ to $\alpha = 60°$ and $\alpha = 45°$ leads to a growth of

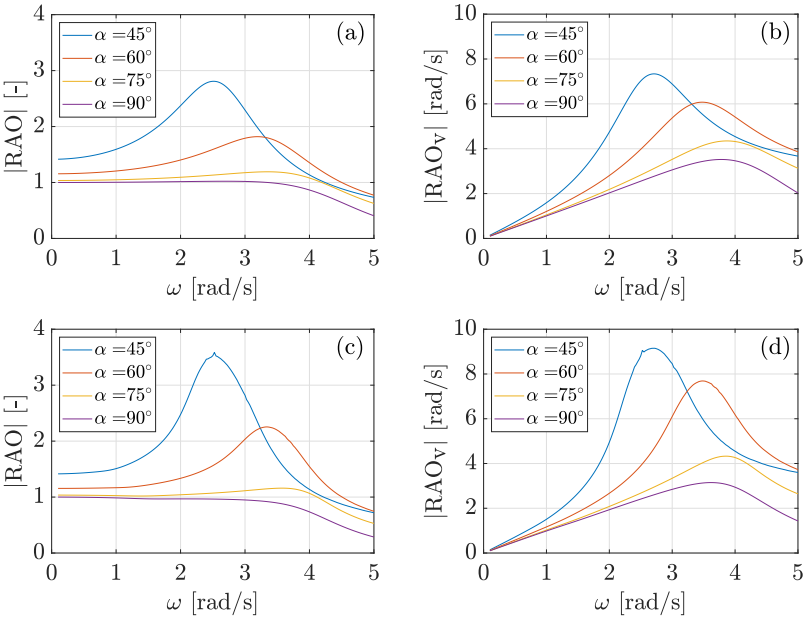

Figure 3.7: Simulated RAOs of the (a) displacement and (b) velocity for the case of linear damping and (c) displacement and (d) velocity for the case of nonlinear damping.

the displacement and velocity of the CFB. Furthermore, an increase of the wave frequency ω to a value larger than 4 rad/s leads to a decrease in the displacement and velocity of the CFB.

Considering Fig. 3.7 and comparing linear with nonlinear mechanical damping, it can be seen that both modeling approaches for the damping result in the same general dynamic behavior described so far. Only the response amplitude changes depending on the used damping approach. For $\alpha = 90°$, the linear mechanical damping approach leads to a larger CFB response amplitude, while for $\alpha = 60°$ and $\alpha = 45°$, the nonlinear mechanical damping approach leads to a larger CFB response amplitude. For $\alpha = 75°$, both modeling approaches for the mechanical damping force F_{mech} result in nearly the same response amplitude. The described behavior of the amplitude response can be explained considering the velocities $\dot{\xi}$ of the CFB. For regular incoming water waves, the amplitude of the velocity $\dot{\xi}$ can be computed from the used water amplitude $A = 0.1\,\text{m}$ and value of RAO_v shown in Figs. 3.7b and 3.7d by $|\dot{\xi}| = |\text{RAO}_\text{v}| \cdot A$. Therefore, the velocities achieved by the CFB for $\alpha = 90°$ have small amplitudes compared to the other considered inclination angles α. From Fig. 3.4b, it can be seen that the linear mechanical damping force F_{mech} exceeds the nonlinear force only for $0.36\,\text{m/s} \leq \dot{\xi} \leq 1\,\text{m/s}$.

As a result, the response amplitude of the CFB is smaller for the case of linear mechanical damping than for nonlinear damping if the amplitude of $\dot{\xi}$ is between 0.36 m/s and 1 m/s. Therefore, for $\alpha = 90°$, the linear mechanical damping results in a larger response amplitude of the CFB than the nonlinear mechanical damping approach. For the other considered inclination angles, the behavior of the response amplitude going from linear to nonlinear mechanical damping approach can be explained in a similar way.
The results shown in Figs. 3.7b and 3.7d are extended by the results presented in Fig. 3.8, where surface plots of $\mathrm{RAO_v}$ are shown about the inclination angle $\alpha \in [10°, 90°]$. It can be seen that with a decrease of α, the RAOs of the velocity get higher maximal values at lower frequencies ω. This results from the fact that due to the multiplication of the stiffness term $\rho g \pi R^2$ in Eq. (3.14) with $\sin(\alpha)^2$, the eigenfrequency of the mechanical system gets lower for decreasing α. In both damping cases, the maximal velocity is obtained for $\omega = 2.3$ rad/s and $\alpha = 38°$. Generally, the lowest velocity response is obtained for the vertically inclined case, i. e. for $\alpha = 90°$, which has been investigated in literature so far, see e.g. [YeungEtAl12].

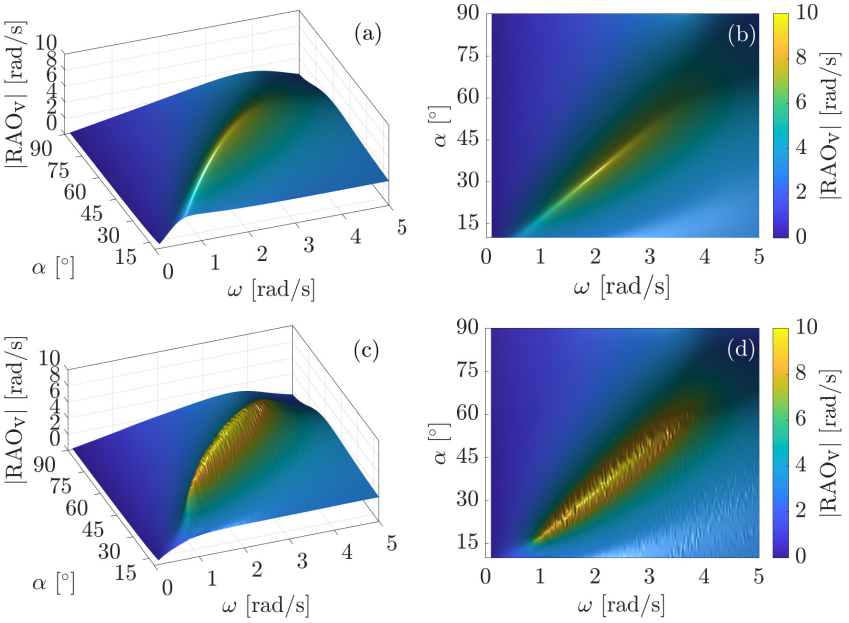

Figure 3.8: (a), (b): RAO of the velocity for the case of linear mechanical damping shown from two different perspectives. (c), (d): RAO of the velocity for the case of nonlinear mechanical damping shown from two different perspectives.

Next, it is investigated whether the WEC can harvest more energy when considering inclination angles $\alpha > 90°$. To this end, the velocity response of the WEC is studied for angles $\alpha \in [10°, 170°]$ in the following. Figures 3.9a and 3.9b shows the RAO of the velocity for the case of linear damping from two different perspectives. The values of $\mathrm{RAO_v}$ for $\alpha = 90°$ are marked in red. It can be seen that the amplitude value of $\mathrm{RAO_v}$ is nearly symmetric around $\alpha = 90°$, i. e. $\mathrm{RAO_v}(\alpha = 90° + \tilde{\alpha}) \approx \mathrm{RAO_v}(\alpha = 90° - \tilde{\alpha})$ for some $\tilde{\alpha} < 90°$.
However, the use of inclination angles $\alpha > 90°$ affects the phase of $\mathrm{RAO_v}$ and the motion of the CFB. In order to show this, Fig. 3.9c depicts the displacement ξ of the CFB in regular waves with amplitude $A = 0.1\,\mathrm{m}$ and frequency $\omega = 2\,\mathrm{rad/s}$ for the inclination angles $\alpha = 60°$ and $\alpha = 120°$. The displacements ξ are calculated considering linear mechanical damping. It can be seen that the displacements ξ of the CFB are shifted in time. This shows that the additional consideration of inclination angles $\alpha > 90°$ does not result in an increasing velocity response of the CFB. Only the phase of the displacement ξ against the sea surface displacement η is changed. Therefore, only inclination angles $\alpha \leq 90°$ are considered in the rest of this work.

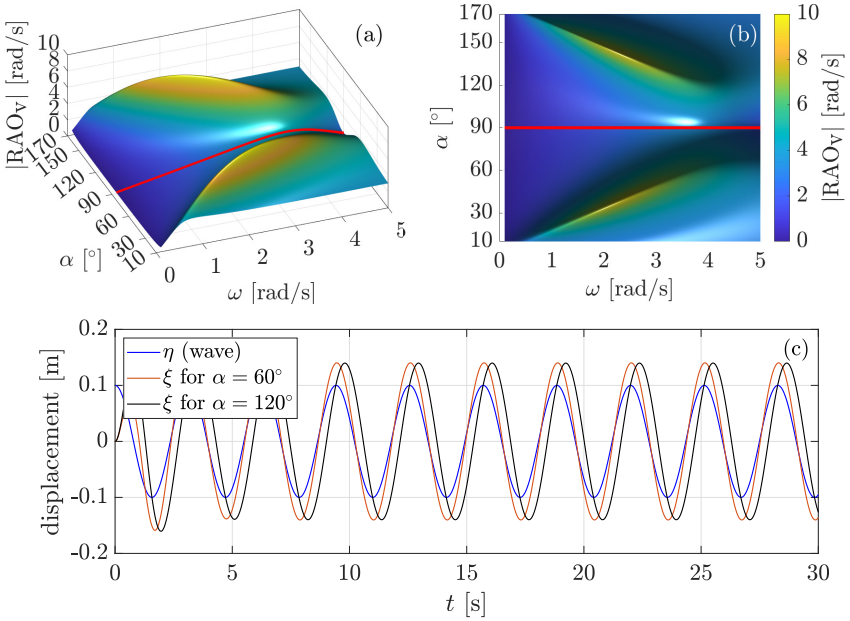

Figure 3.9: (a), (b): RAO of the velocity for the case of linear damping shown from two different perspectives. (c): Comparison of the dynamic behavior of the CFB considering the inclination angles $\alpha = 60°$ and $\alpha = 120°$.

Finally, the mechanical behavior of the point absorber is investigated for the case of a random wave excitation. In Fig. 3.10, the displacement and velocity of the mechanical system are depicted for different inclination angles in the presence of a random water wave with $M_\omega = 100$ regular wave components. The corresponding wave amplitudes are obtained using the PM-spectrum from Eq. (2.23) with peak frequency $\omega_\mathrm{p} = 1\,\mathrm{rad/s}$ and significant wave height $H_\mathrm{s} = 2\,\mathrm{m}$. Nonlinear damping and a water depth of $h = 10\,\mathrm{m}$ are used. It can be seen that the CFB follows the sea surface displacement η for an inclination angle of $\alpha = 90°$. However, by decreasing the inclination angle α from $\alpha = 90°$ to $\alpha = 30°$, the response amplitude of the CFB gets larger, which results in higher velocities. Although the simulated velocities reduce if α is decreased further from $\alpha = 30°$ to $\alpha = 10°$, a higher amount of electrical energy can also be harvested in irregular seas if the CFB is inclined compared to the case where the CFB only exerts pure heave motion.

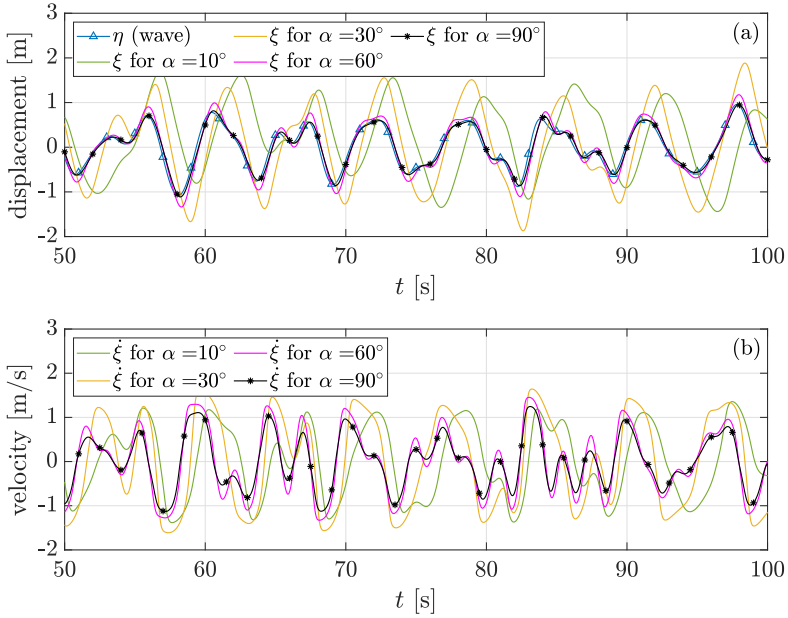

Figure 3.10: (a) Displacement and (b) velocity of the WEC for the case of a random wave excitation, nonlinear damping, and different inclination angles α.

3.6 Simple Control Strategy for the Wave Energy Converter

A known disadvantage of point absorbers is the strong dependency of their energy harvesting performance on the wave frequency of incoming waves. Point absorbers harvest the maximal amount of energy if the eigenfrequency of the oscillating body corresponds to the frequency of the incoming waves, see e.g. [BudarFalnes75, DrewEtAl09, PrudellEtAl10]
In order to match the eigenfrequency of the presented WEC to the frequency of the incoming waves, a useful control strategy could be to adjust the inclination angle of the CFB. This adjustment can be performed very slowly since the mean frequency of incoming waves changes slowly in real seas. Typically, a considerable change of the sea state can be observed after about 20 minutes [ClaussEtAl88]. The effect of an adjustment of the inclination angle α on the amount of harvested energy is discussed for the first time in [HollmEtAl22c] and this chapter follows this publication in an extended version.
To adjust the inclination angle α, the hydrodynamic forces due to incoming water waves can be used to tilt the guidance. In this way, no external electrical energy has to be used to tilt the guidance to the desired inclination angle. The guidance is locked as soon as the desired inclination angle is reached.
In the following, the effect of a fixed or controlled inclination angle α on the amount of harvested energy is investigated. For this purpose, the dynamic behavior of the WEC with the system parameters given in Tab. 3.2 is simulated in regular waves with frequencies $\omega \in \{0.5,\ 1,\ 1.5,\ 2,\ 2.5,\ 3,\ 3.5,\ 4,\ 4.5,\ 5\}\,\mathrm{rad/s}$. Each dynamic behavior of the WEC is simulated for one hour. In order to compute the amount of harvested energy, the corresponding electrical power given by Eq. (3.19) is integrated with respect to time and summed up over all considered wave frequencies. Here, the electrical power is computed using Eq. (3.19) with an electrical damping constant of $d_{\mathrm{elec}} = 10\,\mathrm{kg/s}$ and an efficiency constant of $\eta_{\mathrm{eff}} = 0.8$. The electrical damping constant $d_{\mathrm{elec}} = 10\,\mathrm{kg/s}$ is also considered in the calculation of the dynamic behavior of the system.
In all simulations, the tilt angle α is fixed or controlled based on the incoming wave frequencies so that the CFB reaches high velocities. The results can be seen in Fig. 3.11 for linear and nonlinear mechanical damping. No significant differences between the case with linear and nonlinear damping can be observed. For the uncontrolled case, a fixed inclination angle of $\alpha = 40°$ leads to the highest values of harvested energy outputs in both cases.
If the proposed control strategy is used to adjust the inclination angle α, the energy harvesting performance is further increased. In Fig. 3.11, it can be seen that the controlled case leads to an increase of the energy harvesting output of 34% compared to the best case with a fixed inclination angle α. It can also be seen that a too small or too high fixed angle α results in lower energy outputs.

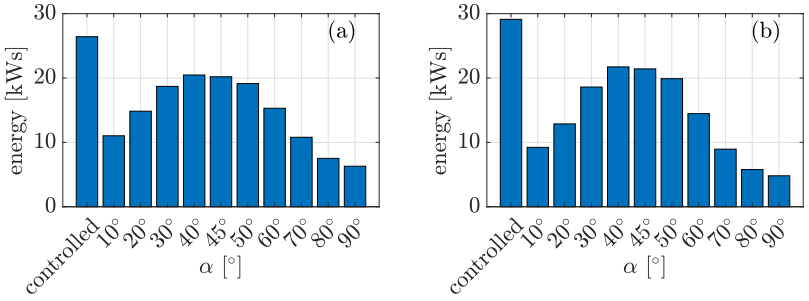

Figure 3.11: Amount of harvested energy for the case of (a) linear and (b) nonlinear damping.

Moreover, compared to the case $\alpha = 90°$, which corresponds to the standard case of a vertically moving point absorber, the controlled case leads to an energy increase of 605%.
In summary, it can be concluded that the proposed adjustment and control of the inclination angle α exposes an efficient way to increase the amount of harvested energy. However, it should be noted that the dynamic behavior of the presented WEC has only been studied using a linear wave theory. The question is how the dynamic behavior of the CFB and the averaged energy harvesting output change when moving from linear to nonlinear wave theory. This is investigated in the following chapters.

Chapter 4

Nonlinear Wave Theory

In order to model the behavior of homogeneous, incompressible, and inviscid fluids, the nonlinear governing equations of fluid motion have been presented in Chap. 2, see Eq. (2.2). However, the nonlinear BCs at the unknown position of the free surface $z = \eta(x, y, t)$ make the computation of a solution of the nonlinear governing equations very difficult. Therefore, these BCs have been linearized in Sect. 2.2 by neglecting higher-order terms in the wave amplitude and associated fluid motion. However, using the linearized wave theory, nonlinear wave effects have been neglected, which can significantly influence the wave motion for higher or faster waves. For example, the phase velocity c_{ph} of waves modeled by the linear wave theory is independent of the wave amplitude, see Eq. (2.19). However, this changes when nonlinearities as present in nonlinear governing equations of fluid motion from Eq. (2.2) are considered. Here, waves of larger wave amplitude move faster than waves of smaller wave amplitude [Newman18]. Therefore, it is impossible, for example, to precisely model the temporal behavior of real random waves with high wave heights over a longer time span with a linear theory.

A second simplification resulting from using the linear wave theory is that the sum of two solutions of the linearized governing equations from Eq. (2.11) is also a solution of those equations. However, this changes when using the nonlinear governing equations. Here, two different solutions of the nonlinear governing equations interact with each other, such that the interactions between the different solutions have to be calculated, see e.g. [SharmaDean79]. If the frequencies corresponding to these interactions are related to the eigenfrequency of some floating mechanical structure, this can lead to relatively large movements of the structure. This can positively affect the performance of the WEC presented in Chap. 3.

The described nonlinear effects motivate the generalization of the linear wave theory presented in Sect. 2.2 to corresponding nonlinear wave theories, where the effect of higher-order terms are considered. This is done using Taylor series expansions of the BCs (2.2b) and (2.2c) at $z = \eta$ in Sect. 4.1. Depending on the order up to which terms in the Taylor series expansions are considered, nonlinear theories of different orders are obtained. However, the resulting nonlinear theories are based on nonlinear partial differential equations (PDEs), which can only be solved numerically using a large computational effort. Therefore, Stokes' expansions are introduced, which are applied to the velocity potential ϕ and sea surface displacement η. As a result, ϕ and η can be calculated by solving a

sequence of linear PDEs [MalenicaMolin95].
Having computed the velocity potential ϕ and sea surface displacement η, it is presented how the nonlinear FSI between a structure and nonlinear water waves can be described. The resulting equations of motion are derived in Sect. 4.2 for the WEC introduced in Sect. 3.1. Afterward, the regular and random wave solutions of the linear wave theory, which have been presented in Sect. 2.2.1 and Sect. 2.2.2, respectively, are generalized to solutions of the nonlinear wave theories in Sect. 4.3. Finally, this chapter ends with Sect. 4.4, which gives a summary over the whole procedure for the computation of the nonlinear FSI between the WEC introduced in Sect. 3.1 and nonlinear water waves. This chapter has partly been published in [HollmSeifried23].

4.1 Fundamental Equations for the Nonlinear Fluid-structure Interaction

In this section, the fundamental equations for the calculation of nonlinear water waves are presented. This is done by developing a procedure that computes the velocity potential of the sea, which is disturbed by the presence and motion of a structure. As already assumed in Sect. 2.2, it is assumed in all following calculations that the structure has no steady forward velocity and no current is present around the structure.
In order to simplify the given problem, the dynamics of nonlinear water waves are first considered in the absence of any structure in Sect. 4.1.1, Sect. 4.1.2, and Sect. 4.1.3. Afterward, the corresponding equations to calculate the influence of a structure on the water waves are presented in Sect. 4.1.4. At the end of Sect. 4.1.4, a schematic representation of the overall procedure for calculating the nonlinear wave dynamics is shown in Fig. 4.2.

4.1.1 Derivation of Nonlinear Higher-order Equations

Since the nonlinearity of the governing equations of fluid motion from Eq. (2.2) comes from the BCs (2.2b) and (2.2c) at $z = \eta$, this section focuses on an approximation of these BCs by equations which are easier to solve. The first step is to combine the two BCs (2.2b) and (2.2c) into one single BC. To this end, the substantial derivative of Eq. (2.2c) is considered [Newman18], i. e.

$$\left(\frac{\partial}{\partial t} + \boldsymbol{\nabla}\phi \cdot \boldsymbol{\nabla}\right)\left[\phi_t + \frac{1}{2}\boldsymbol{\nabla}\phi \cdot \boldsymbol{\nabla}\phi + g\eta\right] = 0, \quad \text{for} \quad z = \eta(x, y, t). \tag{4.1}$$

Here, the substantial derivative expresses the time rate-of-change in a coordinate system moving with the fluid. Using Eq. (2.2b), Eq. (4.1) can be rewritten to, see e.g. [Mei83, Newman18],

$$\phi_{tt} + g\phi_z + 2\boldsymbol{\nabla}\phi \cdot \boldsymbol{\nabla}\phi_t + \frac{1}{2}\boldsymbol{\nabla}\phi \cdot \boldsymbol{\nabla}\left(\boldsymbol{\nabla}\phi \cdot \boldsymbol{\nabla}\phi\right) = 0, \quad \text{for} \quad z = \eta(x, y, t). \tag{4.2}$$

This BC is exact and only depends on ϕ, except that it has to be applied at the unknown position of the sea surface $z = \eta$. The formulation of an exact analytical theory is therefore almost impossible. Retaining only the linear terms, Eq. (4.2) reduces to Eq. (2.8).
Next, the exact BC (4.2) is expanded from the exact free sea surface $z = \eta(x, y, t)$ to $z = 0$. This is done by approximating all occurring derivatives of ϕ in the exact BC (4.2) by Taylor series expansions around $z = 0$ of form

$$\phi(x, y, \eta, t) = \phi(x, y, 0, t) + \eta\,\phi_z(x, y, 0, t) + \frac{1}{2}\eta^2\phi_{zz}(x, y, 0, t) + \mathcal{O}(\eta^3). \tag{4.3}$$

Depending on the approximation order of the Taylor series expansion, a sequence of BCs valid on $z = 0$ is obtained. The value of η appearing in Eq. (4.3) can be computed using Eq. (2.2b), which has to be expanded to $z = 0$ as well. The first three members of the resulting sequence of BCs are given by

$$\phi_{tt} + g\phi_z = 0 + \mathcal{O}(\phi^2), \tag{4.4a}$$

$$\phi_{tt} + g\phi_z + 2\boldsymbol{\nabla}\phi \cdot \boldsymbol{\nabla}\phi_t - \frac{1}{g}\phi_t\frac{\partial}{\partial z}\left(\phi_{tt} + g\phi_z\right) = 0 + \mathcal{O}(\phi^3), \tag{4.4b}$$

$$\begin{aligned}
&\phi_{tt} + g\phi_z + 2\boldsymbol{\nabla}\phi \cdot \boldsymbol{\nabla}\phi_t + \frac{1}{2}\boldsymbol{\nabla}\phi \cdot \boldsymbol{\nabla}\left(\boldsymbol{\nabla}\phi \cdot \boldsymbol{\nabla}\phi\right) \\
&\quad - \frac{1}{g}\phi_t\frac{\partial}{\partial z}\left(\phi_{tt} + g\phi_z + 2\boldsymbol{\nabla}\phi \cdot \boldsymbol{\nabla}\phi_t\right) \\
&\quad - \frac{1}{g}\left(-\frac{1}{g}\phi_t\phi_{tz} + \frac{1}{2}\boldsymbol{\nabla}\phi \cdot \boldsymbol{\nabla}\phi\right)\frac{\partial}{\partial z}\left(\phi_{tt} + g\phi_z\right) \\
&\quad + \frac{1}{2g^2}\left(\phi_t\right)^2\frac{\partial^2}{\partial z^2}\left(\phi_{tt} + g\phi_z\right) = 0 + \mathcal{O}(\phi^4),
\end{aligned} \tag{4.4c}$$

see e.g. [Newman18]. It can be seen that the complexity of the systematic procedure increases rapidly with increasing order of accuracy.
In the same way, the sea surface displacement η can be expressed by a sequence of expressions, which differ in their order of approximation. Applying the Taylor series expansion from Eq. (4.3) on Eq. (2.2c), for the first three approximation

orders, the sea surface displacement η can be expressed as

$$\eta = \left[-\frac{1}{g}\phi_t\right]_{z=0} + \mathcal{O}(\phi^2), \tag{4.5a}$$

$$\eta = \left[-\frac{1}{g}\left(\phi_t + \frac{1}{2}\boldsymbol{\nabla}\phi\cdot\boldsymbol{\nabla}\phi\right) + \frac{1}{g^2}\left(\phi_t\phi_{tz}\right)\right]_{z=0} + \mathcal{O}(\phi^3), \tag{4.5b}$$

$$\begin{aligned}\eta = &\left[-\frac{1}{g}\left(\phi_t + \frac{1}{2}\boldsymbol{\nabla}\phi\cdot\boldsymbol{\nabla}\phi\right) + \frac{1}{g^2}\left(\phi_t\phi_{tz} + \frac{1}{2}\frac{\partial}{\partial z}\left(\phi_t\,\boldsymbol{\nabla}\phi\cdot\boldsymbol{\nabla}\phi\right)\right)\right]_{z=0} \\ &- \left[\frac{1}{2g^3}\frac{\partial}{\partial z}\left(\left(\phi_t\right)^2\phi_{tz}\right)\right]_{z=0} + \mathcal{O}(\phi^4).\end{aligned} \tag{4.5c}$$

Equations (4.5a)-(4.5b) have also been stated by [Newman18]. Summarized, the following two steps of computation have to be done:

- Compute the velocity potential ϕ by solving the corresponding equations

$$\boldsymbol{\nabla}^2\phi = \phi_{xx} + \phi_{yy} + \phi_{zz} = 0, \qquad \text{for} \quad -h \le z \le 0, \tag{4.6a}$$

$$\text{BC (4.4a), (4.4b) or (4.4c)}, \qquad \text{for} \quad z = 0, \tag{4.6b}$$

$$\phi_z = 0, \qquad \text{for} \quad z = -h, \tag{4.6c}$$

  which depend on the used order of approximation.

- Compute the corresponding sea surface displacement η using Eq. (4.5) with the same approximation order, which is used describing the BC (4.4) at $z = 0$.

Using the BC (4.4a), which depends linearly on ϕ, Eq. (4.6) becomes the linearized governing equations of fluid motion from Eqs. (2.11a)-(2.11c).

4.1.2 First Example of Nonlinear Water Waves

In this section, nonlinear effects are examined, which occur when the linearized BC (4.4a) is replaced by the nonlinear BCs (4.4b) and (4.4c). This exemplary study is done by investigating long-crested deep water waves. Considering the linearized governing equations of fluid motion from Eq. (2.11), the velocity potential corresponding to regular water waves is given by Eq. (2.20). Considering waves propagating in x-direction and for $\beta = 0$, Eq. (2.20) simplifies to

$$\phi(x, z, t) = \frac{gA}{\omega}\mathrm{e}^{kz}\sin\left(kx - \omega t\right). \tag{4.7}$$

Here, the wave frequency ω and the wave number k has to fulfill the dispersion relation from Eq. (2.21). Direct substitution of the velocity potential from

Eq. (4.7) into the second-order BC (4.4b) reveals that the velocity potential from Eq. (4.7) is also a solution of the second-order boundary value problem from Eq. (4.6). Moreover, it can be found that the velocity potential from Eq. (4.7) is even a solution of the third-order BC (4.4c) provided that the dispersion relation from Eq. (2.21) is corrected for a second-order effect of the form

$$\omega^2 = kg(1 + k^2A^2) + \mathcal{O}(k^3A^3), \tag{4.8}$$

see e.g. [Newman18]. This relation can be used together with Eq. (2.19) to obtain the corresponding correction of the phase velocity

$$c_{\mathrm{ph}} = \frac{\omega}{k} = \sqrt{\frac{g}{k}}\sqrt{1 + k^2A^2} + \mathcal{O}(k^3A^3) = \sqrt{\frac{g}{k}}\left(1 + \frac{1}{2}k^2A^2\right) + \mathcal{O}(k^3A^3). \tag{4.9}$$

This shows that for nonlinear wave theories, the phase velocity c_{ph} depends on the amplitude of the water waves. Larger waves travel faster than smaller waves. This dependence is known as amplitude dispersion. As a result, the behavior of random waves consisting of wave components with high peak amplitudes cannot be modeled precisely by linear wave theory over a long period. While in the linear wave theory they have the same phase velocity, higher waves pass the smaller waves in the nonlinear theory.

Although the velocity potential from Eq. (4.7) satisfies the different BCs from Eq. (4.4) by just adjusting the dispersion relation, the free sea surface displacement η has to be corrected by some higher order terms. Inserting the velocity potential from Eq. (4.7) into Eq. (4.5), the respected first-, second-, and third-order sea surface displacement η_1, η_2, and η_3 are given by

$$k\eta_1 = kA\cos(\vartheta), \qquad \text{with} \quad \omega^2 = kg, \tag{4.10a}$$

$$k\eta_2 = kA\cos(\vartheta) + \frac{1}{2}(kA)^2\cos(2\vartheta), \quad \text{with} \quad \omega^2 = kg, \tag{4.10b}$$

$$k\eta_3 = kA\cos(\vartheta) + \frac{1}{2}(kA)^2\cos(2\vartheta) + \frac{3}{8}(kA)^3\cos(3\vartheta) - \frac{3}{8}(kA)^3\cos(\vartheta), \quad \text{with} \quad \omega^2 = kg(1 + k^2A^2), \tag{4.10c}$$

whereby $\vartheta = kx - \omega t$. Figure 4.1 compares the sea surface displacements η_1, η_2, and η_3 for the wave amplitude $A = 0.3\,\mathrm{m}$, wave number $k = 1\,\mathrm{m}^{-1}$ and water depth $h = 5\,\mathrm{m}$. Here, Fig. 4.1a presents these sea surface displacements at $t = 0$ varying in space and Fig. 4.1b at $x = 0$ varying in time. It can be seen that while the sea surface displacements η_1, η_2, and η_3 have the same wavelength, the third-order sea surface displacement η_3 has a smaller wave period. This follows from the fact that all sea surface displacements are computed for the same wave number k, but the dispersion relation from Eq. (4.8) increases the value of ω compared to the linear dispersion relation from Eq. (2.21).

Moreover, Fig. 4.1 shows that higher approximation orders lead to steeper water waves. The sea sea surface displacement η_3 is steeper than η_2, which is in turn steeper than η_1. For regular water waves, the wave steepness is defined by the

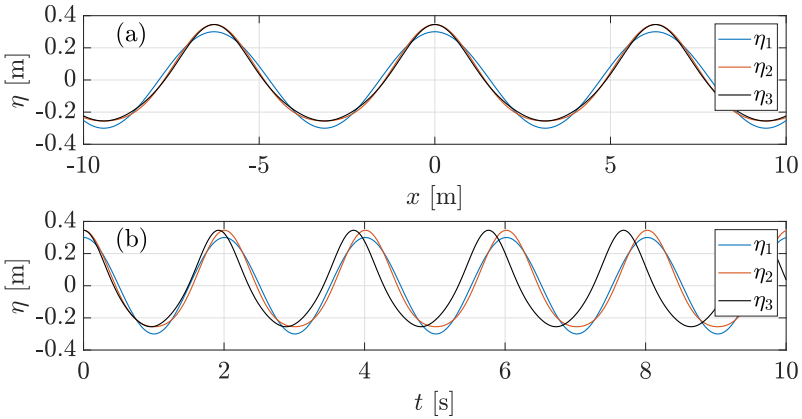

Figure 4.1: Comparison of surface displacements of first- (η_1), second- (η_2), and third-order (η_3) for the wave amplitude of $A = 0.3\,\mathrm{m}$ and wave number $k = 1\,\mathrm{m}^{-1}$. (a): Solutions at $t = 0$ varying in space. (b): Solutions at $x = 0$ varying in time.

quotient of the wave height H and the wavelength λ. However, it has to be noted that the water waves break if the wave steepness is too high. In this case, the value of η is not uniquely defined anymore, such that the behavior of the water waves can no longer be described by the governing equations of fluid motion from Eq. (2.2). Therefore, the question arises, up to which maximum wave steepness do water waves not break. On a sloping beach, there is no simple theory yet for predicting the maximal wave height for which a water wave does not break [Mei83]. However, the maximal wave height for non-breaking waves has been computed for strictly horizontal bottoms. Here, it is assumed that wave breaking occurs when the maximum horizontal velocity of the water particles at the wave crest exceeds the phase velocity c_{ph} of the wave. The condition for the maximal wave height has been computed by [Miche44] and is given by [ClaussEtAl88, Mei83] as

$$\left(\frac{H}{\lambda}\right)_{\max} = 0.142 \tanh(kh). \tag{4.11}$$

Alternatively, the wave steepness can be expressed by the product of the wave amplitude A and the wave number k. Using $H = 2A$ and $\lambda = 2\pi/k$, Eq. (4.11) results in

$$(kA)_{\max} = 0.142\,\pi \tanh(kh). \tag{4.12}$$

In this work, the expressions H/λ and kA are both referred to as the wave steepness of a regular water wave. It has to be noted that the factor kA plays a significant role in the description of the nonlinear dispersion relation, the phase velocity c_{ph}, and the surface displacement η, see Eqs. (4.8)-(4.10). When generalizing $k\eta_1$ to the higher-order surface displacements $k\eta_2$ and $k\eta_3$, additional

terms are considered, which depend on exponents of the wave steepness kA, see Eq. (4.10). Therefore, the magnitude of kA can be used to decide which approximation order has to be used to model the water waves appropriately. This is used again in the following, where general perturbation series of ϕ and η are introduced.

4.1.3 Stokes' Expansions of Higher Order

By deriving Eq. (4.6), the calculation of the velocity potential ϕ has been decoupled from the free sea surface displacement η. However, the nonlinearity of the BC (4.4) makes the computation of solutions still very difficult. Especially there is the question of how nonlinear random wave solutions can be computed efficiently. Therefore, the BC (4.4) is approximated by a sequence of linear equations in the following.
Motivated by the fact that the nonlinear sea surface displacement η has been expressed in Eq. (4.10) by terms dependent on different orders of the wave steepness kA, it is assumed that ϕ and η can be expressed by perturbation series of the form, see e.g. [MalenicaMolin95],

$$\phi = \varepsilon\phi^{(1)} + \varepsilon^2\phi^{(2)} + \varepsilon^3\phi^{(3)} + \mathcal{O}(\varepsilon^4), \tag{4.13a}$$

$$\eta = \varepsilon\eta^{(1)} + \varepsilon^2\eta^{(2)} + \varepsilon^3\eta^{(3)} + \mathcal{O}(\varepsilon^4). \tag{4.13b}$$

Here, ε is a perturbation parameter related to the wave steepness kA and is assumed to be small. Based on the pioneering work of Stokes [Stokes47], who used this approach to find periodic solutions of nonlinear water waves, these perturbation series are known as Stokes' expansions. The terms $\phi^{(i)}$ and $\eta^{(i)}$ are called the i-th Stokes component of the velocity potential and sea surface displacement, respectively. If all terms of the perturbation series from Eq. (4.13) up to ε^n are considered, it is said that Stokes' theory of n-th order is used.
It has to be noted that no velocity potential $\phi^{(0)}$ of zero-th order is considered in Eq. (4.13a). This zero-order term $\phi^{(0)}$ would correspond to the steady potential induced by a weak current or a steady forward motion of the structure [SkourupEtAl00]. However, the corresponding effects of a weak current or a steady forward motion of the structure are not considered in this thesis.
Substituting Eq. (4.13a) into the Laplace equation (4.6a) and the BC at the sea bottom (4.6c), it can be found that all velocity potentials $\phi^{(i)}$, $i = 1, 2, 3, \ldots$, have to satisfy these equations as well. This results in

$$\boldsymbol{\nabla}^2\phi^{(i)} = \phi^{(i)}_{xx} + \phi^{(i)}_{yy} + \phi^{(i)}_{zz} = 0, \qquad \text{for} \quad -h \le z \le 0, \tag{4.14a}$$

$$\phi^{(i)}_z = 0, \qquad \text{for} \quad z = -h. \tag{4.14b}$$

Difficulties appear for the BC at $z = 0$. Substituting Eq. (4.13a) into the

third-order Eq. (4.4c) and sorting for the resulting exponents in ε^i, it holds

$$\varepsilon\left(\phi_{tt}^{(1)}+g\phi_z^{(1)}\right)+\varepsilon^2\left(\phi_{tt}^{(2)}+g\phi_z^{(2)}-F(\phi^{(1)})\right)+\varepsilon^3\left(\phi_{tt}^{(3)}+g\phi_z^{(3)}-Q(\phi^{(1)},\phi^{(2)})\right) = 0+\mathcal{O}(\varepsilon^4). \tag{4.15}$$

Here, the functions F and Q are defined as

$$F(\phi^{(1)}) := -2\boldsymbol{\nabla}\phi^{(1)}\cdot\boldsymbol{\nabla}\phi_t^{(1)}+\frac{1}{g}\phi_t^{(1)}\frac{\partial}{\partial z}\left(\phi_{tt}^{(1)}+g\phi_z^{(1)}\right), \tag{4.16}$$

$$\begin{aligned} Q(\phi^{(1)},\phi^{(2)}) := &-2\boldsymbol{\nabla}\phi^{(1)}\cdot\boldsymbol{\nabla}\phi_t^{(2)}-2\boldsymbol{\nabla}\phi^{(2)}\cdot\boldsymbol{\nabla}\phi_t^{(1)}\\ &-\frac{1}{2}\boldsymbol{\nabla}\phi^{(1)}\cdot\boldsymbol{\nabla}\left(\boldsymbol{\nabla}\phi^{(1)}\cdot\boldsymbol{\nabla}\phi^{(1)}\right)+\frac{1}{g}\phi_t^{(2)}\frac{\partial}{\partial z}\left(\phi_{tt}^{(1)}+g\phi_z^{(1)}\right)\\ &+\frac{1}{g}\phi_t^{(1)}\frac{\partial}{\partial z}\left(\phi_{tt}^{(2)}+g\phi_z^{(2)}\right)+\frac{2}{g}\phi_t^{(1)}\frac{\partial}{\partial z}\left(\boldsymbol{\nabla}\phi^{(1)}\cdot\boldsymbol{\nabla}\phi_t^{(1)}\right)\\ &-\frac{1}{g}\left(\frac{1}{g}\phi_t^{(1)}\phi_{tz}^{(1)}-\frac{1}{2}\boldsymbol{\nabla}\phi^{(1)}\cdot\boldsymbol{\nabla}\phi^{(1)}\right)\frac{\partial}{\partial z}\left(\phi_{tt}^{(1)}+g\phi_z^{(1)}\right)\\ &-\frac{1}{2g^2}\left(\phi_t^{(1)}\right)^2\frac{\partial^2}{\partial z^2}\left(\phi_{tt}^{(1)}+g\phi_z^{(1)}\right). \end{aligned} \tag{4.17}$$

The BC (4.15) holds if the terms multiplied by ε^i vanish for each $i=1,2,3$. As a result of this, the BCs for the first three velocity potentials $\phi^{(1)}$, $\phi^{(2)}$, and $\phi^{(3)}$ are given by

$$\mathcal{O}(\varepsilon)\ :\ \phi_{tt}^{(1)}+g\phi_z^{(1)}=0, \qquad \text{for}\ \ z=0, \tag{4.18a}$$

$$\mathcal{O}(\varepsilon^2):\ \phi_{tt}^{(2)}+g\phi_z^{(2)}=F(\phi^{(1)}), \qquad \text{for}\ \ z=0, \tag{4.18b}$$

$$\mathcal{O}(\varepsilon^3):\ \phi_{tt}^{(3)}+g\phi_z^{(3)}=Q(\phi^{(1)},\phi^{(2)}), \qquad \text{for}\ \ z=0. \tag{4.18c}$$

It has to be noted that BCs (4.18a), (4.18b) have been found several times in literature, see e.g. [Eatock TaylorHung87, RahmanEtAl99]. In contrast to this, BC (4.18c) has not been found by the author of this thesis in this form in literature. However, [MalenicaMolin95] have computed this BC for regular water waves. If such waves are substituted into Eq. (4.18c), the same equations are obtained as in [MalenicaMolin95]. This verifies Eq. (4.18c).
An advantage of using the BCs (4.18) instead of the BCs (4.4) is that the BCs (4.18) are linear with respect to the corresponding highest-order velocity potential. Furthermore, the lower-order velocity potentials are independent of the higher-order potentials. This means that the velocity potentials $\phi^{(i)}$, $i=1,2,3$, can be computed in increasing order by solving the linear Eqs. (4.14) and (4.18). Having computed the first three potentials $\phi^{(1)}$, $\phi^{(2)}$, and $\phi^{(3)}$, the corresponding sea surface displacements $\eta^{(1)}$, $\eta^{(2)}$, and $\eta^{(3)}$ can be computed in a similar way.

In order to derive the corresponding expressions for $\eta^{(1)}$, $\eta^{(2)}$, and $\eta^{(3)}$, the expansions from Eq. (4.13) have to be substituted into Eq. (4.5c). The first three sea surface displacements $\eta^{(1)}$, $\eta^{(2)}$, and $\eta^{(3)}$ are given by

$$\eta^{(1)} = \left[-\frac{1}{g} \phi_t^{(1)} \right]_{z=0}, \tag{4.19a}$$

$$\eta^{(2)} = \left[-\frac{1}{g} \left(\phi_t^{(2)} + \frac{1}{2} \boldsymbol{\nabla} \phi^{(1)} \cdot \boldsymbol{\nabla} \phi^{(1)} \right) + \frac{1}{g^2} \left(\phi_t^{(1)} \phi_{tz}^{(1)} \right) \right]_{z=0}, \tag{4.19b}$$

$$\begin{aligned} \eta^{(3)} = & \left[-\frac{1}{g} \left(\phi_t^{(3)} + \boldsymbol{\nabla} \phi^{(1)} \cdot \boldsymbol{\nabla} \phi^{(2)} \right) + \frac{1}{g^2} \left(\phi_t^{(1)} \phi_{tz}^{(2)} + \phi_t^{(2)} \phi_{tz}^{(1)} \right) \right]_{z=0} \\ & + \left[\frac{1}{2g^2} \frac{\partial}{\partial z} \left(\phi_t^{(1)} \boldsymbol{\nabla} \phi^{(1)} \cdot \boldsymbol{\nabla} \phi^{(1)} \right) - \frac{1}{2g^3} \frac{\partial}{\partial z} \left(\left(\phi_t^{(1)} \right)^2 \phi_{tz}^{(1)} \right) \right]_{z=0}. \end{aligned} \tag{4.19c}$$

The expressions for $\eta^{(1)}$ and $\eta^{(2)}$ can also be found in [Eatock TaylorHung87]. Comparing $\eta^{(1)}$ from Eq. (4.19a) with the linearized sea surface displacement η from Eq. (2.12), it can be seen that $\eta^{(1)}$ exactly represents the sea surface displacement resulting from the linear analysis presented in Sect. 2.2. It can be concluded that $\eta = \varepsilon\eta^{(1)} + \varepsilon^2\eta^{(2)}$ and $\eta = \varepsilon\eta^{(1)} + \varepsilon^2\eta^{(2)} + \varepsilon^3\eta^{(3)}$ are the second- and third-order generalizations of the linear sea surface displacement η presented in Eq. (2.12), respectively.

4.1.4 Body Disturbance

In the previous sections, it has been shown how the velocity potential ϕ is calculated in the case of nonlinear wave theory by solving a sequence of linear PDEs. All presented calculations have been performed in the absence of any mechanical body. However, if a mechanical body is considered, the wave dynamics are disturbed by the presence of the body. In the case of linear wave theory, the corresponding effects of a body on the wave dynamics have been discussed in Sect. 2.3. In this section, it is shown how these disturbances can be computed when nonlinear wave theory is used.

In this thesis, only mechanical bodies are considered that are impermeable to water. Furthermore, as the general case, floating bodies are considered, which include static bodies as a special case. For floating bodies, which are impermeable to water, the fluid at a point next to the moving bodies has the same velocity in the normal direction as the body itself at this point. The resulting BC at the wetted surface of the body is given by Eq. (2.3). It can be seen that the BC depends on the total velocity vector $\boldsymbol{u}$ of the wetted surface of the body. Following the Stokes expansion procedure from Eq. (4.13), the vector $\boldsymbol{u}$ is also expanded into perturbation series of form, see e.g. [BaiTeng13],

$$\boldsymbol{u} = \varepsilon \boldsymbol{u}^{(1)} + \varepsilon^2 \boldsymbol{u}^{(2)} + \varepsilon^3 \boldsymbol{u}^{(3)} + \dots \tag{4.20}$$

In this way, it is possible to specify BCs for each order of ε^i, $i = 1, 2, 3, \ldots$, at the surface of the moving body, whereby the BCs are of the same form as BC (2.3). In general, the presence of the bodies disturbs the dynamics of the incoming water waves. Some occurring effects have been discussed in Sect. 2.3. There, the velocity potential of the linearized problem has been separated into the velocity potential of the incoming water waves, the scattering potential, and the radiation potentials, see Eq. (2.29). Each potential can be calculated independently of each other by solving the Laplace equation with different BCs, see Eq. (2.32). However, in the nonlinear problem, the nonlinearity of the BC at the sea surface does not allow such an independent computation of the different velocity potentials. Therefore, instead of separating the total velocity potential ϕ into incident, scattering, and different radiation potentials, ϕ is divided only into two velocity potentials: the potential ϕ_0 of the incoming water waves and the potential ϕ_B corresponding to the body disturbance.
To replace the nonlinear BC (4.2) at the sea surface $z = \eta$ by a sequence of linear BCs at $z = 0$, both velocity potentials, ϕ_0 and ϕ_B, are expanded following the Stokes expansion procedure presented in Eq. (4.13). This results in

$$\phi = \phi_0 + \phi_\mathrm{B} = \varepsilon \underbrace{(\phi_0^{(1)} + \phi_\mathrm{B}^{(1)})}_{=\phi^{(1)}} + \varepsilon^2 \underbrace{(\phi_0^{(2)} + \phi_\mathrm{B}^{(2)})}_{=\phi^{(2)}} + \varepsilon^3 \underbrace{(\phi_0^{(3)} + \phi_\mathrm{B}^{(3)})}_{=\phi^{(3)}} + \mathcal{O}(\varepsilon^4). \quad (4.21)$$

Here, $\phi_0^{(i)}$ and $\phi_\mathrm{B}^{(i)}$ are the respective velocity potentials coming from the Stokes expansion of ϕ_0 and ϕ_B. Comparing Eq. (4.21) with Eq. (4.13a), it can be seen that the velocity potentials $\phi^{(i)}$ are split into a part corresponding to the incident velocity potential, $\phi_0^{(i)}$, and a part corresponding to the body disturbance, $\phi_B^{(i)}$. It has to be noted that in the absence of the body, the velocity potential corresponding to the body disturbance, ϕ_B, vanishes. It results $\phi = \phi_0$. This means that the velocity potentials $\phi_0^{(i)}$ have to satisfy Eq. (4.14) along with a sequence of BCs at $z = 0$, where the first three members are given by Eq. (4.18). For the incident velocity potentials $\phi_0^{(1)}$ and $\phi_0^{(2)}$, some analytical solutions corresponding to regular and random water waves are given in the Sect. 4.3.
Knowing the incident velocity potentials $\phi_0^{(i)}$, BCs at $z = 0$ for the velocity potentials corresponding to the body disturbance, $\phi_\mathrm{B}^{(i)}$, can be formulated by substituting $\phi^{(i)} = \phi_0^{(i)} + \phi_\mathrm{B}^{(i)}$ into Eq. (4.18). Since the incident velocity potentials $\phi_0^{(i)}$ satisfy Eq. (4.18), the BCs for the computation of the first three velocity potentials corresponding to the body disturbance $\phi_\mathrm{B}^{(1)}$, $\phi_\mathrm{B}^{(2)}$, and $\phi_\mathrm{B}^{(3)}$ are given by

$$\mathcal{O}(\varepsilon) \;:\; \phi_{\mathrm{B},tt}^{(1)} + g\phi_{\mathrm{B},z}^{(1)} = 0, \qquad \text{for } z = 0, \quad (4.22a)$$

$$\mathcal{O}(\varepsilon^2) : \; \phi_{\mathrm{B},tt}^{(2)} + g\phi_{\mathrm{B},z}^{(2)} = F(\phi_0^{(1)} + \phi_\mathrm{B}^{(1)}) - F(\phi_0^{(1)}), \qquad \text{for } z = 0, \quad (4.22b)$$

$$\mathcal{O}(\varepsilon^3) : \; \phi_{\mathrm{B},tt}^{(3)} + g\phi_{\mathrm{B},z}^{(3)} = Q(\phi_0^{(1)} + \phi_\mathrm{B}^{(1)}, \phi_0^{(2)} + \phi_\mathrm{B}^{(2)}) - Q(\phi_0^{(1)}, \phi_0^{(2)}), \qquad \text{for } z = 0. \quad (4.22c)$$

In order to compute the values of the velocity potentials $\phi_{\mathrm{B}}^{(i)}$, BCs at the surface of the floating body also have to be formulated. These BCs can be calculated by substituting Eqs. (4.20) and (4.21) into Eq. (2.3). This results in

$$\mathcal{O}(\varepsilon^i): \ \boldsymbol{\nabla}\phi_{\mathrm{B}}^{(i)}\cdot\boldsymbol{n} = -\boldsymbol{\nabla}\phi_0^{(i)}\cdot\boldsymbol{n}+\boldsymbol{u}^{(i)}\cdot\boldsymbol{n}, \ \text{ at } (x,y,z)\in S_{\mathrm{B0}},\ i=1,2,3,\ldots. \quad (4.23)$$

It has to be noted that the BCs (4.23) are not formulated at the actual wetted surface of the body S_{B}, but at S_{B0}. Here, S_{B0} is defined in Eq. (2.9) and denotes all points at the surface of the body, which are located below the still water level. The BCs (4.23) are not formulated at S_{B}, but at S_{B0}, since the velocity potentials $\phi_{\mathrm{B}}^{(i)}$ are only calculated at positions located below the rest position of the sea surface, i. e. for $z \leq 0$.

Furthermore, it has to be noted that, as in the linear case, a radiation condition has to be formulated, which determines the behavior of $\phi_{\mathrm{B}}^{(i)}$ far away from the floating body. In the linear case, this condition is given by Eq. (2.33). Radiation conditions for the higher-order velocity potentials $\phi_{\mathrm{B}}^{(i)}$, $i>1$, can be found, for example, in [MalenicaMolin95, GrueBiberg93, MalenicaEtAl95]. In this thesis, the velocity potentials $\phi_{\mathrm{B}}^{(i)}$ are computed numerically on a domain of finite length. Instead of radiation conditions, appropriate absorbing BCs are formulated here at the end of the considered spatial domain. These prevent the reflection of the outgoing water waves from propagating back into the domain. Details about the absorbing BCs can be found in Sect. 6.2.

In Fig. 4.2, the nonlinear scheme for the computation of the total velocity potential $\phi = \phi_0 + \phi_{\mathrm{B}}$ is summarized. All corresponding equations for the calculation of the first three components $\phi^{(1)}$, $\phi^{(2)}$, and $\phi^{(3)}$ of the potential ϕ are presented. Let $\boldsymbol{u}^{(1)}$, $\boldsymbol{u}^{(2)}$, and $\boldsymbol{u}^{(3)}$ be the components of the actual body velocity $\boldsymbol{u}$, see Eq. (4.20). It is assumed that the position of the surface S_{B0} as well as the velocities $\boldsymbol{u}^{(1)}$, $\boldsymbol{u}^{(2)}$, and $\boldsymbol{u}^{(3)}$ are known. In the first step, the incident velocity potentials $\phi_0^{(1)}$, $\phi_0^{(2)}$, and $\phi_0^{(3)}$ have to be computed. Afterward, the velocity potentials corresponding to the body disturbance, $\phi_{\mathrm{B}}^{(1)}$, $\phi_{\mathrm{B}}^{(2)}$, and $\phi_{\mathrm{B}}^{(3)}$, have to be calculated. These depend on the geometric shape, the position, and the dynamics of the moving body. Therefore, the velocity potentials $\phi_{\mathrm{B}}^{(1)}$, $\phi_{\mathrm{B}}^{(2)}$, and $\phi_{\mathrm{B}}^{(3)}$ can generally only be calculated numerically.

To summarize, the total velocity potential $\phi = \phi_0 + \phi_{\mathrm{B}}$ and its components $\phi^{(1)}$, $\phi^{(2)}$, and $\phi^{(3)}$ are calculated using the nonlinear scheme presented in Fig. 4.2. Afterward, these potentials can be used to compute the sea surface displacement η of the sea, which is disturbed by the presence of the body, using Eqs. (4.19) and (4.13b).

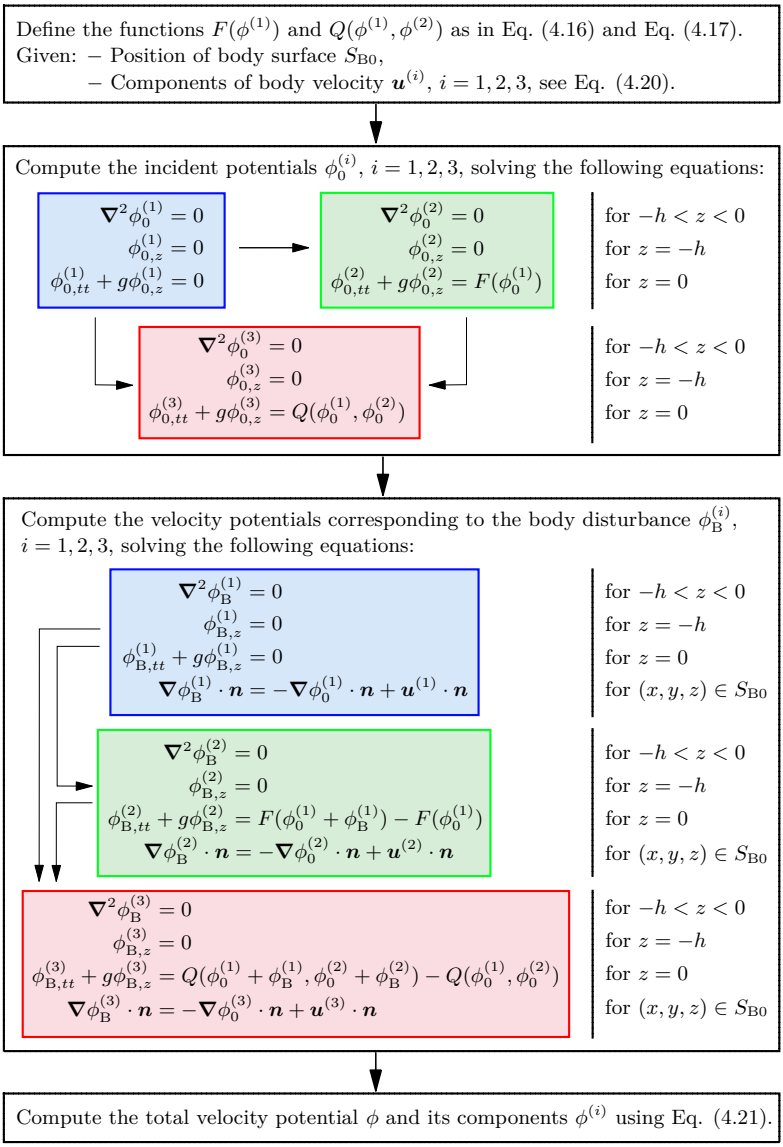

Figure 4.2: Schematic representation of the method for calculating the total velocity potential ϕ disturbed by the presence of a body of arbitrary shape, and its components $\phi^{(1)}$, $\phi^{(2)}$, and $\phi^{(3)}$.

4.2 Dynamics of Mechanical Structures in Nonlinear Water Waves

After showing how the velocity potential of waves disturbed by a moving mechanical structure can be calculated in the nonlinear case by solving a sequence of linear PDEs, it is presented how this potential can be used to calculate the motion of the structure. To this end, general expressions for the hydrodynamic loads acting on a structure are presented. Afterward, the hydrodynamic loads are used to formulate the equations of motion of a floating mechanical system.
In the following, it is presented how the dynamics of the WEC described in Sect. 3.1 can be computed in nonlinear water waves. This is done by determining the acting hydrodynamic forces and the equations of motions of the WEC. The hydrodynamic torques acting on the WEC do not need to be calculated here since the WEC can only perform translational but no rotational motions.

4.2.1 Calculation of Hydrodynamic Forces

The hydrodynamic forces acting on a general mechanical structure are calculated by integrating the hydrodynamic pressure over the wetted surface S_B of the structure, see Eq. (2.6). Here, the hydrodynamic pressure can be computed by means of Bernoulli's equation (2.5), which depends on the velocity potential $\phi = \phi_0 + \phi_\mathrm{B}$.
One difficulty in calculating the hydrodynamic forces is that the wetted surface S_B is time-varying. This means that the hydrodynamic forces depend not only on the velocity potential ϕ but also on the sea surface displacement η. Therefore, the integral over the wetted surface of the mechanical structure is split into the surface S_B0 from Eq. (2.9) and some time-dependent part $\Delta S(t)$. Using the vertical coordinate z, the surface S_B0 denotes the surface of the mechanical structure with $z \leq 0$, while $\Delta S(t)$ is varying with the sea surface displacement η. Thus, it holds for the hydrodynamic forces

$$\boldsymbol{F} = \iint\limits_{S_\mathrm{B}} p\boldsymbol{n}\,\mathrm{d}S = \iint\limits_{S_\mathrm{B0}} p\boldsymbol{n}\,\mathrm{d}S + \iint\limits_{\Delta S(t)} p\boldsymbol{n}\,\mathrm{d}S. \tag{4.24}$$

If the mechanical structure is a cylindrical floating body (CFB) that only performs a translational motion, the cross-section of the surface S_B0 and the still water level at $z = 0$ does not change over time. This cross-section is denoted by C_0. The surface S_B0 and cross-section C_0 are illustrated in Fig. 4.3. Then the integral over $\Delta S(t)$ can be determined by means of C_0 and the sea surface displacement η. It follows that hydrodynamic forces acting on a CFB, which is only able to

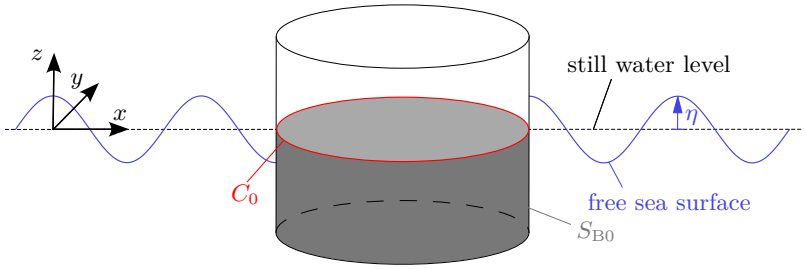

Figure 4.3: Sketch of cylinder in water waves, including the cross-section C_0 and surface S_{B0}.

perform translational motions, can be computed by

$$\boldsymbol{F} = \iint\limits_{S_{\mathrm{B0}}} p\boldsymbol{n}\,\mathrm{d}S + \int\limits_{C_0}\int\limits_{0}^{\eta} p\boldsymbol{n}\,\mathrm{d}z\,\mathrm{d}C. \tag{4.25}$$

Substituting the perturbation series of ϕ from Eq. (4.13a) into Bernoulli's equation (2.5), the pressure p can be computed as a function of $\phi^{(i)}$, $i = 1, 2, 3, \ldots$ Using this and ordering all appearing terms with respect to the corresponding order of ε, the first integral in Eq. (4.25) becomes

$$\begin{aligned}\iint\limits_{S_{\mathrm{B0}}} p\boldsymbol{n}\,\mathrm{d}S = &- \iint\limits_{S_{\mathrm{B0}}} \rho g z\boldsymbol{n}\,\mathrm{d}S - \varepsilon \iint\limits_{S_{\mathrm{B0}}} \rho\phi_t^{(1)}\boldsymbol{n}\,\mathrm{d}S \\ &- \varepsilon^2 \iint\limits_{S_{\mathrm{B0}}} \left(\rho\phi_t^{(2)} + \rho\frac{1}{2}\boldsymbol{\nabla}\phi^{(1)}\cdot\boldsymbol{\nabla}\phi^{(1)}\right)\boldsymbol{n}\,\mathrm{d}S \\ &- \varepsilon^3 \iint\limits_{S_{\mathrm{B0}}} \left(\rho\phi_t^{(3)} + \rho\boldsymbol{\nabla}\phi^{(1)}\cdot\boldsymbol{\nabla}\phi^{(2)}\right)\boldsymbol{n}\,\mathrm{d}S + \mathcal{O}(\varepsilon^4).\end{aligned} \tag{4.26}$$

For the calculation of the second integral in Eq. (4.25) and when $0 < \eta(t)$, it has to be noted that the pressure p has to be integrated over $0 < z < \eta(t)$. However, using the nonlinear scheme presented in Fig. 4.2, the velocity potentials $\phi^{(i)}$ are only determined for $-h \le z \le 0$. In order to be able to compute the pressure $p = p(z)$ for $0 < z < \eta(t)$, Taylor series expansions of $p(z)$ around $z = 0$ are used. Furthermore, it is assumed that the water comes only in contact with the lateral surface of the cylinder. Then the normal vector $\boldsymbol{n}$ is constant in z. Expressing η by the corresponding Stokes' expansion from Eq. (4.13b) and using the calculated expressions for $\eta^{(1)}$ and $\eta^{(2)}$ from Eq. (4.19), it results

$$\int\limits_0^{\eta} p\boldsymbol{n}\,\mathrm{d}z = \left(\varepsilon^2\frac{1}{2}\rho g\left(\eta^{(1)}\right)^2 + \varepsilon^3\left(\rho g\eta^{(1)}\eta^{(2)} + \frac{1}{2}\rho\eta_{tt}^{(1)}\left(\eta^{(1)}\right)^2\right) + \mathcal{O}(\varepsilon^4)\right)\boldsymbol{n}. \tag{4.27}$$

Finally, substituting Eqs. (4.26) and (4.27) into Eq. (4.25), the hydrodynamic forces acting on a CFB are given by

$$\boldsymbol{F} = \iint\limits_{S_\mathrm{B}} p\boldsymbol{n}\,\mathrm{d}S = \boldsymbol{F}^{(0)} + \varepsilon^1\boldsymbol{F}^{(1)} + \varepsilon^2\boldsymbol{F}^{(2)} + \varepsilon^3\boldsymbol{F}^{(3)} + \mathcal{O}(\varepsilon^4), \tag{4.28}$$

with

$$\begin{aligned}
\boldsymbol{F}^{(0)} &= -\iint\limits_{S_{\mathrm{B}0}} \rho g z\boldsymbol{n}\,\mathrm{d}S, & \boldsymbol{F}^{(1)} &= -\iint\limits_{S_{\mathrm{B}0}} \rho\phi_t^{(1)}\boldsymbol{n}\,\mathrm{d}S,\\
\boldsymbol{F}^{(2)} &= -\iint\limits_{S_{\mathrm{B}0}} \left(\rho\phi_t^{(2)} + \rho\frac{1}{2}\boldsymbol{\nabla}\phi^{(1)}\cdot\boldsymbol{\nabla}\phi^{(1)}\right)\boldsymbol{n}\,\mathrm{d}S + \int\limits_{C_0}\frac{1}{2}\rho g\left(\eta^{(1)}\right)^2\boldsymbol{n}\,\mathrm{d}C,\\
\boldsymbol{F}^{(3)} &= -\iint\limits_{S_{\mathrm{B}0}} \left(\rho\phi_t^{(3)} + \rho\boldsymbol{\nabla}\phi^{(1)}\cdot\boldsymbol{\nabla}\phi^{(2)}\right)\boldsymbol{n}\,\mathrm{d}S\\
&\quad + \int\limits_{C_0}\left(\rho g\eta^{(1)}\eta^{(2)} + \frac{1}{2}\rho\eta_{tt}^{(1)}\left(\eta^{(1)}\right)^2\right)\boldsymbol{n}\,\mathrm{d}C.
\end{aligned} \tag{4.29}$$

The formulas for $\boldsymbol{F}^{(1)}$ and $\boldsymbol{F}^{(2)}$ have also been presented in [Eatock TaylorHung87]. For the case of incoming regular water waves, the formula for $\boldsymbol{F}^{(3)}$ has successfully been compared with the corresponding formula presented in [MalenicaMolin95]. Comparing the forces from Eq. (4.28) and Eq. (4.29) with the hydrodynamic forces acting in the linear case, which are given by Eq. (2.34), it can be seen that $\boldsymbol{F}^{(0)} + \varepsilon^1\boldsymbol{F}^{(1)}$ exactly represents the hydrodynamic forces resulting from a linear analysis. It can be concluded that $\boldsymbol{F}^{(0)} + \varepsilon^1\boldsymbol{F}^{(1)} + \varepsilon^2\boldsymbol{F}^{(2)}$ and $\boldsymbol{F}^{(0)} + \varepsilon^1\boldsymbol{F}^{(1)} + \varepsilon^2\boldsymbol{F}^{(2)} + \varepsilon^3\boldsymbol{F}^{(3)}$ are the respective second- and third-order generalizations of the hydrodynamic forces formulated in Eq. (2.34) for the linear case.

4.2.2 Nonlinear Equations of Motion of the Wave Energy Converter

After computing the nonlinear hydrodynamic forces acting on a CFB, the equations of motion of the WEC introduced in Sect. 3.1 are formulated. For simplicity, it is assumed that the WEC moves only translationally in the $x-z$-plane, see Fig. 3.2. The considered WEC consists of a CFB, which moves with the displacement ξ against its resting position in the direction of α. The equation of motion of the CFB is given by Eq. (3.2). The CFB is the only part of the WEC, which comes in contact with the water waves.

The integrals of the hydrodynamic pressure about the wetted surface S_B of the CFB are given by Eqs. (4.28) and (4.29). As already defined in Eq. (3.1), the components of the force $\boldsymbol{F}$ in x-, y-, and z-direction are denoted by F_1, F_2, and F_3, respectively. Using a similar notation for the forces $\boldsymbol{F}^{(i)}$, it holds

$$\boldsymbol{F} = \begin{bmatrix} F_1 \\ F_2 \\ F_3 \end{bmatrix}, \quad \boldsymbol{F}^{(i)} = \begin{bmatrix} F_1^{(i)} \\ F_2^{(i)} \\ F_3^{(i)} \end{bmatrix}, \quad i = 1, 2, 3, \ldots. \tag{4.30}$$

In the following, the hydrodynamic forces resulting from a third-order Stokes theory are considered. Using the notation from Eq. (4.30) and substituting Eq. (4.28) into Eq. (3.2), it follows

$$\begin{aligned} M\ddot{\xi} = &- F_\mathrm{damp}(\dot{\xi}) + \cos(\alpha)\left(\varepsilon F_1^{(1)} + \varepsilon^2 F_1^{(2)} + \varepsilon^3 F_1^{(3)}\right) \\ &+ \sin(\alpha)\left\{F_3^{(0)} + \varepsilon F_3^{(1)} + \varepsilon^2 F_3^{(2)} + \varepsilon^3 F_3^{(3)} - Mg - \sin(\alpha)\lambda_{\mathrm{vis},z}\dot{\xi}\right\}. \end{aligned} \tag{4.31}$$

Again, M is the mass of the CFB and the guiding rods that are part of the WEC, F_damp is the velocity-dependent damping force accounting for mechanical friction effects and damping due to the harvested energy, and $\lambda_{\mathrm{vis},z}$ is the viscous damping in the z-direction resulting from the fluid. In deriving Eq. (4.31), it has been used that the force $F_1^{(0)}$ becomes zero for the considered CFB, since the CFB is rotational symmetric about the z-axis. On the other side, $F_3^{(0)}$ represents the buoyancy force. For the CFB, which has been introduced in Sect. 3.1 and which moves in direction α with displacement ξ, it holds

$$F_3^{(0)} = \rho g \pi R^2 d - \sin(\alpha)\rho g \pi R^2 \xi. \tag{4.32}$$

Inserting Eq. (3.13) in Eq. (4.32) yields

$$F_3^{(0)} - Mg = -\sin(\alpha)\rho g \pi R^2 \xi. \tag{4.33}$$

In the next step, a similar perturbation expansion for the displacement ξ is assumed as has been presented in Eq. (4.13a) for the velocity potential ϕ, i. e.

$$\xi = \varepsilon\,\xi^{(1)} + \varepsilon^2 \xi^{(2)} + \varepsilon^3 \xi^{(3)} + \mathcal{O}(\varepsilon^4). \tag{4.34}$$

Finally, the Eqs. (4.33) and (4.34) are substituted into Eq. (4.31). Furthermore, a damping force F_damp of the form given in Eq. (3.20) is used, which considers mechanical friction effects and the effects of energy harvesting. Here, the corresponding mechanical damping force F_mech is modeled to be linearly dependent on the velocity $\dot{\xi}$ of the CFB, i. e. $F_\mathrm{mech} = d_\mathrm{lin}\dot{\xi}$, see Eq. (3.21). Rearranging the

resulting Eq. (4.31) by the different orders of ε, the corresponding equations for $\xi^{(1)}$, $\xi^{(2)}$, and $\xi^{(3)}$ are given by

$$M\ddot{\xi}^{(1)} + \left(d_{\text{lin}} + d_{\text{elec}} + s_\alpha^2 \lambda_{\text{vis},z}\right)\dot{\xi}^{(1)} + s_\alpha^2 \rho g \pi R^2 \xi^{(1)} = c_\alpha F_1^{(1)} + s_\alpha F_3^{(1)}, \quad (4.35a)$$

$$M\ddot{\xi}^{(2)} + \left(d_{\text{lin}} + d_{\text{elec}} + s_\alpha^2 \lambda_{\text{vis},z}\right)\dot{\xi}^{(2)} + s_\alpha^2 \rho g \pi R^2 \xi^{(2)} = c_\alpha F_1^{(2)} + s_\alpha F_3^{(2)}, \quad (4.35b)$$

$$M\ddot{\xi}^{(3)} + \left(d_{\text{lin}} + d_{\text{elec}} + s_\alpha^2 \lambda_{\text{vis},z}\right)\dot{\xi}^{(3)} + s_\alpha^2 \rho g \pi R^2 \xi^{(3)} = c_\alpha F_1^{(3)} + s_\alpha F_3^{(3)}. \quad (4.35c)$$

Here, the abbreviation $s_\alpha = \sin(\alpha)$, $c_\alpha = \cos(\alpha)$ are used once again.
After solving numerically the ordinary differential equation (4.35), the total displacement ξ of the CFB can be computed using Eq. (4.34). After computing $\xi^{(i)}$ and ξ using the Eqs. (4.35) and (4.34), the velocity vector $\boldsymbol{u}$ of the CFB and its components $\boldsymbol{u}^{(i)}$ are given by

$$\boldsymbol{u} = \dot{\xi}\begin{bmatrix}\cos(\alpha)\\0\\\sin(\alpha)\end{bmatrix}, \quad \boldsymbol{u}^{(i)} = \dot{\xi}^{(i)}\begin{bmatrix}\cos(\alpha)\\0\\\sin(\alpha)\end{bmatrix}, \quad i = 1, 2, 3, \ldots \quad (4.36)$$

The values of $\boldsymbol{u}$ and its components $\boldsymbol{u}^{(i)}$ are needed in the BC (4.23) at the surface S_{B0} to calculate the total velocity potential ϕ of the water waves, which are disturbed by the presence and motion of the CFB.

4.3 Analytical Solutions for Higher-order Stokes Waves

In the previous sections, the fundamental equations for modeling the FSI between nonlinear water waves and a moving mechanical body have been derived. The basic idea is that the total velocity potential ϕ of the waves disturbed by the presence of the body is decomposed into the velocity potential of the incoming undisturbed waves ϕ_0 and the potential ϕ_{B} corresponding to the body disturbance, see Eq. (4.21). In Fig. 4.2, all equations have been summarized, which must be satisfied by the Stokes components of ϕ_0 and ϕ_{B}. It can be seen that the values of $\phi_0^{(i)}$ have to be known to compute $\phi_{\text{B}}^{(i)}$.
The velocity potentials $\phi_{\text{B}}^{(i)}$ are dependent of the geometry and motion of the body and can in general only be computed numerically. However, the incident velocity potentials $\phi_0^{(i)}$ are independent of the geometry and motion of the body and can be calculated in advance. In the case of regular waves, analytical solutions for $\phi_0^{(i)}$ are known, which are presented and analyzed in Sect. 4.3.1 for $i = 1, 2$. Analytical formulations for the random water waves, which are

presented in Sect. 2.2.2 for the linear case, are generalized by corresponding nonlinear second-order components in Sect. 4.3.2.
In this thesis, based on the Stokes perturbation expansion introduced in Eq. (4.13), the undisturbed incoming water waves considered in this section are called the Stokes waves. For the case of a linear wave analysis, these waves are also called linear Stokes waves. Similarly, for the case of a nonlinear wave analysis, these waves are also called nonlinear or higher-order Stokes waves. The incoming Stokes waves are characterized by the incident velocity potentials $\phi_0^{(i)}$, for which analytical solutions are presented in this section. Having computed the incident velocity potentials $\phi_0^{(i)}$, the corresponding sea surface displacements $\eta^{(i)}$ can be computed using Eq. (4.19). By introducing the term Stokes waves, the incoming water waves considered in this section are distinguished from the waves that are considered in Chap. 5.
For the case of regular higher-order Stokes waves, formulas for the second-order component $\phi_0^{(2)}$ of the incident velocity potential are generally known, see e.g. [RahmanEtAl99, Eatock TaylorHung87, SharmaDean79, Molin79]. Analytical solutions for the third-order component $\phi_0^{(3)}$ are not as widely used as the results for the second-order component $\phi_0^{(2)}$. It can be shown that $\phi_0^{(3)}$ consists of two terms, whereby one term is computed in [MalenicaMolin95]. The other term in $\phi_0^{(3)}$ has not received much interest in literature. Still, this term would also be needed in this work to compute the FSI between the fluid and a mechanical structure up to a modeling error of order $\mathcal{O}(\varepsilon^4)$. However, in order to make the scope of this work not too extensive, the corresponding analytic expressions of $\phi_0^{(3)}$ are not derived. In the following chapters, the calculation of the FSI is performed only in the presence of the second-order nonlinear wave theory, which leads to a modeling error of order $\mathcal{O}(\varepsilon^3)$.

4.3.1 Regular Higher-order Stokes Waves

All results presented in this section are based on [MalenicaMolin95]. For the case of regular incoming water waves, the linear incident velocity potential $\phi_0^{(1)}$ behaves harmonically in time with frequency ω. For some function $\varphi = \varphi(x, y, z)$, the linear incident velocity potential $\phi_0^{(1)}$ can be written as

$$\phi_0^{(1)}(x, y, z, t) = \mathrm{Re}\{\varphi^{(1)}(x, y, z)\mathrm{e}^{-\mathrm{i}\omega t}\}. \tag{4.37}$$

Recall that the second-order velocity potential $\phi_0^{(2)}$ has to satisfy the BC (4.18b) at $z = 0$, i. e. $\phi_{0,tt}^{(2)} + g\phi_{0,z}^{(2)} = F(\phi_0^{(1)})$. Here, the function $F = F(\phi^{(1)})$ is defined in Eq. (4.16). Evaluating the function $F = F(\phi^{(1)})$ at $\phi^{(1)} = \phi_0^{(1)}$ given by Eq. (4.37), it can be found that $F(\phi_0^{(1)})$ is of the form

$$F(\phi_0^{(1)}) = \mathrm{Re}\{f^{(1)}(x, y, z)\mathrm{e}^{-2\mathrm{i}\omega t}\} + \mathrm{Re}\{f^{(2)}(x, y, z)\}. \tag{4.38}$$

Substituting the form of $F(\phi_0^{(1)})$ from Eq. (4.38) into the BC (4.18b), it can be deduced that $\phi_0^{(2)}$ is of the form

$$\phi_0^{(2)}(x,y,z,t) = \mathrm{Re}\{\varphi^{(2)}(x,y,z)\mathrm{e}^{-2\mathrm{i}\omega t}\} + \mathrm{Re}\{\widetilde{\varphi}^{(2)}(x,y,z)\} \tag{4.39}$$

This means that $\phi_0^{(2)}$ generally consists of a part oscillating with frequency 2ω and a time-independent part. Therefore, the time-independent functions $\varphi^{(1)}$, $\varphi^{(2)}$, and $\widetilde{\varphi}^{(2)}$ have to be computed to calculate the incident velocity potential $\phi_0 = \varepsilon\phi_0^{(1)} + \varepsilon^2\phi_0^{(2)} + \mathcal{O}(\varepsilon^3)$.
In order to simplify the notation in the following, the phase function

$$\vartheta = k(\cos(\chi)x + \sin(\chi)y) - \omega t + \beta \tag{4.40}$$

is introduced. Here, ω is the frequency, k is the wave number, χ is the angle between the wave direction and the x-axis, and β is the phase shift of the considered regular water waves. In water of depth h, the wave frequency ω and wave number k are related by the dispersion relation from Eq. (2.16). Considering a water wave of amplitude A and frequency ω, the first-order incident velocity potential $\phi_0^{(1)}$ is given by

$$\varepsilon\phi_0^{(1)} = \mathrm{Re}\left\{\frac{-\mathrm{i}gA}{\omega}\frac{\cosh(k(z+h))}{\cosh(kz)}\mathrm{e}^{\mathrm{i}\vartheta}\right\} = \frac{gA}{\omega}\frac{\cosh(k(z+h))}{\cosh(kh)}\sin(\vartheta). \tag{4.41}$$

This is exactly the result that has already been presented in Eq. (2.15).
Substituting $\phi_0^{(1)}$ into $F(\phi_0^{(1)})$, it can be found that the function $f^{(2)}$ from Eq. (4.38) becomes zero. Therefore, the time-independent part $\widetilde{\varphi}^{(2)}$ of $\phi_0^{(2)}$ also becomes zero. The second-order incident velocity potential $\phi_0^{(2)}$ can be found to be, see e.g. [MalenicaMolin95],

$$\varepsilon^2\phi_0^{(2)} = \mathrm{Re}\left\{\frac{-3\mathrm{i}\omega A^2}{8}\frac{\cosh(2k(z+h))}{\sinh^4(kh)}\mathrm{e}^{2\mathrm{i}\vartheta}\right\} = \frac{3\omega A^2}{8}\frac{\cosh(2k(z+h))}{\sinh^4(kh)}\sin(2\vartheta). \tag{4.42}$$

Before the velocity potential of random nonlinear Stokes waves is discussed, it has to be noted that there exist no unique solution for the incident velocity potentials $\phi_0^{(i)}$, $i = 1,2,3,\ldots$. For example, if $\phi_0^{(j)}$ is a solution of the Eqs. (4.14) and (4.18) for some $j = 1,2,3,\ldots$, then also $\phi_0^{(j)} + c_1^{(j)}t + c_2^{(j)}$ is a solution for given constants $c_1^{(j)}$, $c_2^{(j)}$, $j = 1,2,3,\ldots$. However, a change of the j-th velocity potential $\phi_0^{(j)}$ also affects the velocity potentials $\phi_0^{(i)}$ with $i > j$. If the constants $c_1^{(j)}$ and $c_2^{(j)}$ are introduced, corresponding values for these constants have to be chosen. This can be done by considering the physical effects that result from taking into account additional higher-order velocity potentials, see e.g. [Chen06, Whitham99]. However, to make the study not too extensive, the constants $c_1^{(j)}$, $c_2^{(j)}$, $j = 1,2,3,\ldots$, are all set to zero in this thesis.

4.3.2 Random Nonlinear Stokes Waves of Second Order

In the following, the incident velocity potential of a random water wave is discussed, which satisfies the equations of Stokes' theory of second order. For the linear case, the velocity potential $\phi_0^{(1)}$ corresponding to random water waves is discussed in Sect. 2.2.2. In the following, the computation of the corresponding second-order velocity potential $\phi_0^{(2)}$ is sketched. All results presented in this section are based on [SharmaDean79].
The first-order sea surface displacement $\varepsilon\eta^{(1)}$ of an irregular short-crested water wave can be written in the absence of any structure as

$$\varepsilon\eta^{(1)}(x,y,t) = \sum_{m=1}^{M} a_m \cos(\vartheta_m) \tag{4.43}$$

with

$$\vartheta_m = k_m(\cos(\chi_m)x + \sin(\chi_m)y) - \omega_m t + \beta(\omega_m, \chi_m). \tag{4.44}$$

Here, β is a random phase shift, which is uniformly distributed in $[0, 2\pi)$. If the amplitudes a_m are described by the sea spectrum $S(\omega)$ and the spread function $D(\chi)$, Eq. (4.43) represents a generalization of the irregular short-crested sea surface displacement presented in Eq. (2.27). The corresponding first-order incident velocity potential $\varepsilon\phi_0^{(1)}$ is given by

$$\varepsilon\phi_0^{(1)} = \sum_{m=1}^{M} b_m \frac{\cosh(k_m(h+z))}{\cosh(k_m h)} \sin(\vartheta_m) \quad \text{with } b_m = \frac{a_m g}{\omega_m},\ m = 1, \ldots, M. \tag{4.45}$$

For the computation of the second-order incident velocity potential $\phi_0^{(2)}$, the first-order incident velocity potential $\phi_0^{(1)}$ from Eq. (4.45) has to be substituted into Eq. (4.18b) to formulate the corresponding BC at $z = 0$. In this way, the BC (4.18b) becomes

$$\left[\phi_{0,tt}^{(2)} + g\phi_{0,z}^{(2)}\right]_{z=0} = \sum_{m=1}^{M}\sum_{n=1}^{M} b_m b_n \left[d_{mn}^{-} \sin(\vartheta_m - \vartheta_n) + d_{mn}^{+} \sin(\vartheta_m + \vartheta_n)\right]. \tag{4.46}$$

Here, d_{mn}^{-} and d_{mn}^{+} are constants whose values can be found in [SharmaDean79]. The incident velocity potential $\phi_0^{(2)}$ has to satisfy the Laplace equation for $z \leq 0$ together with the BC (4.46) at $z = 0$ and $\phi_{0,z}^{(2)} = 0$ at $z = -h$. Since all these equations are linear in $\phi_0^{(2)}$, the following ansatz for $\phi_0^{(2)}$ presented in [SharmaDean79] is used

$$\begin{aligned}\varepsilon^2\phi_0^{(2)} = \sum_{m=1}^{M}\sum_{n=1}^{M} & c_{mn}^{-} \frac{\cosh(|\boldsymbol{k}_m - \boldsymbol{k}_n|(h+z))}{\cosh(|\boldsymbol{k}_m - \boldsymbol{k}_n|h)} \sin(\vartheta_m - \vartheta_n) \\ & + c_{mn}^{+} \frac{\cosh(|\boldsymbol{k}_m + \boldsymbol{k}_n|(h+z))}{\cosh(|\boldsymbol{k}_m + \boldsymbol{k}_n|h)} \sin(\vartheta_m + \vartheta_n).\end{aligned} \tag{4.47}$$

Here, $\boldsymbol{k}_m = k_m[\cos(\chi_m), \sin(\chi_m)]^{\mathrm{T}}$ is the vector consisting of the wave-numbers in the x- and y- direction, respectively. Then $\phi_0^{(2)}$ from Eq. (4.47) satisfies the Laplace equation and the BC at $z = -h$. The constants c_{mn}^- and c_{mn}^+ have to be specified such that Eq. (4.46) at $z = 0$ is fulfilled. These constants are calculated as

$$c_{mn}^- = \begin{cases} b_m b_n \frac{2(\omega_m - \omega_n)(\boldsymbol{k}_m \cdot \boldsymbol{k}_n + R_m R_n) - [(\omega_m k_n^2 - \omega_n k_m^2) - (\omega_m R_n^2 - \omega_n R_m^2)]}{4[(\omega_m - \omega_n)^2 - g \tanh(|\boldsymbol{k}_m - \boldsymbol{k}_n|h)|\boldsymbol{k}_m - \boldsymbol{k}_n|]}, & \text{for } m \neq n, \\ 0, \text{ for } m = n, \end{cases}$$

(4.48a)

$$c_{mn}^+ = b_m b_n \frac{2(\omega_m + \omega_n)(\boldsymbol{k}_m \cdot \boldsymbol{k}_n - R_m R_n) + [(\omega_m k_n^2 + \omega_n k_m^2) - (\omega_m R_n^2 + \omega_n R_m^2)]}{4[(\omega_m + \omega_n)^2 - g \tanh(|\boldsymbol{k}_m + \boldsymbol{k}_n|h)|\boldsymbol{k}_m + \boldsymbol{k}_n|]}$$

$$\forall m, n \in 1, 2, \ldots, M,$$

(4.48b)

whereby $R_m = k_m \tanh(k_m h)$, $i = 1, 2, \ldots, M$. For $M = 1$, Eqs. (4.47) and (4.48) results in the second-order incident velocity potential $\phi_0^{(2)}$ from Eq. (4.42) for regular waves.

Considering Eq. (4.47), it can be seen that interactions between the components of the first-order incident velocity potential $\phi_0^{(1)}$ have to be considered to compute the corresponding second-order incident velocity potential $\phi_0^{(2)}$. The number of interactions is given by M^2, i. e. by the square of the number of wave components used to calculate $\phi_0^{(1)}$. It follows that the calculation of all nonlinear interactions becomes inefficient for an increasing number of regular components in the irregular first-order sea. As a result, a second-order Stokes theory in the presence of the random nonlinear Stokes waves considered in this section requires a large computational effort. This is a big drawback when, for example, the system parameters of the WEC are optimized so that a large amount of energy is harvested. In this optimization process, the motion of the WEC has to be computed in a large number of different irregular sea states with a long simulation time. If the incident velocity potential ϕ_0 and its components cannot be calculated efficiently, the same holds for the computation of the total velocity potential ϕ disturbed by the presence of the WEC. Therefore, the FSI between the WEC and the water waves also cannot be computed efficiently. The optimization process can then only be performed using a substantial amount of simulation time. Consequently, a scheme has to be found to calculate the incident velocity potential ϕ_0 of random nonlinear waves more efficiently. In the next chapter, it is investigated how the FSI with nonlinear water waves can be computed more efficiently.

4.4 Summary of the Developed Method

In this chapter, it has been shown how the nonlinear FSI between a structure and nonlinear water waves can be calculated. The corresponding equations to compute the velocity potentials $\phi_0^{(i)}$ and $\phi_\mathrm{B}^{(i)}$, the sea surface displacements $\eta^{(i)}$, the hydrodynamic forces $\boldsymbol{F}^{(i)}$, and the displacements $\xi^{(i)}$ of the CFB have been presented. While analytical solutions for the incident velocity potentials $\phi_0^{(i)}$ have been presented for nonlinear regular and random water waves, all other quantities can in general only be computed numerically. In order to solve all appearing differential equations numerically, the time domain has to be discretized and the numerical solution has to be computed at several timepoints t_n. To obtain an overview of the corresponding procedure, Fig. 4.4 shows the computational steps that have to be performed to move from the current timepoint t_n to the next timepoint t_{n+1}.
It is assumed that at the actual timepoint t_n, the position of the CFB and the velocity components $\boldsymbol{u}^{(i)}$ are known. This information is needed to compute the total velocity potential ϕ and its components $\phi^{(i)}$ at the next time point t_{n+1} using the scheme depicted in Fig. 4.2.
After computing the different velocity potentials, the sea surface displacement η and its components $\eta^{(i)}$ can be calculated using Eq. (4.13b) and Eq. (4.19), respectively. The values of $\eta^{(i)}$ and $\phi^{(i)}$ are needed to calculate the hydrodynamic force $\boldsymbol{F}$ and its components $\boldsymbol{F}^{(i)}$, which act on the CFB. The forces can be computed using Eq. (4.28) and Eq. (4.29), respectively. Finally, the total displacement ξ of the CFB and the components of the velocity $\boldsymbol{u}^{(i)}$ of the CFB at time point t_{n+1} can be calculated using Eqs. (4.34), (4.35), and (4.36), respectively. This completes the procedure that has to be applied to move from the current time point t_n to the next timepoint t_{n+1}.
It has to be noted that the scheme presented in Fig. 4.4 can be applied to compute the nonlinear FSI up to a modeling error of order $\mathcal{O}(\varepsilon^{i+1})$ by calculating the first i velocity potentials $\phi^{(j)}$, $j = 1, 2, \ldots, i$. Here, the incident velocity potentials $\phi_0^{(j)}$, $j = 1, 2, \ldots, i$, have to be known, before the velocity potentials $\phi_\mathrm{B}^{(j)}$, $j = 1, 2, \ldots, i$, corresponding to the body disturbance can be calculated. So far, however, only analytical solutions for the first two incident velocity potentials $\phi_0^{(1)}$ and $\phi_0^{(2)}$ have been presented for Stokes waves. For $\phi_0^{(3)}$, different and often inconsistent expressions can be observed [TsuchiyaYasuda81]. In order to make the scope of this thesis not too extensive, the different analytical expressions for $\phi_0^{(3)}$ are not analyzed here.
Considering the first two incident velocity potentials $\phi_0^{(1)}$ and $\phi_0^{(2)}$ using the analytical expressions discussed in Sect. 4.3, the nonlinear FSI can be computed up to a modeling error of order $\mathcal{O}(\varepsilon^3)$. However, the methodology presented in this work remains the same for higher orders of accuracy if the incident velocity potentials $\phi_0^{(j)}$ are computed numerically. This can be done by solving the PDEs

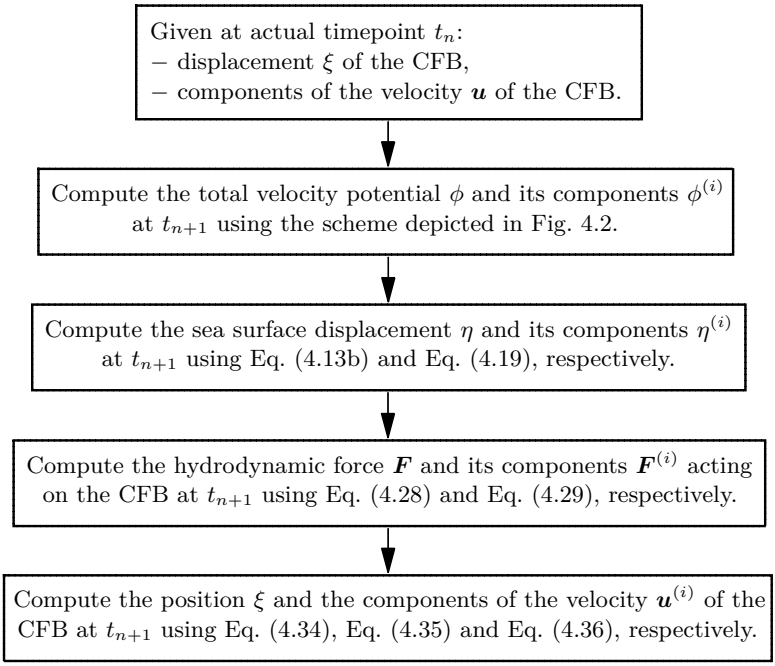

Figure 4.4: Schematic representation of the whole procedure for the computation of the nonlinear FSI between nonlinear water waves and the WEC presented in Sect. 3.1.

numerically, which are summarized Fig. 4.2. However, in order to make the scope of this thesis not too extensive, the incident velocity potential of Stokes waves of j-th order with $j \geq 3$ are not computed numerically. Instead, since the computation of random nonlinear Stokes waves requires a large computational effort, it is investigated in the next chapter how the FSI with nonlinear water waves can be computed more efficiently.

Nonlinear Schrödinger Equation

Calculating nonlinear water waves by solving the Navier-Stokes equations or the nonlinear governing equations of fluid motion form Eq. (2.2) requires a large computational effort. Even if the computational intensity is reduced by simplifying the nonlinear governing equations of fluid motion from Eq. (2.2) using Stokes perturbation expansions from Eq. (4.13), the computation of incoming second-order random Stokes waves still requires a large computational effort, see Sect. 4.3.2. This directly affects the calculation time of the nonlinear FSI between a body and random nonlinear Stokes waves.

In order to calculate nonlinear water waves more efficiently, the nonlinear Schrödinger equation (NLS) can be solved instead. The NLS consists of a PDE that can be used to describe weakly nonlinear deep water waves with a narrow spectral bandwidth and a moderate wave steepness of $H/\lambda \leq 0.05$ [Dysthe79, Witt19, Osborne10]. The solution of the NLS is the envelope ψ of the water waves.

It has been shown by [Zakharov68] that weakly nonlinear solutions of the governing equations of fluid motion from Eq. (2.2) can be reduced to solutions described by complex envelopes, which satisfy the NLS. The NLS offers an universal model that rules the dynamics of weakly nonlinear gravity waves, whose spectrum is narrowbanded [OnoratoEtAl13]. Furthermore, it has been found that the NLS can describe many of the features of the dynamics of rogue waves, which are found to arise as a result of nonlinear self-focusing phenomena [OnoratoEtAl01]. Moreover, it has been conjectured in different studies that specific solutions of the NLS are prototypes of rogue waves in the ocean, see e.g. [DystheTrulsen99, ShriraGeogjaev10, DostalEtAl20].

As is shown in this chapter, the nonlinear interactions between regular components of an irregular sea state are automatically taken into account by solving the NLS. Therefore, nonlinear wave-wave interactions do not require extensive computation, as in the case of the Stokes waves presented in Sect. 4.3.2. Since the NLS can be solved numerically efficiently, it is well suited for approximating the associated solutions of the nonlinear governing equations of fluid motion from Eq. (2.2).

A disadvantage of the NLS is that it accurately models only weakly nonlinear deep water waves with a narrow spectral bandwidth and with moderate wave steepness of $H/\lambda \leq 0.05$ [Dysthe79, Witt19, Osborne10]. Recall that individual regular deep water waves do not break up to a wave steepness of $H/\lambda = 0.142$,

see Eq. (4.11). However, real ocean waves are on average weakly nonlinear with a moderately narrow bandwidth and have an average wave steepness of $H/\lambda \approx 0.03 - 0.04$ [OnoratoEtAl13, TrulsenEtAl00]. Here, it should be noted that real water waves measured in [BSH] from buoys located in the North and Baltic Sea have such a wave steepness on average, see Tab. 1.1 and Fig. 1.1. This justifies the weakly nonlinear approach to model ocean waves with a narrow spectral bandwidth using the NLS.
Starting from the wave envelope ψ, [CarterEtAl20] derived a general representation for the associated incident velocity potential ϕ_0. As has been presented in Chap. 4, the incident velocity potential ϕ_0 provides the basis for calculating the hydrodynamic forces and the associated motion of floating structures in nonlinear water waves. Since the theory of [CarterEtAl20] is very new, it has not yet been used to calculate the acting FSI between floating structures and nonlinear water waves. For the efficiency reasons described above, the NLS is used in this work to calculate the nonlinear FSI. The application areas, accuracy, and stability of the method using the NLS are investigated in this chapter. In later chapters, a comparison with Stokes waves presented in Sect. 4.3 shows the advantages of this method in terms of computational efficiency.
In Sect. 5.1, the NLS is introduced. Afterward, it is presented in Sect. 5.2 how the NLS can be used to compute the FSI between a structure and nonlinear water waves. After that, the NLS is investigated in more detail. Analytical solutions of the NLS are given in Sect. 5.3. Furthermore, numerical schemes are presented in Sect. 5.4 and Sect. 5.5, which are used to compute numerical solutions of the NLS and the corresponding incident velocity potentials $\phi_0^{(i)}$. Based on numerical results, Sect. 5.6 briefly shows to what extent solutions of NLS are stable against small sideband perturbations. This knowledge is needed in Sect. 5.7, where nonlinear random water waves are generated based on solutions of NLS. Finally, the effects of regular and random water waves on the trajectories of water particles are investigated in Sect. 5.8. This chapter has partly been published in [HollmEtAl21, HollmEtAl22b, HollmEtAl24].

5.1 Formulation of the NLS

In this section, the most important equations regarding the NLS are introduced. All formulas presented in this section result from the derivations given in Sect. 5.2.1.
Besides water waves, the NLS can be used to describe the propagation of waves in many different physical systems, such as fiber optics [DudleyEtAl14], Bose-Einstein condensates [BludovEtAl09], and plasma waves [El-TantawyEtAl22].

However, in this thesis, the NLS is only used to describe the behavior of water waves and to compute the FSI with a mechanical structure. For water waves, the derivation of the NLS is sketched in Sect. 5.2.1.
It has been shown that weakly nonlinear solutions of the governing equations of fluid motion from Eq. (2.2) can be reduced to solutions described by complex envelopes [Zakharov68]. In the case of long-crested waves in deep water, whose spectrum is narrowbanded, these complex envelopes satisfy the NLS. Such reduction can be achieved by the method of multiple scales, see e.g. [Mei83, Dysthe79, CarterEtAl20]. Here, similar to the Stokes perturbation expansions from Eq. (4.13), the velocity potential ϕ and sea surface displacement η are expanded with respect to the small parameter ε, which represents the wave steepness.
In terms of the coordinates

$$X := \varepsilon x, \quad T := \varepsilon t, \tag{5.1}$$

the NLS is given by

$$\mathrm{i}(\psi_T + c_{\mathrm{gr}}\psi_X) = \nu\psi_{XX} + \delta|\psi|^2\psi. \tag{5.2}$$

Here, the constants ν and δ are defined as

$$\nu := \varepsilon\frac{\omega_0}{8k_0^2}, \quad \delta := \varepsilon\frac{1}{2}\omega_0 k_0^2. \tag{5.3}$$

Additionally, $\psi = \psi(X,T) \in \mathbb{C}$ describes the wave envelope of the oscillations of a carrier wave with wave number k_0 and wave frequency ω_0. Here, ω_0 and k_0 are linked by the linear dispersion relation in deep water from Eq. (2.21), i. e. $\omega_0^2 = gk_0$. Furthermore, c_{gr} is the group velocity of the carrier wave, which is defined by

$$c_{\mathrm{gr}} := \frac{\omega_0}{2k_0}. \tag{5.4}$$

The NLS yields the complex wave envelope ψ, from which the sea surface displacement $\eta(x,t)$ of the corresponding water waves can be computed by

$$\begin{aligned}\eta(x,t) = \mathrm{Re}\Bigg\{\varepsilon\psi E + \frac{1}{2}\varepsilon^2 k_0\psi^2E^2 + \varepsilon^3\Bigg[\frac{3}{8}k_0^2\psi^3E^3 - \frac{1}{2}\mathrm{i}\psi\psi_X E^2 \\ + \frac{\omega_0}{2g}\frac{\partial}{\partial T}\Big(\mathcal{H}\left(|\psi|^2\right)\Big)\Bigg]\Bigg\} + \mathcal{O}(\varepsilon^4).\end{aligned} \tag{5.5}$$

Here, it is $E = \mathrm{e}^{\mathrm{i}(k_0x-\omega_0t)}$ and $\mathcal{H}$ denotes the Hilbert transform. Using the Fourier transform $\mathcal{F}$ and its inverse $\mathcal{F}^{-1}$, which are defined by

$$\begin{aligned}\widehat{f}(k) = \mathcal{F}\left(f(X)\right) &:= \int_{\mathbb{R}} f(X)\mathrm{e}^{-\mathrm{i}kX}\mathrm{d}X, \\ f(X) = \mathcal{F}^{-1}\left(\widehat{f}(k)\right) &:= \frac{1}{2\pi}\int_{\mathbb{R}} \widehat{f}(k)\mathrm{e}^{\mathrm{i}kX}\mathrm{d}k,\end{aligned} \tag{5.6}$$

the Hilbert transform of a function $f = f(X)$ can be computed by

$$\mathcal{H}\left(f(X)\right) = \mathcal{F}^{-1}\left(-\mathrm{i}\ \mathrm{sgn}(k)\mathcal{F}\left(f\right)\right). \tag{5.7}$$

Here, $\mathrm{sgn}(k)$ is the signum function returning the sign of the real-valued wave number k.
Figure 5.1 shows an example of the wave envelope ψ and the associated sea surface displacement η, whereby only the leading order term in ε is used to calculate η. From Eq. (5.5) and Fig. 5.1, it can be seen that η changes with $k_0 x$ in space and $\omega_0 t$ in time. In comparison, the wave envelope $\psi = \psi(X, T)$ changes only slowly in time and space. Since the wave envelope ψ depends on X and T, which are given by Eq. (5.1), the variables X and T are called the slow variables in the following.
Having computed the wave envelope ψ, the velocity potential ϕ of the corresponding water waves is given by

$$\begin{aligned}\phi(x,z,t) = \mathrm{Re}\Bigg\{\Bigg[-\frac{\mathrm{i}\varepsilon\omega_0}{k_0}\widetilde{\psi} + \frac{\varepsilon^2\omega_0}{2k_0^2}\widetilde{\psi}_X + \varepsilon^3\left(\frac{\mathrm{i}k_0\omega_0}{8}\widetilde{C} + \frac{3\mathrm{i}\omega_0}{8k_0^3}\widetilde{\psi}_{XX}\right)\Bigg]E\mathrm{e}^{k_0 z} \\ + 2\varepsilon^2\bar{\phi}_0 + 2\varepsilon^3\bar{\phi}_1\Bigg\} + \mathcal{O}(\varepsilon^4).\end{aligned} \tag{5.8}$$

Here, it is $\widetilde{\psi}(X, Z, T) := \psi(X - \mathrm{i}Z, T)$, $C := |\psi|^2\psi$, $\widetilde{C}(X, Z, T) := C(X - \mathrm{i}Z, T)$, and

$$Z := \varepsilon z \tag{5.9}$$

is the slow vertical variable. Furthermore, $\bar{\phi}_0 = \bar{\phi}_0(X, Z, T)$ and $\bar{\phi}_1 = \bar{\phi}_1(X, Z, T)$ are velocity potentials representing a mean flow of the water waves. The velocity potential $\bar{\phi}_0$ is given by

$$\mathrm{Re}\left\{2\bar{\phi}_0\right\} = \bar{\phi}_0 + \bar{\phi}_0^* = \mathcal{F}^{-1}\left(\frac{1}{2}\mathrm{i}\omega_0\,\mathrm{sgn}(k)\mathcal{F}\left(|\psi|^2\right)\mathrm{e}^{|k|Z}\right), \tag{5.10}$$

whereby $\bar{\phi}_0^*$ denotes the complex conjugate of $\bar{\phi}_0$. As is shown later in Sect. 5.2.2, the velocity potential $\bar{\phi}_1$ is not needed for the computational method for the FSI formulated in this thesis and is therefore not further specified here.
For the computation of $\widetilde{\psi}$ and $\widetilde{C}$, it has to be noted that ψ and C are unknown at the location $X - \mathrm{i}Z$ if no analytic expression for ψ is given. However, $\widetilde{\psi}$ can be determined by solving the complex transport equation

$$\widetilde{\psi}_Z = -\mathrm{i}\widetilde{\psi}_X, \quad \text{for } Z < 0, \tag{5.11a}$$

$$\widetilde{\psi} = \psi, \qquad \text{for } Z = 0. \tag{5.11b}$$

An analog complex transport equation has to be solved to compute $\widetilde{C}$.

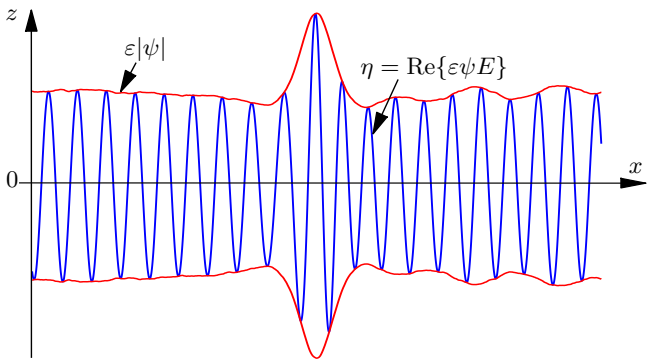

Figure 5.1: Example of the wave envelope ψ together with the associated sea surface displacement η.

It should be noted that [CarterEtAl20] has presented formulas for the sea surface displacement η and velocity potential ϕ for waves corresponding to solutions of the NLS. However, [CarterEtAl20] considered the complex conjugate of the NLS (5.2). In order to calculate the potential of the NLS (5.2) itself, the approach of [CarterEtAl20] has to be adapted using the complex conjugate of the Eqs. (24a-27h) from [CarterEtAl20]. The resulting velocity potential is given by Eq. (5.8). This formula is the corrected version of the result of [CarterEtAl20], who have not considered the last two terms in Eq. (5.8) representing the mean flow velocity potentials. Equation (5.8) has also been published in [HollmEtAl24]. The corresponding derivations of Eqs. (5.2), (5.5), and (5.8) are given in Sect. 5.2.1.

5.2 Computation of the FSI using the NLS

In this section, it is presented how the NLS can be used to compute the FSI between a structure and nonlinear water waves. For this, it must first be understood on which theory the NLS is based. In order to understand how the theory of the NLS is related to the nonlinear wave theory presented in Sect. 4.1.1, the derivation of the NLS is shortly outlined first. The derivation is based on [Mei83, Dysthe79, CarterEtAl20]. In the following, only deep water waves are considered, which propagate in the x-direction.

5.2.1 Derivation of the NLS

The governing equations of fluid motion are given by Eq. (2.2). At the beginning of Sect. 4.1.1, it is shown that the two BCs (2.2b) and (2.2c) at the free sea surface at $z = \eta$ can be combined to Eq. (4.2). Considering deep water waves and using the combined BC (4.2) together with the Eqs. (2.2a), (2.2c), and (2.2d), the governing equations of fluid motion from Eq. (2.2) result in

$$\boldsymbol{\nabla}^2\phi = \phi_{xx} + \phi_{zz} = 0, \quad \text{for} \quad z \leq \eta(x,t), \tag{5.12a}$$

$$\phi_{tt} + g\phi_z + 2\boldsymbol{\nabla}\phi\cdot\boldsymbol{\nabla}\phi_t + \frac{1}{2}\boldsymbol{\nabla}\phi\cdot\boldsymbol{\nabla}\left(\boldsymbol{\nabla}\phi\cdot\boldsymbol{\nabla}\phi\right) = 0, \quad \text{for} \quad z = \eta(x,t), \tag{5.12b}$$

$$\phi_t + \frac{1}{2}\boldsymbol{\nabla}\phi\cdot\boldsymbol{\nabla}\phi + g\eta = 0, \quad \text{for} \quad z = \eta(x,t), \tag{5.12c}$$

$$\phi_z \to 0, \quad \text{for} \quad z \to -\infty. \tag{5.12d}$$

In the next step, the BCs (5.12b) and (5.12c) are expanded from the free sea surface at $z = \eta(x,t)$ to $z = 0$ using Taylor series expansions, see e.g. [Mei83]. Here, it is assumed that $\phi_z = \mathcal{O}(k\phi)$ for a characteristic wave number k. Then, for the wave amplitude A and the sea surface displacement $\eta = \mathcal{O}(A)$, the successive terms in the Taylor series expansions become progressively smaller with increasing powers of kA. Considering only the terms up to third-order $\mathcal{O}\left((kA)^3\right)$, the expanded equations at $z = 0$ are given by

$$\begin{aligned}\phi_{tt} + g\phi_z + \eta\frac{\partial}{\partial z}\left[\phi_{tt} + g\phi_z\right] + 2\boldsymbol{\nabla}\phi\cdot\boldsymbol{\nabla}\phi_t + \frac{1}{2}\eta^2\frac{\partial^2}{\partial z^2}\left[\phi_{tt} + g\phi_z\right] \\ +\eta\frac{\partial}{\partial z}\left[2\boldsymbol{\nabla}\phi\cdot\boldsymbol{\nabla}\phi_t\right] + \frac{1}{2}\boldsymbol{\nabla}\phi\cdot\boldsymbol{\nabla}\left(\boldsymbol{\nabla}\phi\cdot\boldsymbol{\nabla}\phi\right) = 0, \text{ for } z = 0,\end{aligned} \tag{5.13a}$$

$$-g\eta = \phi_t + \eta\phi_{tz} + \frac{1}{2}\boldsymbol{\nabla}\phi\cdot\boldsymbol{\nabla}\phi + \frac{1}{2}\eta^2\phi_{tzz} + \eta\frac{\partial}{\partial z}\left[\frac{1}{2}\boldsymbol{\nabla}\phi\cdot\boldsymbol{\nabla}\phi\right], \text{ for } z = 0. \tag{5.13b}$$

These equations has also been presented, for example, by [Mei83]. Following [CarterEtAl20, Dysthe79], a generalized Stokes perturbation expansion is used of the form

$$\phi(x,z,t) = \varepsilon^2\bar{\phi} + \varepsilon A_1 \mathrm{e}^{k_0 z + \mathrm{i}\vartheta} + \varepsilon^2 A_2 \mathrm{e}^{2(k_0 z + \mathrm{i}\vartheta)} + \cdots + \text{c.c.}, \tag{5.14a}$$

$$\eta(x,t) = \varepsilon^3\bar{\eta} + \varepsilon B\mathrm{e}^{\mathrm{i}\vartheta} + \varepsilon^2 B_2\mathrm{e}^{2\mathrm{i}\vartheta} + \varepsilon^3 B_3\mathrm{e}^{3\mathrm{i}\vartheta} + \cdots + \text{c.c.} \tag{5.14b}$$

Here, it is $\vartheta = k_0 x - \omega_0 t$, c.c. represents the complex conjugate, and $\bar{\phi}$ and $\bar{\eta}$ are functions slowly varying in space and time, which represent the mean flow and mean surface elevation. Furthermore, the complex functions A_1, A_2, …, B, B_2, B_3, … are slowly varying in time and space. As will be defined later, the complex envelope ψ appearing in the NLS (5.2) is given by $\psi = 2B$.
It has to be noted that the BC (5.12d) is directly fulfilled for ϕ given by Eq. (5.14a), if $\bar{\phi}_z \to 0$ and A_i, $A_{i,z}$ are bounded for $z \to -\infty$, $i = 1, 2, 3, \ldots$

Finally, as it is described in [CarterEtAl20], it is assumed

$$\bar{\phi} = \bar{\phi}(X,Z,T) = \bar{\phi}_0(X,Z,T) + \varepsilon\bar{\phi}_1(X,Z,T) + \varepsilon^2\bar{\phi}_2(X,Z,T) + \dots, \tag{5.15a}$$

$$\begin{aligned} A_j &= A_j(X,Z,T) = A_{j0}(X,Z,T) + \varepsilon A_{j1}(X,Z,T) \\ &\quad + \varepsilon^2 A_{j2}(X,Z,T) + \dots, \quad \text{for } j = 1,2,3,\dots, \end{aligned} \tag{5.15b}$$

$$\bar{\eta} = \bar{\eta}(X,T) = \bar{\eta}_0(X,T) + \varepsilon\bar{\eta}_1(X,T) + \varepsilon^2\bar{\eta}_2(X,T) + \dots, \tag{5.15c}$$

$$B = B(X,T), \tag{5.15d}$$

$$\begin{aligned} B_j &= B_j(X,Z,T) = B_{j0}(X,Z,T) + \varepsilon B_{j1}(X,Z,T) \\ &\quad + \varepsilon^2 B_{j2}(X,Z,T) + \dots, \quad \text{for } j = 2,3,4,\dots \end{aligned} \tag{5.15e}$$

Next, the expressions from Eqs. (5.14) and (5.15) are substituted into the Laplace equation (5.12a) and the BCs (5.13a) and (5.13b) at $z = 0$. Doing this, expressions appear, which consist of terms depending on different orders of ε and $\mathrm{e}^{k_0 z \pm \mathrm{i}\vartheta}$, respectively. In the following, all terms depending on different orders of ε and $\mathrm{e}^{k_0 z \pm \mathrm{i}\vartheta}$ are considered separately. Inserting the Eqs. (5.14) and (5.15) in Eq. (5.12a) and sorting the terms according to the different orders in ε, the resulting terms of order $\mathcal{O}(\varepsilon^2)$ have to satisfy for $Z < 0$

$$\varepsilon^2 \left\{ 2k_0 \left[A_{10,Z} + \mathrm{i}A_{10,X} \right] \mathrm{e}^{k_0 z + \mathrm{i}\vartheta} + 2k_0 \left[A^*_{10,Z} - \mathrm{i}A^*_{10,X} \right] \mathrm{e}^{k_0 z - \mathrm{i}\vartheta} \right\} = 0. \tag{5.16}$$

Here, A^*_{10} denotes the complex conjugate of A_{10}, which results from the c.c. part in Eq. (5.14). Inserting the Eqs. (5.14) and (5.15) in the BCs (5.13a) and (5.13b) and sorting the terms according to the different orders in ε, the resulting terms of order $\mathcal{O}(\varepsilon)$ have to satisfy

$$\varepsilon \left\{ \left[-\omega_0^2 + gk_0 \right] A_{10} \mathrm{e}^{\mathrm{i}\vartheta} + \left[-\omega_0^2 + gk_0 \right] A^*_{10} \mathrm{e}^{-\mathrm{i}\vartheta} \right\} = 0, \text{ for } Z = 0 \tag{5.17a}$$

$$\varepsilon \left\{ \left[gB - \mathrm{i}\omega_0 A_{10,X} \right] \mathrm{e}^{\mathrm{i}\vartheta} + \left[gB^* + \mathrm{i}\omega_0 A^*_{10,X} \right] \mathrm{e}^{-\mathrm{i}\vartheta} \right\} = 0, \text{ for } Z = 0. \tag{5.17b}$$

Equation (5.17a) directly reveal the dispersion relation $\omega_0^2 = gk_0$. Equations (5.16) and (5.17b) result in

$$A_{10} = -\frac{\mathrm{i}\omega_0}{k_0}\widetilde{B}, \quad A^*_{10} = \frac{\mathrm{i}\omega_0}{k_0}\widetilde{B}^*, \quad \text{with } \widetilde{B}(X,Z,T) = B(X - iZ, T). \tag{5.18}$$

In the same manner, the functions A_{jk}, B_{jk}, $\bar{\phi}_j$, and $\bar{\eta}_j$, which appear in Eq. (5.14) and Eq. (5.15) in combination with a higher order in ε, can be computed. The resulting PDEs and BCs at $Z = 0$ for the unknowns A_{ij} and $\bar{\phi}_i$, which appear in

Eq. (5.15) up to the order $\mathcal{O}(\varepsilon^3)$, are given by

$$\begin{cases} A_{20,Z} + \mathrm{i}A_{20,X} = 0, & \text{for } Z < 0, \\ A_{20} = 0, & \text{for } Z = 0, \end{cases} \tag{5.19a}$$

$$\begin{cases} A_{11,Z} + \mathrm{i}A_{11,X} = -\frac{1}{2k_0}\left(A_{10,XX} + A_{10,ZZ}\right), & \text{for } Z < 0, \\ A_{11} = \frac{\omega_0}{2k_0^2} B_X, & \text{for } Z = 0, \end{cases} \tag{5.19b}$$

$$\begin{cases} A_{30,Z} + \mathrm{i}A_{30,X} = 0, & \text{for } Z < 0, \\ A_{30} = 0, & \text{for } Z = 0, \end{cases} \tag{5.19c}$$

$$\begin{cases} A_{21,Z} + \mathrm{i}A_{21,X} = -\frac{1}{4k_0}\left(A_{20,XX} + A_{20,ZZ}\right), & \text{for } Z < 0, \\ A_{21} = 0, & \text{for } Z = 0, \end{cases} \tag{5.19d}$$

$$\begin{cases} A_{12,Z} + \mathrm{i}A_{12,X} = -\frac{1}{2k_0}\left(A_{11,XX} + A_{11,ZZ}\right), & \text{for } Z < 0, \\ A_{12} = \frac{1}{2}\mathrm{i}k_0\omega_0|B|^2 B + \frac{3\mathrm{i}\omega_0}{8k_0^3} B_{XX}, & \text{for } Z = 0, \end{cases} \tag{5.19e}$$

$$\begin{cases} \bar{\phi}_{0,XX} + \bar{\phi}_{0,ZZ} + \bar{\phi}^*_{0,XX} + \bar{\phi}^*_{0,ZZ} = 0, & \text{for } Z < 0, \\ \bar{\phi}_{0,Z} + \bar{\phi}^*_{0,Z} = 2\omega_0 \left(|B|^2\right)_X, & \text{for } Z = 0. \end{cases} \tag{5.19f}$$

It has to be noted that along with the functions appearing in Eq. (5.19), the mean velocity potential $\bar{\phi}_1$ also appears in Eq. (5.15) with order $\mathcal{O}(\varepsilon^3)$. However, as is shown in Sect. 5.2.2, the mean velocity potential $\bar{\phi}_1$ is not needed to formulate the FSI method used in this thesis. Furthermore, it can be observed that the complex conjugate functions A^*_{ij} also appear in Eq. (5.15), which are solutions of the complex conjugate equations to Eqs. (5.19a)-(5.19e).
Solving Eq. (5.19), the functions A_{ij}, which appear in Eq. (5.14a) up to the order $\mathcal{O}(\varepsilon^3)$, are given in terms of B by

$$\begin{gathered} A_{10} = -\frac{\mathrm{i}\omega_0}{k_0}\widetilde{B}, \quad A_{11} = \frac{\omega_0}{2k_0}\widetilde{B}_X, \quad A_{12} = \frac{1}{16}\mathrm{i}k_0\omega_0\widetilde{C} + \frac{3\mathrm{i}\omega_0}{8k_0^3}\widetilde{B}_{XX}, \\ A_{20} = 0, \quad A_{21} = 0, \quad A_{30} = 0, \end{gathered} \tag{5.20}$$

with

$$C(X,T) = 8|B(X,T)|^2 B(X,T), \quad \widetilde{C}(X,Z,T) = C(X - \mathrm{i}Z, T). \tag{5.21}$$

Furthermore, the functions B_{ij} and $\bar{\eta}_0 + \bar{\eta}^*_0$, which appear in Eq. (5.14b) up to the order $\mathcal{O}(\varepsilon^3)$, are given in terms of B and $\bar{\phi}_0$ by

$$\begin{aligned} &B_{20} = k_0 B^2, \quad B_{30} = \frac{3}{2}k_0^2 B^3, \quad B_{21} = -\mathrm{i}k_0 B B_X, \\ &\bar{\eta}_0 + \bar{\eta}^*_0 = -\frac{1}{g}\left(\bar{\phi}_0 + \bar{\phi}^*_0\right)_T, \quad \text{for } Z = 0. \end{aligned} \tag{5.22}$$

At this point, the mean velocity potential $\bar{\phi}_0$ and the mean surface displacement $\bar{\eta}_0$ still need to be determined in terms of B. For the computation of $\bar{\phi}_0$, Eq. (5.19f)

has to be solved. This is done using the Fourier transform $\mathcal{F}$ and its inverse $\mathcal{F}^{-1}$, which are both defined in Eq. (5.6). Furthermore, the solution approach presented in [LoMei85] is followed. Applying the Fourier transform with respect to the coordinate X on Eq. (5.19f) and using $\mathcal{F}\left(\bar{\phi}_{0,X}\right) = \mathrm{i}k\mathcal{F}\left(\bar{\phi}_0\right)$, the mean velocity potential $\bar{\phi}_0$ can be calculated to be

$$\bar{\phi}_0(X,Z,T) + \bar{\phi}_0^*(X,Z,T) = \mathcal{F}^{-1}\left(2\mathrm{i}\omega_0\,\mathrm{sgn}(k)\mathcal{F}\left(|B|^2\right)\mathrm{e}^{|k|Z}\right). \tag{5.23}$$

Having computed $\bar{\phi}_0$, the mean sea surface displacement $\bar{\eta}_0$ is given by

$$\bar{\eta}_0 + \bar{\eta}_0^* = -\frac{1}{g}\left[\left(\bar{\phi}_0 + \bar{\phi}_0^*\right)_T\right]_{Z=0} = \frac{2\omega_0}{g}\frac{\partial}{\partial T}\left(\mathcal{H}\left(|B|^2\right)\right). \tag{5.24}$$

Here, $\mathcal{H}$ defines the Hilbert transform, which can be computed using Eq. (5.7). Now, all functions A_{jk}, B_{jk}, $\bar{\phi}_j$, and $\bar{\eta}_j$, which appear in Eq. (5.15) up to the order $\mathcal{O}(\varepsilon^3)$, have been calculated in terms of B. It remains to calculate the function B. This is done is two steps. First, the functions A_{ij} and $\bar{\phi}_0$, which are given in Eqs. (5.20) and (5.23), are substituted into Eq. (5.14a). In this way, the velocity potential ϕ is computed up to an error of order $\mathcal{O}(\varepsilon^4)$. Afterward, the resulting velocity potential ϕ is substituted into the BC (4.4c). The BC (4.4c) forms a combination of the two BCs (5.13a) and (5.13b) at $Z = 0$, which have been used to compute A_{ij} and $\bar{\phi}_0$.
Substituting the resulting velocity potential ϕ from Eq. (5.14a) into the BC (4.4c) and then considering only the terms up to order $\mathcal{O}(\varepsilon^3)$, it is found that B has to satisfy

$$\mathrm{i}\varepsilon^2\left(B_T + \frac{\omega_0}{2k_0}B_X\right) = \varepsilon^3\left(\frac{\omega_0}{8k_0^2}B_{XX} + 2\omega_0 k_0^2 B|B|^2\right). \tag{5.25}$$

After solving Eq. (5.25), the corresponding velocity potential ϕ and sea surface displacement η can be computed by substituting Eqs. (5.20), (5.22), (5.23) and (5.24) into Eq. (5.14).
The resulting expressions for η and ϕ can sightly be simplified by introducing

$$\psi(X,T) = 2B(X,T). \tag{5.26}$$

Substituting Eq. (5.26) into Eq. (5.25), the NLS (5.2) is obtained. The corresponding formulas for the sea surface displacement η and velocity potential ϕ are given by Eq. (5.5) and Eq. (5.8), respectively.
It has to be noted that only the terms from Eq. (5.14) up to the order $\mathcal{O}(\varepsilon^3)$ were considered and computed in this section. The nonlinear BC (4.4c) at $z = 0$ was also approximated accurately to the order $\mathcal{O}(\varepsilon^3)$. Terms of order $\mathcal{O}(\varepsilon^4)$ or higher have been neglected in this section. Therefore, the NLS is accurate to the third order in the wave steepness ε. This has also been stated, for example, in [ShemerDorfman08].

5.2.2 FSI using the NLS

In Sect. 5.2.1, it has been shown that the behavior of nonlinear water waves can be computed by solving the NLS (5.2), which results in the wave envelope ψ. Starting from ψ, the corresponding sea surface displacement η and velocity potential ϕ can be determined using Eq. (5.5) and Eq. (5.8), respectively. In this section, it is presented how the FSI between nonlinear water waves and a mechanical structure can be computed efficiently using the NLS.
In Fig. 4.2, the nonlinear scheme for the computation of the total velocity potential ϕ and its components $\phi^{(i)}$ is sketched. There, it has been assumed that the total velocity potential ϕ can be written as the sum of the incident velocity potential ϕ_0 and the velocity potential corresponding to the body disturbance ϕ_B, see Eq. (4.21). Before ϕ_B can be calculated, the incident velocity potential ϕ_0 has to be known. This has to fulfill the PDEs summarized in the second block of Fig. 4.2. Analytic formulas for the components of incident velocity potential, $\phi_0^{(i)}$, for regular and random Stokes waves are given in Sect. 4.3. It has been shown that an analytic formulation of the incident velocity potentials $\phi_0^{(i)}$, $i > 1$, gets complicated if random nonlinear Stokes waves are considered. However, the NLS forms a possibility to compute the incident velocity potentials $\phi_0^{(i)}$ in a simpler way.
The computation of the nonlinear FSI sketched in Fig. 4.2 and 4.4 assumes that the incident velocity potential ϕ_0 can be expressed by perturbation expansions with perturbation parameter ε, see Eq. (4.21). In the derivation of the NLS, a generalized perturbation approach has been applied to ϕ and η, see Eq. (5.14). Comparing Eq. (4.21) with Eq. (5.14), it can be seen that the i-th order incident velocity potential $\phi_0^{(i)}$ from Eq. (4.21) is given in Eq. (5.14) by the sum of all terms multiplied by ε^i. Therefore, for the velocity potential ϕ from Eq. (5.8), which can be computed after solving the NLS, the first three corresponding incident velocity potentials $\phi_0^{(i)}$, $i = 1, 2, 3$, are given by

$$\phi_0^{(1)}(x,z,t) = \mathrm{Re}\left\{ -\frac{\mathrm{i}\omega_0}{k_0}\widetilde{\psi} E \mathrm{e}^{k_0 z} \right\}, \tag{5.27a}$$

$$\phi_0^{(2)}(x,z,t) = \mathrm{Re}\left\{ \frac{\omega_0}{2k_0^2}\widetilde{\psi}_X E \mathrm{e}^{k_0 z} + 2\bar{\phi}_0 \right\}, \tag{5.27b}$$

$$\phi_0^{(3)}(x,z,t) = \mathrm{Re}\left\{ \left(\frac{\mathrm{i}k_0\omega_0}{8}\widetilde{C} + \frac{3\mathrm{i}\omega_0}{8k_0^3}\widetilde{\psi}_{XX} \right) E \mathrm{e}^{k_0 z} + 2\bar{\phi}_1 \right\}. \tag{5.27c}$$

The mean velocity potential $\bar{\phi}_0$ is given by Eq. (5.10).
The following can be concluded: after solving the NLS (5.2) for the wave envelope ψ, the first three incident velocity potentials $\phi_0^{(i)}$ can be computed using Eq. (5.27). Furthermore, the approach via the NLS is more efficient than the use of the analytic formulas for $\phi_0^{(i)}$, which have been presented in Sect. 4.3 for Stokes waves. There, it has been observed that nonlinear interactions between water

waves of first order have to be considered to formulate the velocity potential of random nonlinear water waves of second order. Therefore, the calculation of Stokes waves of higher order can lead to large computation times. However, using the NLS, nonlinear wave-wave interactions must not be computed in an additional step, but nonlinear water waves can be computed solving the NLS (5.2) and using Eq. (5.27) to calculate the incident velocity potentials $\phi_0^{(i)}$, $i = 1, 2, 3$. As it has been shown in the derivation of the NLS, solutions of the NLS can be used to accurately model water waves up to the third order in the wave steepness ε. This makes the approach using the NLS more efficient than the computation of $\phi_0^{(i)}$ presented in Sect. 4.3.
In the following, several remarks about the incident velocity potentials $\phi_0^{(i)}$ from Eq. (5.27) and the computation of the corresponding FSI are presented. Afterward, this section ends with a summary of how the NLS can be used to compute the nonlinear FSI between nonlinear water waves and the WEC presented in Sect. 3.1.

Mean Velocity Potential $\bar{\phi}_1$

First, it is explained why the mean velocity potential $\bar{\phi}_1$ is not needed in the formulation of the FSI considered in this thesis. The nonlinear FSI is computed using the method, which is sketched in Figs. 4.2 and 4.4. In this method, only the velocity potentials up to order $\mathcal{O}(\varepsilon^3)$ are considered. Going through the PDEs summarized in Fig. 4.2, which need to be solved to compute the body disturbance potentials $\phi_{\mathrm{B}}^{(i)}$, it can be seen that the incident velocity potentials $\phi_0^{(i)}$ appear in these equations only in combination with derivatives with respect to x, z, and t. However, the mean potential $\bar{\phi}_1$ depends only on the slow variables $X = \varepsilon x$, $Z = \varepsilon z$, and $T = \varepsilon t$. At this point, it holds

$$\bar{\phi}_{1,t} = \varepsilon \bar{\phi}_{1,T}, \quad \bar{\phi}_{1,x} = \varepsilon \bar{\phi}_{1,X}, \quad \bar{\phi}_{1,z} = \varepsilon \bar{\phi}_{1,Z}. \tag{5.28}$$

Since $\bar{\phi}_1$ is of order $\mathcal{O}(\varepsilon^3)$, the derivatives $\bar{\phi}_{1,t}$, $\bar{\phi}_{1,x}$, and $\bar{\phi}_{1,z}$ are of order $\mathcal{O}(\varepsilon^4)$. Therefore, considering $\bar{\phi}_1$ only affects the nonlinear FSI of order $\mathcal{O}(\varepsilon^4)$. Since the effects of order $\mathcal{O}(\varepsilon^4)$ are not considered in this thesis, $\bar{\phi}_1$ is not specified here. In the further course of this thesis, $\bar{\phi}_1$ is not considered.

Boundary Condition at $z = -h$

A corresponding BC at the sea bottom has to be considered in the numerical computation of the FSI. In the formulation of the NLS, only deep water is considered. As a result of this, the value of ϕ_z vanishes only for $z \to -\infty$, see Eq. (5.12d).
In contrast, the FSI between nonlinear water waves and a mechanical structure is computed numerically in this thesis using the method sketched in Figs. 4.2 and 4.4. There, it is assumed that the value of $\phi_{0,z}^{(i)}$ vanishes at $z = -h$. Therefore, in the numerical calculation of the FSI, where no spatial domain

of infinite size can be considered, it is assumed that the value of $\phi_{0,z}^{(i)}$ vanishes at $z = -h$. However, as stated before, this condition is not fulfilled by the incident velocity potentials $\phi_0^{(i)}$ of the NLS for any $h < \infty$. Therefore, the use of the incident velocity potentials $\phi_0^{(i)}$ of the NLS leads to errors in the numerical results. However, due to the exponential dependency of the incident velocity potentials $\phi_0^{(i)}$ in z, see Eq. (5.27), this error becomes small for a large water depth h. Therefore, for the case that the FSI is computed using the NLS, the value of the water depth h is always selected so that the deep water condition is fulfilled, i. e. $h > \frac{1}{2}\lambda = \frac{\pi}{k_0}$.

Boundary Conditions at $z = 0$

The next remark refers to the BCs at $z = 0$ given in Eq. (4.18), which have to be satisfied by $\phi_0^{(1)}$, $\phi_0^{(2)}$, and $\phi_0^{(3)}$, respectively. Substituting $\phi_0^{(1)}$ from Eq. (5.27a) into Eq. (4.18a) yields

$$\left[\phi_{0,tt}^{(1)} + g\phi_{0,z}^{(1)}\right]_{z=0} = \varepsilon^2 \mathrm{Re}\left\{-\frac{\mathrm{i}\omega_0}{k_0}\left(\psi_{TT} - 2\omega_0\left[\frac{\omega_0}{8k_0^2}\psi_{XX} + \frac{1}{2}\omega_0 k_0^2|\psi|^2\psi\right]\right)E\right\}. \tag{5.29}$$

Here, the relations $\omega_0^2 = k_0 g$, $\widetilde{\psi}_Z = -\mathrm{i}\widetilde{\psi}_X$, $\frac{g}{2\omega_0} = \frac{\omega_0}{2k_0}$ and the NLS (5.2) have been used to derive Eq. (5.29). Equation (5.29) shows that the first-order velocity potential $\phi_0^{(1)}$ from Eq. (5.27a) does not satisfy the BC (4.18a) exactly, but only up to an error of order $\mathcal{O}(\varepsilon^2)$. In the same way, substituting $\phi_0^{(1)}$, $\phi_0^{(2)}$, and $\phi_0^{(3)}$ from Eq. (5.27) into the BCs (4.18b) and (4.18c) at $z = 0$ results in

$$\begin{cases} \phi_{0,tt}^{(2)} + g\phi_{0,z}^{(2)} = \varepsilon g\left(\bar{\phi}_{0,Z} + \bar{\phi}_{0,Z}^*\right) + \mathcal{O}(\varepsilon^2), \\ F(\phi_0^{(1)}) = -2\varepsilon\omega_0^2 \mathrm{Re}\left\{\psi^*\psi_T\right\} + \mathcal{O}(\varepsilon^2), \\ \Rightarrow \phi_{0,tt}^{(2)} + g\phi_{0,z}^{(2)} - F(\phi_0^{(1)}) \overset{(*)}{=} \mathcal{O}(\varepsilon^2), \end{cases} \tag{5.30a}$$

$$\begin{cases} \left[\phi_{0,tt}^{(3)} + g\phi_{0,z}^{(3)}\right]_{z=0} = \mathcal{O}(\varepsilon), \\ Q(\phi_0^{(1)}, \phi_0^{(2)}) = \mathrm{Re}\left\{\mathrm{i}k_0\omega_0^3|\psi|^2\psi E\right\} + \mathcal{O}(\varepsilon), \\ \Rightarrow \phi_{0,tt}^{(3)} + g\phi_{0,z}^{(3)} - Q(\phi_0^{(1)}, \phi_0^{(2)}) = -\mathrm{Re}\left\{\mathrm{i}k_0\omega_0^3|\psi|^2\psi E\right\} + \mathcal{O}(\varepsilon). \end{cases} \tag{5.30b}$$

The equality $(*)$ in Eq. (5.30a) is obtained using Eq. (5.19f) and the NLS (5.2), from which follows

$$\mathrm{i}\psi_T = -\mathrm{i}c_{\mathrm{gr}}\psi_X + \nu\psi_{XX} + \delta|\psi|^2\psi = -\mathrm{i}\frac{\omega_0}{2k_0}\psi_X + \mathcal{O}(\varepsilon). \tag{5.31}$$

As a result of Eqs. (5.29) and (5.30), it can be concluded that the incident velocity potentials $\phi_0^{(1)}$, $\phi_0^{(2)}$, and $\phi_0^{(3)}$ from Eq. (5.27) do not satisfy the BCs (4.18)

exactly. This results from a simplification that has been used in deriving the BCs (4.18). The BCs (4.18) have been derived by substituting the velocity potential $\phi = \varepsilon\phi^{(1)} + \varepsilon^2\phi^{(2)} + \varepsilon^3\phi^{(3)} + \mathcal{O}(\varepsilon^4)$ into the nonlinear BC (4.4c) at $z = 0$. Here, all terms are sorted by the corresponding exponents of ε, which results in Eq. (4.15). Afterward, it has been used that the BC (4.15) holds if each term multiplied by ε^i vanishes on its own, $i = 1, 2, 3, \ldots$. In contrast, however, the NLS has been derived by substituting the generalized Stokes perturbation expansion from Eq. (5.14) into Eq. (5.13). Therefore, the incident velocity potential $\phi_0 = \varepsilon\phi_0^{(1)} + \varepsilon^2\phi_0^{(2)} + \varepsilon^3\phi_0^{(3)}$ satisfies the BC (4.4c) up to an error of order $\mathcal{O}(\varepsilon^4)$. In other words, the incident velocity potentials of the NLS do not fulfill all terms multiplied by ε^i on their own but the sum of all terms multiplied by the different exponents ε^i. This can also be seen by inserting the incident velocity potentials $\phi_0^{(i)}$ from Eq. (5.27) into the BC (4.15), which results in

$$\begin{aligned}
&\varepsilon\left(\phi_{0,tt}^{(1)} + g\phi_{0,z}^{(1)}\right) + \varepsilon^2\left(\phi_{0,tt}^{(2)} + g\phi_{0,z}^{(2)} - F(\phi_0^{(1)})\right) \\
&\qquad + \varepsilon^3\left(\phi_{0,tt}^{(3)} + g\phi_{0,z}^{(3)} - Q(\phi_0^{(1)}, \phi_0^{(2)})\right) \\
&= \varepsilon^3 \mathrm{Re}\left\{-\frac{\mathrm{i}\omega_0}{k_0}\left(\psi_{TT} - \left(\frac{\omega_0}{2k_0}\right)^2 \psi_{XX}\right)\right\} + \mathcal{O}(\varepsilon^4) \overset{(*)}{=} \mathcal{O}(\varepsilon^4).
\end{aligned} \tag{5.32}$$

The equality $(*)$ is obtained using the derivative of the NLS (5.2) with respect to the slow variable T.

It can be concluded that $\phi_0 = \varepsilon\phi_0^{(1)} + \varepsilon^2\phi_0^{(2)} + \varepsilon^3\phi_0^{(3)}$ fulfills the BC (4.15) up to an error of order $\mathcal{O}(\varepsilon^4)$ and thus up to an accuracy of order $\mathcal{O}(\varepsilon^3)$. On the other side, the incident velocity potentials $\phi_0^{(i)}$ from Eq. (5.27) do not fulfill the corresponding BCs (4.18) up to an error of order $\mathcal{O}(\varepsilon^4)$. However, using the scheme, which is sketched in Figs. 4.2 and 4.4 to compute the nonlinear FSI, a corresponding accuracy of order $\mathcal{O}(\varepsilon^3)$ can only be obtained if the incident velocity potentials $\phi_0^{(i)}$ satisfy the BCs (4.18). Therefore, if the nonlinear FSI is computed for waves corresponding to the NLS, an accuracy of order $\mathcal{O}(\varepsilon^3)$ cannot be obtained using the scheme sketched in Figs. 4.2 and 4.4.

In order to maintain an accuracy of order $\mathcal{O}(\varepsilon^3)$, the BC (4.4c) at $z = 0$ can be used in the computation of the FSI, since the BC (4.4c) is satisfied by the incident velocity potential $\phi_0 = \varepsilon\phi_0^{(1)} + \varepsilon^2\phi_0^{(2)} + \varepsilon^3\phi_0^{(3)}$ up to an accuracy of order $\mathcal{O}(\varepsilon^3)$. However, the BC (4.4c) is nonlinear in the velocity potential ϕ. This makes the numerical computation of the FSI not efficient, since a system of nonlinear equations has to be solved in each time step.

However, the BCs (4.18) and the method sketched in Figs. 4.2 and 4.4 can be used to compute the nonlinear FSI up to an accuracy of order $\mathcal{O}(\varepsilon^2)$. Substituting the incident velocity potentials of the NLS into the BCs (4.18) and

using the Eqs. (5.29) and (5.30), it results

$$\varepsilon \left(\phi_{0,tt}^{(1)} + g\phi_{0,z}^{(1)} \right) = \mathcal{O}(\varepsilon^3), \tag{5.33a}$$

$$\varepsilon^2 \left(\phi_{0,tt}^{(2)} + g\phi_{0,z}^{(2)} - F(\phi_0^{(1)}) \right) = \mathcal{O}(\varepsilon^4), \tag{5.33b}$$

$$\varepsilon^3 \left(\phi_{0,tt}^{(3)} + g\phi_{0,z}^{(3)} - Q(\phi_0^{(1)}, \phi_0^{(2)}) \right) = \mathcal{O}(\varepsilon^3). \tag{5.33c}$$

It can be seen that the BCs (4.18) are fulfilled up to an error of order $\mathcal{O}(\varepsilon^3)$ and thus up to an accuracy of order $\mathcal{O}(\varepsilon^2)$. Using the method sketched in Figs. 4.2 and 4.4, this shows that it is possible to compute the nonlinear FSI between nonlinear water waves corresponding to the NLS and a mechanical structure if a modeling error of order $\mathcal{O}(\varepsilon^3)$ is accepted.
It has to be noted that the incident velocity potential $\phi_0^{(1)}$ fulfills the first-order BC (5.33a) only up to an error of order $\mathcal{O}(\varepsilon^3)$. This means that the use of the incident velocity potential $\phi_0^{(3)}$ does not further increase the order of accuracy. Therefore, it is enough to use the incident velocity potentials $\phi_0^{(1)}$ and $\phi_0^{(2)}$ of the NLS to compute the nonlinear FSI up to a modeling error of order $\mathcal{O}(\varepsilon^3)$.

Sea Surface Displacement η

The final remark refers to the sea surface displacement η. Having computed the wave envelope ψ, the corresponding sea surface displacement η of the incoming water waves corresponding to the NLS (5.2) is given by Eq. (5.5). On the other side, using Eq. (5.27) to compute the first three components of the incident velocity potential ϕ_0, i. e. $\phi_0^{(i)}$ for $i = 1, 2, 3$, the Stokes components of the corresponding sea surface displacement η, i. e. $\eta^{(i)}$ for $i = 1, 2, 3$, can be computed using Eq. (4.19). It has to be noted that using Eq. (4.19) instead of Eq. (5.5) to calculate the sea surface displacement $\eta^{(i)}$ for $i = 1, 2, 3$ can lead to different results, whereby the differences are of higher order in the wave steepness ε. This is explained in the following.
The first Stokes component of the sea surface displacement η, i. e. $\eta^{(1)}$, is given by Eq. (4.19a). To calculate $\eta^{(1)}$ for incoming waves corresponding to the NLS, the time derivative of the velocity potential $\phi_0^{(1)}$ from Eq. (5.27a) is needed, which is given by

$$\phi_{0,t}^{(1)} = \mathrm{Re}\left\{ -\frac{\mathrm{i}\omega_0}{k_0} \left[(-\mathrm{i}\omega_0)\widetilde{\psi} + \varepsilon \widetilde{\psi}_T \right] E \mathrm{e}^{k_0 z} \right\}. \tag{5.34}$$

Using Eq. (4.19a), $\widetilde{\psi}(X, T, Z = 0) = \psi(X, T)$, and the dispersion relation from Eq. (2.21), the first component of the sea surface displacement, $\eta^{(1)}$, results into

$$\varepsilon\eta^{(1)} = \varepsilon \left[-\frac{1}{g}\phi_{0,t}^{(1)} \right]_{z=0} = \mathrm{Re}\left\{ \varepsilon\psi E \right\} + \mathrm{Re}\left\{ \frac{\mathrm{i}\varepsilon^2\omega_0}{gk_0} \psi_T E \right\}. \tag{5.35}$$

However, by definition, the first-order component $\eta^{(1)}$ of the total sea surface displacement η should only consist of all terms, which depend linearly on ε. Therefore, using Eq. (5.5) to compute the sea surface displacement η corresponding to the NLS, the first-order component $\eta^{(1)}$ is given by $\varepsilon\eta^{(1)} = \mathrm{Re}\{\varepsilon\psi E\}$. On the other side, using Eq. (4.19a) to compute the first-order component of the sea surface displacement, the result for $\eta^{(1)}$ also includes contributions of second order in ε, see Eq. (5.35). These second-order contributions of $\eta^{(1)}$ have to be remembered when the value of $\eta^{(1)}$ is computed using Eq. (4.19a) instead of Eq. (5.5). This fact is taken into account in Chap. 7 when investigating the FSI between a mechanical structure and waves corresponding to the NLS.
A similar results holds for the second-order component of the sea surface displacement, $\eta^{(2)}$. Considering all terms in Eq. (5.5), which are of order $\mathcal{O}(\varepsilon^2)$, yields

$$\varepsilon^2\eta^{(2)} = \mathrm{Re}\{\frac{1}{2}\varepsilon^2 k_0\psi^2 E^2\}. \tag{5.36}$$

On the other side, using the formula for $\eta^{(2)}$ from Eq. (4.19b) and considering the velocity potentials $\phi_0^{(1)}$ and $\phi_0^{(2)}$ from Eqs. (5.27a) and (5.27b), algebraic calculations result in

$$\begin{aligned}\varepsilon^2\eta^{(2)} =& \varepsilon^2\left[-\frac{1}{g}\left(\phi_{0,t}^{(2)} + \frac{1}{2}\boldsymbol{\nabla}\phi_0^{(1)}\cdot\boldsymbol{\nabla}\phi_0^{(1)}\right) + \frac{1}{g^2}\left(\phi_{0,t}^{(1)}\phi_{0,tz}^{(1)}\right)\right]_{z=0} \\ =& \mathrm{Re}\left\{\frac{1}{2}\varepsilon^2 k_0\psi^2E^2\right\} + \mathrm{Re}\left\{\frac{\mathrm{i}\varepsilon^2\omega_0^2}{2gk_0^2}\psi_X E\right\} + \mathcal{O}(\varepsilon^3).\end{aligned} \tag{5.37}$$

Comparing the results for $\eta^{(2)}$ from Eqs. (5.36) and (5.37) with each other, it can be seen that the use of Eq. (4.19b), which leads to Eq. (5.37), introduces additional effects of order $\mathcal{O}(\varepsilon^2)$ in $\eta^{(2)}$. With $E = \mathrm{e}^{\mathrm{i}(k_0x-\omega_0t)}$, it can be seen that the value of $\eta^{(2)}$ from Eq. (5.36) oscillates in time with frequency $2\omega_0$. In contrast, the value of $\eta^{(2)}$ from Eq. (5.37) also includes a component which oscillates in time with frequency ω_0. Furthermore, the value of $\eta^{(2)}$ from Eq. (5.37) contains components of third order in ε. These different additional contributions of $\eta^{(2)}$ are taken into account in Chap. 7 when the FSI between a mechanical structure and waves corresponding to the NLS is investigated.
As a result, it has been shown that Eqs. (4.19) and (5.5) lead to different values for the sea surface displacements $\eta^{(i)}$, $i = 1, 2$. However, it has to be noted that Eqs. (4.19) and (5.5) both lead to the same result for the total sea surface displacement η, which is computed by adding the sea surface displacements $\eta^{(i)}$, $i = 1, 2$, i. e. $\eta = \varepsilon\eta^{(i)} + \varepsilon^2\eta^{(2)} + \mathcal{O}(\varepsilon^3)$. To be more precise, an addition of Eq. (5.35) and Eq. (5.37) leads to the total sea surface displacement

$$\begin{aligned}\eta &= \varepsilon\eta^{(1)} + \varepsilon^2\eta^{(2)} + \mathcal{O}(\varepsilon^3) \\ &= \mathrm{Re}\Bigg\{\varepsilon\psi E + \underbrace{\frac{\mathrm{i}\varepsilon^2\omega_0}{gk_0}\psi_T E + \frac{\mathrm{i}\varepsilon^2\omega_0^2}{2gk_0^2}\psi_X E}_{=0+\mathcal{O}(\varepsilon^3),\text{ with Eq. (5.31)}} + \frac{1}{2}\varepsilon^2 k_0\psi^2E^2\Bigg\} + \mathcal{O}(\varepsilon^3).\end{aligned} \tag{5.38}$$

This gives the same result as Eq. (5.5) when considering all terms up to order $\mathcal{O}(\varepsilon^2)$.
In summary, it has been shown that the use of Eq. (4.19) instead of Eq. (5.5) leads to different values for the sea surface displacements $\eta^{(i)}$. However, both computation approaches lead to the same total sea surface displacement η.

5.2.3 Summary of the Computation of the Nonlinear FSI using the NLS

Using the NLS, the corresponding nonlinear FSI can be computed up to an error of order $\mathcal{O}(\varepsilon^3)$. Here, the total velocity potential $\phi = \phi_0 + \phi_\mathrm{B}$ is calculated using the first- and second-order potential components, i. e.

$$\phi = \phi_0 + \phi_\mathrm{B} = \varepsilon(\phi_0^{(1)} + \phi_\mathrm{B}^{(1)}) + \varepsilon^2(\phi_0^{(2)} + \phi_\mathrm{B}^{(2)}). \tag{5.39}$$

The incident velocity potentials $\phi_0^{(1)}$ and $\phi_0^{(2)}$ are given in Eq. (5.27). The velocity potentials $\phi_\mathrm{B}^{(1)}$ and $\phi_\mathrm{B}^{(2)}$ corresponding to the body disturbance can be calculated solving the PDEs summarized in Fig. 4.2. When the hydrodynamic forces acting on a floating structure and the resulting motion of the structure are computed, only the corresponding first- and second-order components of the forces and motions must be considered. For the WEC presented in Sect. 3.1, an overview of the computation of the FSI can be found in Fig. 4.4.
Summarized, the FSI between nonlinear water waves corresponding to the NLS and a mechanical structure can be computed using the following steps:

1. Compute the wave envelope ψ by solving the NLS (5.2).
2. Compute the incident velocity potentials $\phi_0^{(1)}$ and $\phi_0^{(2)}$ using Eq. (5.27).
3. Compute the velocity potentials $\phi_\mathrm{B}^{(1)}$ and $\phi_\mathrm{B}^{(2)}$, which correspond to the body disturbance, using the PDEs summarized in Fig. 4.2.
4. Compute the corresponding hydrodynamic forces acting on the mechanical structure as well as the motion of the structure. For the WEC presented in Sect. 3.1, the corresponding method is summarized in Fig. 4.4.

It should be noted that the first- and second-order incident velocity potentials $\phi_0^{(1)}$ and $\phi_0^{(2)}$ are calculated using the wave envelope, which satisfies the NLS (5.2). Since the NLS is accurate to the third order in the wave steepness, the NLS also accounts corresponding nonlinear wave effects. For example, the NLS can be used to calculate waves whose phase velocity c_ph depends on the wave amplitudes. This is also shown in the next section. Therefore, the algorithm summarized above computes the dynamics of the incident nonlinear water waves with a modeling error of order $\mathcal{O}(\varepsilon^4)$. However, as shown, the corresponding nonlinear FSI is calculated with a modeling error of order $\mathcal{O}(\varepsilon^3)$. In Fig. 5.2, this is illustrated for the WEC presented in Sect. 3.1.

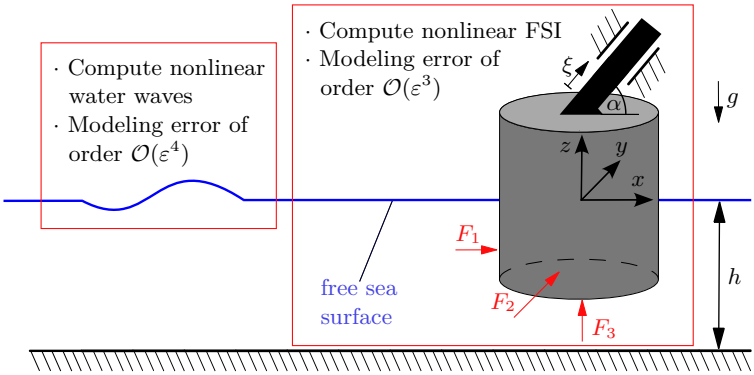

Figure 5.2: Illustration of the computation of the FSI between the WEC presented in Sect. 3.1 and water waves, which are calculated using the NLS.

So far, two different approaches for the calculation of the incident velocity potentials $\phi_0^{(i)}$ have been presented:

- Calculate the incident velocity potentials $\phi_0^{(1)}$ and $\phi_0^{(2)}$ of regular and random Stokes waves using the equations presented in Sect. 4.3.
- Compute the incident velocity potentials $\phi_0^{(1)}$ and $\phi_0^{(2)}$ corresponding to the NLS using Eq. (5.27).

Both approaches have different advantages and disadvantages. Table 5.1 summarizes the PDEs and BCs that are satisfied by the corresponding incident velocity potentials $\phi_0^{(i)}$. Moreover, Tab. 5.1 summarizes the properties that both approaches have. Again, it is shown that the computational method, which uses the NLS, computes the corresponding FSI accurately only up to a modeling error of order $\mathcal{O}(\varepsilon^3)$. However, the computation of the incident velocity potentials $\phi_0^{(1)}$ and $\phi_0^{(2)}$ depends only on the wave envelope ψ, which has to satisfy the NLS (5.2). As it is shown in the next sections, several analytical solutions of the wave envelope ψ are well-known, and numerical solutions of the NLS can be computed very efficiently. Therefore, the computation of the incident velocity potentials $\phi_0^{(1)}$ and $\phi_0^{(2)}$ corresponding to the NLS can also be executed very efficiently. Furthermore, nonlinear wave-wave interactions are directly considered in the formulation of the NLS when computing random waves. This does not apply to the approach via Stokes waves, where nonlinear wave-wave interactions have to be explicitly calculated in the case of nonlinear random water waves. As is shown in Sect. 4.3.2, the computation of these nonlinear wave-wave interactions becomes more expensive the more components the linear irregular sea state include. All this makes the approach via the NLS very promising for an efficient computation of the nonlinear FSI.

Table 5.1: Comparison of the two presented approaches for the computation of the incident velocity potentials $\phi_0^{(i)}$.

Properties	Use incident potentials $\phi_0^{(i)}$ $(i = 1, 2)$ of Stokes waves, which are presented in Sect. 4.3	Use incident potentials $\phi_0^{(i)}$ $(i = 1, 2)$ from NLS, which are presented in Eq. (5.27)
$\boldsymbol{\nabla}^2\phi_0^{(i)} = 0$?	Fulfilled	Fulfilled
$\phi_{0,z}^{(i)} = 0$ at $z = -h$?	Fulfilled	Not fulfilled, error decreases exponentially in h
$\phi_{0,tt}^{(1)} + g\phi_{0,z}^{(1)} = 0$ at $z = 0$?	Fulfilled	Not fulfilled, error of order $\mathcal{O}(\varepsilon^2)$
$\phi_{0,tt}^{(2)} + g\phi_{0,z}^{(2)} = F(\phi_0^{(1)})$ at $z = 0$?	Fulfilled	Not fulfilled, error of order $\mathcal{O}(\varepsilon^2)$
Advantages	• All PDEs and BCs are exactly fulfilled	• Straightforward and efficient computation • Nonlinear wave-wave interactions are directly considered • Nonlinear wave effects from the use of a third-order wave theory are taken into account
Disadvantages	• Interactions between water waves have to be explicitly considered in the irregular case • Computation of nonlinear wave-wave interactions is very time-consuming • Nonlinear wave effects from the use of a third-order wave theory are not considered	• All PDEs and BCs are only fulfilled up to a small error

Before the FSI between water waves corresponding to the NLS and a floating structure is computed and analyzed in Chap. 6 and Chap. 7, the NLS is investigated in more detail in the next sections. In the further course of this chapter, the waves are studied in the absence of any structure. In this way, solutions of the NLS as well as the corresponding incident velocity potentials $\phi_0^{(1)}$ and $\phi_0^{(2)}$ are investigated in more detail. For this, in the next section, analytical solutions for the wave envelope ψ are introduced. Afterward, numerical methods are presented, which are used to compute numerical solutions of the NLS and the corresponding incident velocity potentials $\phi_0^{(1)}$ and $\phi_0^{(2)}$.

5.3 Analytical Solutions of the NLS

In contrast to the governing equations of fluid motion from Eq. (2.2), analytical solutions for the NLS (5.2) are well-known and closed-form expressions are available. In the following, three of these solutions are presented and discussed.

5.3.1 Plane-wave Solution

The plane-wave solution of the NLS has an amplitude that is constant in time and space, and is given by

$$\psi(X,T) = \psi_0 \mathrm{e}^{\mathrm{i}k_{\mathrm{pw}}(X-X_{\mathrm{s}})-\mathrm{i}\left(k_{\mathrm{pw}}c_{\mathrm{gr}}-\nu k_{\mathrm{pw}}^2+\delta\psi_0^2\right)T}, \tag{5.40}$$

see e.g. [CarterEtAl20]. Here, $\psi_0 \in \mathbb{R}$ is the amplitude of the solution, $X_{\mathrm{s}} \in \mathbb{R}$ is a shift in space, and $k_{\mathrm{pw}} \in \mathbb{R}$ is an arbitrary constant. Substituting ψ from Eq. (5.40) into Eqs. (5.5) and (5.8), the corresponding sea surface displacement η and velocity potential ϕ for $k_{\mathrm{pw}} = 0$ becomes

$$\eta(x,t) = \varepsilon\psi_0\cos(\vartheta) + \frac{1}{2}\varepsilon^2 k_0\psi_0^2\cos(2\vartheta) + \frac{3}{8}\varepsilon^3 k_0^2\psi_0^3\cos(3\vartheta) + \mathcal{O}(\varepsilon^4), \tag{5.41a}$$

$$\phi(x,z,t) = \left[\varepsilon\frac{\omega_0}{k_0}\psi_0\sin(\vartheta) - \frac{1}{8}\varepsilon^3 k_0\omega_0\psi_0^3\sin(\vartheta)\right]\mathrm{e}^{k_0 z} + 2\varepsilon^3\mathrm{Re}\{\bar{\phi}_1\} + \mathcal{O}(\varepsilon^4), \tag{5.41b}$$

whereby $\vartheta = k_0 x - \omega_0(1+\frac{1}{2}\varepsilon^2 k_0^2\psi_0^2)t$. It has to be noted that for $k_{\mathrm{pw}} = 0$, the mean terms $\bar{\phi}_0$ and $\bar{\eta}_0$ are zero [CarterEtAl20]. Figure 5.3 shows the amplitude $|\psi|$ of the plane-wave solution and the sea surface displacement $\eta = \mathrm{Re}\{\varepsilon\psi E\}$ for $k_0 = 0.5\,\mathrm{m}^{-1}$, $\psi_0 = 2\,\mathrm{m}$, $\varepsilon = 0.1$, $X_{\mathrm{s}} = 0$, and $k_{\mathrm{pw}} = 0$.
Considering Eq. (5.41) and Fig. 5.3, it can be seen that the plane-wave solution of the NLS leads to regular water waves. The corresponding velocity potential ϕ and sea surface displacement η from Eq. (5.41) oscillate in time with the wave frequency ω_{NLS}, which is given by

$$\omega_{\mathrm{NLS}}^2 = \left(\omega_0(1+\frac{1}{2}\varepsilon^2 k_0^2\psi_0^2)\right)^2 = k_0 g(1+\varepsilon^2 k_0^2\psi_0^2) + \mathcal{O}(\varepsilon^4). \tag{5.42}$$

For $A = \varepsilon\psi_0$, this results in the nonlinear dispersion relation from Eq. (4.8), which is induced by the nonlinear wave theory of third-order, see Sect. 4.1.2. Therefore, the NLS recovers the nonlinear dispersion relation from Eq. (4.8).
It has to be noted that the amplitude ψ_0 of the plane-wave solution from Eq. (5.40) cannot be chosen independently from the wave number k_0 and wave steepness ε. Recall that ε is related to the wave steepness of the wave. For a random water wave, the wave steepness varies in space. However, for a regular wave, the wave

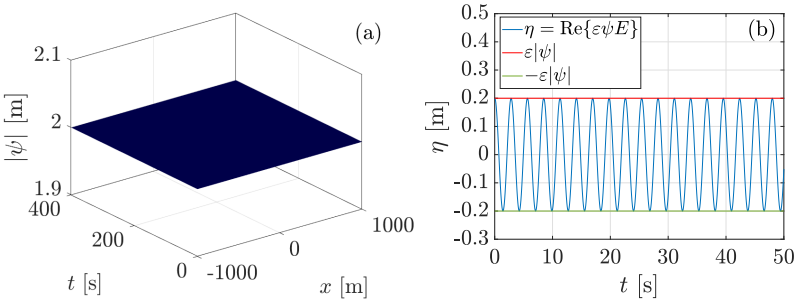

Figure 5.3: (a): Amplitude of wave envelope ψ of the plane-wave solution for $k_0 = 0.5\,\mathrm{m}^{-1}$, $\psi_0 = 2\,\mathrm{m}$, $\varepsilon = 0.1$, $X_\mathrm{s} = 0$, and $k_\mathrm{pw} = 0$. (b): Corresponding sea surface displacement $\eta = \mathrm{Re}\{\varepsilon\psi E\}$ at $x = 0$.

steepness is given by $\varepsilon = Ak_0$, see Eq. (4.12). Together with $A = \varepsilon\psi_0$, which has been already stated above, it holds

$$\varepsilon = Ak_0 \overset{A=\varepsilon\psi_0}{=} \varepsilon\,(\psi_0 k_0) \Rightarrow \psi_0 k_0 = 1. \tag{5.43}$$

Therefore, for the plane-wave solution from Eq. (5.40), the parameters ψ_0 and k_0 have to satisfy $\psi_0 k_0 = 1$. However, this is not the case for other solutions of the NLS, where the amplitude of ψ is not constant in time and space. Here, the wave steepness of the sea surface displacement η cannot be expressed accurately by a single value ε in the whole spatial and temporal domain.
In the following, two analytical solutions of the NLS (5.2) are presented, where the amplitude of ψ varies in space and where ε is assumed to be a characteristic or mean wave steepness of the whole wave.

5.3.2 Peregrine Breather Solution

An important analytical solution of the NLS, which is localized in time and space, has been found by Peregrine [Peregrine83] and is known as the Peregrine breather solution. This solution is given by

$$\psi(X,T) = \psi_0 \left(\frac{4\nu\left(1 - 2\mathrm{i}\delta\psi_0^2 T\right)}{\nu\left[1 + \left(2\delta\psi_0^2 T\right)^2\right] + 2\delta\psi_0^2\left(X - c_\mathrm{gr}T - X_\mathrm{s}\right)^2} - 1 \right) \mathrm{e}^{-\mathrm{i}\delta\psi_0^2 T}. \tag{5.44}$$

Figure 5.4a shows the amplitude $|\psi|$ of the Peregrine breather solution for $\psi_0 = 1.5\,\mathrm{m}$, $k_0 = 0.5\,\mathrm{m}^{-1}$, $\varepsilon = 0.1$, and $X_\mathrm{s} = c_\mathrm{gr}\varepsilon \cdot 200\,\mathrm{s} = 44.29\,\mathrm{m}$. The spatial shift X_s is chosen in such a way that the Peregrine breather solution gets its

peak value for $t = -200\,\mathrm{s}$ at $x = 0\,\mathrm{m}$, see Fig. 5.4a. In order to get a better view of the Peregrine breather solution, Fig. 5.4b illustrates the same solution with respect to the moving space coordinate $\zeta = x - c_{\mathrm{gr}}t$, which moves with the group velocity c_{gr}. Figure 5.4c shows the corresponding sea surface displacement $\eta = \mathrm{Re}\{\varepsilon\psi E\}$ at $x = X_{\mathrm{s}}/\varepsilon = 442.9\,\mathrm{m}$, where the Peregrine breather solution reaches its maximal peak amplitude over time.
The Peregrine breather solution represents a regular water wave, which contains a small perturbation at a specific location in the past. This perturbation amplifies over time until it shows an amplitude three times as high as the amplitude of the regular background waves. As the amplitude of the wave envelope of the regular background waves is given by ψ_0, this means that the peak amplitude of the Peregrine breather solution is given by $|\psi|_{\max} = 3\psi_0$, see also Figs. 5.4a and 5.4b with $\psi_0 = 1.5\,\mathrm{m}$.
In Figs. 5.4a and 5.4b, it is clearly shown that the Peregrine breather solution is doubly localized. Therefore, the Peregrine breather solution describes a unique

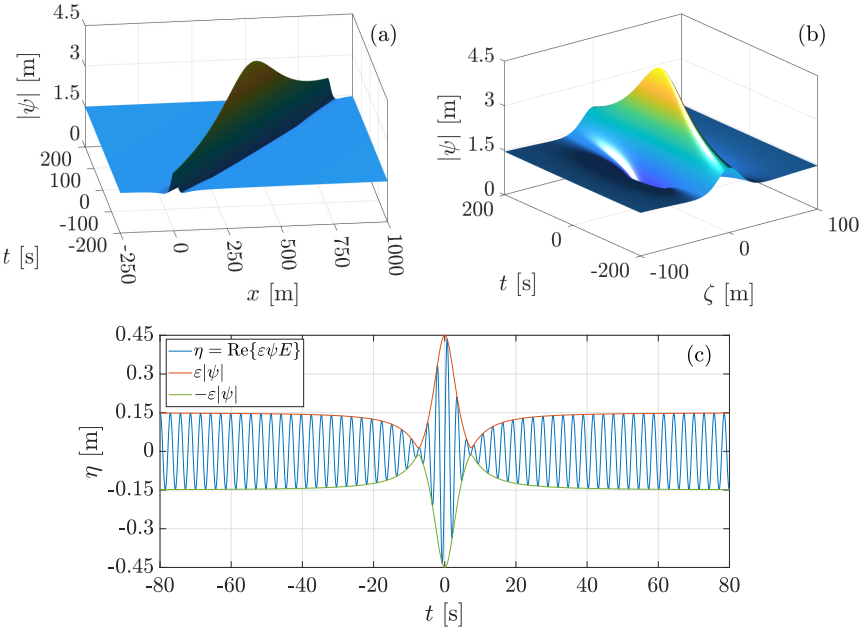

Figure 5.4: (a): Amplitude of wave envelope ψ of the Peregrine breather solution for $k_0 = 0.5\,\mathrm{m}^{-1}$, $\psi_0 = 1.5\,\mathrm{m}$, $\varepsilon = 0.1$, and $X_{\mathrm{s}} = 44.29\,\mathrm{m}$. (b): Corresponding Peregrine breather solution from (a) shown with respect to the moving space coordinate $\zeta = x - c_{\mathrm{gr}}t$. (c): Sea surface displacement $\eta = \mathrm{Re}\{\varepsilon\psi E\}$ at $x = X_{\mathrm{s}}/\varepsilon = 442.9\,\mathrm{m}$.

wave event in which large amplitude waves seem to come out of nowhere and disappear without a trace [ChabchoubEtAl12]. In different studies, it has been conjectured that the Peregrine is a prototype of rogue waves in the ocean, see e.g. [DystheTrulsen99, ShriraGeogjaev10, DostalEtAl20]. According to the definition of oceanographers, rogue waves are very rare events in random ocean waves with an extraordinarily large wave height, which exceeds the significant wave height H_s of a measured wave train, also known as wave packet, by a factor of 2.2, see [OnoratoEtAl01, Chabchoub13]. One example of a measured rogue wave is the Draupner wave, which has been recorded on January 1st 1995 in the central North Sea [AdcockEtAl11]. The remarkable height of the Draupner wave is 25.6m. As has been shown, for example, in [Chabchoub13, Witt19], the Peregrine model fits very well to the wave records of the Draupner wave, although the Peregrine breather solution is just a single distorted regular wave train solution.
In [ChabchoubEtAl12], laboratory experimental results are presented on the study of doubly localized surface wave events that can be modeled using the Peregrine breather solution. A very good agreement between the theory and the experiments is shown for small steepness values of the background carrier wave of $\varepsilon \leq 0.116$. For higher steepness values, the Peregrine breather solution starts to break. In order to prevent breaking, in this work, the Peregrine breather solution is always considered for waves with a wave steepness of $\varepsilon \leq 0.1$.

5.3.3 Soliton Solution

One important solution of the NLS is an isolated and stationary sech-shape nonlinear wave group on zero background. This solution is known as the soliton solution and is given by

$$\psi(X,T) = \psi_0 \mathrm{sech}\left(\psi_0\sqrt{\frac{\delta}{2\nu}}\,(X - c_\mathrm{gr}T - X_\mathrm{s})\right)\mathrm{e}^{-\frac{1}{2}\mathrm{i}\delta\psi_0^2 T}, \tag{5.45}$$

see e.g. [SlunyaevEtAl13a]. Figure 5.5a shows the amplitude of the soliton solution for $k_0 = 0.5\,\mathrm{m}^{-1}$, $\psi_0 = 1.5\,\mathrm{m}$, $\varepsilon = 0.1$, and $X_\mathrm{s} = 0$. In order to get a better view of the soliton solution, Fig. 5.5b illustrates the same solution with respect to the moving space coordinate $\zeta = x - c_\mathrm{gr}t$. It can be seen that the solution represents a wave packet on an otherwise calm sea surface. The shape of the envelope of the wave packet remains unchanged in propagation. Figure 5.5c shows the corresponding sea surface displacement $\eta = \mathrm{Re}\{\varepsilon\psi E\}$ at $x = c_\mathrm{gr}\cdot 200\,\mathrm{s} = 442.9\,\mathrm{m}$, where the soliton solution reaches its peak amplitude at $t = 200\,\mathrm{s}$.
In [SlunyaevEtAl13a], laboratory experimental results are presented on the dynamics of the soliton solution. Soliton solutions with a wave steepness at the crest of the solution of about $\varepsilon \approx 0.3$ have been successfully reproduced in laboratory experiments. For higher steepness values, the soliton solutions are found to be

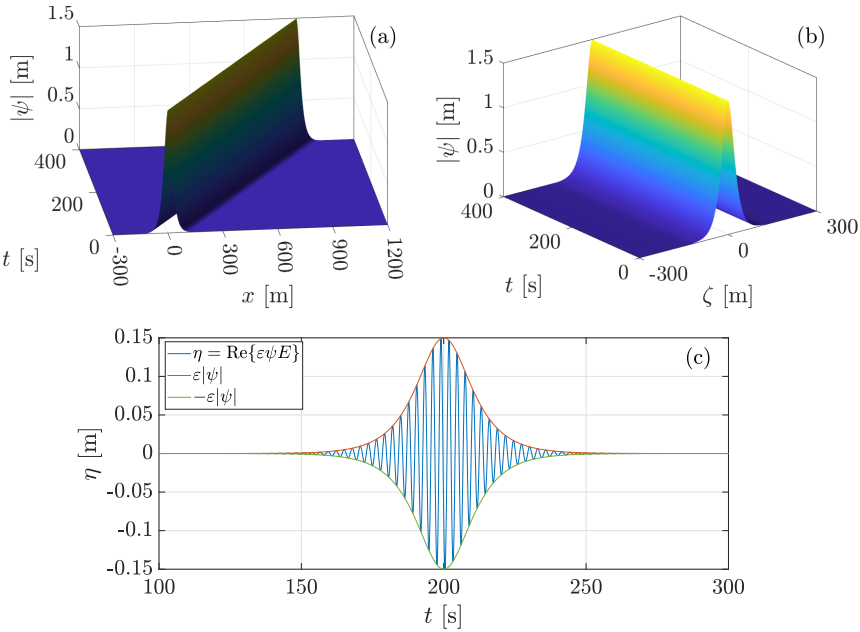

Figure 5.5: (a): Amplitude of wave envelope ψ of the soliton solution for $k_0 = 0.5\,\mathrm{m}^{-1}$, $\psi_0 = 1.5\,\mathrm{m}$, $\varepsilon = 0.1$, and $X_\mathrm{s} = 0$. (b): Corresponding soliton solution from (a) shown with respect to the moving space coordinate $\zeta = x - c_\mathrm{gr}t$. (c): Sea surface displacement $\eta = \mathrm{Re}\{\varepsilon\psi E\}$ at $x = c_\mathrm{gr} \cdot 200\,\mathrm{s} = 442.9\,\mathrm{m}$.

structurally unstable or start to break. In order to prevent breaking, in this work, soliton solutions are always considered for waves with a wave steepness of $\varepsilon \leq 0.3$.

5.4 Numerical Solution of the NLS

In order to compute the velocity potential of the NLS, two PDEs have to be solved, namely the NLS (5.2) and the complex transport equation (5.11). In this section, a numerical method is presented to solve the NLS (5.2) numerically. In the next section, it is dealt with the complex transport equation (5.11).
In order to solve the NLS (5.2) numerically, the relaxation pseudo-spectral (ReSP) scheme is applied, which has been used, for example, in [AntoineDuboscq15]. In

the ReSP scheme, the time derivative is discretized by finite differences, and a spectral approximation is performed in space. In contrast to Crank–Nicolson-type schemes, the ReSP scheme does not need to fulfill a Courant–Friedrichs–Lewy condition. The ReSP scheme is sketched in the following.
Since the NLS (5.2) is defined on an unbounded domain, the temporal and spatial computational domain has first to be bounded, for which the numerical solution is calculated, i. e.

$$\begin{aligned}
&\mathrm{i}(\psi_T + c_{\mathrm{gr}}\psi_X) = \nu\psi_{XX} + \delta|\psi|^2\psi, \quad \text{for } X \in (-X_{\max}, X_{\max}),\ T \in (0, T_{\max}],\\
&\psi(X, T=0) = \psi_{\mathrm{IC}}(X), \qquad\qquad \text{for } X \in [-X_{\max}, X_{\max}],\\
&\psi(-X_{\max}, T) = \psi(X_{\max}, T),\ \psi_X(-X_{\max}, T) = \psi_X(X_{\max}, T), \quad \text{for } T \in (0, T_{\max}].
\end{aligned} \tag{5.46}$$

Here, the length $X_{\max}$ is assumed to be so large that the basic physical behavior takes place in $(-X_{\max}, X_{\max})$. Furthermore, the maximal simulation time $T_{\max}$ is smaller than some time $\mathcal{T}$, whereby it is assumed that the solution exists up to time $\mathcal{T}$. At $T = 0$, the solution ψ is equal to a given initial condition (IC) denoted by ψ_{IC}. Periodic boundary conditions are applied in space.
Next, the temporal and spatial domain are discretized using equidistant grids of the form

$$\begin{aligned}
T_n &:= n\Delta T, \quad \text{for } n \in \{0, \dots, N\},\ \Delta T = \frac{T_{\max}}{N},\\
X_j &:= j\Delta X - X_{\max}, \quad \text{for } j \in \{0, \dots, J\},\ \Delta X = \frac{2X_{\max}}{J}.
\end{aligned} \tag{5.47}$$

Using this notation, the ReSP scheme applied at the NLS (5.46) is given by, see e.g. [AntoineDuboscq15],

$$\begin{aligned}
&\frac{\Lambda^{n+\frac{1}{2}} + \Lambda^{n-\frac{1}{2}}}{2} = \delta|\Psi^n|^2,\\
&\mathrm{i}\frac{\Psi^{n+1} - \Psi^n}{\Delta T} = -\mathrm{i}c_{\mathrm{gr}}\left(\frac{\Psi^{n+1} + \Psi^n}{2}\right)_X + \nu\left(\frac{\Psi^{n+1} + \Psi^n}{2}\right)_{XX} + \Lambda^{n+\frac{1}{2}}\frac{\Psi^{n+1} + \Psi^n}{2},\\
&\Psi^0(X_j) = \psi_{\mathrm{IC}}(X_j), \quad \Lambda^{-1/2}(X_j) = \nu|\Psi^0(X_j)|^2.
\end{aligned} \tag{5.48}$$

Here, Ψ is a grid function with $\Psi_j^n = \Psi(X_j, T_n)$, which approximates the exact solution ψ of the NLS (5.46) at the grid points, i. e. $\Psi_j^n \approx \psi(X_j, T_n)$.
Using the ReSP scheme from Eq. (5.48), the cubic nonlinearity of the NLS (5.46) is circumvented by an additional intermediate time step using the auxiliary variable Λ. Thus, it is not necessary to solve a nonlinear system of equations at each time step.

The computation of the spatial derivatives appearing in Eq. (5.48) is based on truncated Fourier series expansions of Ψ of the form

$$\Psi_j^n = \sum_{m=-J/2}^{J/2-1} \widehat{\Psi}_m^n \mathrm{e}^{\mathrm{i}\mu_m X_j}, \quad \text{with} \quad \widehat{\Psi}_m^n = \frac{1}{J} \sum_{j=0}^{J-1} \Psi_j^n \mathrm{e}^{-\mathrm{i}\mu_m X_j}, \tag{5.49}$$

whereby $\mu_m := \frac{m\pi}{X_{\max}}$. Then the corresponding first- and second-order derivatives with respect to X are given by

$$\left(\Psi_j^n\right)_X = \sum_{m=-J/2}^{J/2-1} \mathrm{i}\mu_m \widehat{\Psi}_m^n \mathrm{e}^{\mathrm{i}\mu_m X_j}, \quad \left(\Psi_j^n\right)_{XX} = \sum_{m=-J/2}^{J/2-1} -\mu_m^2 \widehat{\Psi}_m^n \mathrm{e}^{\mathrm{i}\mu_m X_j}. \tag{5.50}$$

The presented ReSP scheme from Eq. (5.48) can be implemented such that a linear system of equations is solved in each time step. It is an implicit method, which is second-order accurate in time and spectrally accurate in space. Furthermore, it is unconditionally stable [AntoineDuboscq15].

5.5 Numerical Integration of the Complex Transport Equation

After solving the NLS (5.2) for the complex wave envelope ψ, the velocity potential ϕ can be calculated using Eq. (5.8). However, for the computation of the variables $\widetilde{\psi}$ and $\widetilde{C}$, the complex transport equation (5.11) has to be solved. Although this equation is much simpler than the NLS (5.2), there are two issues that make solving the complex transport equation (5.11) difficult: the instability of the velocity potential ϕ from Eq. (5.8), which corresponds to solutions of the NLS, in large water depths and the instability of numerical methods solving the complex transport equation. These two instabilities are dealt with in the following.

5.5.1 Instability of Solutions of the NLS in the Depth

In [CarterEtAl20], it is noted that the velocity potential corresponding to solutions of the NLS (5.2) can have singularities at $z = \mathcal{O}\left(\varepsilon^{-1}\right)$. However, the origin of these singularities is not known.

In this section, the behavior of these singularities is investigated. This investigation extends the study presented in [CarterEtAl20]. It is studied where the singularities are located and how the wave parameters (ψ_0, ω_0,ε) affect the location of the singularities. It is found that the appearance and behavior of the singularities depend on the considered solution of the NLS (5.2).
In the following, the singularities are investigated for the three analytical solutions presented in Sect. 5.3. In order to simplify the investigation, only the singularities appearing in $\widetilde{\psi}$ are considered in detail. For $\widetilde{C}$, only the results for the locations of the singularities are presented.

Singularities of the Plane-Wave Solution

The plane-wave solution $\psi(X,T)$ of the NLS (5.2) is given by Eq. (5.40). The corresponding auxiliary variable $\widetilde{\psi}$ is then given by

$$\widetilde{\psi}(X,Z,T) = \underbrace{\psi_0 \mathrm{e}^{\mathrm{i}k_{\mathrm{pw}}(X-X_{\mathrm{s}})-\mathrm{i}\left(k_{\mathrm{pw}}c_{\mathrm{gr}}-\nu k_{\mathrm{pw}}^2+\delta\psi_0^2\right)T}}_{\psi(X,T)} \mathrm{e}^{k_{\mathrm{pw}}Z} = \psi(X,T)\mathrm{e}^{k_{\mathrm{pw}}Z}. \quad (5.51)$$

Since $Z < 0$, it can be observed that $\widetilde{\psi}$ decays exponentially for an increasing water depth. Consequently, $\widetilde{\psi}$ shows no singularities. The same holds for the variable $\widetilde{C}$, which is given by $\widetilde{C}(X,Z,T) = \psi_0^2\widetilde{\psi}(X,Z,T)$. Therefore, the corresponding velocity potential $\phi(x,z,t)$ can be computed for each depth $z < 0$.

Singularities of the Peregrine Breather solution

The Peregrine breather solution $\psi(X,T)$ of the NLS (5.2) is given by Eq. (5.44). The corresponding auxiliary variable $\widetilde{\psi}$ is given by

$$\widetilde{\psi}(X,Z,T) = \left(\frac{\psi_0 4\nu\left(1-2\mathrm{i}\delta\psi_0^2T\right)}{\nu\left[1+\left(2\delta\psi_0^2T\right)^2\right]+2\delta\psi_0^2\left(X-\mathrm{i}Z-c_{\mathrm{gr}}T-X_{\mathrm{s}}\right)^2} - \psi_0 \right) \mathrm{e}^{-\mathrm{i}\delta\psi_0^2T}. \quad (5.52)$$

It can be seen that $\widetilde{\psi}$ can contain singularities by forming poles. Therefore, the question arises whether the denominator in Eq. (5.52) can reach zero for some depth Z. It can be found that the imaginary part of the denominator vanishes for $Z = 0$ or $X - c_{\mathrm{gr}}T - X_{\mathrm{s}} = 0$. For $Z = 0$, it holds $\widetilde{\psi}(X, Z = 0, T) = \psi(X,T)$ and the denominator in Eq. (5.52) is nonzero for all $X, T \in \mathbb{R}$. However, for $X - c_{\mathrm{gr}}T - X_{\mathrm{s}} = 0$, the denominator in Eq. (5.52) reaches zero for

$$Z = \pm\sqrt{\frac{\nu}{2\delta\psi_0^2} + 2\nu\delta\psi_0^2T^2}. \quad (5.53)$$

Since the square root is strictly monotonically increasing in its argument, $|Z|$ reaches its smallest value for $T = 0$. Substituting ν and δ from Eq. (5.3) into

Eq. (5.53), it is found that the denominator of $\widetilde{\psi}$ reaches zero for

$$T = 0, \quad X = X_\mathrm{s}, \quad \text{and} \quad Z = -\frac{1}{2\sqrt{2}\psi_0 k_0^2}. \tag{5.54}$$

Here, only the negative choice of Z is considered since the water domain is located at $Z < 0$. It has to be noted that the Peregrine breather solution from Eq. (5.44) reaches its peak amplitude at $T = 0$ and $X = X_\mathrm{s}$ with $\psi(X = X_\mathrm{s}, T = 0) = 3\psi_0$. This means that the singularity, which is located at the position given in Eq. (5.54), is located below the location of the peak amplitude of the Peregrine.
It can be concluded that $\widetilde{\psi}$ contains poles for depths $Z \leq -\frac{1}{2\sqrt{2}\psi_0 k_0^2}$. The same is true for $\widetilde{C}$, which is given by

$$\widetilde{C}(X, Z, T) = \psi_0^2 \frac{f(X, Z, T)}{\left[\nu\left[1 + (2\delta\psi_0^2 T)^2\right] + 2\delta\psi_0^2 \left(X - \mathrm{i}Z - c_\mathrm{gr}T - X_\mathrm{s}\right)^2\right]^2} \widetilde{\psi}(X, Z, T) \tag{5.55}$$

with some function $f = f(X, Z, T)$. Since the denominator appearing in Eq. (5.55) is the same as in Eq. (5.52), $\widetilde{C}$ has a singularity at the same depth as $\widetilde{\psi}$. This means that the velocity potential $\phi(x, z, t)$ corresponding to the Peregrine breather solution can be computed without any singularity only for water depths

$$z = \frac{Z}{\varepsilon} > z_\mathrm{Per} := -\frac{1}{2\sqrt{2}\varepsilon\psi_0 k_0^2}. \tag{5.56}$$

Singularities of the Soliton Solution

The soliton solution $\psi(X, T)$ of the NLS (5.2) is given by Eq. (5.45). The corresponding auxiliary variable $\widetilde{\psi}$ is given by

$$\widetilde{\psi}(X, Z, T) = \psi_0 \mathrm{sech}\left(\psi_0 \sqrt{\frac{\delta}{2\nu}} \left(X - \mathrm{i}Z - c_\mathrm{gr}T - X_\mathrm{s}\right)\right) \mathrm{e}^{-\frac{1}{2}\mathrm{i}\delta\psi_0^2 T}. \tag{5.57}$$

In order to investigate whether $\widetilde{\psi}$ contains any singularity, it has to be noted that for any variables a,$b \in \mathbb{R}$, the relation

$$\mathrm{sech}\,(a - \mathrm{i}b) = \frac{1}{\cosh(a - \mathrm{i}b)} = \frac{1}{\cosh(a)\cos(b) - \mathrm{i}\sinh(a)\sin(b)} \tag{5.58}$$

holds. This term gets singular for $a = 0$ and $b = \pm\frac{\pi}{2}(2n + 1)$, $n = 0, 1, 2, \ldots$ Applying this to Eq. (5.57), it can be observed that $\widetilde{\psi}$ contains poles periodically in Z. The poles are located at

$$X = c_\mathrm{gr}T + X_\mathrm{s} \quad \text{and} \quad Z = \pm\frac{\pi}{2\psi_0}\sqrt{\frac{2\nu}{\delta}}(2n + 1) = \pm\frac{\pi}{2\sqrt{2}\psi_0 k_0^2}(2n + 1). \tag{5.59}$$

The same poles are contained by $\widetilde{C}$, which is given by

$$\widetilde{C}(X,Z,T) = \psi_0^2 \operatorname{sech}^2\left(\psi_0\sqrt{\frac{\delta}{2\nu}}\,(X - \mathrm{i}Z - c_{\mathrm{gr}}T - X_{\mathrm{s}})\right)\widetilde{\psi}(X,Z,T). \quad (5.60)$$

It has to be noted that poles from Eq. (5.59) are located below the position, where the soliton solution reaches its peak amplitude $|\psi| = \psi_0$.
Since the water domain is located at $Z < 0$, only the poles with a negative value of Z are considered in the following. The presence of the poles leads to the fact that the velocity potential ϕ can only be computed up to the depth of the first pole. For $n = 0$ and substituting ν and δ from Eq. (5.3) into Eq. (5.59), it is found that the velocity potential $\phi(x,z,t)$ of the soliton solution can be computed without any singularity only for depths

$$z = \frac{Z}{\varepsilon} > z_{\mathrm{Sol}} := -\frac{\pi}{2\sqrt{2}\varepsilon\psi_0 k_0^2}. \quad (5.61)$$

Summary and Conclusions for the Calculation of the FSI

It has been shown that some analytic solutions of the NLS (5.2) lead to velocity potentials, which contain a singularity at $z = \mathcal{O}(\varepsilon^{-1})$. This is due to the fact that $\widetilde{\psi}$ can contain poles.
For the computation of the FSI between a structure and nonlinear water waves, the parameters ψ_0, ε, and k_0 have to be chosen in such a way that the structure never reaches the corresponding positions of the singularities. Moreover, for the numerical computation of the FSI, the water depth h has to be prescribed. However, the NLS (5.2) is only valid for deep water. Using the wavelength $\lambda = \frac{2\pi}{k_0}$, the water depth h has to satisfy the deep water condition, i. e. $h > \frac{1}{2}\lambda = \frac{\pi}{k_0}$. On the other hand, h should be small so that the numerical effort for the calculation of the FSI does not become too expensive.
It can be concluded that the wave parameters ψ_0, k_0, and ε have to be chosen in such a way that the singularities from Eqs. (5.56) and (5.61) are located below h, which should be small. For example, this is possible for the parameter combination $\{\psi_0, k_0, \varepsilon\} = \{1.5\,\mathrm{m}, 0.5\,\mathrm{m}^{-1}, 0.1\}$, which results in $h > 2\pi$, $z_{\mathrm{Per}} = -9.43\,\mathrm{m}$, and $z_{\mathrm{Sol}} = -29.62\,\mathrm{m}$. The corresponding solutions for the wave envelope ψ are depicted in Figs. 5.4 and 5.5.
It has to be noted that the wave steepness ε appears in the denominator in Eq. (5.56) and (5.61), respectively. This means that steeper water waves lead to smaller values of z_{Per} and z_{Sol} and thus to smaller water depths up to which the velocity potential ϕ can be computed without containing singularities. However, it has to be remembered that the NLS can only be used to accurately model weakly nonlinear deep water waves with a moderate wave steepness of $H/\lambda \leq 0.05$ or $\varepsilon \leq 0.15$ [Dysthe79, Witt19, Osborne10]. Therefore, only a wave steepness with a value of $\varepsilon \leq 0.15$ should be used in Eq. (5.56) and (5.61), which in turn leads to larger values of z_{Per} and z_{Sol}, respectively.

5.5.2 Instability of the Numerical Method Solving the Complex Transport Equation

In order to calculate the velocity potential ϕ corresponding to solutions ψ of the NLS (5.2), the auxiliary variables $\widetilde{\psi}(X,Z,T)$ and $\widetilde{C}(X,Z,T)$ have to be computed. However, if no analytical expression for ψ is given, $\widetilde{\psi}$ can in general only be computed numerically by solving the complex transport equation (5.11). The variable $\widetilde{C}(X,Z,T)$ can be computed in the same way using a different IC at $Z=0$.
In this section, it is investigated how the complex transport equation can be solved numerically. As is shown below, the stability of numerical schemes is a big issue. In order to simplify the notation in this section, it is only referred to the calculation of $\widetilde{\psi}$. The calculation of $\widetilde{C}$ follows analogously.
Since the complex transport equation (5.11) is defined on an unbounded domain, the $X-Z$-domain has first to be bounded, for which the solution is computed, i. e.

$$\begin{aligned}
&\widetilde{\psi}_Z = -\mathrm{i}\widetilde{\psi}_X, \quad \text{for } X \in (-X_{\max}, X_{\max}),\ Z \in [Z_{\min}, 0),\\
&\widetilde{\psi}(X, Z=0) = \psi(X), \quad \text{for } X \in [-X_{\max}, X_{\max}],\\
&\widetilde{\psi}(-X_{\max}, Z) = \widetilde{\psi}(X_{\max}, Z),\ \widetilde{\psi}_X(-X_{\max}, Z) = \widetilde{\psi}_X(X_{\max}, Z) \ \text{ for } Z \in [Z_{\min}, 0).
\end{aligned} \tag{5.62}$$

The length $X_{\max}$ is the same as used in Sect. 5.4, where the ReSP scheme has been presented to solve the NLS. Furthermore, the value of the water depth $Z_{\min} < 0$ is larger than some $\mathcal{Z} < 0$, i. e. $\mathcal{Z} < Z_{\min} < 0$. Here, it is assumed that the solution $\widetilde{\psi}$ exists without singularity up to the depth $\mathcal{Z}$. For the Peregrine breather and soliton solution, the respective values of $\mathcal{Z}$ are given by $\mathcal{Z} = -\frac{1}{2\sqrt{2}\psi_0 k_0^2}$ and $\mathcal{Z} = -\frac{\pi}{2\sqrt{2}\psi_0 k_0^2}$, see Eqs. (5.56) and (5.61). Periodic boundary conditions are applied in X-direction.
Next, the domain $[-X_{\max}, X_{\max}] \times [Z_{\min}, 0]$ is discretized using the equidistant grid

$$\begin{aligned}
Z_n &:= n\Delta Z, \quad \text{for } n \in \{0, \dots, N\},\ \Delta Z = \frac{Z_{\min}}{N} < 0,\\
X_j &:= j\Delta X - X_{\max}, \quad \text{for } j \in \{0, \dots, J\},\ \Delta X = \frac{2X_{\max}}{J} > 0.
\end{aligned} \tag{5.63}$$

Finally, the grid function P is introduced with $P_j^n = P(X_j, Z_n)$, which approximates the exact solution of the complex transport equation at the grid points, i. e. $P_j^n \approx \widetilde{\psi}(X_j, Z_n)$.
The complex transport equation (5.62) is discretized on the grid defined in Eq. (5.63) by replacing all derivatives with corresponding finite difference approximations. The Z-derivative is replaced by a forward and the X-derivative by a central finite difference. This combination is standard and can be found in many

standard textbooks like [GrossmannEtAl07, Logan14]. The resulting scheme is given by

$$\frac{P_j^{n+1} - P_j^n}{\Delta Z} = -\mathrm{i}\frac{P_{j+1}^n - P_{j-1}^n}{2\Delta X}. \tag{5.64}$$

This scheme has consistency order two in X and consistency order one in Z. However, it is not stable when solving the complex transport equation. This is shown below using a von Neumann stability analysis, which is a standard and powerful tool for analyzing the stability of finite difference methods. Information about the von Neumann stability analysis can be found in many standard textbooks like [TveitoWinther98, Marsal76].
Let the numerical approximation error be defined as

$$\epsilon_j^n := P_j^n - p_j^n. \tag{5.65}$$

Here, P_j^n is the solution of Eq. (5.64) in the absence of any rounding errors, and p_j^n is the numerical solution obtained in a finite precision arithmetic. Both P_j^n and p_j^n satisfy Eq. (5.64). Therefore, the numerical error ϵ_j^n also satisfies Eq. (5.64), i. e.

$$\frac{\epsilon_j^{n+1} - \epsilon_j^n}{\Delta Z} = -\mathrm{i}\frac{\epsilon_{j+1}^n - \epsilon_{j-1}^n}{2\Delta X}. \tag{5.66}$$

Since periodic boundary conditions are assumed, ϵ_j^n can be expressed as a truncated Fourier series expansion of the form

$$\epsilon_j^n = \sum_{m=-J/2}^{J/2-1} \widehat{\epsilon}_m^n \mathrm{e}^{\mathrm{i}\mu_m X_j}, \quad \text{with } \mu_m = \frac{m\pi}{X_{\max}}. \tag{5.67}$$

Inserting Eq. (5.67) into Eq. (5.66) and considering only the m-th component of the Fourier series yields

$$\frac{\widehat{\epsilon}_m^{n+1}\mathrm{e}^{\mathrm{i}\mu_m X_j} - \widehat{\epsilon}_m^n \mathrm{e}^{\mathrm{i}\mu_m X_j}}{\Delta Z} = -\mathrm{i}\frac{\widehat{\epsilon}_m^n \mathrm{e}^{\mathrm{i}\mu_m X_{j+1}} - \widehat{\epsilon}_m^n \mathrm{e}^{\mathrm{i}\mu_m X_{j-1}}}{2\Delta X}. \tag{5.68}$$

Dividing Eq. (5.68) by $\widehat{\epsilon}_m^n \mathrm{e}^{\mathrm{i}\mu_m X_j}$ and introducing the amplification factor

$$G = \frac{\widehat{\epsilon}_m^{n+1}}{\widehat{\epsilon}_m^n} \tag{5.69}$$

yields

$$G = 1 - \mathrm{i}\frac{\Delta Z}{2\Delta X}\underbrace{\left(\mathrm{e}^{\mathrm{i}\mu_m \Delta X} - \mathrm{e}^{-\mathrm{i}\mu_m \Delta X}\right)}_{=2\mathrm{i}\sin(\mu_m \Delta X)} = 1 + \frac{\Delta Z}{\Delta X}\sin(\mu_m \Delta X). \tag{5.70}$$

The numerical scheme is stable if the error ϵ_j^n does not increase in depth Z. This is the case if $|G| < 1$ for all $\mu_m \in \mathbb{R}$. However, for each choice of ΔZ and ΔX, there exist some μ_m such that $|G| > 1$, see Eq. (5.70). Therefore, the finite

difference method from Eq. (5.64) is unstable when solving the complex transport equation.
A natural way to overcome this problem is to use other schemes to approximate $\widetilde{\psi}$ numerically. Table 5.2 lists other famous finite difference methods, which are frequently used to discretize the general transport equation $\widetilde{\psi}_Z + c\widetilde{\psi}_X = 0$ for an arbitrary constant c. These schemes can be found, for example, in [Langtangen03, LeVeque92]. The corresponding computation rule and the amplification factor $|G|$ for $c = \mathrm{i}$ are also stated in Tab. 5.2. For completeness, the first row summarizes the results for the finite difference scheme from Eq. (5.64). In order to simplify the notation, the abbreviation $\vartheta = \mu_m \Delta X$ is introduced. However, the stated amplification factors G show that all of these methods are unstable if they are applied to the complex transport equation (5.62).
To further investigate the stability of the schemes listed in Tab. 5.2, Fig. 5.6 shows the corresponding maximal value of G for $\vartheta \in [0, 2\pi]$ against $\Delta Z/\Delta X$. It has to be noted that the explicit forward and implicit forward difference scheme lead to the same amplification factors as the explicit backward and implicit backward scheme, respectively. Furthermore, the explicit forward, implicit forward, and the Leapfrog scheme lead to approximately the same values of $|G|$. Therefore, results for the implicit forward, explicit backward, implicit backward, and Leapfrog scheme are not shown in Fig. 5.6. However, Fig. 5.6 shows that all schemes listed in Tab. 5.2 result in amplification factors G with a maximal value larger than one for all $\Delta Z/\Delta X \neq 0$. Therefore, they are all unstable when solving the complex transport equation.
However, in order to compute $\widetilde{\psi}$, the complex transport equation (5.62) has to be solved numerically. Figure 5.6 shows that of all the schemes considered, the Lax-Friedrichs scheme gives the smallest value of $|G|$ for different values of $\Delta Z/\Delta X$. The question arises as to whether the Lax-Friedrichs scheme is the most suitable of the presented schemes for the discretization of the complex transport equation (5.62). This is investigated in the following:
The Lax-Friedrichs scheme can be derived from the scheme presented in Eq. (5.64) by replacing P_j^n with its spatial average, i. e. $P_j^n \approx \frac{1}{2}\left(P_{j+1}^n + P_{j-1}^n\right)$. This correction is equivalent to the introduction of numerical diffusion. In order to see this, the Lax-Friedrichs scheme is written in the form

$$\frac{P_j^{n+1} - P_j^n}{\Delta Z} + c\frac{P_{j+1}^n - P_{j-1}^n}{2\Delta X} = \frac{\Delta X^2}{2\Delta Z}\frac{P_{j+1}^n - 2P_j^n + P_{j-1}^n}{\Delta X^2}. \tag{5.71}$$

This represents a finite difference discretization of the equation

$$\widetilde{\psi}_Z + c\widetilde{\psi}_X = \frac{\Delta X^2}{2\Delta Z}\widetilde{\psi}_{XX}. \tag{5.72}$$

It can be seen that a diffusion term is introduced, which is proportional to $\frac{\Delta X^2}{2\Delta Z}$. Since the complex transport equation (5.62) does not contain such a diffusion term, numerical solutions of the Lax-Friedrichs scheme only approximate solutions of the complex transport equation (5.62) well if $\frac{\Delta X^2}{2\Delta Z}$ is small.

Table 5.2: Listing of schemes, which are frequently used to discretize the general transport equation $\widetilde{\psi}_Z + c\widetilde{\psi}_X = 0$ for an arbitrary constant c. For each scheme, the computation rules are stated. Furthermore, the corresponding amplification factors $|G|^2$ are given for $c = \mathrm{i}$ with $\vartheta = \mu_m \Delta X$.

Name of scheme	Computation rule for PDE $\widetilde{\psi}_Z + c\widetilde{\psi}_X = 0$	$\lvert G\rvert^2$ for $c = \mathrm{i}$
Explicit central difference scheme	$P_j^{n+1} = P_j^n - c\frac{\Delta Z}{2\Delta X}\left(P_{j+1}^n - P_{j-1}^n\right)$	$\left(1 + \frac{\Delta Z}{\Delta X}\sin(\vartheta)\right)^2$
Explicit forward difference scheme	$P_j^{n+1} = P_j^n - c\frac{\Delta Z}{\Delta X}\left(P_{j+1}^n - P_j^n\right)$	$\left(1 + \frac{\Delta Z}{\Delta X}\sin(\vartheta)\right)^2 + \frac{\Delta Z^2}{\Delta X^2}\left(1 - \cos(\vartheta)\right)^2$
Explicit backward difference scheme	$P_j^{n+1} = P_j^n - c\frac{\Delta Z}{\Delta X}\left(P_j^n - P_{j-1}^n\right)$	$\left(1 + \frac{\Delta Z}{\Delta X}\sin(\vartheta)\right)^2 + \frac{\Delta Z^2}{\Delta X^2}\left(1 - \cos(\vartheta)\right)^2$
Implicit central difference scheme	$P_j^{n+1} = P_j^n - c\frac{\Delta Z}{2\Delta X}\left(P_{j+1}^{n+1} - P_{j-1}^{n+1}\right)$	$1/\left[1 - \frac{\Delta Z}{\Delta X}\sin(\vartheta)\right]^2$
Implicit forward difference scheme	$P_j^{n+1} = P_j^n - c\frac{\Delta Z}{\Delta X}\left(P_{j+1}^{n+1} - P_j^{n+1}\right)$	$1/\left[\left(1 - \frac{\Delta Z}{\Delta X}\sin(\vartheta)\right)^2 + \frac{\Delta Z^2}{\Delta X^2}\left(1 - \cos(\vartheta)\right)^2\right]$
Implicit backward difference scheme	$P_j^{n+1} = P_j^n - c\frac{\Delta Z}{\Delta X}\left(P_j^{n+1} - P_{j-1}^{n+1}\right)$	$1/\left[\left(1 - \frac{\Delta Z}{\Delta X}\sin(\vartheta)\right)^2 + \frac{\Delta Z^2}{\Delta X^2}\left(1 - \cos(\vartheta)\right)^2\right]$
Lax-Wendroff scheme	$P_j^{n+1} = P_j^n - c\frac{\Delta Z}{2\Delta X}\left(P_{j+1}^n - P_{j-1}^n\right) + c^2\frac{\Delta Z^2}{2\Delta X^2}\left(P_{j+1}^n - 2P_j^n + P_{j-1}^n\right)$	$\left[1 + \frac{\Delta Z}{\Delta X}\sin(\vartheta) + \frac{\Delta Z^2}{\Delta X^2}\left(1 - \cos(\vartheta)\right)\right]^2$
Lax-Friedrichs scheme	$P_j^{n+1} = \frac{1}{2}\left(P_{j+1}^n + P_{j-1}^n\right) - c\frac{\Delta Z}{2\Delta X}\left(P_{j+1}^n - P_{j-1}^n\right)$	$\left[\cos(\vartheta) + \frac{\Delta Z}{\Delta X}\sin(\vartheta)\right]^2$
Crank-Nicolson scheme	$P_j^{n+1} = P_j^n - c\frac{\Delta Z}{4\Delta X}\left[\left(P_{j+1}^{n+1} - P_{j-1}^{n+1}\right) + \left(P_{j+1}^n - P_{j-1}^n\right)\right]$	$\left[\left(1 + \frac{\Delta Z}{2\Delta X}\sin(\vartheta)\right) / \left(1 - \frac{\Delta Z}{2\Delta X}\sin(\vartheta)\right)\right]^2$
Leapfrog scheme	$P_j^{n+1} = P_j^{n-1} - c\frac{\Delta Z}{\Delta X}\left(P_{j+1}^n - P_{j-1}^n\right)$	$\left[\frac{\Delta Z}{\Delta X}\sin(\vartheta) \pm \sqrt{\left(\frac{\Delta Z}{\Delta X}\sin(\vartheta)\right)^2 + 1}\right]^2$

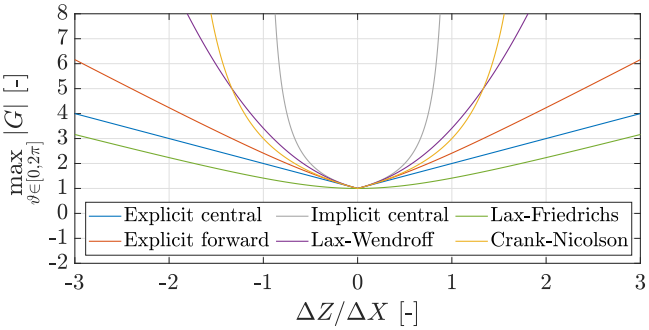

Figure 5.6: Amplification factor $|G|$ for different schemes, which are applied to the complex transport equation (5.62). The maximal value of $|G|$ for $\vartheta \in [0, 2\pi]$ is shown against $\Delta Z/\Delta X$.

On the other side, the value of $\Delta Z/\Delta X$ should be small such that the amplification factor G becomes small, see Fig. 5.6. Going from Z_n to $Z_{\mathrm{n+1}}$, it has to be remembered that numerical errors are amplified by $|G|$. Therefore, going from $Z = 0$ to $Z = Z_{\max}$, errors in the IC at $Z = 0$ are amplified in total by a factor of $|G|^{|Z_{\max}/\Delta Z|} = |G|^N$. For a given maximal depth $Z_{\max}$, this means that N has to be small to obtain only small numerical errors. However, this also means that ΔZ must be large. As the value of $\frac{\Delta Z}{\Delta X}$ should also be small, it must hold $\Delta X > \Delta Z$. However, this also means that the diffusion coefficient $\frac{\Delta X^2}{2\Delta Z}$, which appears in the Lax-Friedrichs scheme given by Eq. (5.71), becomes large. In this case, however, numerical solutions of Lax-Friedrichs scheme do not approximate the solutions of the complex transport equation (5.62) very well. Therefore, the Lax-Friedrichs scheme should not be used to approximate solutions of the complex transport equation (5.62).
Looking again at Fig. 5.6, it can be seen that the explicit central difference scheme from Eq. (5.64) offers the second smallest amplification factor of all studied numerical schemes after the Lax-Friedrichs scheme. Therefore, the explicit central difference scheme from Eq. (5.64) is used in this thesis to solve Eq. (5.62) numerically. However, the values of ΔX and ΔZ have to be chosen with care. If these values are too large, the consistency error $\mathcal{O}(\Delta Z + \Delta X^2)$ will also become large. If $\Delta Z/\Delta X$ is too large, the amplification factor $|G|$ becomes large, and rounding errors will significantly affect the behavior of the numerical solution. If ΔZ is too small, the effect of rounding errors will also significantly affect the solution behavior, since $|Z_{\max}/\Delta Z| = N$ and thus $|G|^N$ will become large. Therefore, the values of ΔX and ΔZ have to be chosen with care.

5.6 Benjamin-Feir Instability

In Sect. 5.5, numerical instabilities that occur in the computation of the velocity potential ϕ corresponding to the NLS (5.2) have been investigated. In this section, the stability of propagating water waves is discussed.

It is a common experience in the laboratory that a regular wave train with relatively steep water waves is difficult to maintain in a long wave tank [Mei83]. This difficulty was explained theoretically by Benjamin and Feir [BenjaminFeir67], who found that Stokes waves are unstable to sideband disturbances. These are disturbances whose frequencies deviate slightly from the fundamental frequency of the carrier waves. The instability of Stokes waves to sideband disturbances is also known as Benjamin-Feir instability and has been found in an enormous amount of experimental and theoretical investigations, see e.g. [TulinWaseda99, OnoratoEtAl01, DeconinckOliveras11, Akers15].

The Benjamin-Feir instability may also be the reason for the high occurrence of rogue waves. Although a superposition of many regular waves, like in Sect. 2.2.2, can generate extremely high waves, it has been noticed that rogue waves occur more often than such a linear theory predicts, see e.g. [OnoratoEtAl04, OnoratoEtAl06]. Instead, it is nowadays believed that the nonlinear effect of the Benjamin-Feir instability of deep-water wave trains is the main reason why the occurrence of rogue waves is so high compared to the predictions of the linear wave theory [SlunyaevEtAl13b].

The Benjamin-Feir instability is briefly sketched in this section by means of a stability analysis of the NLS (5.2). The corresponding stability analysis is based on [YuenLake82, Mei83, Osborne10]. The results of this analysis are needed to explain the temporal behavior of solutions of the NLS (5.2), which are perturbed by irregular sea surfaces in the following sections.

The plane-wave solution of the NLS (5.2) is given by Eq. (5.40). In the following, for $k_{\mathrm{pw}} = 0$, the plane-wave solution from Eq. (5.40) is perturbed using a sideband perturbation of the form

$$\psi(X,T) = \underbrace{\psi_0 \mathrm{e}^{-\mathrm{i}\delta\psi_0^2 T}}_{\text{plane-wave solution}} + \gamma(X,T)\mathrm{e}^{-\mathrm{i}\delta\psi_0^2 T} = \left[\psi_0 + \gamma(X,T)\right]\mathrm{e}^{-\mathrm{i}\delta\psi_0^2 T}, \quad (5.73)$$

whereby

$$\gamma(X,T) := \gamma_+ \mathrm{e}^{\mathrm{i}\omega_{\mathrm{mod}}T + \mathrm{i}k_{\mathrm{mod}}\left(X - c_{\mathrm{gr}}T\right)} + \gamma_- \mathrm{e}^{\mathrm{i}\omega_{\mathrm{mod}}T - \mathrm{i}k_{\mathrm{mod}}\left(X - c_{\mathrm{gr}}T\right)}. \quad (5.74)$$

Such a perturbation has also been used, for example, in [Osborne10, Chabchoub13]. Using Eq. (5.73), the plane-wave solution from Eq. (5.40) is perturbed by the term $\gamma(X,T)\mathrm{e}^{-\mathrm{i}\delta\psi_0^2 T}$. The perturbation is described by the small modulation amplitudes $\gamma_\pm$, the modulation wave number k_{mod}, and the modulation wave frequency ω_{mod}.

Substituting Eq. (5.73) into the NLS (5.2), a linearization results in the modulation dispersion relation, see [Osborne10],

$$\omega_{\mathrm{mod}}^2 = \frac{\omega_0^2}{8k_0^2}\left(\frac{k_{\mathrm{mod}}^2}{8k_0^2} - k_0^2\psi_0^2\right)k_{\mathrm{mod}}^2. \tag{5.75}$$

The perturbed wave from Eq. (5.73) becomes unstable if ω_{mod} is imaginary. This is the case for

$$0 < k_{\mathrm{mod}} < 2\sqrt{2}k_0^2\psi_0. \tag{5.76}$$

In terms of the so-called Benjamin-Feir parameter

$$I_{\mathrm{BF}} = \frac{2\sqrt{2}k_0^2\psi_0}{k_{\mathrm{mod}}}, \tag{5.77}$$

the nonlinear modes of the NLS become unstable if $I_{\mathrm{BF}} > 1$, which leads to an exponential growth of the perturbed solution. The growth rate is given by the imaginary part of ω_{mod}. The growth rate is zero for $k_{\mathrm{mod}} = 0$ and $k_{\mathrm{mod}} \geq 2\sqrt{2}k_0^2\psi_0$, and gets maximal for $k_{\mathrm{mod}} = 2k_0^2\psi_0$ with $\omega_{\mathrm{mod}} = \pm\frac{1}{2}\mathrm{i}\omega_0 k_0^2\psi_0^2$.
In other words, if the wave envelope is disturbed by a sideband perturbation as in Eq. (5.73) and the corresponding modulation wave number k_{mod} is too small, i. e. $k_{\mathrm{mod}} \in (0, 2\sqrt{2}k_0^2\psi_0)$, the perturbation grows exponentially with time. Therefore, a small amplitude modulation in the far past evolves into an extreme wave event in the present [Osborne10].
In the following, the described instability is illustrated. Therefore, the temporal behavior of the perturbed plane-wave solution from Eq. (5.73) is calculated using the ReSP scheme presented in Sect. 5.4. Here, the perturbed plane-wave solution at $T = 0$ is taken as IC using $k_0 = 0.5\,\mathrm{m}^{-1}$, $\psi_0 = 2\,\mathrm{m}$, $\varepsilon = 0.1$, $\gamma_\pm = 0.01\,\mathrm{m}$, and different modulation wave numbers k_{mod}. The corresponding unperturbed solution is shown in Fig. 5.3. Figure 5.7 shows the respective temporal behaviors of the perturbed solution for $k_{\mathrm{mod}} = 1\,\mathrm{m}^{-1}$ and $k_{\mathrm{mod}} = 2\,\mathrm{m}^{-1}$ with respect to the moving coordinate $\zeta = x - c_{\mathrm{gr}}t$. While $k_{\mathrm{mod}} = 2\,\mathrm{m}^{-1}$ leads to $I_{\mathrm{BF}} = 0.71$ and a stable behavior, $k_{\mathrm{mod}} = 1$ results in $I_{\mathrm{BF}} = 1.41$ and an unstable solution. An exponential growth of the solution can be observed. However, it can be seen that the solution does not grow for all times but increases to a maximum value and decrease for later times. This oscillation repeats periodically over time. It has already been observed in different experimental and numerical studies and is known as the Fermi-Pasta-Ulam recurrence phenomenon [YuenLake80, Osborne10], which has been first discovered in [FermiEtAl55].
Finally, the effect of the Benjamin-Feir instability on the Peregrine breather and soliton solution is investigated. Therefore, the temporal behavior of the corresponding perturbed solutions is calculated using the ReSP scheme presented in Sect. 5.4. As IC, the function $\psi_{\mathrm{IC,perturb}}(X)$ is used, which is defined by

$$\psi_{\mathrm{IC,perturb}}(X) := \left(1 + \frac{\gamma(X,0)}{\psi_0}\right)\psi(X,T_0). \tag{5.78}$$

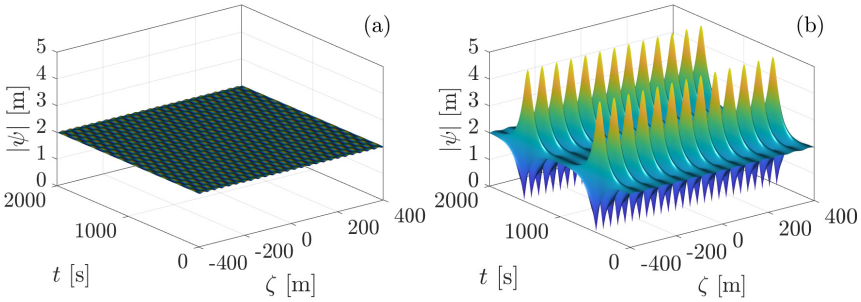

Figure 5.7: Perturbation of the wave envelope of the plane-wave solution using different modulation wave numbers k_{mod}. (a): $k_{\mathrm{mod}} = 2\,\mathrm{m}^{-1}$, resulting to $I_{\mathrm{BF}} = 0.71$. (b): $k_{\mathrm{mod}} = 1\,\mathrm{m}^{-1}$, resulting to $I_{\mathrm{BF}} = 1.41$.

The perturbation function γ is given by Eq. (5.74), whereby a modulation amplitude of $\gamma_{\pm} = 0.01\,\mathrm{m}$ is used. In Eq. (5.78), the wave envelope ψ is given by the respected analytical solutions from Eq. (5.44) and Eq. (5.45) with $k_0 = 0.5\,\mathrm{m}^{-1}$, $\psi_0 = 1.5\,\mathrm{m}$, and $\varepsilon = 0.1$. The unperturbed wave envelope ψ is evaluated at some time point T_0 and the perturbation γ is evaluated at $T = 0$. Here, the perturbation γ is evaluated at $T = 0$, such that an initial exponential growth resulting from a possible imaginary modulation frequency ω_{mod} is not considered. The time point T_0 is chosen as $T_0 = -500\,\mathrm{s}$ for the case of the Peregrine breather solution and $T_0 = 0$ for the soliton solution.
Corresponding numerical results for the perturbed Peregrine breather and soliton solution are depicted in Figs. 5.8 and 5.9. In both cases, modulation wave numbers of $k_{\mathrm{mod}} = 0.5\,\mathrm{m}^{-1}$ and $k_{\mathrm{mod}} = 2\,\mathrm{m}^{-1}$ are used, which result in a Benjamin-Feir parameter of $I_{\mathrm{BF}} = 2.12$ and $I_{\mathrm{BF}} = 0.53$, respectively. It can be seen that a Benjamin-Feir parameter of $I_{\mathrm{BF}} = 2.12$ leads to an unstable temporal behavior of the Peregrine breather solution. However, as in the case of the plane-wave solution, this instability does not grow for all times but increases to a maximum value and decreases for later times. In comparison, the temporal behavior of the perturbed soliton solution does not show an instability for both used modulation wave numbers k_{mod} and resulting Benjamin-Feir parameters I_{BF}. Therefore, the soliton solution from Eq. (5.45) is stable against modulation instabilities. Further details about the instabilities of deep water waves can be found, for example, in [YuenLake80].

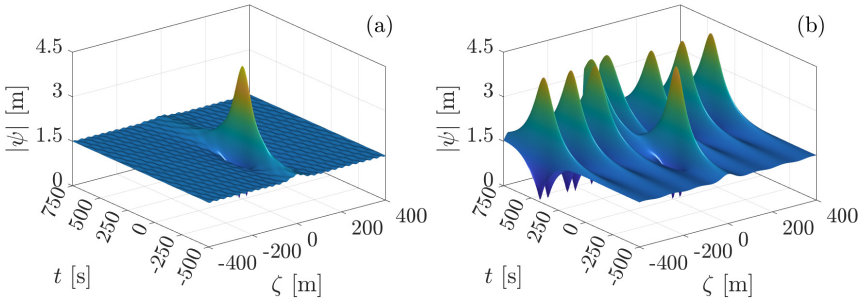

Figure 5.8: Perturbation of the wave envelope of the Peregrine breather solution using different modulation wave numbers k_{mod}. (a): $k_{\mathrm{mod}} = 2\,\mathrm{m}^{-1}$, resulting to $I_{\mathrm{BF}} = 0.53$. (b): $k_{\mathrm{mod}} = 0.5\,\mathrm{m}^{-1}$, resulting to $I_{\mathrm{BF}} = 2.12$.

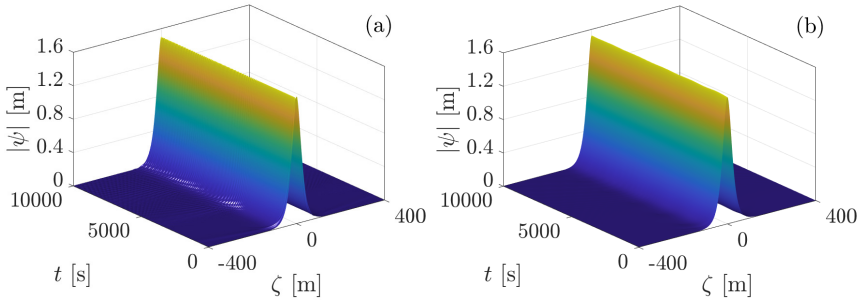

Figure 5.9: Perturbation of the wave envelope of the soliton solution using different modulation wave numbers k_{mod}. (a): $k_{\mathrm{mod}} = 2\,\mathrm{m}^{-1}$, resulting to $I_{\mathrm{BF}} = 0.53$. (b): $k_{\mathrm{mod}} = 0.5\,\mathrm{m}^{-1}$, resulting to $I_{\mathrm{BF}} = 2.12$.

5.7 Perturbation of Solutions of the NLS

In Sect. 5.4, the ReSP scheme for the numerical computation of solutions of the NLS (5.2) is presented. Here, an IC $\psi_{\mathrm{IC}}(X) = \psi(X, 0)$ has to be given. The IC can be generated, for example, using the analytical solutions of the NLS (5.2), which have been presented in Sect. 5.3. However, in contrast to the water waves corresponding to the introduced analytical solutions of the NLS, real water waves are irregular. In this section, it is presented how an irregular sea state can be modeled using the NLS by adding an irregular sea surface to the IC ψ_{IC}.
In Sect. 2.2.2, it has been introduced how realistic random water waves can be modeled by the superposition of many regular water waves. Let $\eta_{\mathrm{LC}}(x, y, t)$ be the sea surface displacement of a corresponding long-crested random water wave. For sim-

plification, it is assumed that the main direction of progress of the waves is $\chi_0 = 0$. Based on Eq. (2.28), the sea surface displacement $\eta_{\mathrm{LC}}(x, y, t) = \eta_{\mathrm{LC}}(x, t)$ of a random water wave is given by

$$\eta_{\mathrm{LC}}(x,t) = \sum_{m=1}^{M_\omega} \cos(k(\omega_m)x - \omega_m t + \beta(\omega_m))\sqrt{2S(\omega_m)\Delta\omega_m}. \tag{5.79}$$

Again, the spectrum $S(\omega)$ is discretized in M_ω parts with respective widths $\Delta\omega_m$ and frequencies $\omega_m \in [\omega_{\min}, \omega_{\max}]$, which do not need to be equidistant.
In order to obtain a perturbed IC $\psi_{\mathrm{IC,perturb}}$ from an analytical solution ψ of the NLS (5.2), the phase and the amplitude of ψ have to be adjusted. In this thesis, the adjustment is simplified by only perturbing the amplitude of ψ, whereby the approach originally presented in [HollmEtAl21, HollmEtAl22b] is used. Here, based on some unperturbed IC ψ_{IC} of the NLS (5.2), the corresponding perturbed IC $\psi_{\mathrm{IC,perturb}}$ is given by

$$\psi_{\mathrm{IC,perturb}}(X) = \left(1 + \frac{\eta_{\mathrm{LC}}(x(X),0)}{|\psi_{\mathrm{IC}}(X)|}\right)\psi_{\mathrm{IC}}(X), \quad \text{with } x(X) = X/\varepsilon. \tag{5.80}$$

Using this approach, the amplitude of ψ_{IC} is perturbed by η_{LC}. It results

$$|\psi_{\mathrm{IC,perturb}}(X)| = ||\psi_{\mathrm{IC}}(X)| + \eta_{\mathrm{LC}}(x(X),0)|. \tag{5.81}$$

Therefore, the amplitude of $\psi_{\mathrm{IC,perturb}}$ is given by the absolute value of the sum of the amplitude of the unperturbed wave envelope ψ_{IC} and the perturbation $\eta_{\mathrm{LC}}(X, 0)$. Using Eq. (5.80), $\psi_{\mathrm{IC,perturb}}$ and ψ_{IC} differ in their amplitude, but not in their phase angles. This means that $\psi_{\mathrm{IC,perturb}}$ and ψ_{IC} do have the same phase angles. Figure 5.10 visualizes this by showing the values of $\psi_{\mathrm{IC,perturb}}(X_0)$ and $\psi_{\mathrm{IC}}(X_0)$ at some given point X_0 in the complex plane.
Figure 5.11a shows the sea surface displacement $\eta_{\mathrm{LC}}(x, 0)$ of a random water wave calculated by means of Eq. (5.79), which is generated using the Pierson-Moskowitz spectrum S_{PM} from Eq. (2.23) with peak frequency $\omega_{\mathrm{p}} = 0.25\,\mathrm{rad/s}$ and significant wave height $H_{\mathrm{s}} = 1\,\mathrm{m}$. The effect of this perturbation on the Peregrine breather solution with wave number $k_0 = 0.5\,\mathrm{m}^{-1}$, amplitude $\psi_0 = 1.5\,\mathrm{m}$, and wave steepness $\varepsilon = 0.1$ is shown in Fig. 5.11b. It can be seen that the sea surface displacement η_{LC}, which has been used to perturb the Peregrine breather solution of the NLS, can be found directly in the amplitude of the perturbed IC $\psi_{\mathrm{IC,perturb}}$. It has to be noted that the perturbation of ψ by an irregular sea surface with significant wave height H_{s} results in a sea surface displacement η, which is perturbed by an irregular sea with significant wave height $\varepsilon H_{\mathrm{s}}$ due to the parameterization of Eq. (5.5).

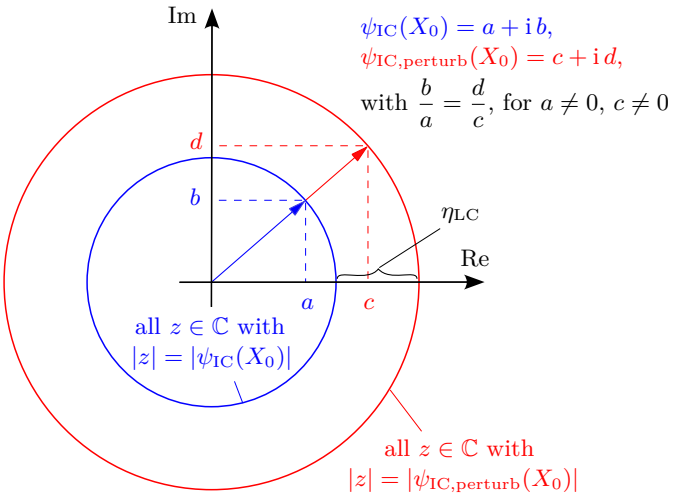

Figure 5.10: Values of ICs $\psi_{\mathrm{IC}}(X_0)$ and $\psi_{\mathrm{IC,perturb}}(X_0)$ at some given point X_0, shown in the complex plane.

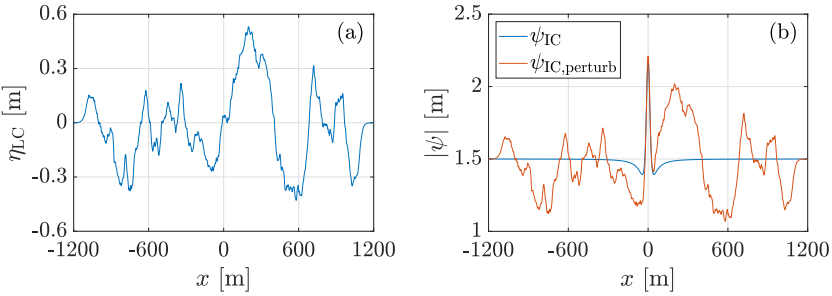

Figure 5.11: (a): Example of the sea surface displacement $\eta_{\mathrm{LC}}(x, 0)$ of a long-crested random water wave. (b): Comparison of an IC with and without the irregular perturbation shown in (a).

5.8 Particle Trajectories

In this section, the effect of the irregularity introduced by the IC $\psi_{\mathrm{IC,perturb}}$ from Eq. (5.80) on the temporal behavior of solutions of the NLS is studied. This is done by investigating the temporal behavior of trajectories of water particles, which move due to the motion of water waves corresponding to solutions of the NLS. Furthermore, the contribution of the different orders of the incident

velocity potentials $\phi_0^{(i)}$ on the overall dynamics of the water waves and the trajectories of water particles is investigated. Since the hydrodynamic forces acting on a mechanical structure result from the corresponding hydrodynamic pressure, an investigation of the trajectories of the water particles gives first insights into the temporal behavior of the forces acting on the structure.
In this section, the Peregrine breather and soliton solution of the NLS, which have been introduced in Sect. 5.3, are considered for $k_0 = 0.5\,\mathrm{m}^{-1}$, $\psi_0 = 1.5\,\mathrm{m}$ and $\varepsilon = 0.1$. The effects of an initial perturbation by an irregular sea surface are investigated. The corresponding sea surface displacements $\eta_{\mathrm{LC}} = \eta_{\mathrm{LC}}(x, 0)$ are calculated using the Pierson-Moskowitz spectrum S_{PM} from Eq. (2.23) with peak frequency $\omega_{\mathrm{p}} = 0.25\,\mathrm{rad/s}$ and different significant wave heights H_{s}. Here, it has to be mentioned that the numerical scheme presented in Sect. 5.4 assumes a periodic IC. In order to make the perturbed IC $\psi_{\mathrm{IC,perturb}}$ periodic in X, the value of η_{LC} is set to zero at the boundaries of the considered spatial domain by multiplying η_{LC} with appropriate $\tanh(X)$ functions. Figure 5.11a depicts the sea surface displacements $\eta_{\mathrm{LC}}(X, 0)$ of a resulting random water wave.
All numerical solutions are computed using the ReSP scheme presented in Sect. 5.4, which is applied on the spatial domain $X \in [-120\,\mathrm{m}, 120\,\mathrm{m}]$ using $J + 1 = 2^{11} + 1$ spatial grid points. This leads to a spatial step size of $\Delta X = 240\,\mathrm{m}/2^{11} = 0.117\,\mathrm{m}$. The results for the Peregrine breather and soliton solution are computed on the time domain $T \in [-20\,\mathrm{s}, 20\,\mathrm{s}]$ and $T \in [0, 40\,\mathrm{s}]$, respectively. The corresponding time domains are discretized using $N + 1 = 8001$ temporal grid points, which leads to a temporal step size of $\Delta T = 40\,\mathrm{s}/8000 = 0.005\,\mathrm{s}$. To calculate the corresponding velocity potential ϕ, the auxiliary variable $\widetilde{\psi}$ is computed numerically. Here, the complex transport equation (5.11) is solved numerically using the scheme introduced in Eq. (5.64), which is applied on the spatial domain $Z \in [-0.7\,\mathrm{m}, 0]$ using $N + 1 = 29$ spatial grid points. This leads to a step size of $\Delta Z = -0.7\,\mathrm{m}/28 = -0.025\,\mathrm{m}$ in Z-direction.
It has to be noted that T, X, and Z denote the slow temporal and spatial coordinates. These coordinates can be computed from t, x, z by $T = \varepsilon t$, $X = \varepsilon x$, and $Z = \varepsilon z$, see Eqs. (5.1) and (5.9). Therefore, since $\varepsilon = 0.1$ is used in this section, all results shown in this section are presented for the spatial domain $x \in [-1200\,\mathrm{m}, 1200\,\mathrm{m}]$, $z \in [-7\,\mathrm{m}, 0]$ and the time domains $t \in [-200\,\mathrm{s}, 200\,\mathrm{s}]$ and $t \in [0, 400\,\mathrm{s}]$.

5.8.1 Behavior of the Unperturbed and Perturbed Peregrine Breather Solution

First, the effect of the irregularity introduced by the IC from Eq. (5.80) on the temporal behavior of the Peregrine breather solution is studied. Therefore, the NLS (5.2) is solved numerically, whereby the unperturbed and perturbed IC shown in Fig. 5.11b are used. Here, the perturbed IC $\psi_{\mathrm{IC,perturb}}$ is computed using

an irregular sea surface displacement η_{LC} with significant wave height $H_{\mathrm{s}} = 1\,\mathrm{m}$. The corresponding numerical solutions are compared in Fig. 5.12. Although fluctuations in the amplitude can be observed, it is shown that the Peregrine breather solution can clearly be identified in the considered temporal domain. However, it can also be observed that the fluctuations are increasing in time. At the end of the considered time domain at $t = 200\,\mathrm{s}$, the fluctuations even become larger than the peak amplitude of the unperturbed Peregrine breather solution at $t = 200\,\mathrm{s}$. Therefore, the structure of the Peregrine breather solution is destroyed for larger times. The solution behavior is unstable against the induced irregularity. This effect has already been observed in Sect. 5.6, where the Benjamin-Feir instability has been considered. There, it has been shown that the Peregrine breather is unstable for small sideband perturbations.
It has to be noted that Fig. 5.12b shows only one realization of the Peregrine breather solution, which is initially perturbed by an irregular sea surface. Different realizations of the corresponding irregular sea surface would lead to different temporal behaviors of the perturbed Peregrine breather solution.
In order to investigate the effect of the introduced irregular perturbation on the fluid dynamics, the temporal behavior of different particle trajectories is investigated. Since the gradient of the velocity potential, $\boldsymbol{\nabla}\phi$, computes the velocity of the water at any point in the water domain, the trajectory $(x(t), z(t))$ of a water particle starting at $(x(0) = x_0, z(0) = z_0)$ is described by

$$\begin{aligned} \frac{\mathrm{d}x}{\mathrm{d}t} &= \frac{\partial\phi}{\partial x}(x(t), z(t), t), \\ \frac{\mathrm{d}z}{\mathrm{d}t} &= \frac{\partial\phi}{\partial z}(x(t), z(t), t). \end{aligned} \tag{5.82}$$

Here, ϕ is the velocity potential of the NLS, which can be computed from the wave envelope ψ using Eq. (5.8). Equation (5.82) is solved using the classical Runge-Kutta fourth order method. Figure 5.13a shows the paths of water particles

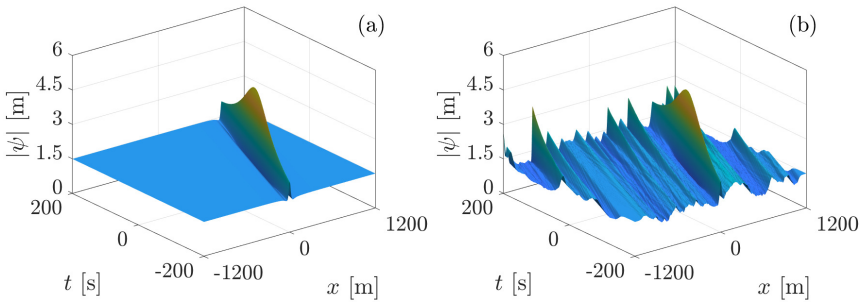

Figure 5.12: Comparison of the temporal behavior of the wave envelope of the Peregrine breather solution (a) without and (b) with an initial perturbation η_{LC}, which is generated using a significant wave height of $H_{\mathrm{s}} = 1\,\mathrm{m}$.

during the propagation of the unperturbed Peregrine breather solution presented in Fig. 5.12a. The water particles are starting at $x_0 = 442.94\,\mathrm{m}$ and heights going from $z_0 = -0.5\,\mathrm{m}$ to $z_0 = -6.5\,\mathrm{m}$. With the chosen value of x_0, the water particles start at the x-position where the analytical Peregrine breather solution reaches its maximal peak amplitude. For the background waves of the Peregrine breather solution, the particles move in ellipsoidal orbits with a drift in the positive x-direction. As is shown in Fig. 5.13a, this horizontal drift decays exponentially in z. The ellipsoidal paths get larger when the peak amplitude of the Peregrine breather solution reaches the water particles. In order to show this in a better way, Fig. 5.13b presents the trajectory of the water particle starting at $(x_0, z_0) = (442.94\,\mathrm{m}, -0.5\,\mathrm{m})$ during the propagation of the Peregrine breather solution without an initial irregular perturbation.
Next, the effect of the introduced irregular perturbation on the fluid dynamics is examined. Figure 5.13c shows the path of a water particle starting at the same initial position as before, but during the propagation of the perturbed Peregrine breather solution shown in Fig. 5.12b. It can be seen that due to the induced irregularity, the temporal behavior of the particle trajectory changes. Furthermore, after the peak amplitude of the perturbed Peregrine breather

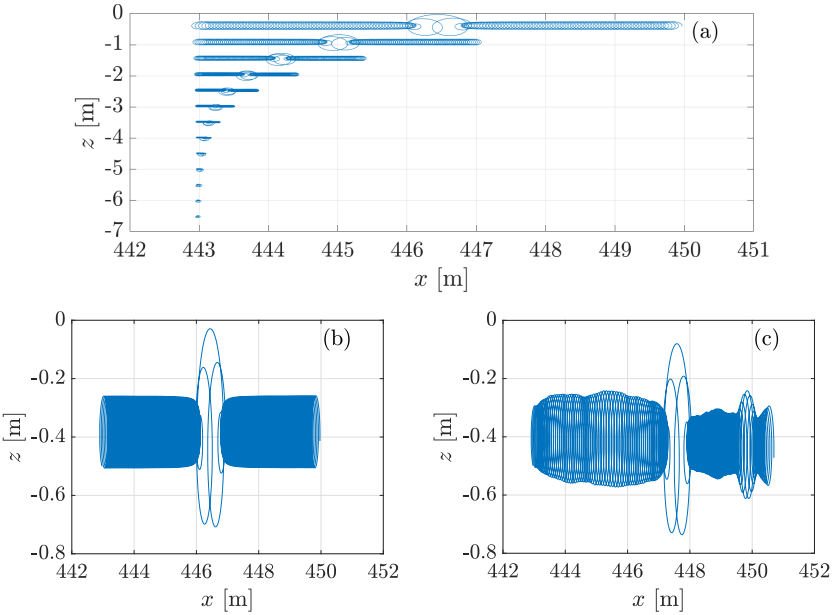

Figure 5.13: Particle trajectories during the propagation of the Peregrine breather solution (a)-(b) without and (c) with an initial perturbation η_{LC}, which is generated using a significant wave height of $H_{\mathrm{s}} = 1\,\mathrm{m}$.

solution reaches water particle, the ellipsoidal path gets larger once again at the location around $x = 450\,\mathrm{m}$. This is due to the fluctuations, which can be observed in the solution behavior presented in Fig. 5.12b.
It has to be noted that Figs. 5.12 and 5.13 show results corresponding to the Peregrine breather solution, which is initially perturbed by an irregular sea surface with significant wave height $H_\mathrm{s} = 1\,\mathrm{m}$. The question arises about how the results change with a different value of H_s. Therefore, Fig. 5.14 shows the temporal behavior of the Peregrine breather solution and the corresponding particle trajectories if the IC is perturbed by a realization of an irregular sea surface with significant wave height $H_\mathrm{s} \in \{0.3\,\mathrm{m}, 0.75\,\mathrm{m}, 1.5\,\mathrm{m}, 2\,\mathrm{m}\}$. Compared to the background amplitude $\psi_0 = 1.5\,\mathrm{m}$ of the used analytical Peregrine breather solution, this corresponds to a relative perturbation of the IC of about $H_\mathrm{s}/\psi_0 = \{20\,\%, 50\,\%, 100\,\%, 133\,\%\}$. It can be seen that the fluctuations in ψ increase faster in time for larger values of H_s. Corresponding to this, the temporal behavior of the considered water particle starting at $(x_0, z_0) = (442.94\,\mathrm{m}, -0.5\,\mathrm{m})$ experience larger changes for larger values of H_s. Furthermore, the induced perturbation can lead to larger shifts of the water particles in the horizontal direction for larger values of H_s. This becomes obvious when comparing Figs. 5.14b and 5.14f. Therefore, it can be concluded that the perturbation of the Peregrine breather solution of the NLS (5.2) considerably influences the corresponding water wave dynamics. In Sect. 7.2, it is shown how this influences the dynamics of the WEC presented in Sect. 3.1.

5.8.2 Behavior of the Unperturbed and Perturbed Soliton Solution

After investigating the influence of an initial perturbation on the temporal behavior of the Peregrine breather solution, the temporal behavior of the soliton solution in the presence of a perturbation introduced in the IC from Eq. (5.80) is studied in this section. Here, a soliton solution with $k_0 = 0.5\,\mathrm{m}^{-1}$, $\psi_0 = 1.5\,\mathrm{m}$, and $\varepsilon = 0.1$ is considered. Figure 5.15 shows the corresponding temporal behavior of the soliton solution without and with an initial irregular perturbation η_LC. Here, the irregular perturbation η_LC is generated using the Pierson-Moskowitz spectrum S_PM from Eq. (2.23) with peak frequency $\omega_\mathrm{p} = 0.25\,\mathrm{rad/s}$ and significant wave height $H_\mathrm{s} = 1\,\mathrm{m}$. It can be seen that the initial irregular perturbation does not destroy the structure of the soliton solution. Especially, no time-increasing fluctuations can be observed. This agrees with the results presented in Sect. 5.6, where it has been shown that the soliton solution is stable against sideband perturbations.
The influence of the initial perturbation on the trajectory of a water particle is shown in Fig. 5.16. Here, the water particle starts at $(x_0, z_0) = (442.94\,\mathrm{m}, -0.5\,\mathrm{m})$. It can be observed that the introduced perturbation leads to small motions of the

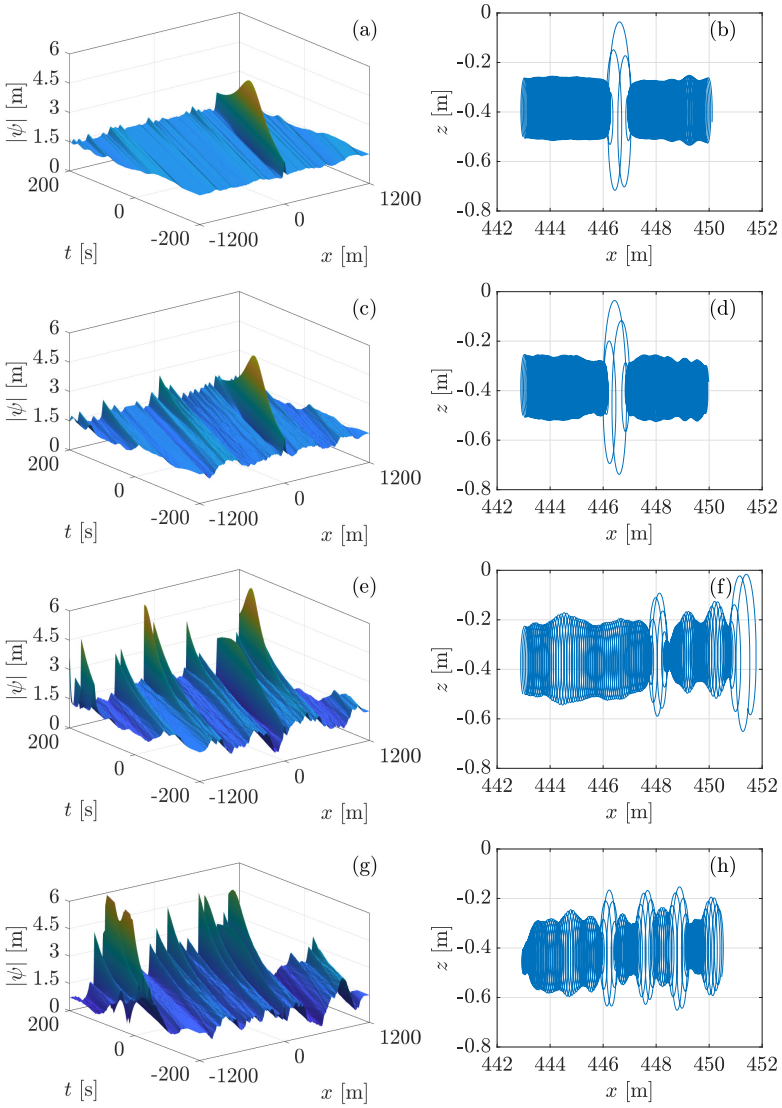

Figure 5.14: Comparison of the temporal behavior of the wave envelope of the Peregrine breather solution and particle trajectories, considering initial irregular perturbations η_{LC} with different significant wave heights H_{s}. (a)-(b): $H_{\mathrm{s}} = 0.3\,\mathrm{m}$, (c)-(d): $H_{\mathrm{s}} = 0.75\,\mathrm{m}$, (e)-(f): $H_{\mathrm{s}} = 1.5\,\mathrm{m}$, (g)-(h): $H_{\mathrm{s}} = 2\,\mathrm{m}$.

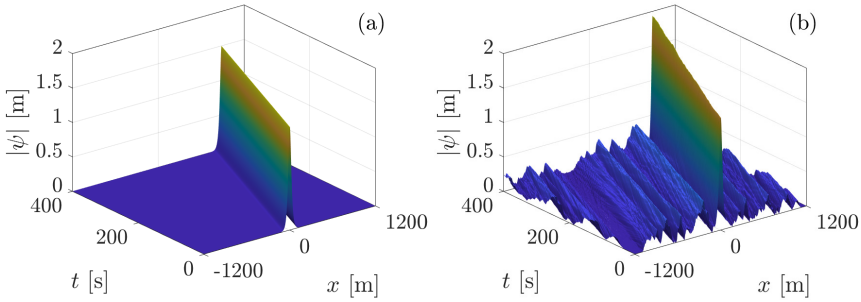

Figure 5.15: Comparison of the temporal behavior of the wave envelope of the soliton solution (a) without and (b) with an initial perturbation η_{LC}, which is generated using a significant wave height of $H_{\mathrm{s}} = 1\,\mathrm{m}$.

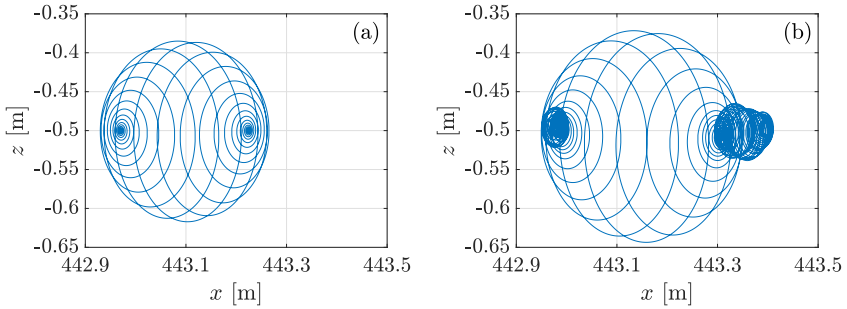

Figure 5.16: Particle trajectories during the propagation of the soliton solution (a) without and (b) with an initial perturbation η_{LC}, which is generated using a significant wave height of $H_{\mathrm{s}} = 1\,\mathrm{m}$.

water particle before and after the main amplitude of the soliton solution reaches the water particle. Regarding the wave excitation of a prescribed mechanical structure, this would lead to small hydrodynamic forces acting on the structure over the whole time domain. Furthermore, since the perturbation leads to a larger maximal amplitude of the soliton solution, the water particle experiences larger vertical and horizontal displacements.

Next, it is observed how the soliton solution behaves in the presence of initial irregular perturbations η_{LC}, which are generated using different significant wave heights H_{s}. Figure 5.17 shows the soliton solution, which is initially perturbed by irregular sea surface displacements η_{LC} with significant wave height $H_{\mathrm{s}} \in \{0.3\,\mathrm{m}, 0.75\,\mathrm{m}, 1.5\,\mathrm{m}, 2\,\mathrm{m}\}$. Furthermore, Fig. 5.17 shows the corresponding particle trajectories of water particles starting at $(x_0, z_0) = (442.94\,\mathrm{m}, -0.5\,\mathrm{m})$. It can be observed that a perturbation does not necessarily lead to a larger

maximal amplitude of the soliton solution. Moreover, the structure of the soliton solution is clearly visible for smaller significant wave heights H_s. However, this changes for larger values of H_s, for which the perturbation can be as large as the amplitude $\psi_0 = 1.5\,\mathrm{m}$ of the used unperturbed soliton solution shown in Fig. 5.15a. Moreover, it is shown that the maximal displacements of the water particles in horizontal and vertical directions significantly change depending on the corresponding irregular sea surface, which is used to perturb the IC. Therefore, the considered initial perturbation of the soliton solution can also significantly affect the hydrodynamic forces, which act on structures floating in the corresponding water waves. This is investigated in more detail in Sect. 7.3, where the FSI between water waves corresponding to the soliton solution and the WEC presented in Sect. 3.1 is studied.
It has to be noted that in contrast to the study about the Peregrine breather solution, none of the numerical solutions presented in Fig. 5.17 shows rapidly increasing fluctuations. However, not all perturbed soliton solutions show a stable temporal behavior. For example, Fig. 5.18a shows the temporal behavior of a soliton solution, which has been initially perturbed by an irregular sea surface with significant wave height $H_\mathrm{s} = 3\,\mathrm{m}$. The corresponding trajectory of a water particle starting at $(x_0, z_0) = (442.94\,\mathrm{m}, -0.5\,\mathrm{m})$ is shown in Figure 5.18b. It is shown that the initial fluctuations at $t = 0$ increase rapidly in time. Such behavior can already be observed for smaller values of H_s. However, in order not to make the scope of this study too extensive, a study on the occurrence of rapidly increasing fluctuations for different significant wave heights H_s of the corresponding irregular sea surfaces is not included here.

5.8.3 Influence of Different Orders of the Velocity Potential

Given the wave envelope ψ, the corresponding velocity potential ϕ can be computed using Eq. (5.8). It can be seen that ϕ consists of components $\phi^{(i)}$, whereby the first three components $\phi^{(1)}$, $\phi^{(2)}$, and $\phi^{(3)}$ are given by Eq. (5.27). However, in Sect. 5.2.2, it has been shown that a FSI between a structure and nonlinear water waves corresponding to the NLS can only be computed accurately up to an error of order $\mathcal{O}(\varepsilon^3)$. Here, it has been shown that it is enough to use only the first two components $\phi^{(1)}$ and $\phi^{(2)}$ of the velocity potential ϕ to compute the FSI accurately up to an error of order $\mathcal{O}(\varepsilon^3)$. The third-order component $\phi^{(3)}$ will not lead to a higher accuracy for the FSI. However, if $\phi^{(3)}$ is used in addition to the first two components $\phi^{(1)}$ and $\phi^{(2)}$ of the velocity potential ϕ, the dynamics of the water waves corresponding to the NLS can be described accurately up to an error of order $\mathcal{O}(\varepsilon^4)$ instead of an error of order $\mathcal{O}(\varepsilon^3)$, see Fig. 5.2. The question is whether the third-order velocity potential $\phi^{(3)}$ nevertheless has a significant effect on the dynamics of the water waves or not.
In this section, it is studied how the overall dynamics of the water waves corresponding to the NLS change if only the first two components of the velocity

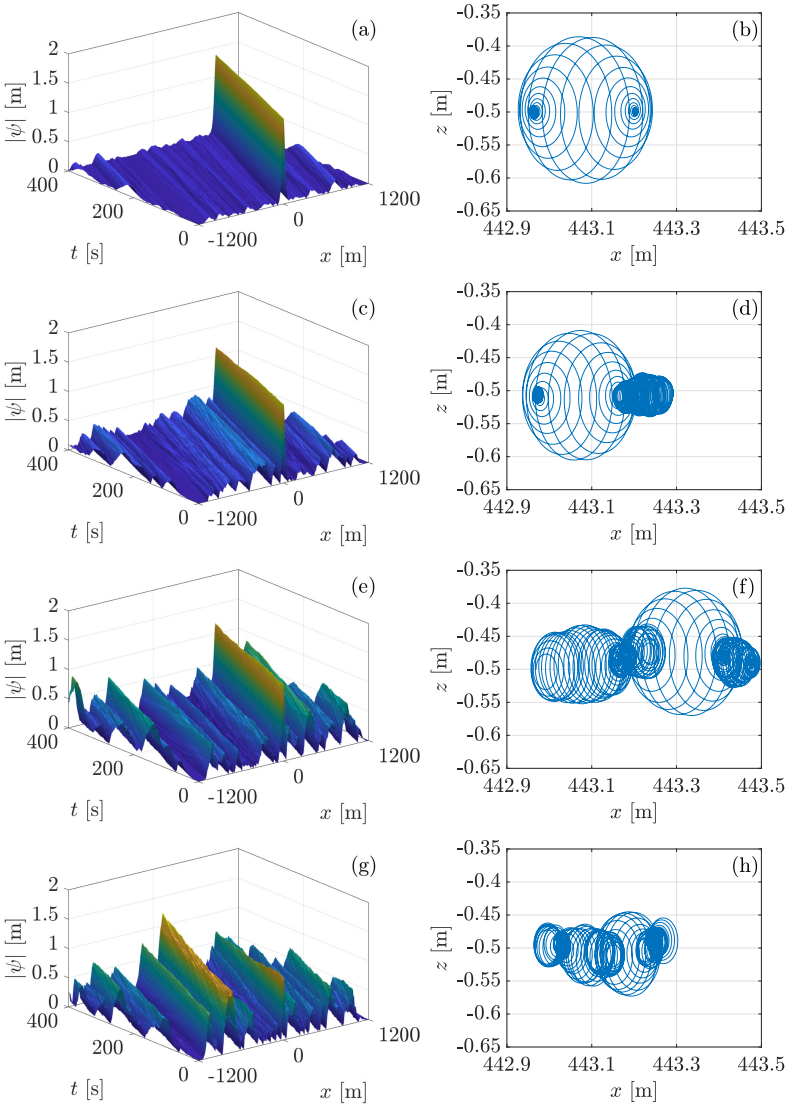

Figure 5.17: Comparison of the temporal behavior of the wave envelope of the soliton solution and particle trajectories, considering initial irregular perturbations η_{LC} with different significant wave heights. (a)-(b): $H_{\mathrm{s}} = 0.3\,\mathrm{m}$, (c)-(d): $H_{\mathrm{s}} = 0.75\,\mathrm{m}$, (e)-(f): $H_{\mathrm{s}} = 1.5\,\mathrm{m}$, (g)-(h): $H_{\mathrm{s}} = 2\,\mathrm{m}$.

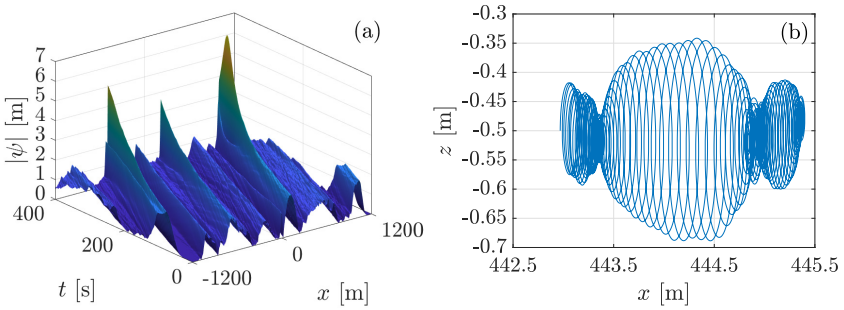

Figure 5.18: Temporal behavior of the wave envelope of the soliton solution and particle trajectory, considering an initial irregular perturbation η_{LC} with significant wave height $H_{\mathrm{s}} = 3\,\mathrm{m}$.

potential ϕ, i. e. $\phi^{(1)}$ and $\phi^{(2)}$, are considered instead of the corresponding first three components. To this end, different particle trajectories are computed solving Eq. (5.82), whereby the velocity potential ϕ includes only the components of lower-order. Let $\Phi^{(i)}$ be the velocity potential resulting from the NLS, which includes only the components of the velocity potential ϕ up to order i, i. e.

$$\Phi^{(1)} = \varepsilon\phi^{(1)}, \tag{5.83a}$$

$$\Phi^{(2)} = \varepsilon\phi^{(1)} + \varepsilon^2\phi^{(2)}, \tag{5.83b}$$

$$\Phi^{(3)} = \varepsilon\phi^{(1)} + \varepsilon^2\phi^{(2)} + \varepsilon^3\phi^{(3)}. \tag{5.83c}$$

Figures 5.19 and 5.20 show different particle trajectories during the propagation of the Peregrine breather and soliton solution, respectively. Here, the Peregrine breather and soliton solution are computed using $k_0 = 0.5\,\mathrm{m}^{-1}$, $\psi_0 = 1.5\,\mathrm{m}$, $\varepsilon = 0.1$, and are initially perturbed by irregular sea surfaces with significant wave height $H_{\mathrm{s}} = 1\,\mathrm{m}$. In all cases, the water particles start at $(x_0, z_0) = (442.94\,\mathrm{m}, -0.5\,\mathrm{m})$. The velocity potentials $\phi = \Phi^{(i)}$, $i = 1, 2, 3$, are used in Eq. (5.82) to compute the corresponding particle trajectories.
In Figs. 5.19 and 5.20, the particle trajectories resulting from the computation using $\phi = \Phi^{(3)}$ are shown in blue. These are the same particle trajectories, which are presented in Fig. 5.13c and Fig. 5.16b, respectively. In Figs. 5.19a and 5.20a, the corresponding particle trajectories are presented in red, which result from solving Eq. (5.82) using $\phi = \Phi^{(1)}$. Finally, Figs. 5.19b and 5.20b show the corresponding trajectories in green, which result from solving Eq. (5.82) using $\phi = \Phi^{(2)}$.
It can be seen that the particle trajectories experience a large change if $\Phi^{(1)}$ is used instead of $\Phi^{(3)}$ to compute the particle trajectories. In contrast to this, using $\Phi^{(2)}$ instead of $\Phi^{(3)}$ leads only to small changes in the trajectories. Similar results can be obtained, if the behavior of the particle trajectories presented in

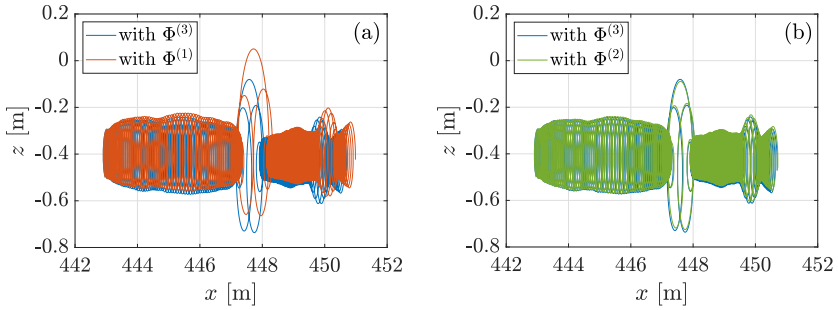

Figure 5.19: Comparison of water particle trajectories, which are computed using the velocity potentials $\Phi^{(1)}$, $\Phi^{(2)}$, and $\Phi^{(3)}$, respectively. The particle trajectories are computed for a Peregrine breather solution, which is initially perturbed by an irregular sea surface with significant wave height $H_\mathrm{s} = 1\,\mathrm{m}$.

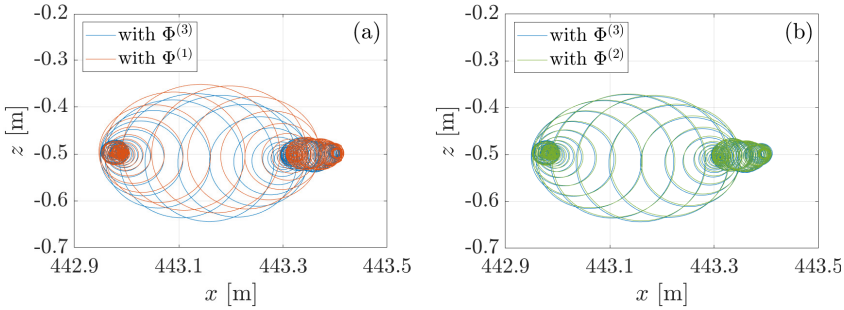

Figure 5.20: Comparison of water particle trajectories, which are computed using the velocity potentials $\Phi^{(1)}$, $\Phi^{(2)}$ and $\Phi^{(3)}$, respectively. The particle trajectories are computed for a soliton solution, which is initially perturbed by an irregular sea surface with significant wave height $H_\mathrm{s} = 1\,\mathrm{m}$.

Figs. 5.14 and 5.17 is computed and investigated using the different orders of the velocity potential $\phi = \Phi^{(i)}$, $i = 1, 2, 3$. It can be concluded that the use of $\Phi^{(2)}$ instead of $\Phi^{(3)}$ introduces only a small error in the modeling of the dynamics of the considered water waves. Therefore, the third-order component $\phi^{(3)}$ of the velocity potential ϕ does only slightly affect the dynamics of the considered water waves.

It has to be noted that all results shown in this section have been presented for a wave steepness of $\varepsilon = 0.1$. If larger values for the wave steepness ε are considered, the higher-order velocity potentials $\phi^{(i)}$, $i = 2, 3$, will contribute more to the velocity potential $\phi = \Phi^{(3)} = \varepsilon\phi^{(1)} + \varepsilon^2\phi^{(2)} + \varepsilon^3\phi^{(3)}$. As a result, for example, if a wave steepness of $\varepsilon > 0.1$ is considered and the particle trajectories

are computed using $\Phi^{(2)}$ instead of $\Phi^{(3)}$, the resulting particle trajectories will show larger differences than those presented in Figs. 5.19b and 5.20b. However, it has to be remembered that the NLS can only be used to accurately model weakly nonlinear deep water waves with a moderate wave steepness of $H/\lambda \leq 0.05$ or $\varepsilon \leq 0.15$ [Dysthe79, Witt19, Osborne10]. For waves with such values of the wave steepness ε, the results presented in this section show that the use of $\Phi^{(2)}$ instead of $\Phi^{(3)}$ introduces only a small error in the modeling of the dynamics of the water waves. Therefore, in the next chapters, the velocity potential ϕ of the water waves corresponding to the NLS is computed using only the first two components of ϕ, i. e. $\phi = \Phi^{(2)} = \varepsilon\phi^{(1)} + \varepsilon^2\phi^{(2)}$.
After the incident velocity potential of the incoming water waves has been calculated, the nonlinear FSI with a structure can be calculated using the method summarized in Figs. 4.2 and 4.4. It remains only to develop a scheme to compute the nonlinear FSI between a structure and nonlinear water waves numerically. A corresponding numerical scheme is developed in the next chapter.

Numerical Computation of the Nonlinear Fluid-structure Interaction

In the previous chapters, the theoretical fundamentals and equations to compute the FSI between a structure and nonlinear water waves have been derived. It has been shown that the presence of a structure disturbs the dynamics of the incoming water waves. This disturbance has to be considered in the computation of the hydrodynamic forces acting on the structure. Since the disturbance depends on the position, geometry, and dynamics of the structure, the FSI between water waves and the structure can generally only be computed numerically. The numerical computation of the FSI includes the calculation of the body disturbance potential ϕ_{B}, the hydrodynamic forces acting on the structure, and the resulting motion of the structure.
Several methods have been presented in literature to calculate the FSI between water waves and moving structures of specific or general geometry. Here, the fully nonlinear governing equations of fluid motion from Eq. (2.2) have been solved using different schemes. Among others, these schemes are based on the

- boundary element method [BaiEatock Taylor09, ZhangTeng21],
- finite element method [WangWu06, SunEtAl15],
- finite difference method [BinghamZhang07, DucrozetEtAl14], and
- harmonic polynomial cell method [HanssenEtAl18, TongEtAl21].

However, solving the fully nonlinear equations of fluid motion from Eq. (2.2) with the methods mentioned above takes too much computation time to be heavily applied in the design of offshore structures [ShaoEtAl22]. Therefore, the governing equations of fluid motion from Eq. (2.2) have been simplified using, for example, the Stokes perturbation expansions presented in Chap. 4. Within the second-order nonlinear wave theory, analytical and numerical methods have been presented in literature to solve the associated water wave problems. Here, pioneering works started in the 1970s. Examples are given by [FaltinsenLøken79, Molin79]. For simple structures like truncated or bottom-mounted vertical cylinders, semi-analytical solutions have been developed, see e.g. [Eatock TaylorHung87]. These solutions become relevant to validate numerical methods, which compute the FSI between nonlinear water waves and a structure of arbitrary geometry. In this regard, efficient and accurate frequency-domain and time-domain schemes have been developed. Examples of frequency-domain methods can be found

in [Molin79, ChenEtAl95, CongEtAl21]. However, considering transient effects or nonlinear effects like restoring forces from a mooring system, it can be necessary to solve directly for the particular solution in the time domain. Examples of time-domain schemes can be found in [BüchmannEtAl98, SkourupEtAl00, FerrantEtAl03, WangWu07, BaiTeng13, ShaoFaltinsen13, ShaoEtAl22].
In this thesis, the advantages and limitations of using the NLS to compute the FSI are investigated. To this end, this chapter presents a numerical scheme to calculate the FSI between nonlinear water waves and the WEC introduced in Sect. 3.1. Here, the incoming water waves are not further specified, such that nonlinear waves corresponding to the NLS presented in Sect. 5.1 or the Stokes waves presented in Sect. 4.3 can be used. The WEC introduced in Sect. 3.1 is used as an application example here to show the potential of the presented method. The WEC consists of a cylindrical floating body (CFB) moving along a guidance. Only the CFB has contact with the water. Therefore, the numerical computation of the FSI between the WEC and water waves can be reduced to the calculation the FSI between one CFB and water waves.
In order to calculate the FSI with lower computational effort, the following assumptions are made for the CFB:

- The considered CFB and the considered computational water domain are rotationally symmetric along the vertical axis.
- The CFB can only perform translational motion in the vertical direction.
- The CFB does not contain sharp edges or corners.

The CFB, which is considered in this chapter, is sketched in Fig. 6.1 and has the radius R and draft d. However, compared to the CFB, which has been used in Chap. 3, the CFB shown in Fig. 6.1 contains a semispherical bottom now. Here, the sharp corners of the bottom of the cylinder are replaced by a spherical segment of radius R_S. This spherical segment prevents numerical difficulties, which would occur in the numerical discretization of the water domain around the sharp corner. Concerning the motion of the CFB, it should be noted that the hydrodynamic damping of a floater with a semispherical bottom can decrease by up to 50% compared to the damping of a floater with a flat bottom [TomYeung13]. Therefore, going from a flat-bottom geometry to a semispherical bottom can also increase the motion of the WEC presented in Chap. 3.
In the following sections, a numerical scheme for the computation of the FSI between the CFB sketched in Fig. 6.1 and nonlinear water waves is presented and analyzed. First, the computational domain is introduced in Sect. 6.1, for which the velocity potential ϕ_B corresponding to the disturbance of the CFB is computed numerically. Since the computational domain has a finite length, it is necessary to specify a BC at the outer boundary of the domain. An absorbing BC is presented in Sect. 6.2. Afterward, a numerical scheme to compute the velocity potential ϕ_B is introduced in Sect. 6.3 and Sect. 6.4. Here, a time-domain finite difference method is used. Using the numerical values for ϕ_B, the corresponding

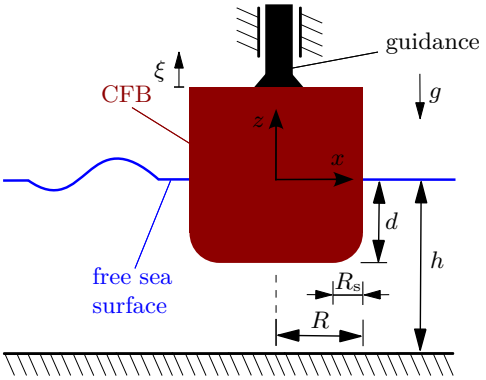

Figure 6.1: Sketch of the considered CFB, which is used for numerical computations.

hydrodynamic forces acting on the CFB are computed in Sect. 6.5. A numerical scheme to calculate the displacement of the CFB is presented in Sect. 6.6, which solves the equations of motion from Eq. (4.35). Finally, the empirical order of convergence of the presented numerical method is analyzed in Sect. 6.7.

6.1 Specification of the Computational Domain

First, the computational domain is specified, for which the velocity potential ϕ_B is computed numerically. Since the CFB shown in Fig. 6.1 is rotationally symmetric, the spatial computational domain is not only considered in Cartesian coordinates $(x, y, z) \in \mathbb{R}^3$ but also in cylindrical coordinates $(r, \theta, z) \in \mathbb{R}_+ \times (0, 2\pi] \times \mathbb{R}$. Here, $\mathbb{R}_+$ is defined as $\mathbb{R}_+ := \{x \in \mathbb{R} \mid x \geq 0\}$. The origins of the cylindrical and Cartesian coordinate systems are the same and are located in the geometric center of the CFB at the height of the still water level, see Fig. 6.1. The Cartesian coordinates can be computed from the cylindrical coordinates by

$$x = r\cos(\theta), \quad y = r\sin(\theta), \quad z = z. \tag{6.1}$$

The set of all points, which are located inside the CFB shown in Fig. 6.1, is denoted by C_3. Using cylindrical coordinates, C_3 is defined as

$$C_3 := \Big\{ (r,\theta,z) \in \mathbb{R}^3 \mid (0 \le r \le R,\, 0 < \theta \le 2\pi,\, -d + R_\mathrm{S} \le z \le 0) \\ \vee\, (r \le R - R_\mathrm{S} + R_\mathrm{S}\cos(\phi_\mathrm{S}),\, 0 < \theta \le 2\pi,\, -d \le z < -d + R_\mathrm{S}) \Big\} \tag{6.2}$$

with $\phi_\mathrm{S} = \arcsin\left(|z + d - R_\mathrm{S}|/R_\mathrm{S}\right)$. Since the CFB is moving in vertical direction, the boundary of C_3 changes in time.
The corresponding computational water domain has to be bounded for the numerical computation of the velocity potential ϕ_B. In z-direction, it is bounded by the still water level at $z = 0$ from above and by the sea bottom at $z = -h$ from below. In r-direction, it is bounded by some arbitrary value $R_\Omega \in \mathbb{R}_+$. Let Ω_3 denote the computational water domain. Then it holds

$$\Omega_3 := \{(r,\theta,z) \in \mathbb{R}^3 \setminus C_3 \mid 0 \le r \le R_\Omega,\, 0 < \theta \le 2\pi,\, -h \le z \le 0\}. \tag{6.3}$$

Figure 6.2 shows a sketch of the domains Ω_3 and C_3 for a CFB with $R_\mathrm{S} = 0$.
In order to calculate the body disturbance velocity potential ϕ_B, the corresponding components $\phi_\mathrm{B}^{(i)}$, $i = 1, 2, 3, \ldots$, have to be computed. Knowing the components of the incident velocity potential $\phi_0^{(i)}$, a scheme for the computation of $\phi_\mathrm{B}^{(i)}$ is sketched in Fig. 4.2. However, in Chap. 5, it has been shown that the NLS can only be used to calculate the corresponding FSI accurately up to an error of order $\mathcal{O}(\varepsilon^3)$. Therefore, in this chapter, only the first two components of the body disturbance velocity potential ϕ_B, i. e. $\phi_\mathrm{B}^{(1)}$ and $\phi_\mathrm{B}^{(2)}$, are calculated. Considering Fig. 4.2 and using the notation introduced in this section, the corresponding equations for $\phi_\mathrm{B}^{(i)}$, $i = 1, 2$, in Cartesian coordinates are given by

$$\boldsymbol{\nabla}^2 \phi_\mathrm{B}^{(i)} = 0, \qquad \text{in } \mathring{\Omega}_3, \tag{6.4a}$$

$$\boldsymbol{\nabla}\phi_\mathrm{B}^{(i)} \cdot \boldsymbol{n} = -\boldsymbol{\nabla}\phi_0^{(i)} \cdot \boldsymbol{n} + \boldsymbol{u}^{(i)} \cdot \boldsymbol{n}, \qquad \text{on } \partial C_3, \tag{6.4b}$$

$$\phi_{\mathrm{B},z}^{(i)} = 0, \qquad \text{for } r \le R_\Omega,\, z = -h, \tag{6.4c}$$

$$\phi_{\mathrm{B},tt}^{(1)} + g\phi_{\mathrm{B},z}^{(1)} = 0, \qquad \text{for } R \le r \le R_\Omega,\, z = 0, \tag{6.4d}$$

$$\phi_{\mathrm{B},tt}^{(2)} + g\phi_{\mathrm{B},z}^{(2)} = F(\phi_0^{(1)} + \phi_\mathrm{B}^{(1)}) - F(\phi_0^{(1)}), \qquad \text{for } R \le r \le R_\Omega,\, z = 0. \tag{6.4e}$$

Here, the function F is given by Eq. (4.16), $\mathring{\Omega}_3$ denotes the interior of the set Ω_3, and ∂C_3 is the boundary of the set C_3.
Additionally to Eq. (6.4), a BC at $r = R_\Omega$ has to be formulated. This is done in the next section.

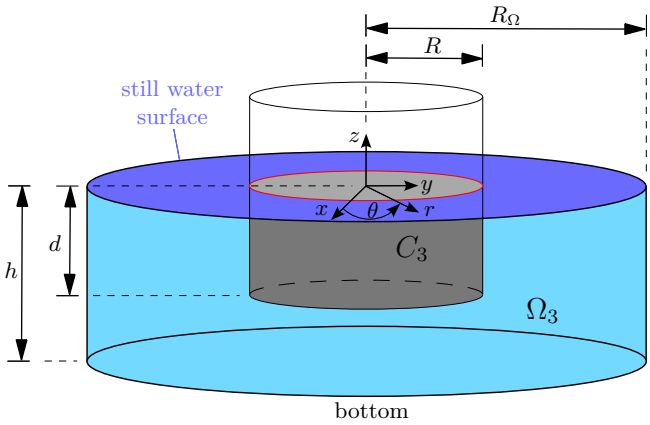

Figure 6.2: Sketch of the domains C_3 and Ω_3 for a CFB with $R_S = 0$. The used Cartesian and cylindrical coordinate systems are also shown.

6.2 Absorbing Boundary Conditions at the Outer Boundary

The presence and motion of a structure disturbs the dynamics of the incoming water waves and generate water waves corresponding to the velocity potential $\phi_B^{(i)}$, which propagate to the outside of the computational domain. In order to prevent these waves from being reflected at the non-physical outer boundary of the computational domain at $r = R_\Omega$, corresponding absorbing BCs have to be formulated. These BCs let the waves exit the domain as they would in the open sea.
Several methods are frequently used in literature to implement absorbing BCs. Some of them are sketched in Sect. 6.2.1. Afterward, an absorbing BC is implemented, which is used in this thesis to compute the potentials $\phi_B^{(i)}$.

6.2.1 Introduction to Absorbing Boundary Conditions

The determination of absorbing BCs is a common problem in the numerical modeling of wave propagation in many fields of physics. A variety of methods have been developed in the past. An extensive review of absorbing BCs in the numerical solution of wave problems can be found in [Givoli91]. Examples of absorbing BCs are given by

(i) periodic BCs,

(ii) Orlanski's condition,

(iii) simple far field solutions, and

(iv) the introduction of artificial damping using sponge layers.

The basic ideas of these four examples of absorbing BCs are stated in the following:

(i) Period BCs has been favored in most two-dimensional nonlinear models [Romate92]. The solution is assumed to be periodic in space, so unknowns on two different vertical boundaries of the domain can be set equal. This method is straightforward to implement, and the domain boundaries can be located at very short distances equal to the largest modeled wavelength [CaoEtAl93]. However, the application of this method is limited due to the requirement of periodicity.

(ii) Orlanski's condition [Orlanski76] states a differential equation as BC at the outer boundary of the computational domain. However, Orlanski's condition contains the phase velocity c_{ph} of the waves, which must be absorbed. For regular waves, the phase velocity is given by Eq. (2.19). However, it is not clear which value should be used for the phase velocity c_{ph} for random water waves. As a result, some schemes have been developed to determine the value of the phase velocity c_{ph}, see e.g. [Orlanski76, Pearson74, Jagannathan88]. However, in [Clément96], it has been pointed out that the application of Orlanski's condition should be limited to cases of regular incident waves of known frequency or very long waves. This is because, in both cases, the phase velocity c_{ph} of the outgoing waves becomes constant after the transient phase of the flow from rest.
However, since both regular and random waves are considered in this thesis, an absorption strategy is sought independent of the incident water waves.

(iii) When using simple far field solutions, the whole spatial domain is decomposed into an interior and an exterior part. While the considered mechanical structure and other complicated boundary geometries, like a changing sea bottom, are located in the interior domain, boundaries and boundary conditions in the exterior domain are simplified. This allows the finding of closed-form analytical solutions in the exterior domain, which are usually expressed as eigenfunction expansions [Romate92]. At the interface between the interior and exterior domain, the analytical solution in the exterior domain is then matched with the solution of the interior domain. In this way, the FSI between mechanical structures and incoming water waves has been computed by many authors, see e.g. [LiuAbbaspour82, TsayLiu83]. More works in which this approach has been used are cited by [Romate92].
However, the disadvantage of this method is that the search for analytical

solutions becomes complicated when random or nonlinear incoming water waves are considered.

(iv) The introduction of artificial damping using sponge layers does not prevent reflections at the outer boundary of the computational domain from being generated. However, the reflected waves are prevented from reaching the mechanical structure, which is located within the computational domain. This is done by adding a dissipative term in the BC at $z = 0$ in a limited area that is far away from the considered structure. Water waves lose energy if they pass through this damping zone on their way out of the domain and then, for the part that is reflected at the outer boundary, on their way back. In this way, the waves are entirely absorbed if the damping zone is sufficiently long and the magnitude of dissipation is large enough. This method is sometimes called the sponge layer method [IsraeliOrszag81, Romate92, BüchmannEtAl98] or the numerical beach method [Clément96].
The drawback of this method is that the resulting computational domain has to be larger than the domain considered in the other methods since it has to contain an additional damping zone. This increases the computational effort. However, regular and random waves are absorbed completely for a sufficiently long damping zone. Furthermore, the method can be applied to linear and nonlinear wave theories.

Considering the methods mentioned above, method (iv) is most promising for the investigations taken in this thesis and is used in the further course of this thesis to implement an absorbing BC for the given problem. In the following, method (iv) is further explained and applied to Eq. (6.4)

6.2.2 Application of the Absorbing Boundary Conditions

The nature of the dissipative term, which is added to the BC at $z = 0$, is arbitrary. The dissipative term can be introduced in several ways and can be chosen to depend on the velocity potential ϕ, sea surface displacement η, water particle velocity, or any combination of them [Clément96]. In this work, the dissipative term depends on the sea surface displacement η and velocity potential ϕ, respectively. It is introduced by reformulating the BCs (2.2b) and (2.2c) to

$$\eta_t + \phi_x\eta_x + \phi_y\eta_y + \mu(x,y)\eta = \phi_z, \quad \text{for} \quad R \leq r \leq R_\Omega,\ z = \eta(x,y,t), \tag{6.5a}$$

$$\phi_t + \frac{1}{2}\boldsymbol{\nabla}\phi \cdot \boldsymbol{\nabla}\phi + g\eta + \mu(x,y)\phi = 0, \quad \text{for} \quad R \leq r \leq R_\Omega,\ z = \eta(x,y,t). \tag{6.5b}$$

Here, $\mu = \mu(x,y)$ is a function which has still to be defined. A similar approach for introducing the dissipative term has been used several times in literature, see e.g. [BüchmannEtAl98, SkourupEtAl00, ShaoFaltinsen13].

Next, the computational domain Ω_3 from Eq. (6.3) is divided into an inner layer of radius R_i and a damping zone with length L, whereby $R_\Omega = R_\mathrm{i} + L$. Damping is only considered in the damping zone. This is achieved by setting $\mu = 0$ in the inner layer and $\mu \neq 0$ in the damping zone. A sketch of the resulting computational domain is shown in Fig. 6.3 for $y = 0$ and $x \geq 0$. At the end of the damping zone, reflecting BCs are implemented using a Neumann BC, i. e.

$$\boldsymbol{\nabla}\phi \cdot \boldsymbol{n} = 0, \quad \text{for } r = R_\Omega,\ 0 < \theta \leq 2\pi,\ -h \leq z \leq \eta. \tag{6.6}$$

It has to be mentioned that the efficiency of the presented approach to absorb reflections coming from the outer boundary strongly depends on the ratio between the wavelength λ of the incoming water waves and the length L. The larger the wavelength λ of the incoming water waves, the larger the length L must be to achieve a certain absorption level [Clément96]. Therefore, this absorbing method behaves like a low-pass filter for the incoming water waves. Here, the cutoff frequency of the filter has to be tuned in such a way that the spectral content of the incoming water waves is absorbed.
Furthermore, it has to be mentioned that the function μ has to be chosen with care. For small values of μ, there is little dissipation, and waves reflected at the end of the damping zone could reach the mechanical structure in the inner layer. For large values of μ, the damping zone itself acts as a boundary, i. e. waves are reflected at the beginning of the damping zone [Romate92]. This work uses the same value for μ as in [ShaoFaltinsen13]. In terms of the cylindrical coordinate r, the damping μ is defined as

$$\mu(r) := \begin{cases} 0, & \text{for } 0 \leq r < R_\mathrm{i}, \\ \mu_0 \sqrt{\dfrac{g}{\lambda}} \left[-2 \left(\dfrac{r - R_\mathrm{i}}{L} \right)^3 + 3 \left(\dfrac{r - R_\mathrm{i}}{L} \right)^2 \right], & \text{for } R_\mathrm{i} \leq r \leq R_\Omega. \end{cases} \tag{6.7}$$

Here, λ is the wavelength of the incoming waves, which is given for regular waves with wave number k by Eq. (2.17). In [ShaoFaltinsen13], the length L of the damping zone has been chosen to be twice as large as the wavelength, i. e. $L = 2\lambda$. Finally, for incoming regular waves with wave frequency ω, the empirical damping coefficient μ_0 in Eq. (6.7) is proposed in [ShaoFaltinsen13] as

$$\mu_0 = -\frac{g \ln(0.5 \times 10^{-5})}{2\omega L} \sqrt{\frac{\lambda}{g}}. \tag{6.8}$$

For incoming random waves, ω is replaced in Eq. (6.8) by the peak frequency ω_p of the corresponding sea spectrum $S(\omega)$ and λ is replaced by the wavelength of waves, which oscillates in time with peak frequency ω_p. In this way, wave components of the irregular sea with wave frequencies $\omega \geq \omega_\mathrm{p}$ are absorbed. Recall that for $\omega = \omega_\mathrm{p}$, the highest energy waves occur in the entire wave spectrum. These waves are absorbed using the method described above.

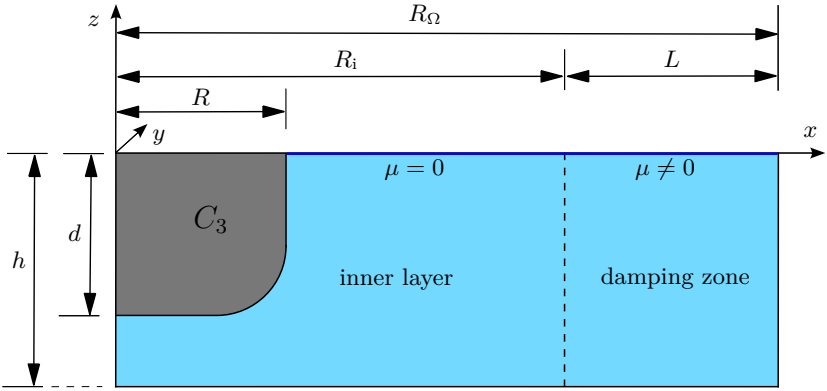

Figure 6.3: Sketch of the domains C_3 and Ω_3 for $y = 0$ and $x \geq 0$. Here, Ω_3 is divided into an inner layer and a damping zone.

In the presented way, dissipative terms have been introduced in the BCs (2.2b) and (2.2c), which results in Eq. (6.5). However, to compute the velocity potentials $\phi_\mathrm{B}^{(i)}$, dissipative terms have to be introduced in Eq. (6.4). In the following, the derivation of equations is sketched that correspond to Eq. (6.4) but include dissipation effects. Here, the method is followed, which is presented in Sect. 4.1.1 and Sect. 4.1.3 to derive the equations summarized in Fig. 4.2 and Eq. (6.4), respectively. First of all, the substantial derivative of Eq. (6.5b) is considered, i. e.

$$0 = \left(\frac{\partial}{\partial t} + \boldsymbol{\nabla}\phi \cdot \boldsymbol{\nabla}\right)\left[\phi_t + \frac{1}{2}\boldsymbol{\nabla}\phi \cdot \boldsymbol{\nabla}\phi + g\eta + \mu\phi\right], \quad \text{for} \quad z = \eta(x, y, t). \tag{6.9}$$

Next, Eq. (6.5a) is used to compute η_t. The resulting expression for η_t is inserted in Eq. (6.9), which becomes

$$\begin{aligned} &\phi_{tt} + g\phi_z + \mu\phi_t - g\mu\eta + 2\boldsymbol{\nabla}\phi \cdot \boldsymbol{\nabla}\phi_t + \mu\boldsymbol{\nabla}\phi \cdot \boldsymbol{\nabla}\phi + \phi\left(\boldsymbol{\nabla}\phi \cdot \boldsymbol{\nabla}\mu\right) \\ &\quad + \frac{1}{2}\boldsymbol{\nabla}\phi \cdot \boldsymbol{\nabla}\left(\boldsymbol{\nabla}\phi \cdot \boldsymbol{\nabla}\phi\right) = 0, \quad \text{for} \quad z = \eta(x, y, t). \end{aligned} \tag{6.10}$$

Using Eq. (6.5b) to compute η and inserting the expression for η in Eq. (6.10), it results

$$\begin{aligned} &\phi_{tt} + g\phi_z + 2\mu\phi_t + \mu^2\phi + 2\boldsymbol{\nabla}\phi \cdot \boldsymbol{\nabla}\phi_t + \frac{3}{2}\mu\boldsymbol{\nabla}\phi \cdot \boldsymbol{\nabla}\phi + \phi\left(\boldsymbol{\nabla}\phi \cdot \boldsymbol{\nabla}\mu\right) \\ &\quad + \frac{1}{2}\boldsymbol{\nabla}\phi \cdot \boldsymbol{\nabla}\left(\boldsymbol{\nabla}\phi \cdot \boldsymbol{\nabla}\phi\right) = 0, \quad \text{for} \quad z = \eta(x, y, t). \end{aligned} \tag{6.11}$$

Next, Eq. (6.11) is expanded from $z = \eta$ to $z = 0$ by applying Taylor series expansions of the form given in Eq. (4.3). Considering all terms up to order $\mathcal{O}(\phi^2)$,

Eq. (6.11) results in

$$\begin{aligned}&\phi_{tt} + g\phi_z + 2\mu\phi_t + \mu^2\phi + 2\boldsymbol{\nabla}\phi\cdot\boldsymbol{\nabla}\phi_t + \frac{3}{2}\mu\boldsymbol{\nabla}\phi\cdot\boldsymbol{\nabla}\phi + \phi\left(\boldsymbol{\nabla}\phi\cdot\boldsymbol{\nabla}\mu\right)\\ &-\frac{1}{g}\left[\phi_t + \mu\phi\right]\frac{\partial}{\partial z}\left(\phi_{tt} + g\phi_z + 2\mu\phi_t + \mu^2\phi\right) = 0 + \mathcal{O}(\phi^3), \quad \text{for} \quad z = 0.\end{aligned} \tag{6.12}$$

For $\mu = 0$, Eq. (6.12) simplifies to Eq. (4.4b). This means that Eq. (6.12) represents a generalization of Eq. (4.4b) by including dissipative effects.
The nonlinearity of the BC (6.12) makes the computation of solutions ϕ very difficult. Therefore, the BC (6.12) is approximated by a sequence of linear equations by applying Stokes' perturbation expansions. Substituting the perturbation expansions from Eq. (4.13a) for ϕ into Eq. (6.12), it is found that the first two velocity potentials $\phi^{(1)}$ and $\phi^{(2)}$ have to satisfy

$$\mathcal{O}(\varepsilon) \;:\; \phi^{(1)}_{tt} + g\phi^{(1)}_z + 2\mu\phi^{(1)}_t + \mu^2\phi^{(1)} = 0, \qquad \text{for} \quad z = 0, \tag{6.13a}$$

$$\mathcal{O}(\varepsilon^2) : \; \phi^{(2)}_{tt} + g\phi^{(2)}_z + 2\mu\phi^{(2)}_t + \mu^2\phi^{(2)} = F^{\mu}(\phi^{(1)}), \qquad \text{for} \quad z = 0. \tag{6.13b}$$

Here, the function F^{μ} is defined as

$$\begin{aligned}F^{\mu}(\phi^{(1)}) := &-2\boldsymbol{\nabla}\phi^{(1)}\cdot\boldsymbol{\nabla}\phi^{(1)}_t - \frac{3}{2}\mu\boldsymbol{\nabla}\phi^{(1)}\cdot\boldsymbol{\nabla}\phi^{(1)} - \phi^{(1)}\left(\boldsymbol{\nabla}\phi^{(1)}\cdot\boldsymbol{\nabla}\mu\right)\\ &+\frac{1}{g}\left[\phi^{(1)}_t + \mu\phi^{(1)}\right]\frac{\partial}{\partial z}\left(\phi^{(1)}_{tt} + g\phi^{(1)}_z + 2\mu\phi^{(1)}_t + \mu^2\phi^{(1)}\right).\end{aligned} \tag{6.14}$$

For $\mu = 0$, F^{μ} simplifies to the function F defined in Eq. (4.16).
Finally, the velocity potentials $\phi^{(i)}$, $i = 1, 2$, are divided into the velocity potential $\phi^{(i)}_0$ of the incoming undisturbed water waves and velocity potential $\phi^{(i)}_{\mathrm{B}}$ corresponding to the body disturbance. The respective decomposition has also been presented in Eq. (4.21) for the general case. It has to be noted that in the absence of any mechanical structure, the potentials $\phi^{(i)}$ consists only of the velocity potentials of the incoming water waves $\phi^{(i)}_0$. Therefore, the potentials $\phi^{(1)}_0$ and $\phi^{(2)}_0$ have also to satisfy Eqs. (6.13a) and (6.13b), respectively. Using this fact and substituting $\phi^{(i)} = \phi^{(i)}_0 + \phi^{(i)}_{\mathrm{B}}$ into Eq. (6.13), it is found that the velocity potentials $\phi^{(i)}_{\mathrm{B}}$ have to satisfy

$$\mathcal{O}(\varepsilon) \;:\; \phi^{(1)}_{\mathrm{B},tt} + g\phi^{(1)}_{\mathrm{B},z} + 2\mu\phi^{(1)}_{\mathrm{B},t} + \mu^2\phi^{(1)}_{\mathrm{B}} = 0, \tag{6.15a}$$

$$\mathcal{O}(\varepsilon^2) : \; \phi^{(2)}_{\mathrm{B},tt} + g\phi^{(2)}_{\mathrm{B},z} + 2\mu\phi^{(2)}_{\mathrm{B},t} + \mu^2\phi^{(2)}_{\mathrm{B}} = F^{\mu}(\phi^{(1)}_0 + \phi^{(1)}_{\mathrm{B}}) - F^{\mu}(\phi^{(1)}_0) \tag{6.15b}$$

at $z = 0$. For $\mu = 0$, the BCs (6.15a) and (6.15b) simplify to Eq. (6.4d) and Eq. (6.4e), respectively. This means that the BCs (6.15a) and (6.15b) represents a generalization of Eqs. (6.4d) and (6.4e) by including dissipative effects.
In summary, with the presented approach to absorb reflections coming from the outer boundary, the body disturbance velocity potentials $\phi^{(i)}_{\mathrm{B}}$, $i = 1, 2$, can be

computed by solving

$$\boldsymbol{\nabla}^2 \phi_{\mathrm{B}}^{(i)} = 0, \qquad \text{in } \mathring{\Omega}_3, \tag{6.16a}$$

$$\boldsymbol{\nabla}\phi_{\mathrm{B}}^{(i)} \cdot \boldsymbol{n} = -\boldsymbol{\nabla}\phi_0^{(i)} \cdot \boldsymbol{n} + \boldsymbol{u}^{(i)} \cdot \boldsymbol{n}, \quad \text{on } \partial C_3, \tag{6.16b}$$

$$\phi_{\mathrm{B},z}^{(i)} = 0, \qquad \text{on } \partial\Omega_3 \cap \{z = -h\}, \tag{6.16c}$$

$$\phi_{\mathrm{B},tt}^{(i)} + g\phi_{\mathrm{B},z}^{(i)} + 2\mu\phi_{\mathrm{B},t}^{(i)} + \mu^2\phi_{\mathrm{B}}^{(i)} = G^{(i)}(\phi_0^{(1)}, \phi_{\mathrm{B}}^{(1)}), \quad \text{on } \partial\Omega_3 \cap \{z = 0\}, \tag{6.16d}$$

$$\boldsymbol{\nabla}\phi_{\mathrm{B}}^{(i)} \cdot \boldsymbol{n} = 0, \qquad \text{on } \partial\Omega_3 \cap \{r = R_\Omega\}, \tag{6.16e}$$

whereby

$$G^{(i)}(\phi_0^{(1)}, \phi_{\mathrm{B}}^{(1)}) := \begin{cases} 0, & \text{for } i = 1, \\ F^{\mu}(\phi_0^{(1)} + \phi_{\mathrm{B}}^{(1)}) - F^{\mu}(\phi_0^{(1)}), & \text{for } i = 2. \end{cases} \tag{6.17}$$

A numerical scheme to solve Eq. (6.16) is presented in the following sections.

6.3 Transformation of Governing Equations

Before a numerical scheme to solve the governing equations of fluid motion given by Eq. (6.16) is presented, it is shown how the computational effort can be reduced by transforming Eq. (6.16) from a three-dimensional problem to multiple uncoupled two-dimensional problems. Here, the assumptions are used that the CFB only performs translational motion in the vertical direction and that the computational domain Ω_3 is rotationally symmetric along the vertical axis. The transformation from a three-dimensional problem to multiple uncoupled two-dimensional problems is done in three steps, which are described in the following.

6.3.1 Step 1: Transformation to the Resting Position

Since the CFB is moving, the domains C_3 and Ω_3 are time-dependent. Therefore, Eq. (6.16) has to be solved for a different computational domain at each time point. In order to simplify the study, it is possible to consider the resting position of the CFB for the whole computation time and to transform the corresponding BC at the wetted surface of the CFB accordingly. This procedure is explained in the following:
Let $\bar{C}_3$ be the domain C_3 for the case that the CFB is located at its resting position. Furthermore, let $\partial\bar{C}_3$ the denote the boundary of $\bar{C}_3$ and thus the corresponding

mean wetted surface of the CFB in its resting position. If the CFB does not show any displacement against its resting position, i. e. $\xi = 0$, the boundary $\partial\bar{C}_3$ becomes ∂C_3. Computing the body disturbance velocity potentials $\phi_{\mathrm{B}}^{(i)}$, $i = 1, 2$, and considering only the mean wetted surface $\partial\bar{C}_3$ instead ∂C_3, the BC (6.16b) at the surface of the CFB has to be transformed from ∂C_3 to $\partial\bar{C}_3$. Since the CFB considered in this thesis only performs translational motion in the vertical direction with displacement ξ, a Taylor series expansion around $\partial\bar{C}_3$ results in

$$[\boldsymbol{\nabla}\phi]_{(x,y,z)\in\partial C_3} = [\boldsymbol{\nabla}\phi]_{(x,y,z)\in\partial\bar{C}_3} + \xi\left[\frac{\partial}{\partial z}\boldsymbol{\nabla}\phi\right]_{(x,y,z)\in\partial\bar{C}_3} + \mathcal{O}(\xi^2). \tag{6.18}$$

Using the Stokes perturbation expansion of ξ, which is given in Eq. (4.34), and applying Eq. (6.18) on the BC (6.16b), it results

$$\boldsymbol{\nabla}\phi_{\mathrm{B}}^{(i)} \cdot \boldsymbol{n} = -\boldsymbol{\nabla}\phi_0^{(i)} \cdot \boldsymbol{n} + \boldsymbol{u}^{(i)} \cdot \boldsymbol{n} + V^{(i)}(\phi_0^{(1)}, \phi_{\mathrm{B}}^{(1)}, \xi^{(1)}), \quad \text{on } \partial\bar{C}_3, \tag{6.19}$$

whereby

$$V^{(i)}(\phi_0^{(1)}, \phi_{\mathrm{B}}^{(1)}, \xi^{(1)}) := \begin{cases} 0, & \text{for } i = 1, \\ -\xi^{(1)}\dfrac{\partial}{\partial z}\boldsymbol{\nabla}(\phi_0^{(1)} + \phi_{\mathrm{B}}^{(1)}) \cdot \boldsymbol{n}, & \text{for } i = 2. \end{cases} \tag{6.20}$$

In [Ogilvie83], the corresponding transformation of the BC (6.16b) from ∂C_3 to $\partial\bar{C}_3$ is presented for the case of a general three-dimensional motion. For the case of a translational motion in the vertical direction, the formulas presented in [Ogilvie83] simplify to Eq. (6.19).
Replacing the BC (6.16b) by Eq. (6.19), it is possible to compute the velocity potentials $\phi_{\mathrm{B}}^{(i)}$ considering the CFB in its resting position. It should be noted that the change from ∂C_3 to $\partial\bar{C}_3$ also changes the computational water domain from Ω_3, which is given by Eq. (6.3), to

$$\bar{\Omega}_3 := \{(r, \theta, z) \in \mathbb{R}^3 \setminus \bar{C}_3 \mid 0 \leq r \leq R_\Omega,\, 0 < \theta \leq 2\pi,\, -h \leq z \leq 0\}. \tag{6.21}$$

6.3.2 Step 2: Consideration of Equations in Cylindrical Coordinates

In the next step, the Eqs. (6.16) and (6.19) are considered in cylindrical coordinates. This is done by considering the velocity potentials $\phi_{\mathrm{B}}^{(i)}$ and $\phi_0^{(i)}$ in cylindrical coordinates. In the following, ${}^{\mathrm{K}}\phi_{\mathrm{B}}^{(i)} = {}^{\mathrm{K}}\phi_{\mathrm{B}}^{(i)}(x, y, z, t)$ denotes the velocity potential $\phi_{\mathrm{B}}^{(i)}$ in Cartesian coordinates, while ${}^{\mathrm{Z}}\phi_{\mathrm{B}}^{(i)} = {}^{\mathrm{Z}}\phi_{\mathrm{B}}^{(i)}(r, \theta, z, t)$ denotes the velocity potential $\phi_{\mathrm{B}}^{(i)}$ in cylindrical coordinates. The same notation applies to the incident velocity potential $\phi_0^{(i)}$. It holds for the coordinate transformation

$${}^{\mathrm{Z}}\phi_{\mathrm{B}}^{(i)}(r, \theta, z, t) = {}^{\mathrm{K}}\phi_{\mathrm{B}}^{(i)}(x(r, \theta), y(r, \theta), z, t), \tag{6.22}$$

and

$$ {}^{\mathrm{Z}}\phi_0^{(i)}(r,\theta,z,t) = {}^{\mathrm{K}}\phi_0^{(i)}(x(r,\theta),y(r,\theta),z,t). \tag{6.23} $$

Using cylindrical coordinates, the Laplace equation (6.16a) can be written as

$$ \boldsymbol{\nabla}^2\, {}^{\mathrm{K}}\phi_{\mathrm{B}}^{(i)} = {}^{\mathrm{K}}\phi_{\mathrm{B},xx}^{(i)} + {}^{\mathrm{K}}\phi_{\mathrm{B},yy}^{(i)} + {}^{\mathrm{K}}\phi_{\mathrm{B},zz}^{(i)} = {}^{\mathrm{Z}}\phi_{\mathrm{B},rr}^{(i)} + \frac{{}^{\mathrm{Z}}\phi_{\mathrm{B},r}^{(i)}}{r} + \frac{{}^{\mathrm{Z}}\phi_{\mathrm{B},\theta\theta}^{(i)}}{r^2} + {}^{\mathrm{Z}}\phi_{\mathrm{B},zz}^{(i)} = 0. \tag{6.24} $$

Here, it has been used that derivatives of ${}^{\mathrm{Z}}\phi_{\mathrm{B}}^{(i)}(r,\theta,z,t)$ with respect to r, θ, and z can be expressed in terms of derivatives of ${}^{\mathrm{K}}\phi_{\mathrm{B}}^{(i)}(r,\theta,z,t)$ with respect to x, y, and z. For example, it holds

$$ {}^{\mathrm{Z}}\phi_{\mathrm{B},r}^{(i)} = {}^{\mathrm{K}}\phi_{\mathrm{B},x}^{(i)} x_r + {}^{\mathrm{K}}\phi_{\mathrm{B},y}^{(i)} y_r = {}^{\mathrm{K}}\phi_{\mathrm{B},x}^{(i)} \cos\theta + {}^{\mathrm{K}}\phi_{\mathrm{B},y}^{(i)} \sin\theta, \tag{6.25a} $$

$$ {}^{\mathrm{Z}}\phi_{\mathrm{B},\theta}^{(i)} = {}^{\mathrm{K}}\phi_{\mathrm{B},x}^{(i)} x_\theta + {}^{\mathrm{K}}\phi_{\mathrm{B},y}^{(i)} y_\theta = -{}^{\mathrm{K}}\phi_{\mathrm{B},x}^{(i)} r\sin\theta + {}^{\mathrm{K}}\phi_{\mathrm{B},y}^{(i)} r\cos\theta, \tag{6.25b} $$

$$ {}^{\mathrm{Z}}\phi_{\mathrm{B},z}^{(i)} = {}^{\mathrm{K}}\phi_{\mathrm{B},z}^{(i)}. \tag{6.25c} $$

When considering the BC (6.16b) in cylindrical coordinates, it has to be noted that the intersection of planes parallel to the $x-y$-plane with the rotationally symmetric CFB sketched in Fig. 6.1 always results in circles. Therefore, a normal vector $\boldsymbol{n}$ pointing out of the fluid and inside the rotationally symmetric floating body has, in cylindrical coordinates, the form

$$ {}^{\mathrm{Z}}\boldsymbol{n} = \begin{bmatrix} n^r \\ 0 \\ n^z \end{bmatrix}, \quad \text{with } n^r \le 0, n^z \ge 0, \text{ and } \sqrt{(n^r)^2 + (n^z)^2} = 1. \tag{6.26} $$

Using Eq. (6.1), the normal vector in Cartesian coordinates is given by

$$ {}^{\mathrm{K}}\boldsymbol{n} = \begin{bmatrix} n_1 \\ n_2 \\ n_3 \end{bmatrix} = \begin{bmatrix} n^r\cos(\theta) \\ n^r\sin(\theta) \\ n^z \end{bmatrix}. \tag{6.27} $$

Therefore, with regard to the BC (6.16b), it holds

$$ \boldsymbol{\nabla}\, {}^{\mathrm{K}}\phi_{\mathrm{B}}^{(i)} \cdot {}^{\mathrm{K}}\boldsymbol{n} = n^r \underbrace{\left({}^{\mathrm{K}}\phi_{\mathrm{B},x}^{(i)} \cos(\theta) + {}^{\mathrm{K}}\phi_{\mathrm{B},y}^{(i)} \sin(\theta) \right)}_{={}^{\mathrm{Z}}\phi_{\mathrm{B},r}^{(i)}} + \underbrace{{}^{\mathrm{K}}\phi_{\mathrm{B},z}^{(i)}}_{={}^{\mathrm{Z}}\phi_{\mathrm{B},z}^{(i)}} n^z. \tag{6.28} $$

As a result of this and using the fact that the CFB can only perform translational motion in the vertical direction, the BC (6.19) at $\partial\bar{C}_3$ becomes in cylindrical coordinates

$$ {}^{\mathrm{Z}}\phi_{\mathrm{B},r}^{(i)} n^r + {}^{\mathrm{Z}}\phi_{\mathrm{B},z}^{(i)} n^z = -{}^{\mathrm{Z}}\phi_{0,r}^{(i)} n^r - {}^{\mathrm{Z}}\phi_{0,z}^{(i)} n^z + u_3^{(i)} n^z + V^{(i)}({}^{\mathrm{Z}}\phi_0^{(1)}, {}^{\mathrm{Z}}\phi_{\mathrm{B}}^{(1)}, \xi^{(1)}). \tag{6.29} $$

Here, $u_3^{(i)}$ is the component of $\boldsymbol{u}^{(i)}$ in the z-direction, i. e. $\boldsymbol{u}^{(i)} = \left[0,\, 0,\, u_3^{(i)}\right]^{\mathrm{T}}$.

In the same way, the BC (6.16e) can be transformed into cylindrical coordinates. Here, it has to be noted that the BC (6.16e) is valid on the vertical wall at $r = R_\Omega$. Therefore, the normal vector ${}^{\mathrm{Z}}\boldsymbol{n}$ has components only in r-direction, i. e. ${}^{\mathrm{Z}}\boldsymbol{n} = [1\,,\,0\,,\,0]^{\mathrm{T}}$. The BC (6.16e) becomes in cylindrical coordinates

$$ {}^{\mathrm{Z}}\phi^{(i)}_{\mathrm{B},r} = 0. \tag{6.30} $$

Since derivatives with respect to t and z do not change going from Cartesian to cylindrical coordinates, the BCs (6.16c) and (6.16d) do not change as well. Therefore, the governing equations (6.16) for computing the body disturbance velocity potentials $\phi^{(i)}_{\mathrm{B}}$, $i = 1, 2$, are given in cylindrical coordinates by

$$ {}^{\mathrm{Z}}\phi^{(i)}_{\mathrm{B},rr} + \frac{{}^{\mathrm{Z}}\phi^{(i)}_{\mathrm{B},r}}{r} + \frac{{}^{\mathrm{Z}}\phi^{(i)}_{\mathrm{B},\theta\theta}}{r^2} + {}^{\mathrm{Z}}\phi^{(i)}_{\mathrm{B},zz} = 0, \qquad \text{in } \mathring{\bar{\Omega}}_3, \tag{6.31a} $$

$$ \begin{aligned} {}^{\mathrm{Z}}\phi^{(i)}_{\mathrm{B},r} n^r + {}^{\mathrm{Z}}\phi^{(i)}_{\mathrm{B},z} n^z = &- {}^{\mathrm{Z}}\phi^{(i)}_{0,r} n^r - {}^{\mathrm{Z}}\phi^{(i)}_{0,z} n^z + u^{(i)}_3 n^z \\ &+ V^{(i)}({}^{\mathrm{Z}}\phi^{(1)}_0, {}^{\mathrm{Z}}\phi^{(1)}_{\mathrm{B}}, \xi^{(1)}), \end{aligned} \qquad \text{on } \partial\bar{C}_3, \tag{6.31b} $$

$$ {}^{\mathrm{Z}}\phi^{(i)}_{\mathrm{B},z} = 0, \qquad \text{on } \partial\bar{\Omega}_3 \cap \{z = -h\}, \tag{6.31c} $$

$$ {}^{\mathrm{Z}}\phi^{(i)}_{\mathrm{B},tt} + g\,{}^{\mathrm{Z}}\phi^{(i)}_{\mathrm{B},z} + 2\mu\,{}^{\mathrm{Z}}\phi^{(i)}_{\mathrm{B},t} + \mu^2\,{}^{\mathrm{Z}}\phi^{(i)}_{\mathrm{B}} = G^{(i)}({}^{\mathrm{Z}}\phi^{(1)}_0, {}^{\mathrm{Z}}\phi^{(1)}_{\mathrm{B}}), \quad \text{on } \partial\bar{\Omega}_3 \cap \{z = 0\}, \tag{6.31d} $$

$$ {}^{\mathrm{Z}}\phi^{(i)}_{\mathrm{B},r} = 0, \qquad \text{on } \partial\bar{\Omega}_3 \cap \{r = R_\Omega\}. \tag{6.31e} $$

Here, $\mathring{\bar{\Omega}}_3$ denotes the interior of $\bar{\Omega}_3$.

6.3.3 Step 3: Application of Fourier Transform

Finally, the velocity potential ${}^{\mathrm{Z}}\phi^{(i)}_{\mathrm{B}}$ is approximated by a Fourier series expansion. Since the solution ${}^{\mathrm{Z}}\phi^{(i)}_{\mathrm{B}}$ is periodic in θ, it can be approximated by a truncated Fourier series of the form

$$ {}^{\mathrm{Z}}\phi^{(i)}_{\mathrm{B}}(r, \theta, z, t) = \sum_{m=-N_{\mathrm{F}}/2}^{N_{\mathrm{F}}/2-1} {}^{\mathrm{Z}}\widehat{\phi}^{(i)}_{\mathrm{B},m}(r, z, t) \mathrm{e}^{\mathrm{i}m\theta}. \tag{6.32} $$

Here, the complex Fourier coefficients ${}^{\mathrm{Z}}\widehat{\phi}^{(i)}_{\mathrm{B},m}$ are given by

$$ {}^{\mathrm{Z}}\widehat{\phi}^{(i)}_{\mathrm{B},m}(r, z, t) = \frac{1}{N_{\mathrm{F}}} \sum_{j=0}^{N_{\mathrm{F}}-1} {}^{\mathrm{Z}}\phi^{(i)}_{\mathrm{B}}(r, \theta_j, z, t) \mathrm{e}^{-\mathrm{i}m\theta_j}, \tag{6.33} $$

whereby $\theta_j = 2j\pi/N_{\mathrm{F}}$ and N_{F} is the number of grid points along a circle. If N_{F} is a power of two, the transformation mentioned above between the physical

space and Fourier space can be efficiently implemented using the algorithm of the fast Fourier transform (FFT), which has been introduced in [CooleyTukey65]. Using the FFT algorithm, the transformation mentioned above can be performed with $\mathcal{O}(N_\mathrm{F} \log_2(N_\mathrm{F}))$ arithmetic operations.

Next, equations for the Fourier coefficients ${}^{\mathrm{Z}}\widehat{\phi}^{(i)}_{\mathrm{B},m}$ are derived by substituting Eq. (6.32) into Eq. (6.31). Since the functions $\mathrm{e}^{\mathrm{i}m_1\theta}$ and $\mathrm{e}^{\mathrm{i}m_2\theta}$ are independent of each other for $m_1 \neq m_2$, the Fourier coefficients ${}^{\mathrm{Z}}\widehat{\phi}^{(i)}_{\mathrm{B},m_1}$ and ${}^{\mathrm{Z}}\widehat{\phi}^{(i)}_{\mathrm{B},m_2}$ can also be computed independently of each other. Substituting Eq. (6.32) into Eq. (6.31) shows that the Fourier coefficients ${}^{\mathrm{Z}}\widehat{\phi}^{(i)}_{\mathrm{B},m}$, $m = -\frac{N_\mathrm{F}}{2}, \ldots, \frac{N_\mathrm{F}}{2} - 1$, have to satisfy

$$ {}^{\mathrm{Z}}\widehat{\phi}^{(i)}_{\mathrm{B},m,rr} + \frac{{}^{\mathrm{Z}}\widehat{\phi}^{(i)}_{\mathrm{B},m,r}}{r} - \frac{m^2}{r^2}\,{}^{\mathrm{Z}}\widehat{\phi}^{(i)}_{\mathrm{B},m} + {}^{\mathrm{Z}}\widehat{\phi}^{(i)}_{\mathrm{B},m,zz} = 0, \quad \text{in } \mathring{\bar{\Omega}}_2, \tag{6.34a} $$

$$ {}^{\mathrm{Z}}\widehat{\phi}^{(i)}_{\mathrm{B},m,r} n^r + {}^{\mathrm{Z}}\widehat{\phi}^{(i)}_{\mathrm{B},m,z} n^z = -{}^{\mathrm{Z}}\widehat{\phi}^{(i)}_{0,m,r} n^r - {}^{\mathrm{Z}}\widehat{\phi}^{(i)}_{0,m,z} n^z + u_3^{(i)} n^z \widehat{1}_m + \widehat{V}^{(i)}_m, \quad \text{on } \partial\bar{C}_2, \tag{6.34b} $$

$$ {}^{\mathrm{Z}}\widehat{\phi}^{(i)}_{\mathrm{B},m,z} = 0, \quad \text{on } \partial\bar{\Omega}_2 \cap \{z = -h\}, \tag{6.34c} $$

$$ {}^{\mathrm{Z}}\widehat{\phi}^{(i)}_{\mathrm{B},m,tt} + g\,{}^{\mathrm{Z}}\widehat{\phi}^{(i)}_{\mathrm{B},m,z} + 2\mu\,{}^{\mathrm{Z}}\widehat{\phi}^{(i)}_{\mathrm{B},m,t} + \mu^2\,{}^{\mathrm{Z}}\widehat{\phi}^{(i)}_{\mathrm{B},m} = \widehat{G}^{(i)}_m, \quad \text{on } \partial\bar{\Omega}_2 \cap \{z = 0\}, \tag{6.34d} $$

$$ {}^{\mathrm{Z}}\widehat{\phi}^{(i)}_{\mathrm{B},m,r} = 0, \quad \text{on } \partial\bar{\Omega}_2 \cap \{r = R_\Omega\}. \tag{6.34e} $$

Here, the sets $\bar{\Omega}_2$ and $\bar{C}_2$ are defined by

$$ \bar{\Omega}_2 := \{(r,z) \in \mathbb{R}^2 \mid (r,\theta,z) \in \bar{\Omega}_3,\ 0 < \theta \leq 2\pi\}, \text{ and} \tag{6.35a} $$

$$ \bar{C}_2 := \{(r,z) \in \mathbb{R}^2 \mid (r,\theta,z) \in \bar{C}_3,\ 0 < \theta \leq 2\pi\}. \tag{6.35b} $$

Furthermore, the respective m-th Fourier coefficient of the incident velocity potential ${}^{\mathrm{Z}}\widehat{\phi}_{0,m}$ and the right-hand side functions $\widehat{G}^{(i)}_m$ and $\widehat{V}^{(i)}_m$ is defined similarly to Eq. (6.33). Furthermore, $\widehat{1}_m$ is the m-th Fourier coefficient of the constant function $f(r,\theta,z) = 1$. The Fourier coefficient $\widehat{1}_m$ has to be considered in BC (6.34b), since the term $u_3^{(i)} n^z$ is independent of θ.

A sketch of the domains $\bar{C}_2$ and $\bar{\Omega}_2$ is shown in Fig. 6.4 along with Eq. (6.34). For a better understanding of the components n^r and n^z of the normal vector ${}^{\mathrm{Z}}\boldsymbol{n}$, which is pointing into the domain $\bar{C}_2$, the vector ${}^{\mathrm{Z}}\tilde{\boldsymbol{n}} := [n^r, n^z]^{\mathrm{T}}$ is shown in Fig. 6.4 as well.

Considering Fig. 6.4, it has to be noted that no BC has yet been defined at the boundary $(r,z) = \{0\} \times [-h,-d]$, where Eq. (6.34a) contains a singularity. However, as will be shown in Sect. 6.4.1, it is not necessary to define a BC at $r = 0$ to compute the Fourier coefficients ${}^{\mathrm{Z}}\widehat{\phi}^{(i)}_{\mathrm{B},m}$ numerically.

All in all, it can be seen that the velocity potentials ${}^{\mathrm{Z}}\phi^{(i)}_{\mathrm{B}}$, $i = 1, 2$, can be computed by solving Eq. (6.34) for the Fourier coefficients ${}^{\mathrm{Z}}\widehat{\phi}^{(i)}_{\mathrm{B},m}$, $m = -\frac{N_\mathrm{F}}{2}, \ldots, \frac{N_\mathrm{F}}{2} - 1$, and using Eq. (6.32) to get back from the Fourier space to the physical space.

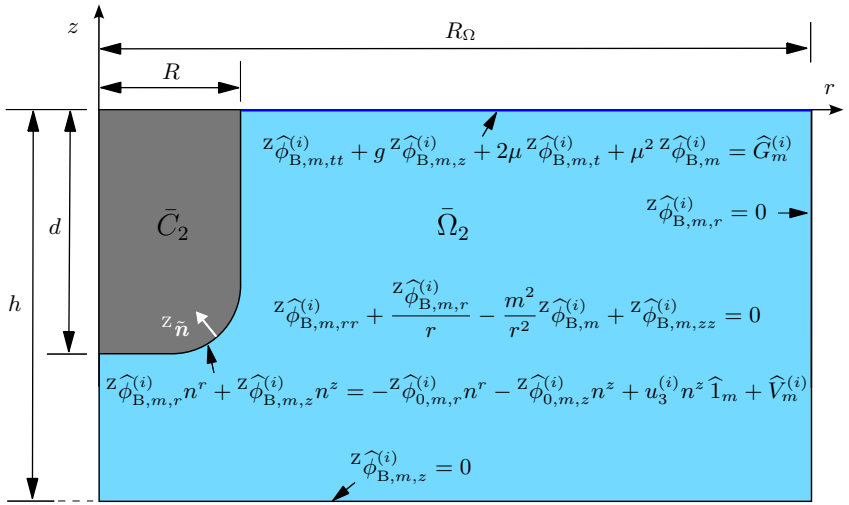

Figure 6.4: Sketch of the domains $\bar{C}_2$ and $\bar{\Omega}_2$ together with the PDE and BCs, which have to be solved to compute ${}^{\mathrm{Z}}\widehat{\phi}^{(i)}_{\mathrm{B},m}$.

In this way, the problem of computing the velocity potentials ${}^{\mathrm{Z}}\phi^{(i)}_{\mathrm{B}}$ in a three-dimensional spatial domain was simplified to computing N_F Fourier coefficients in a two-dimensional spatial domain. However, it has to be noted that the computational effort can be reduced even further. Since ${}^{\mathrm{Z}}\phi^{(i)}_{\mathrm{B}} \in \mathbb{R}$, it holds

$$\begin{aligned}\left({}^{\mathrm{Z}}\widehat{\phi}^{(i)}_{\mathrm{B},-m}(r,z,t)\right)^* &= \left(\frac{1}{N_\mathrm{F}}\sum_{j=0}^{N_\mathrm{F}-1}\underbrace{{}^{\mathrm{Z}}\phi^{(i)}_{\mathrm{B}}(r,\theta_j,z,t)}_{\in\mathbb{R}}\,\mathrm{e}^{\mathrm{i}m\theta_j}\right)^* \\ &= \frac{1}{N_\mathrm{F}}\sum_{j=0}^{N_\mathrm{F}-1}{}^{\mathrm{Z}}\phi^{(i)}_{\mathrm{B}}(r,\theta_j,z,t)\mathrm{e}^{-\mathrm{i}m\theta_j} = {}^{\mathrm{Z}}\widehat{\phi}^{(i)}_{\mathrm{B},m}(r,z,t).\end{aligned} \tag{6.36}$$

Therefore, it is not necessary to calculate all N_F Fourier coefficients ${}^{\mathrm{Z}}\widehat{\phi}^{(i)}_{\mathrm{B},m}$, $m = -\frac{N_\mathrm{F}}{2},\ldots,\frac{N_\mathrm{F}}{2}-1$, numerically. Instead, the Fourier coefficients ${}^{\mathrm{Z}}\widehat{\phi}^{(i)}_{\mathrm{B},m}$, $m = -\frac{N_\mathrm{F}}{2},\ldots,-1$, can be computed by taking the complex conjugate of ${}^{\mathrm{Z}}\widehat{\phi}^{(i)}_{\mathrm{B},m}$, $m = 1,\ldots,\frac{N_\mathrm{F}}{2}$. It follows that only the coefficients ${}^{\mathrm{Z}}\widehat{\phi}^{(i)}_{\mathrm{B},m}$, $m = 0,\ldots,\frac{N_\mathrm{F}}{2}$, have to be computed to calculate the velocity potential ${}^{\mathrm{Z}}\phi^{(i)}_{\mathrm{B}}$ corresponding to the body disturbance in cylindrical coordinates. In this way, the computational effort is reduced by half.

6.4 Numerical Computation of the Body Disturbance Velocity Potential ϕ_{B}

So far, it has been shown how the computational effort for calculating the velocity potential of the body disturbance, ϕ_{B}, can be reduced. Here, it has been assuming that the CFB only performs translational motion in the vertical direction and that the computational domain $\bar{\Omega}_3$ is rotationally symmetric along the vertical axis. Solving Eq. (6.34), the Fourier coefficients ${}^{\mathrm{Z}}\widehat{\phi}^{(i)}_{\mathrm{B},m}$ of the velocity potentials ${}^{\mathrm{Z}}\phi^{(i)}_{\mathrm{B}}$ are computed. In this section, a finite difference scheme is presented, which is used to discretize Eq. (6.34) and to compute the Fourier coefficients ${}^{\mathrm{Z}}\widehat{\phi}^{(i)}_{\mathrm{B},m}$. Here, only one index $m \in \{-\frac{N_{\mathrm{F}}}{2}, \ldots, \frac{N_{\mathrm{F}}}{2} - 1\}$ and $i \in \{1, 2\}$ is considered. In order to simplify the notation for readability, the indices Z, m, (i) and B are omitted in this section, i. e. ${}^{\mathrm{Z}}\widehat{\phi}^{(i)}_{\mathrm{B},m}$ becomes simply $\widehat{\phi}$.

For some numbers $N, M, P \in \mathbb{N}$ and some time $T \in \mathbb{R}_+$, the solution $\widehat{\phi}$ is computed on the (r, z, t)-grid with the grid points

$$\begin{aligned} &0 < r_1 < r_2 < \ldots < r_{N+1} = R_\Omega, \\ &0 = z_1 > z_2 > \ldots > z_{M+1} = -h, \\ &0 = t^1 < t^2 < \ldots < t^{P+1} = T. \end{aligned} \tag{6.37}$$

For $i = 1, \ldots, N+1$, $j = 1, \ldots, M+1$ and $p = 1, \ldots, P+1$, the grid points are defined as

$$r_i := (i - \frac{1}{2})\Delta r, \quad z_j := -(j-1)\Delta z, \quad t^p := (p-1)\Delta t, \tag{6.38}$$

with

$$\Delta r := \frac{R_\Omega}{N + 1/2}, \ \Delta z := \frac{h}{M}, \ \Delta t := \frac{T}{P}. \tag{6.39}$$

Furthermore, $N_{\mathrm{i}} \in \mathbb{N}$ is chosen such that $r_{N_{\mathrm{i}}} < R \leq r_{N_{\mathrm{i}}+1}$. Since R is the radius of the CFB at the still water level, this means that N_{i} denotes the number of grid points inside the CFB at the level of the still water surface. Therefore, $(r_{N_{\mathrm{i}}+1}, z = 0)$ is the first point at the level of the still water surface, which is located outside the CFB or at the boundary of the CFB.

Using the chosen grid in r, which has also been used in [LaiEtAl02], it holds $r_1 = \frac{\Delta r}{2}$. Therefore, the polar singularity at $r = 0$, which would occur dealing with Eq. (6.34a), is omitted. Furthermore, it is shown in Sect. 6.4.1 that Eq. (6.34a) can be discretized at (r_1, z_j) without introducing some BC at $(r, z) = \{0\} \times [-h, -d]$.

The numerical approximation of $\widehat{\phi}$ at the space point (r_i, z_j) and time point t^p is defined by $\widehat{\phi}^p_{i,j}$, i. e. $\widehat{\phi}^p_{i,j} \approx \widehat{\phi}(r_i, z_j, t^p)$. In the following, Eq. (6.34) is discretized to compute numerically the solution $\widehat{\phi}^p_{i,j}$ at time point t^p at all $(N+1)(M+1)$ space points (r_i, z_j), $i = 1, \ldots, N+1$, $j = 1, \ldots, M+1$. It has to be noted that

some of these $(N+1)(M+1)$ space points are located in $\bar{C}_2$. Most unknowns $\widehat{\phi}^p_{i,j}$ corresponding to these points located inside the CFB are set to zero. However, it is necessary that interior grid points (r_i, z_j) in $\bar{C}_2$, which have at least one horizontal or vertical neighbor in $\mathring{\bar{\Omega}}_2$, must be treated separately. These points are needed to compute the unknowns $\widehat{\phi}^p_{i,j}$, which have a neighbor in $\bar{C}_2$. Points (r_i, z_j) in $\bar{C}_2$, which have at least one horizontal or vertical neighbor in $\mathring{\bar{\Omega}}_2$, are so-called ghost points.
Figure 6.5 shows the resulting spatial grid defined in Eq. (6.37) and the CFB, which is considered in this chapter. The mentioned ghost points are colored green. The boundary $\partial\bar{C}_2$ of the CFB is colored blue and the boundary $\partial\bar{\Omega}_2 \setminus \partial\bar{C}_2$ is colored red. Using the grid, which is defined in Eq. (6.37), Eq. (6.34) is discretized in the following using a finite difference method with an accuracy of second order in time and space.

6.4.1 Laplace Equation Inside the Fluid

At grid points $(r_i, z_j) \in \mathring{\bar{\Omega}}_2$, which are located inside the fluid, it holds at time point t^p

$$\widehat{\phi}_{rr} + \frac{\widehat{\phi}_r}{r_i} - \frac{m^2}{r_i^2}\widehat{\phi} + \widehat{\phi}_{zz} = 0, \tag{6.40}$$

see Eq. (6.34a). In order to discretize Eq. (6.40), a central finite difference approximation of second order is applied. The corresponding approximation has also been used in [LaiEtAl02]. At the grid point $(r_i, z_j) \in \mathring{\bar{\Omega}}_2$ and timpoint t^p, the corresponding approximation of Eq. (6.40) reads

$$\begin{aligned}\frac{\widehat{\phi}^p_{i+1,j} - 2\widehat{\phi}^p_{i,j} + \widehat{\phi}^p_{i-1,j}}{\Delta r^2} + \frac{1}{r_i}\frac{\widehat{\phi}^p_{i+1,j} - \widehat{\phi}^p_{i-1,j}}{2\Delta r} \\ - \frac{m^2}{r_i^2}\widehat{\phi}^p_{i,j} + \frac{\widehat{\phi}^p_{i,j+1} - 2\widehat{\phi}^p_{i,j} + \widehat{\phi}^p_{i,j-1}}{\Delta z^2} = 0.\end{aligned} \tag{6.41}$$

Note that for $i = 1$, the grid points $(r_i, z_j) \in \mathring{\bar{\Omega}}_2$ do not have a neighbor in the negative r-direction. However, for $i = 1$, all terms depending on $\widehat{\phi}^p_{i-1,j}$ simplify to

$$\left[\frac{1}{\Delta r^2} - \frac{1}{2r_i\Delta r}\right]\widehat{\phi}^p_{i-1,j} \overset{r_i=\frac{\Delta r}{2}}{=} \left[\frac{1}{\Delta r^2} - \frac{1}{\Delta r^2}\right]\widehat{\phi}^p_{i-1,j} = 0. \tag{6.42}$$

Therefore, the values of $\widehat{\phi}^p_{i-1,j}$ are not needed for $i = 1$, and the approximation from Eq. (6.41) can also be applied for $i = 1$.
However, at all other grid points $(r_i, z_j) \in \mathring{\bar{\Omega}}_2$ with some neighboring point $(r_{i\pm1}, z_{j\pm1}) \notin \mathring{\bar{\Omega}}_2$, a corresponding BC has to be discretized. This is done in the following.

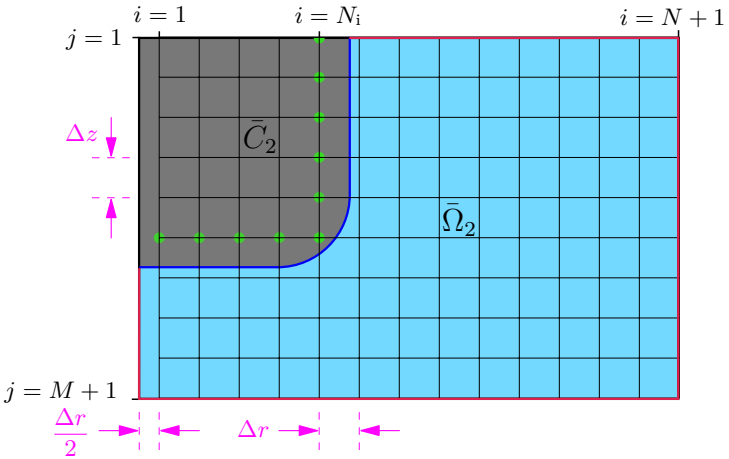

Figure 6.5: Sketch of the discretized computational domain using the grid, which is defined in Eq. (6.37). Ghost points are colored green, the boundary $\partial\bar{C}_2$ of the CFB is colored blue, and the boundary $\partial\bar{\Omega}_2 \setminus \partial\bar{C}_2$ is colored red.

6.4.2 Boundary Conditions at the Outer Boundary and Bottom of the Sea

For $r_{N+1} = R_\Omega$, $-h \leq z_j \leq 0$, and time point t^p, the BC at the outer boundary is given by Eq. (6.34e) and reads

$$\widehat{\phi}_r = 0. \tag{6.43}$$

Furthermore, for $0 \leq r_i \leq R_\Omega$, $z_{M+1} = -h$, and time point t^p, the BC at the bottom of the sea is given by Eq. (6.34c) and reads

$$\widehat{\phi}_z = 0. \tag{6.44}$$

The respective second-order approximations of Eqs. (6.43) and (6.44) at the outer boundary and the bottom of the sea are given by

$$\frac{\widehat{\phi}_{N-1,j} - 4\widehat{\phi}_{N,j} + 3\widehat{\phi}_{N+1,j}}{2\Delta r} = 0, \quad \text{for} \quad j = 1, \ldots, M+1, \tag{6.45}$$

$$\frac{\widehat{\phi}_{i,M-1} - 4\widehat{\phi}_{i,M} + 3\widehat{\phi}_{i,M+1}}{2\Delta z} = 0, \quad \text{for} \quad i = 1, \ldots, N+1. \tag{6.46}$$

It has to be noted that both Eqs. (6.45) and (6.46) can be applied at the corner point (r_{N+1}, z_{M+1}). Therefore, two equations can be used to compute the unknown $\widehat{\phi}_{N+1,M+1}$. In this thesis, the sum of those two equations is used to obtain a single equation that is used to calculate $\widehat{\phi}_{N+1,M+1}$.

6.4.3 Boundary Condition at the Sea Surface

For $z_1 = 0$, $R \leq r_i \leq R_\Omega$, and time point t^p, the BC at the sea surface is given by Eq. (6.34d) and reads

$$\widehat{\phi}_{tt} + g\widehat{\phi}_z + 2\mu\widehat{\phi}_t + \mu^2\widehat{\phi} = \widehat{G}. \tag{6.47}$$

Equation (6.47) is the only BC summarized in Eq. (6.34) that contains derivatives with respect to time t. Therefore, not only space derivatives must be discretized, but also the time derivative $\widehat{\phi}_{tt}$. In the following, a discretization of Eq. (6.47) is performed, which is accurate up to second order in time and space.
A second-order approximation of the derivative $\widehat{\phi}_{tt}$ is given by

$$\widehat{\phi}_{tt}(r_i, z_1, t^p) = \frac{\widehat{\phi}(r_i, z_1, t^{p+1}) - 2\widehat{\phi}(r_i, z_1, t^p) + \widehat{\phi}(r_i, z_1, t^{p-1})}{\Delta t^2} + \mathcal{O}(\Delta t^2) \tag{6.48}$$

for $i = N_\mathrm{i} + 1, \ldots, N + 1$. For the term $\widehat{\phi}_z$ in Eq. (6.47), it has to be decided at which time point $\widehat{\phi}_z$ is evaluated. In the following, an implicit discretization of Eq. (6.47) is considered since it offers much better stability than an explicit discretization. Since a system of equations must be solved anyway when discretizing Eq. (6.40) by the scheme presented in Eq. (6.41), an implicit discretization of Eq. (6.48) increases the computational effort only slightly. An implicit scheme, which is used to discretize Eq. (6.47) accurately up to second order in time, is given by

$$\begin{aligned}
&\frac{\widehat{\phi}(r_i, z_1, t^{p+1}) - 2\widehat{\phi}(r_i, z_1, t^p) + \widehat{\phi}(r_i, z_1, t^{p-1})}{\Delta t^2} \\
&\quad + g\frac{\widehat{\phi}_z(r_i, z_1, t^{p+1}) + 2\widehat{\phi}_z(r_i, z_1, t^p) + \widehat{\phi}_z(r_i, z_1, t^{p-1})}{4} \\
&\quad + 2\mu(r_i)\frac{\widehat{\phi}(r_i, z_1, t^{p+1}) - \widehat{\phi}(r_i, z_1, t^{p-1})}{2\Delta t} \\
&\quad + \mu^2(r_i)\frac{\widehat{\phi}(r_i, z_1, t^{p+1}) + 2\widehat{\phi}(r_i, z_1, t^p) + \widehat{\phi}(r_i, z_1, t^{p-1})}{4} = \widehat{G}(r_i, z_1, t^p)
\end{aligned} \tag{6.49}$$

for $i = N_\mathrm{i} + 1, \ldots, N + 1$. Here, the second-order accuracy in time follows from the Taylor series expansion

$$\widehat{\phi}(r_i, z_1, t^{p+1}) = \widehat{\phi}(r_i, z_1, t^p) + \Delta t\widehat{\phi}_t(r_i, z_1, t^p) + \frac{\Delta t^2}{2}\widehat{\phi}_{tt}(r_i, z_1, t^p) + \mathcal{O}(\Delta t^3), \tag{6.50}$$

which results in

$$\begin{aligned}
&\frac{\widehat{\phi}(r_i, z_1, t^{p+1}) + 2\widehat{\phi}(r_i, z_1, t^p) + \widehat{\phi}(r_i, z_1, t^{p-1})}{4} \\
&\qquad = \widehat{\phi}(r_i, z_1, t^p) + \frac{\Delta t^2}{4}\widehat{\phi}_{tt}(r_i, z_1, t^p) + \mathcal{O}(\Delta t^3).
\end{aligned} \tag{6.51}$$

In Eq. (6.49), the derivative $\widehat{\phi}_z$ still needs to be discretized at the time points t^{p-1}, t^p and t^{p+1}. This is done using backward differences in the z-direction of second order. The resulting numerical scheme to discretize the BC (6.47) at $z = 0$ is given by

$$\begin{aligned}
&\frac{\widehat{\phi}_{i,1}^{p+1} - 2\widehat{\phi}_{i,1}^{p} + \widehat{\phi}_{i,1}^{p-1}}{\Delta t^2} + \frac{g}{4}\left\{ \frac{3\widehat{\phi}_{i,1}^{p+1} - 4\widehat{\phi}_{i,2}^{p+1} + \widehat{\phi}_{i,3}^{p+1}}{2\Delta z} + 2\frac{3\widehat{\phi}_{i,1}^{p} - 4\widehat{\phi}_{i,2}^{p} + \widehat{\phi}_{i,3}^{p}}{2\Delta z} \right. \\
&\quad \left. + \frac{3\widehat{\phi}_{i,1}^{p-1} - 4\widehat{\phi}_{i,2}^{p-1} + \widehat{\phi}_{i,3}^{p-1}}{2\Delta z} \right\} + 2\mu_i \frac{\widehat{\phi}_{i,1}^{p+1} - \widehat{\phi}_{i,1}^{p-1}}{2\Delta t} + \mu_i^2 \frac{\widehat{\phi}_{i,1}^{p+1} + 2\widehat{\phi}_{i,1}^{p} + \widehat{\phi}_{i,1}^{p-1}}{4} \\
&\quad = \widehat{G}(r_i, z_1, t^p), \quad \text{for } i = N_\mathrm{i} + 1, \ldots, N + 1,
\end{aligned} \tag{6.52}$$

whereby $\mu_i := \mu(r_i)$. In order to compute the solution at $p+1 = 1$, corresponding initial values $\widehat{\phi}_{i,j}^{0}$, $\widehat{\phi}_{i,j}^{-1}$, $j = 1, 2, 3$, have to be defined. In the further course of this thesis, corresponding initial values $\widehat{\phi}_{i,j}^{0}$, $\widehat{\phi}_{i,j}^{-1}$ are always stated when numerical results are presented.

The overall consistency order of the proposed scheme from Eq. (6.52) can be obtained using two-dimensional Taylor series expansions with respect to t and z. Substituting the resulting Taylor series expansion into the numerical scheme from Eq. (6.52), the consistency error of the scheme from Eq. (6.52) can be computed to be

$$\begin{aligned}
&\frac{\widehat{\phi}(r_i, z_1, t^{p+1}) - 2\widehat{\phi}(r_i, z_1, t^p) + \widehat{\phi}(r_i, z_1, t^{p-1})}{\Delta t^2} \\
&\quad + \frac{g}{4}\left\{ \frac{3\widehat{\phi}(r_i, z_1, t^{p+1}) - 4\widehat{\phi}(r_i, z_2, t^{p+1}) + \widehat{\phi}(r_i, z_3, t^{p+1})}{2\Delta z} \right. \\
&\qquad + 2\frac{3\widehat{\phi}(r_i, z_1, t^{p}) - 4\widehat{\phi}(r_i, z_2, t^{p}) + \widehat{\phi}(r_i, z_3, t^{p})}{2\Delta z} \\
&\qquad \left. + \frac{3\widehat{\phi}(r_i, z_1, t^{p-1}) - 4\widehat{\phi}(r_i, z_2, t^{p-1}) + \widehat{\phi}(r_i, z_3, t^{p-1})}{2\Delta z} \right\} \\
&\quad + 2\mu(r_i)\frac{\widehat{\phi}(r_i, z_1, t^{p+1}) - \widehat{\phi}(r_i, z_1, t^{p-1})}{2\Delta t} \\
&\quad + \mu^2(r_i)\frac{\widehat{\phi}(r_i, z_1, t^{p+1}) + 2\widehat{\phi}(r_i, z_1, t^{p}) + \widehat{\phi}(r_i, z_1, t^{p-1})}{4} - \widehat{G}(r_i, z_1, t^p) \\
&= 0 + \Delta t^2 \left\{ \frac{\widehat{\phi}_{tt}}{12} + \frac{g\widehat{\phi}_{ztt}}{4} + \frac{\mu\widehat{\phi}_{ttt}}{3} + \frac{\mu^2\widehat{\phi}_{tt}}{4} \right\} - \frac{g\Delta z^2}{3}\widehat{\phi}_{zzz} + \ldots
\end{aligned} \tag{6.53}$$

Here, all derivatives of $\widehat{\phi}$, which appear in the last line of Eq. (6.53), are evaluated at (r_i, z_1, t^p). Equation (6.53) proves that the proposed method has a consistency error of second order in time and space.

It has to be noted that both Eqs. (6.45) and (6.52) can be applied at the corner point (r_{N+1}, z_1). Therefore, two equations can be used to compute $\widehat{\phi}_{N+1,1}$. To make the computation rule for $\widehat{\phi}_{N+1,1}$ uniquely defined, similar to Sect. 6.4.2, the sum of those two equations is used to obtain a single equation that is used to calculate $\widehat{\phi}_{N+1,1}$.

6.4.4 Boundary Condition at the Surface of the Cylindrical Floating Body

In Sect. 6.4.1, the Laplace equation (6.40) has been discretized at all grid points $(r_i, z_j) \in \mathring{\bar{\Omega}}_2$. However, at grid points, which are neighbored to the boundary $\partial\bar{C}_2$ of the CFB, the discretization of the Laplace equation (6.40) needs information of the unknown $\widehat{\phi}$ located inside the CFB. As already mentioned at the beginning of Sect. 6.4, corresponding points $(r_i, z_j) \in \bar{C}_2$, which have at least one horizontal or vertical neighbor in $\mathring{\bar{\Omega}}_2$, are called ghost points. In Fig. 6.5, ghost points have been marked in green. In this section, equations are derived to compute the unknown $\widehat{\phi}$ at the ghost points inside the CFB. For this, the BC at the boundary $\partial\bar{C}_2$ of the CFB at time point t^p is discretized. The corresponding BC is given by Eq. (6.34b) and reads

$$\widehat{\phi}_r n^r + \widehat{\phi}_z n^z = -\widehat{\phi}_{0,r} n^r - \widehat{\phi}_{0,z} n^z + u_3 n^z \widehat{1} + \widehat{V}. \tag{6.54}$$

The approach of discretizing the BC (6.54) using ghost points is similar to that approach used in [CocoRusso13]. Here, the authors present a numerical method for solving elliptic equations in an arbitrarily shaped domain on Cartesian grids using finite difference discretization and non-eliminated ghost values.
Let $\mathcal{G}$ be the set of all ghost points and grid points on the boundary of the CFB, i. e.

$$\begin{aligned}\mathcal{G} := \big\{ \boldsymbol{g} = (r_i, z_j),\, (i,j) \in \{1,\dots,N+1\} \times \{1,\dots,M+1\} \mid \\ \boldsymbol{g} \in \partial\bar{C}_2 \vee \big(\boldsymbol{g} \in \bar{C}_2 \wedge (r_{i\pm1}, z_j) \in \bar{\Omega}_2\big) \vee \big(\boldsymbol{g} \in \bar{C}_2 \wedge (r_i, z_{j\pm1}) \in \bar{\Omega}_2\big) \big\}.\end{aligned} \tag{6.55}$$

Let $\boldsymbol{g} = (r_i, z_j) \in \mathcal{G}$ and let $\boldsymbol{p}$ be the nearest point to $\boldsymbol{g}$ on $\partial\bar{C}_2$, i. e.

$$\boldsymbol{p} \in \partial\bar{C}_2, \quad \text{such that} \quad \boldsymbol{p} = \underset{\boldsymbol{x} \in \partial\bar{C}_2}{\operatorname{argmin}} \, ||\boldsymbol{x} - \boldsymbol{g}||_2 \,. \tag{6.56}$$

Here, $||\boldsymbol{x}||_2 = \sqrt{\boldsymbol{x} \cdot \boldsymbol{x}}$ denotes the Euclidean norm of the vector $\boldsymbol{x}$. Let $\tilde{\boldsymbol{n}} = (n^r, n^z)$ be the normal vector in $\boldsymbol{p}$ at $\partial\bar{C}_2$, which points inside the CFB. Furthermore, let $\boldsymbol{\delta} := \boldsymbol{p} - \boldsymbol{g} = (\delta^r, \delta^z)$ be the directional distance from $\boldsymbol{g}$ to the boundary $\partial\bar{C}_2$. For $\boldsymbol{g} \notin \partial\bar{C}_2$, it holds $\tilde{\boldsymbol{n}} = -\boldsymbol{\delta} / ||\boldsymbol{\delta}||_2$. Figure 6.6a shows for one considered ghost point $\boldsymbol{g} \in \mathcal{G}$ the nearest point $\boldsymbol{p} \in \partial\bar{C}_2$, the distance vector $-\boldsymbol{\delta}$ from $\boldsymbol{p}$ to $\boldsymbol{g}$, and the normal vector $\tilde{\boldsymbol{n}}$ in $\boldsymbol{p}$ at $\partial\bar{C}_2$.

It has to be noted that the vectors $\boldsymbol{p}$, $\boldsymbol{\delta}$, and $\tilde{\boldsymbol{n}}$ depend on the point $\boldsymbol{g}$. However, to simplify the notation, it is refrained to give the vectors $\boldsymbol{p}$, $\boldsymbol{\delta}$, and $\tilde{\boldsymbol{n}}$ a corresponding index.
Moreover, it has to be noted that the boundary $\partial\bar{C}_2$ passes through at least one of the cells, which is adjacent to $\boldsymbol{g}$, see Fig. 6.6a. It results $||\boldsymbol{\delta}||_2 \leq \sqrt{\Delta r^2 + \Delta z^2}$. Therefore, defining $\Delta_{\mathrm{M}} := \max(\Delta r, \Delta z)$, it holds $\mathcal{O}(||\boldsymbol{\delta}||_2) = \mathcal{O}(\Delta_{\mathrm{M}})$.
In the following, it is assumed that $\boldsymbol{g}$, $\boldsymbol{p}$ and $\tilde{\boldsymbol{n}}$ are known. Since $\boldsymbol{p} \in \partial\bar{C}_2$, the BC (6.54) also holds at $\boldsymbol{p}$. Therefore, an approximation of the term $\widehat{\phi}_r n^r + \widehat{\phi}_z n^z$ at $\boldsymbol{p}$ has to be found using the value of $\widehat{\phi}$ at $\boldsymbol{g}$ and other grid points. In order to approximate the term $\widehat{\phi}_r n^r + \widehat{\phi}_z n^z$ at $\boldsymbol{p}$, the grid points (r_i, z_j) are used, which correspond to the index set

$$\mathcal{I} := \{(i,j), (i+1,j), (i+2,j), (i,j+1), (i,j+2), (i+1,j+1)\}. \tag{6.57}$$

Figure 6.6b shows for one ghost point $\boldsymbol{g} \in \mathcal{G}$ the corresponding point $\boldsymbol{p} \in \partial\bar{C}_2$, and the grid points corresponding to the index set $\mathcal{I}$.
In order to approximate the value of $\widehat{\phi}_r n^r + \widehat{\phi}_z n^z$ at $\boldsymbol{p}$ using the value of $\widehat{\phi}$ at the grid points defined by $\mathcal{I}$, Taylor series expansion of $\widehat{\phi}$ around $\boldsymbol{p}$ are used. Let $(a,b) \in \{(0,0), (1,0), (2,0), (0,-1), (0,-2), (1,-1)\}$. Using $\boldsymbol{g} = \boldsymbol{p} - \boldsymbol{\delta}$, it

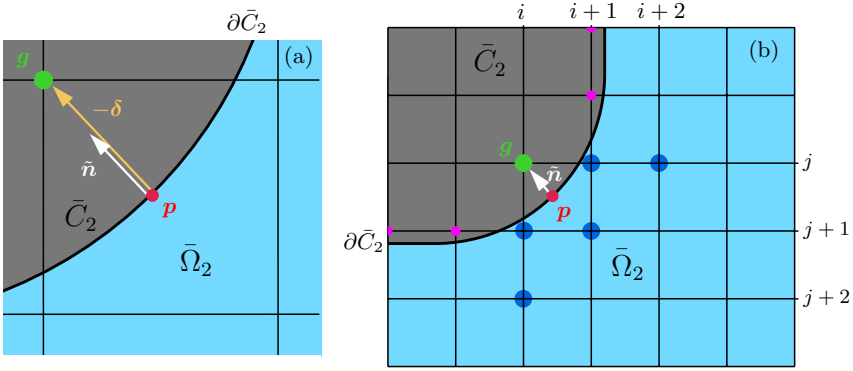

Figure 6.6: (a): One ghost point $\boldsymbol{g} \in \mathcal{G}$ and the corresponding nearest point $\boldsymbol{p} \in \partial\bar{C}_2$, distance vector $-\boldsymbol{\delta}$ from $\boldsymbol{p}$ to $\boldsymbol{g}$, and normal vector $\tilde{\boldsymbol{n}}$ in $\boldsymbol{p}$ at $\partial\bar{C}_2$. (b): Grid points, which correspond to the set $\mathcal{I}$ from Eq. (6.57). The considered ghost point $\boldsymbol{g} \in \mathcal{G}$ is colored green, the nearest point $\boldsymbol{p} \in \partial\bar{C}_2$ is colored red, and the grid points corresponding to the index set $\mathcal{I}$ are colored blue. Other ghost points in $\mathcal{G}$ are colored purple.

holds

$$\begin{aligned}\widehat{\phi}\left(\boldsymbol{g}+\begin{bmatrix}a\Delta r\\ b\Delta z\end{bmatrix}\right) &= \widehat{\phi}\left(\boldsymbol{p}-\boldsymbol{\delta}+\begin{bmatrix}a\Delta r\\ b\Delta z\end{bmatrix}\right) = \widehat{\phi}\left(\boldsymbol{p}+\begin{bmatrix}a\Delta r-\delta^r\\ b\Delta z-\delta^z\end{bmatrix}\right)\\ &= \widehat{\phi}(\boldsymbol{p}) + (a\Delta r-\delta^r)\widehat{\phi}_r(\boldsymbol{p}) + (b\Delta z-\delta^z)\widehat{\phi}_z(\boldsymbol{p})\\ &\quad + \frac{(a\Delta r-\delta^r)^2}{2}\widehat{\phi}_{rr}(\boldsymbol{p}) + (a\Delta r-\delta^r)(b\Delta z-\delta^z)\widehat{\phi}_{rz}(\boldsymbol{p})\\ &\quad + \frac{(b\Delta z-\delta^z)^2}{2}\widehat{\phi}_{zz}(\boldsymbol{p}) + \frac{(a\Delta r-\delta^r)^3}{6}\widehat{\phi}_{rrr}(\boldsymbol{p})\\ &\quad + \frac{(a\Delta r-\delta^r)^2(b\Delta z-\delta^z)}{2}\widehat{\phi}_{rrz}(\boldsymbol{p}) + \frac{(b\Delta z-\delta^z)^3}{6}\widehat{\phi}_{zzz}(\boldsymbol{p})\\ &\quad + \frac{(a\Delta r-\delta^r)(b\Delta z-\delta^z)^2}{2}\widehat{\phi}_{rzz}(\boldsymbol{p}) + \mathcal{O}(\Delta_{\mathrm{M}}^4).\end{aligned} \tag{6.58}$$

Here, $\widehat{\phi}$ and all derivatives of $\widehat{\phi}$ are evaluated at time t^p.
Let $\boldsymbol{q}_I \in \mathbb{R}^2$ denote the grid point corresponding to the index $I \in \mathcal{I}$. Using the expansion from Eq. (6.58), an approximation of $\widehat{\phi}_r n^r + \widehat{\phi}_z n^z$ of second order is searched of the form

$$\widehat{\phi}_r(\boldsymbol{p},t^p)n^r + \widehat{\phi}_z(\boldsymbol{p},t^p)n^z \approx \sum_{I\in\mathcal{I}} h_I \widehat{\phi}(\boldsymbol{q}_I,t^p). \tag{6.59}$$

Replacing the terms $\widehat{\phi}(\boldsymbol{q}_I,t^p)$ in Eq. (6.59) by the corresponding Taylor series expansions from Eq. (6.58) and aiming for an approximation error of the form $\mathcal{O}(\Delta_{\mathrm{M}}^2)$, the coefficients h_I, $I \in \mathcal{I}$, can be computed by solving a linear system of equations of the form

$$\boldsymbol{B}\boldsymbol{h} = \begin{bmatrix}0\\ n^r\\ n^z\\ 0\\ 0\\ 0\end{bmatrix}, \quad \text{with} \quad \boldsymbol{B} \in \mathbb{R}^{6\times 6} \quad \text{and} \quad \boldsymbol{h} = \begin{bmatrix}h_{i,j}\\ h_{i+1,j}\\ h_{i+2,j}\\ h_{i,j+1}\\ h_{i,j+2}\\ h_{i+1,j+1}\end{bmatrix} \in \mathbb{R}^6. \tag{6.60}$$

Since the entries of the matrix $\boldsymbol{B}$ depend on Δr, Δz, δ^r, and δ^z, also the coefficients h_I, $I \in \mathcal{I}$, depend on these values.
In the described way, Eq. (6.59) is fulfilled up to an approximation error of the form $\mathcal{O}(\Delta_{\mathrm{M}}^2)$. Therefore, the BC (6.54) can be approximated with a consistency error of order two.
Let $\widehat{\phi}_I^p$ be the finite difference approximation of $\widehat{\phi}$, which is evaluated at $(\boldsymbol{q}_I,t^p)$, i. e. $\widehat{\phi}_I^p \approx \widehat{\phi}(\boldsymbol{q}_I,t^p)$. Then the approximation of the BC (6.54) of second order is given by

$$\sum_{I\in\mathcal{I}} h_I \widehat{\phi}_I^p = -\widehat{\phi}_{0,r}(\boldsymbol{p},t^p)n^r - \widehat{\phi}_{0,z}(\boldsymbol{p},t^p)n^z + u_3 n^z \widehat{1} + \widehat{V}. \tag{6.61}$$

If the radius R of the CFB coincides with the value $r_{N_\mathrm{i}+1}$, the point $(r_{N_\mathrm{i}+1}, z_1)$ also becomes part of the boundary of the CFB. In this case, BC (6.54) can also be applied at the point $\boldsymbol{p} = (r_{N_\mathrm{i}+1}, z_1)$. However, the BC (6.47) at $z = 0$ also holds at the grid point $(r_{N_\mathrm{i}+1}, z_1)$. As a result of this, Eqs. (6.52) and (6.61) can both be applied at the corner point $(r_{N_\mathrm{i}+1}, z_1)$ to compute $\widehat{\phi}_{N_\mathrm{i}+1,1}$. To make the computation rule for $\widehat{\phi}_{N_\mathrm{i}+1,1}$ uniquely defined, similar to Sect. 6.4.2, the sum of those two equations is used to obtain a single equation that is used to calculate $\widehat{\phi}_{N_\mathrm{i}+1,1}$.

6.4.5 Summary of the Finite Difference Method

In this section, a numerical method has been presented to solve Eq. (6.34). Here, the proposed scheme shows a consistency error of second order in time and space. Table 6.1 summarizes the equations, which are used to solve Eq. (6.34) numerically. Using the proposed method, the values of the Fourier coefficients ${}^{\mathrm{Z}}\widehat{\phi}^{(1)}_{\mathrm{B},m}$ and ${}^{\mathrm{Z}}\widehat{\phi}^{(2)}_{\mathrm{B},m}$ at the spatial grid points (r_i, z_j) and time point t^p, $i = 1, \ldots, N+1$, $j = 1, \ldots, M+1$, $p = 1, \ldots, P+1$, are approximated by corresponding finite difference approximations ${}^{\mathrm{Z}}\widehat{\phi}^{p}_{i,j}$. Here, the values ${}^{\mathrm{Z}}\widehat{\phi}^{p}_{i,j}$ are computed by solving a linear system of equations.
It has to be noted that Eq. (6.52) introduces an implicit discretization of the BC (6.34d) at $z = 0$ and contains values of the finite difference approximations $\widehat{\phi}^{q}_{i,j}$ at the time points $t^q \in \{t^{p-1}, t^p, t^{p+1}\}$. In order to compute $\widehat{\phi}^{p+1}_{i,j}$ at the still water level at $z = z_1 = 0$, equations for the values $\widehat{\phi}^{p+1}_{i,j}$ inside the fluid have to be known. To obtains these equations, the Eqs. (6.41), (6.45), (6.46), and (6.61) have to be evaluated at time point t^{p+1}.
After finite difference approximations of the Fourier coefficients ${}^{\mathrm{Z}}\widehat{\phi}^{(1)}_{\mathrm{B},m}$ and ${}^{\mathrm{Z}}\widehat{\phi}^{(2)}_{\mathrm{B},m}$

Table 6.1: Overview of the Eqs. (6.34a)-(6.34e), which need to be solved to compute the Fourier coefficients of the velocity potentials ${}^{\mathrm{Z}}\phi^{(1)}_{\mathrm{B}}$ and ${}^{\mathrm{Z}}\phi^{(2)}_{\mathrm{B}}$ and the corresponding approximating equations using a finite difference method.

Equation, which needs to be approximated	Where does the equation hold?	Approximating equation
(6.34a)	Inside the fluid: $(r, z) \in \mathring{\bar{\Omega}}_2$	(6.41)
(6.34b)	On the boundary of the CFB: $(r, z) \in \partial\bar{C}_2$	(6.61)
(6.34c)	On the bottom of the sea: $(r, z) \in \partial\bar{\Omega}_2 \cap \{z = -h\}$	(6.46)
(6.34d)	At the sea surface: $(r, z) \in \partial\bar{\Omega}_2 \cap \{z = 0\}$	(6.52)
(6.34e)	At the outer boundary of the computational domain: $(r, z) \in \partial\bar{\Omega}_2 \cap \{r = R_\Omega\}$	(6.45)

have been computed, the velocity potentials ${}^{\mathrm{Z}}\phi_{\mathrm{B}}^{(1)}$ and ${}^{\mathrm{Z}}\phi_{\mathrm{B}}^{(2)}$ can be calculated using Eq. (6.32). Adding these velocity potentials with the incident velocity potentials ${}^{\mathrm{Z}}\phi_{0}^{(1)}$ and ${}^{\mathrm{Z}}\phi_{0}^{(2)}$, the velocity potentials $\phi^{(1)}$ and $\phi^{(2)}$ can be computed, which are the Stokes components of the total velocity potential ϕ, see Eq. (4.21). With $\phi^{(1)}$, $\phi^{(2)}$, and ϕ, the velocity potentials are determined that correspond to the fluid motion of the water waves, which are disturbed by the presence of the CFB.
Having computed the values of the total velocity potential ϕ and its Stokes components $\phi^{(1)}$ and $\phi^{(2)}$, the hydrodynamic forces acting on the CFB can be computed numerically. This is done in the next section.

6.5 Numerical Computation of the Hydrodynamic Forces

After computing the velocity potentials $\phi^{(i)}$, $i = 1, 2$, the hydrodynamic forces acting on the CFB can be calculated using Eqs. (4.28) and (4.29). Recall that the FSI is computed in this chapter only up to an approximation error of order $\mathcal{O}(\varepsilon^3)$. Therefore, it is sufficient to consider only the first two components of the hydrodynamic force vector $\boldsymbol{F}$ acting on the CFB. Using the notation, which has been introduced in this chapter, Eqs. (4.28) and (4.29) become

$$\boldsymbol{F} = \iint_{S_{\mathrm{B}}} p\, {}^{\mathrm{K}}\boldsymbol{n}\, \mathrm{d}S = \boldsymbol{F}^{(0)} + \varepsilon^1 \boldsymbol{F}^{(1)} + \varepsilon^2 \boldsymbol{F}^{(2)} + \mathcal{O}(\varepsilon^3) \tag{6.62}$$

with

$$\begin{aligned}
\boldsymbol{F}^{(0)} &= -\iint_{{}^{\mathrm{K}}\partial C_3} \rho g z\, {}^{\mathrm{K}}\boldsymbol{n}\, \mathrm{d}S, & \boldsymbol{F}^{(1)} &= -\iint_{{}^{\mathrm{K}}\partial C_3} \rho\, {}^{\mathrm{K}}\phi_t^{(1)}\, {}^{\mathrm{K}}\boldsymbol{n}\, \mathrm{d}S, \\
\boldsymbol{F}^{(2)} &= -\iint_{{}^{\mathrm{K}}\partial C_3} \left(\rho\, {}^{\mathrm{K}}\phi_t^{(2)} + \rho \frac{1}{2} \boldsymbol{\nabla}\, {}^{\mathrm{K}}\phi^{(1)} \cdot \boldsymbol{\nabla}\, {}^{\mathrm{K}}\phi^{(1)}\right) {}^{\mathrm{K}}\boldsymbol{n}\, \mathrm{d}S + \int_{C_0} \frac{1}{2} \rho g \left({}^{\mathrm{K}}\eta^{(1)}\right)^2 {}^{\mathrm{K}}\boldsymbol{n}\, \mathrm{d}C.
\end{aligned} \tag{6.63}$$

Here, all integrals are evaluated in Cartesian coordinates, which is also indicated by the left superscript K. Furthermore, ${}^{\mathrm{K}}\partial C_3$, ${}^{\mathrm{K}}\boldsymbol{n}$, ${}^{\mathrm{K}}\phi^{(i)}$, and ${}^{\mathrm{K}}\eta^{(1)}$ denote the boundary ∂C_3 of the CFB, the normal vector $\boldsymbol{n}$, the velocity potential $\phi^{(i)}$, and the sea surface displacement $\eta^{(1)}$ in Cartesian coordinates. From ${}^{\mathrm{K}}\phi^{(1)}$, the sea

surface displacement ${}^{\mathrm{K}}\eta^{(1)}$ can be computed using Eq. (4.19a). For the considered CFB, C_0 denotes a circle with radius R.
Considering Eq. (6.63), it has to be noted that all appearing integrands are integrated over the wetted surface ${}^{\mathrm{K}}\partial C_3$, which is changing in time with the moving CFB. However, the velocity potentials $\phi_{\mathrm{B}}^{(i)}$ have only been computed in the inside of the domain $\bar{\Omega}_3$. In order to compute the forces $\boldsymbol{F}^{(1)}$ and $\boldsymbol{F}^{(2)}$, the corresponding integrals must therefore be transformed from ${}^{\mathrm{K}}\partial C_3$ to ${}^{\mathrm{K}}\partial \bar{C}_3$. Here, the results presented in [Ogilvie83] are used, which transform the integral from ${}^{\mathrm{K}}\partial C_3$ to ${}^{\mathrm{K}}\partial \bar{C}_3$ for a structure of general shape that can move freely in all directions.
In this thesis, the considered CFB performs only a translational motion in the vertical direction, whereby the displacement is given by $\xi = \varepsilon\xi^{(1)} + \varepsilon^2\xi^{(2)}$. Transforming the integrals from ${}^{\mathrm{K}}\partial C_3$ to ${}^{\mathrm{K}}\partial \bar{C}_3$ according to the corresponding results presented in [Ogilvie83], the forces $\boldsymbol{F}^{(1)}$ and $\boldsymbol{F}^{(2)}$ become

$$
\begin{aligned}
\boldsymbol{F}^{(1)} &= -\iint\limits_{{}^{\mathrm{K}}\partial \bar{C}_3} \rho\, {}^{\mathrm{K}}\phi_t^{(1)}\, {}^{\mathrm{K}}\boldsymbol{n}\, \mathrm{d}S, \\
\boldsymbol{F}^{(2)} &= -\iint\limits_{{}^{\mathrm{K}}\partial \bar{C}_3} \left(\rho\, {}^{\mathrm{K}}\phi_t^{(2)} + \rho\frac{1}{2}\boldsymbol{\nabla}\, {}^{\mathrm{K}}\phi^{(1)} \cdot \boldsymbol{\nabla}\, {}^{\mathrm{K}}\phi^{(1)} + \rho\, \xi^{(1)}\, {}^{\mathrm{K}}\phi_{tz}^{(1)}\right) {}^{\mathrm{K}}\boldsymbol{n}\, \mathrm{d}S \\
&\quad + \int\limits_{\bar{C}_0} \frac{1}{2}\rho g \left({}^{\mathrm{K}}\eta^{(1)} - \xi^{(1)}\right)^2 {}^{\mathrm{K}}\boldsymbol{n}\, \mathrm{d}C.
\end{aligned}
\tag{6.64}
$$

Since $\boldsymbol{F}^{(0)}$ does not depend on any velocity potential and the position of the boundary ${}^{\mathrm{K}}\partial C_3$ is known, it is possible to directly compute $\boldsymbol{F}^{(0)}$ without any transformation of the corresponding integral.
In the numerical evaluation of the integrands appearing in Eq. (6.64), the time derivatives of the occurring velocity potentials ${}^{\mathrm{K}}\phi^{(1)}$ and ${}^{\mathrm{K}}\phi^{(2)}$ are approximated using second-order backward finite difference approximations. The gradient $\boldsymbol{\nabla}{}^{\mathrm{K}}\phi^{(1)}$ includes the derivatives of ${}^{\mathrm{K}}\phi^{(1)}$ with respect to the Cartesian coordinates x, y, and z. This gradient is evaluated by first computing the derivatives with respect to the cylindrical coordinates r, θ, and z on the spatial grid defined in Eq. (6.37). Here, the derivatives with respect to r, θ, and z are computed using second-order finite difference approximations. Afterward, the derivatives with respect to r, θ, and z are used to calculate the derivatives with respect to the Cartesian coordinates x, y, and z.
Next, the forces $\boldsymbol{F}^{(0)}$, $\boldsymbol{F}^{(1)}$, and $\boldsymbol{F}^{(2)}$ are computed by evaluating the corresponding integrals from Eq. (6.64). Going from Cartesian to cylindrical coordinates,

the second integral in $\boldsymbol{F}^{(2)}$ becomes

$$\begin{aligned}&\int_{C_0} \frac{1}{2}\rho g \left({}^{\mathrm{K}}\eta^{(1)}(x,y,t) - \xi^{(1)}(t)\right)^2 {}^{\mathrm{K}}\boldsymbol{n}(x,y,z=0,t)\,\mathrm{d}C(x,y)\\ &\quad= \int_0^{2\pi} \frac{1}{2}\rho g \left({}^{\mathrm{Z}}\eta^{(1)}(r=R,\theta,t) - \xi^{(1)}(t)\right)^2 R \begin{bmatrix} -\cos(\theta) \\ -\sin(\theta) \\ 0 \end{bmatrix} \mathrm{d}\theta.\end{aligned} \tag{6.65}$$

Here, ${}^{\mathrm{Z}}\eta^{(1)}$ denotes the sea surface displacement ${}^{\mathrm{K}}\eta^{(1)}$ in cylindrical coordinates. Using Eq. (6.65), the second integral in $\boldsymbol{F}^{(2)}$ from Eq. (6.64) can be evaluated using a numerical integration over θ.
Next, the surface integrals are evaluated, which occur in the forces $\boldsymbol{F}^{(0)}$, $\boldsymbol{F}^{(1)}$, and $\boldsymbol{F}^{(2)}$. Exemplary, it is shown for the force $\boldsymbol{F}^{(1)}$ how these surface integrals can be evaluated efficiently. Going from Cartesian to cylindrical coordinates, the force $\boldsymbol{F}^{(1)}$ can be calculated by

$$\begin{aligned}\boldsymbol{F}^{(1)} &= -\iint_{{}^{\mathrm{K}}\partial\bar{C}_3} \rho\, {}^{\mathrm{K}}\phi_t^{(1)}(x,y,z,t)\, {}^{\mathrm{K}}\boldsymbol{n}(x,y,z,t)\,\mathrm{d}S(x,y,z,t)\\ &= -\iint_{\partial\bar{C}_3} \rho\, {}^{\mathrm{Z}}\phi_t^{(1)}(r,\theta,z,t)\, {}^{\mathrm{Z}}\boldsymbol{n}(r,\theta,z,t)\; r\,\mathrm{d}S(r,\theta,z,t).\end{aligned} \tag{6.66}$$

Here, ${}^{\mathrm{Z}}\phi^{(1)}$ denotes the velocity potential ${}^{\mathrm{K}}\phi^{(1)}$ in cylindrical coordinates. Recall that the domain C_3 has been expressed in Eq. (6.2) in cylindrical coordinates. Since $\partial\bar{C}_3$ denotes the boundary of C_3 in the resting position of the CFB, the superscript Z is not needed here to indicate that $\partial\bar{C}_3$ is expressed in cylindrical coordinates.
In order to evaluate the integral from Eq. (6.66) over $\partial\bar{C}_3$, it is necessary to parameterize the boundary $\partial\bar{C}_3$. Let s be the path coordinate along the contour of the CFB. Here, the contour of the CFB is given by the boundary $\partial\bar{C}_2$, which represents the boundary of the CFB in the (r,z)-plane. The boundary of the set $\bar{C}_2$ can be seen, for example, in Fig. 6.4. A possible parameterization of the boundary $\partial\bar{C}_3$ is given by

$$\boldsymbol{\Xi} : (0,2\pi] \times [0,s_3) \to \partial\bar{C}_3,\ \begin{bmatrix}\theta\\ s\end{bmatrix} \mapsto \begin{bmatrix}\Xi_1(s)\\ \theta\\ \Xi_3(s)\end{bmatrix}, \tag{6.67}$$

whereby $s_1 = d - R_\mathrm{S},\ s_2 = s_1 + \frac{\pi}{2} R_\mathrm{S},\ s_3 = s_2 + R - R_\mathrm{S}$, and

$$\boldsymbol{\Xi}(\theta, s) = \begin{bmatrix} \Xi_1(s) \\ \theta \\ \Xi_3(s) \end{bmatrix} = \begin{cases} \begin{bmatrix} R \\ \theta \\ -s \end{bmatrix} & : s \in [0, s_1), \\ \begin{bmatrix} (R - R_\mathrm{S}) + R_\mathrm{S} \cos\left(\dfrac{s - s_1}{R_\mathrm{S}}\right) \\ \theta \\ (R_\mathrm{S} - h) - R_\mathrm{S} \sin\left(\dfrac{s - s_1}{R_\mathrm{S}}\right) \end{bmatrix} & : s \in [s_1, s_2), \\ \begin{bmatrix} (R - R_\mathrm{S}) - (s - s_2) \\ \theta \\ -h \end{bmatrix} & : s \in [s_2, s_3). \end{cases} \tag{6.68}$$

Here, d is the draft of the CFB in its resting position. For a fixed value of θ, the function $\boldsymbol{\Xi}$ maps on the boundary $\partial \bar{C}_2$.
Finally, using the transformation rule for surface integrals, Eq. (6.66) results in

$$\begin{aligned} \boldsymbol{F}^{(1)} &= -\iint_{\partial \bar{C}_3} \rho\, {}^{\mathrm{Z}}\phi_t^{(1)}(r, \theta, z, t)\, {}^{\mathrm{Z}}\boldsymbol{n}(r, \theta, z, t)\, r \,\mathrm{d}S(r, \theta, z, t) \\ &= -\int_0^{2\pi} \int_0^{s_3} \rho\, {}^{\mathrm{Z}}\phi_t^{(1)}(\boldsymbol{\Xi}(\theta, s), t)\, {}^{\mathrm{Z}}\boldsymbol{n}(\boldsymbol{\Xi}(\theta, s), t)\, \Xi_1(s)\, ||\boldsymbol{\Xi}_\theta \times \boldsymbol{\Xi}_s||_2 \,\mathrm{d}s \,\mathrm{d}\theta. \end{aligned} \tag{6.69}$$

Therefore, the force $\boldsymbol{F}^{(1)}$ can be computed using a numerical integration over θ and s. In the same way, the surface integrals appearing in the expressions for $\boldsymbol{F}^{(0)}$ and $\boldsymbol{F}^{(2)}$ can be computed.
Using the method and formulas presented in this section, the hydrodynamic forces acting on the CFB can be calculated. After calculating the hydrodynamic forces, the equations of motion of the CFB can be solved numerically. A corresponding numerical scheme is presented in the next section.

6.6 Numerical Solution of the Equation of Motion

In Sect. 3.1, a WEC has been introduced, where the corresponding CFB moves along guidance rods with the displacement ξ in a plane inclined by the angle α. Expanding ξ in a Stokes expansion of the form $\xi = \varepsilon\xi^{(1)} + \varepsilon^2\xi^{(2)} + \varepsilon^3\xi^{(3)} + \mathcal{O}(\varepsilon^4)$, the corresponding equations of motions for $\xi^{(i)}$, $i = 1, 2, 3$, are given by Eq. (4.35).

In this chapter, a CFB is considered, which can only perform vertical motion with inclination angle $\alpha = 90°$. Furthermore, the FSI is computed only up to an error of order $\mathcal{O}(\varepsilon^3)$ in this chapter. Therefore, Eq. (4.35) simplifies to

$$M\ddot{\xi}^{(1)} + (d_{\text{lin}} + d_{\text{elec}} + \lambda_{\text{vis},z})\,\dot{\xi}^{(1)} + \rho g \pi R^2 \xi^{(1)} = F_3^{(1)}, \tag{6.70a}$$

$$M\ddot{\xi}^{(2)} + (d_{\text{lin}} + d_{\text{elec}} + \lambda_{\text{vis},z})\,\dot{\xi}^{(2)} + \rho g \pi R^2 \xi^{(2)} = F_3^{(2)}. \tag{6.70b}$$

Here, $F_3^{(1)}$ and $F_3^{(2)}$ are the z-components of the forces $\boldsymbol{F}^{(1)}$ and $\boldsymbol{F}^{(2)}$, which are given by Eq. (6.63).
In order compute the displacements $\xi^{(1)}$ and $\xi^{(2)}$, Eq. (6.70) has to be transformed in state space. Defining $y_1 = \xi^{(1)}$, $y_2 = \dot{\xi}^{(1)}$, $y_3 = \xi^{(2)}$, $y_4 = \dot{\xi}^{(2)}$ and $\boldsymbol{y} = [\,y_1\,, y_2\,, y_3\,, y_4\,]^{\mathrm{T}}$, Eq. (6.70) can be rewritten as

$$\dot{\boldsymbol{y}}(t) = \boldsymbol{f}(\boldsymbol{y}, t), \tag{6.71}$$

with

$$\boldsymbol{f}(\boldsymbol{y}, t) = \begin{bmatrix} y_2 \\ \dfrac{1}{M}\left[F_3^{(1)} - (d_1 + d_{\text{elec}} + \lambda_{\text{vis},z})\,y_2 - \rho g \pi R^2 y_1\right] \\ y_4 \\ \dfrac{1}{M}\left[F_3^{(2)} - (d_1 + d_{\text{elec}} + \lambda_{\text{vis},z})\,y_4 - \rho g \pi R^2 y_3\right] \end{bmatrix}. \tag{6.72}$$

In order to solve the ordinary differential equation (6.71), different numerical methods can be applied. Let the numerical approximation of $\boldsymbol{y}$ at time point t^p be denoted by $\boldsymbol{y}_p$, i. e. $\boldsymbol{y}_p \approx \boldsymbol{y}(t^p)$. The corresponding evaluation of $\boldsymbol{f}$ is denoted by $\boldsymbol{f}_p$, i. e. $\boldsymbol{f}_p = \boldsymbol{f}(\boldsymbol{y}_p, t^p)$. It has to be noted that the hydrodynamic forces $F_3^{(i)}$ have to be computed in each function evaluation of $\boldsymbol{f}$. Therefore, also the velocity potentials $\phi_{\text{B}}^{(i)}$ $i = 1, 2$, have to be computed in each function evaluation of $\boldsymbol{f}$. Depending on the step sizes Δr, Δz, and the size of the computational domain, the computation of $\phi_{\text{B}}^{(i)}$ can be computationally expensive. Therefore, the number of evaluations of $\boldsymbol{f}$ should be small in each time step.
In this thesis, the fourth-order Adams-Bashforth-Moulton predictor-corrector scheme is used to solve Eq. (6.71). Going from time point t^p to time point t^{p+1}, an approximation of the value $\boldsymbol{y}_{p+1}$ is computed using the third-order explicit Adams-Bashforth scheme. The resulting approximation of $\boldsymbol{y}_{p+1}$ is denoted by $\tilde{\boldsymbol{y}}_{p+1}$. In order to compute a correction $\boldsymbol{y}_{p+1}$ from $\tilde{\boldsymbol{y}}_{p+1}$, the implicit fourth-order Adams-Moulton scheme is used. After each computation of $\boldsymbol{y}_{p+1}$ and $\tilde{\boldsymbol{y}}_{p+1}$, an evaluation step is necessary to compute $\tilde{\boldsymbol{f}}_{p+1} = \boldsymbol{f}(\tilde{\boldsymbol{y}}_{p+1}, t^{p+1})$ and $\boldsymbol{f}_{p+1} = \boldsymbol{f}(\boldsymbol{y}_{p+1}, t^{p+1})$, respectively. The resulting fourth-order numerical scheme is given by

$$\begin{aligned}
\text{Predictor step:}\quad & \tilde{\boldsymbol{y}}_{p+1} = \boldsymbol{y}_p + \frac{\Delta t}{12}\left(5\boldsymbol{f}_{p-2} - 16\boldsymbol{f}_{p-1} + 23\boldsymbol{f}_p\right), \\
\text{Evaluation step:}\quad & \tilde{\boldsymbol{f}}_{p+1} = \boldsymbol{f}(\tilde{\boldsymbol{y}}_{p+1}, t^{p+1}), \\
\text{Corrector step:}\quad & \boldsymbol{y}_{p+1} = \boldsymbol{y}_p + \frac{\Delta t}{24}\left(\boldsymbol{f}_{p-2} - 5\boldsymbol{f}_{p-1} + 19\boldsymbol{f}_p + 9\tilde{\boldsymbol{f}}_{p+1}\right), \\
\text{Evaluation step:}\quad & \boldsymbol{f}_{p+1} = \boldsymbol{f}(\boldsymbol{y}_{p+1}, t^{p+1}).
\end{aligned} \tag{6.73}$$

Using this scheme, the function $\boldsymbol{f}$ must be evaluated twice in each time step. In order to apply this scheme, three initial conditions $\boldsymbol{y}_0$, $\boldsymbol{y}_{-1}$, and $\boldsymbol{y}_{-2}$ are needed. In all numerical simulations presented in this thesis, the CFB starts from its resting position, i. e. $\boldsymbol{y}_0 = \boldsymbol{y}_{-1} = \boldsymbol{y}_{-2} = \boldsymbol{0}$.

6.7 Analysis of Numerical Results

In the previous sections, numerical methods to compute the velocity potentials $\phi_{\mathrm{B}}^{(i)}$, the hydrodynamic forces $\boldsymbol{F}^{(i)}$ acting on the considered CFB, and the resulting displacements $\xi^{(i)}$ of the CFB, $i = 1, 2$, have been presented. These methods can be used to compute the FSI between the CFB and nonlinear water waves. In this section, the numerical solution of the resulting FSI simulation is verified, and a convergence analysis is presented.
In all numerical results presented in this section, the CFB is excited by incoming regular Stokes waves, which have been introduced in Sect. 4.3. The CFB is starting from its resting position. In order to compute the BC at the sea surface, corresponding initial values of the Fourier coefficients of the velocity potential, ${}^{\mathrm{Z}}\widehat{\phi}_{\mathrm{B},m}^{(i)}$, have to be defined, see Sect. 6.4.3. These initial values are set to zero. This corresponds to a vanishing body disturbance potential ϕ_{B} at the beginning of the computation. However, a vanishing body disturbance potential ϕ_{B} occurs only for an incoming water wave with vanishing amplitude. Therefore, the incident velocity potentials $\phi_0^{(i)}$ of the regular Stokes waves, which have been presented in Sect. 4.3, are multiplied by a factor of the form

$$F_{\tanh} = \tanh(at - b), \quad \text{with } a, b \geq 0. \tag{6.74}$$

In this section, the constants a and b are set to $a = 0.4$, $b = 0$. Multiplied by the factor $F_{\tanh}$, the incoming waves reach 99% of their amplitude after $t = 6.6\,\mathrm{s}$.
In the first step, results are presented in Sect. 6.7.1, which show the temporal behavior of the CFB in the presence of regular Stokes waves of first and second order. Here, the results are compared with corresponding results shown in Chap. 3 and results published in [KinoshitaBao00]. In this way, the numerical results computed by the numerical method, which has been presented in the previous sections, are validated. In the second step, the convergence of the numerical results with respect to a decreasing spatial and temporal step size is investigated in Sect. 6.7.2.
The CFB is not connected to an electrical generator in this section, so the electrical damping d_{elec} vanishes. Furthermore, the linear mechanical and viscous damping add together to $3000\,\mathrm{kg/s}$, i. e. $d_{\mathrm{lin}} + \lambda_{\mathrm{vis},z} = 3000\,\mathrm{kg/s}$. The CFB

is moving in salt water with density $\rho = 1023\,\mathrm{kg/m^3}$. Only long-crested water waves are considered, which propagate in the x-direction.

6.7.1 Validation of Numerical Results

In the following, the temporal behavior of the CFB in the presence of regular Stokes waves of first and second order is presented. The corresponding used parameter values of the floating system and incoming water waves are given in Tab. 6.2. Using these parameters, the respective wave number k and wavelength λ of the incoming water waves is given by $k = 0.171\,\mathrm{m^{-1}}$ and $\lambda = 36.673\,\mathrm{m}$. Using the damping μ from Eq. (6.7) and the settings used in [ShaoFaltinsen13], the length of the inner layer R_i and the length of the damping layer L shown in Fig. 6.3 is set to $R_\mathrm{i} = 37\,\mathrm{m}$ and $L = 74\,\mathrm{m}$, respectively. Therefore, the radius of the computational domain is given by $R_\Omega = 111\,\mathrm{m}$. Corresponding numerical results are calculated on the time domain $t \in [0, 50\,\mathrm{s}]$ using the step sizes $\Delta r = \Delta z = 0.04\,\mathrm{m}$ and $\Delta t = 0.05\,\mathrm{s}$.
The velocity potentials ${}^{\mathrm{Z}}\phi_\mathrm{B}^{(i)}$, $i = 1, 2$, are computed using Fourier series expansions with $N_\mathrm{F} = 16$ Fourier coefficients. Further investigations have shown that larger values for N_F do not change the numerical results significantly for the considered system parameters.
Figure 6.7 presents the hydrodynamic forces acting on the CFB in the x- and z-direction. Here, the system is considered in its steady state, which is obtained after 30 s of simulation time. The first- and second-order components of the forces and the total forces up to the second order are presented. It can be seen that while the first-order force components oscillate in time with frequency ω, the second-order force components oscillate in time with frequency 2ω. Therefore, the transition from linear to nonlinear wave theory leads to higher frequency components in the spectrum of the acting hydrodynamic forces.
Furthermore, it has to be noted that while the first-order component forces $\varepsilon F_1^{(1)}$ and $\varepsilon F_3^{(1)}$ are oscillating in Fig. 6.7 around zero, the second-order component forces $\varepsilon^2 F_1^{(2)}$ and $\varepsilon^2 F_3^{(2)}$ contain some non-oscillating drift forces. However, these drift forces are well-known in literature, see e.g. [Eatock TaylorHung87]. Therefore, they will not be discussed further.
In the considered case, the amplitudes of the second-order wave forces are relatively large compared to those of the corresponding first-order wave forces. Denoting the amplitude of the force F by $|F|$ and considering the quotient

Table 6.2: Parameter values of the floating system and incoming water waves.

R [m]	R_S [m]	d [m]	h [m]	$\omega \left[\frac{\mathrm{rad}}{\mathrm{s}}\right]$	A [m]
1	0	1.5	4	1	0.4

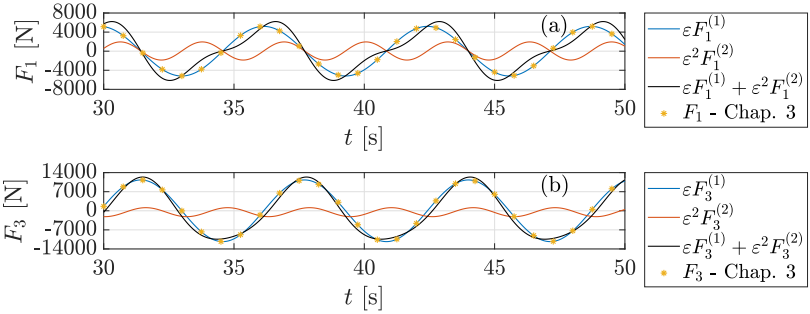

Figure 6.7: Forces in (a) x-direction and (b) z-direction, which act on the CFB in regular Stokes waves of first and second order. Furthermore, the forces are shown, which result from the linear method presented in Chap. 3.

of the amplitude of the second-order and first-order wave forces, it results $|\varepsilon^2 F_1^{(2)}|/|\varepsilon F_1^{(1)}| = 36.6\%$, $|\varepsilon^2 F_3^{(2)}|/|\varepsilon F_3^{(1)}| = 14.9\%$. Therefore, the second-order component of the forces, $\varepsilon^2 F^{(2)}$, contribute significantly to the total forces, $F = \varepsilon F^{(1)} + \varepsilon^2 F^{(2)}$, and cannot be neglected in the computation of the FSI for the considered water wave and structure.

The corresponding motion of the CFB is shown in Fig. 6.8. Here, the displacement and velocity of the CFB is depicted. The first- and second-order components of the motion and the total motion up to second order are presented, i. e. $\varepsilon\xi^{(1)}$, $\varepsilon^2\xi^{(2)}$, $\varepsilon\xi^{(1)} + \varepsilon^2\xi^{(2)}$, and the corresponding time derivatives. As has already be seen in the results for the acting hydrodynamic forces, the second-order components of the motion, $\varepsilon^2\xi^{(2)}$, contribute largely to the total motion $\varepsilon\xi^{(1)} + \varepsilon^2\xi^{(2)}$. This is also important for the WEC investigated in Chap. 3. The amount of energy, which is harvested by the WEC, depends on the velocity of the CFB. Since the temporal behavior of the velocity of the CFB changes significantly going from a linear to a nonlinear analysis, the amount of harvested energy can also change significantly. This again shows the importance of efficiently calculating the FSI between nonlinear water waves and a moving structure.

In order to validate the numerical results for the first-order components of the motion and forces, Figs. 6.7 and 6.8 also show the corresponding results obtained using the linear method presented in Chap. 3. Here, the related hydrodynamic forces are computed using Eq. (3.12), and the motion of the CFB is calculated by solving the equation of motion from Eq. (3.14). It can be seen that the numerical results for the first-order components of the motion and hydrodynamic forces, which are obtained using the method presented in the previous parts of this chapter and using the linear method presented in Chap. 3, agree with each other. The relative errors between the corresponding results on forces, displacements, and velocities are all between 0.1 % and 0.22 %. This validates the results on the first-order components of the motion and forces.

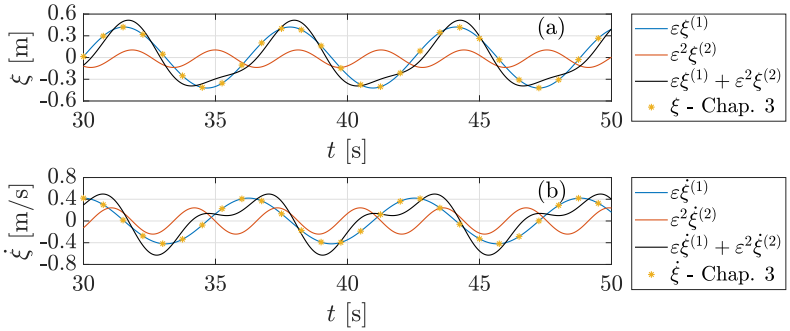

Figure 6.8: (a) Displacement and (b) velocity of the CFB in regular Stokes waves of first and second order. Furthermore, the motion is shown, which results from the linear method presented in Chap. 3.

In order to validate the results for second-order components of the hydrodynamic forces, the numerical results are compared with the semi-analytical results presented in [KinoshitaBao00]. Here, the authors investigate the forces acting on a cylinder that is unable to move.
First, the amplitudes of the second-order hydrodynamic forces $\varepsilon^2 F_1^{(2)}$ and $\varepsilon^2 F_3^{(2)}$ are studied for incoming regular Stokes waves with a varying wave number k. The results are presented in Fig. 6.9. The forces are normalized according to [KinoshitaBao00]. A CFB is considered with radius $R = 1\,\mathrm{m}$, $R_\mathrm{S} = 0$, and draft $d = 4\,\mathrm{m}$, which is positioned in water of depth $h = 10\,\mathrm{m}$. The amplitude of the incoming regular Stokes waves is $A = 0.15\,\mathrm{m}$. Figure 6.9 also shows the corresponding results presented in [KinoshitaBao00, Fig. 5]. It can be seen that both results agree well with each other.
Next, the amplitudes of the first- and second-order components of the hydrodynamic forces are studied, which act on a CFB with a varying draft d in the horizontal and vertical direction. Again, the CFB is unable to move. The results are presented in Fig. 6.10, where the forces are normalized according to [KinoshitaBao00]. A CFB is considered with radius $R = 1\,\mathrm{m}$ and $R_\mathrm{S} = 0$ in water of depth $h = 10\,\mathrm{m}$. The incoming regular Stokes waves have the amplitude $A = 0.4\,\mathrm{m}$ and wave number $k = 0.5\,\mathrm{m}^{-1}$. Figure 6.10 also shows the corresponding results, which are presented in [KinoshitaBao00, Fig. 7]. Again, it can be seen that both results agree well with each other. Therefore, all numerical results presented in this section, which are obtained using the method presented in the previous parts of this chapter, are validated by the corresponding results computed by the linear method from Chap. 3 and shown in [KinoshitaBao00], respectively.

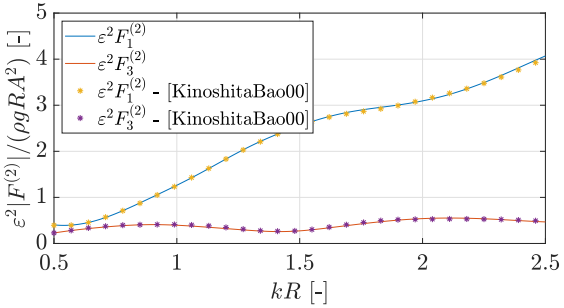

Figure 6.9: Amplitudes of the second-order hydrodynamic forces acting in the horizontal and vertical direction against a varying wave number k, normalized by the radius R. The numerical results are compared with the values presented in [KinoshitaBao00, Fig. 5].

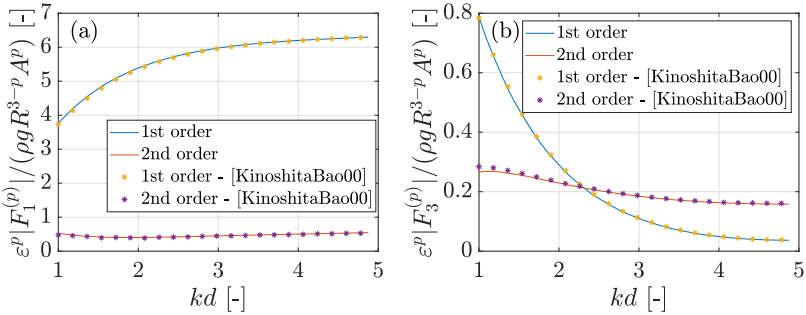

Figure 6.10: Amplitudes of first two components of the hydrodynamic forces acting in the (a) horizontal and (b) direction against a varying draft d, normalized by the wave number k. The numerical results are compared with the values presented in [KinoshitaBao00, Fig. 7].

6.7.2 Analysis of Convergence Rate

After validating the numerical results, the order of convergence of the numerical method is analyzed. The methods presented in Sect. 6.4, Sect. 6.5, and Sect. 6.6 approximate all considered differential equations by second-order finite difference approximations. It is now examined whether and to what order the overall corresponding numerical results converge. This is done by computing the FSI between the CFB and incoming Stokes waves, whereby different step sizes in time and space are used.

Before showing the corresponding numerical results, it has to be noted that very small temporal and spatial step sizes are considered in the following. In order to make the numerical calculation of the corresponding results feasible concerning

used memory and computation time, the radius R_Ω of the computational domain is decreased. However, the computational domain still consists of an inner layer of length R_i and a damping layer of length L. In all upcoming results, the radius R_Ω is chosen so that the numerical calculation is feasible concerning used memory and computation time, and the reflections coming from the outer boundary at $r = R_\Omega$ do not affect the FSI between the waves and the moving CFB. In particular, R_i, L, R_Ω are given by $R_\mathrm{i} = L = 5\,\mathrm{m}$, $R_\Omega = 10\,\mathrm{m}$. All upcoming results are computed on the time domain $t \in [0, 30\,\mathrm{s}]$.

First, the CFB and the incoming water waves are considered, which are described by the parameter values summarized in Tab. 6.2. In particular, a CFB with a sharp edge at its bottom is considered, i. e. $R_\mathrm{S} = 0$. Numerical results are computed for decreasing step sizes in time and space, whereby Δz and Δr are set equal, and the quotient $\Delta t/\Delta r$ is kept constant over all calculations with $\Delta t/\Delta r = 4.25\,\mathrm{s/m}$. The resulting time series of the hydrodynamic force $\varepsilon^2 F_3^{(2)}$ acting on the moving CFB are presented in Fig. 6.11a for different values of Δr. In Fig. 6.11b, the results are zoomed in around the time point $t = 22.2\,\mathrm{s}$. Furthermore, Fig. 6.11c shows the corresponding maximal values of the force $\varepsilon^2 F_3^{(2)}$ around the time point $t = 22.2\,\mathrm{s}$ against the used values of Δr. It can be seen that the different discretizations do not affect the phase of the hydrodynamic forces. Furthermore, the amplitude of the forces is for all considered discretizations of the same order of magnitude. However, the forces are not converging for decreasing values of Δt, Δr, and Δz. This is due to the corner of the CFB at $(r, z) = (R, -d)$, which leads to some difficulties. For example, the normal vector is not defined at such a corner. Furthermore, the existence and regularity of weak and classical solutions $\phi_\mathrm{B}^{(i)}$ of Eq. (6.31) is not guaranteed if the boundary of the considered computational domain is not sufficiently smooth. Details about this topic can be found, for example, in [KnabnerAngermann03, HinzeEtAl09, Evans10, Jost13].

To avoid the mentioned difficulties, the corner of the CFB at $(r, z) = (R, -d)$ is replaced by a spherical segment with radius $R_\mathrm{S} = 0.2\,\mathrm{m}$. The resulting system parameters, which are used in the further course of this section, are summarized in Tab. 6.3.

In the following, the orders of convergence are calculated for the hydrodynamic forces acting on the CFB and the motion of the CFB. Here, it is investigated how the corresponding errors behave with decreasing step sizes in time and space. It should be noted that no analytical solutions are available for the hydrodynamic forces and motion of the CFB that could be used to calculate the corresponding convergence rate. Instead, the convergence rate is calculated by comparing the results obtained with a given discretization to those obtained with the corresponding discretization of half the step size in time and space.

In the following, a sequence of different discretizations is considered. For the n-th discretization, the obtained numerical solution of the hydrodynamic force $\boldsymbol{F}$ and motion ξ of the CFB is denoted by ${}^n\boldsymbol{F}$ and ${}^n\xi$, respectively. The corresponding solutions, which are used to calculate the related errors and which are obtained using the corresponding discretization of half the step size in time and space, are

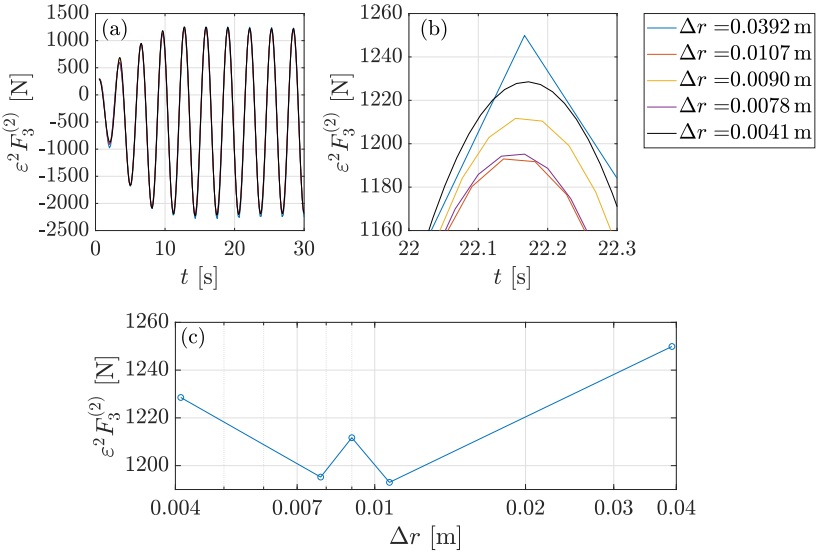

Figure 6.11: Time series of the force $\varepsilon^2 F_3^{(2)}$, which is calculated using different discretizations. (a): Complete time series. (b): Zoom into the results from (a) around the time point $t = 22.2\,\mathrm{s}$. (c): Corresponding maximal values of force $\varepsilon^2 F_3^{(2)}$ around the time point $t = 22.2\,\mathrm{s}$ against the used values of Δr.

Table 6.3: Parameter values of the floating system and incoming water waves.

R [m]	R_S [m]	d [m]	h [m]	$\omega \left[\frac{\mathrm{rad}}{\mathrm{s}}\right]$	A [m]
1	0.2	1.5	4	1	0.4

denoted by ${}^{C_n}\boldsymbol{F}$ and ${}^{C_n}\xi$, respectively.
For the hydrodynamic force F acting on the CFB in the x- or z-direction and the displacement ξ of the CFB, the respective total error of the n-th discretization is defined by

$$E_\mathrm{F}^n := \max_t |{}^n F - {}^{C_n} F|, \tag{6.75a}$$

$$E_\xi^n := \max_t |{}^n \xi - {}^{C_n} \xi|. \tag{6.75b}$$

After computing a sequence of real-valued scalar errors E^n, $n = 1, \ldots, N$, with decreasing step sizes in time and space, the corresponding empirical order of convergence is defined by

$$q^n := \frac{\ln\left(\frac{E^n}{E^{n+1}}\right)}{\ln\left(\frac{\Delta^n}{\Delta^{n+1}}\right)}, \quad n = 1, \ldots, N-1. \tag{6.76}$$

Here, Δ^n is some discretization parameter of the n-th discretization and can be chosen, for example, to be equal to the step size Δz, Δr, or Δt used in the n-th discretization. The empirical order of convergence from Eq. (6.76) is motivated by the fact that if convergence exists with order q in Δr, then there exists a constant $C \in \mathbb{R}$ such that

$$E^n \approx C\,(\Delta r_n)^q\,. \tag{6.77}$$

Here, Δr_n is the step size in r-direction used in the n-th discretization. Then it holds

$$\frac{E^n}{E^{n+1}} \approx \left(\frac{\Delta r_n}{\Delta r_{n+1}}\right)^q. \tag{6.78}$$

Using algebraic transformations, Eq. (6.76) results for $\Delta^n = \Delta r_n$.
In the following, a sequence of discretizations is considered, whereby Δz and Δr are set equal, and the quotient $\Delta t/\Delta r$ is kept constant over all discretizations with $\Delta t/\Delta r = 4.25\,\mathrm{s/m}$. The discretization parameter Δ^n is set to Δr_n.
First, the convergence of the hydrodynamic forces acting on the CFB is investigated. Figures 6.12a and 6.12b present the empirical order of convergence q^n of the first- and second-order components of the hydrodynamic forces acting in the x- and z-direction. The corresponding errors E_F^n, which are defined in Eq. (6.75a), for the first- and second-order hydrodynamic forces are shown against the step size Δr in Figs. 6.12c and 6.12d. Figures 6.12c and 6.12d show that the errors E_F^n decrease for a decreasing step size Δr. This indicates a convergence of the numerical results. Moreover, Figs. 6.12a and 6.12b show that all numerical results for the hydrodynamic forces converge on average with an empirical order of convergence of two.
It has to be noted that the hydrodynamic forces acting on the CFB are computed by integrating the hydrodynamic pressure p, which depends on the velocity potentials ${}^{\mathrm{Z}}\phi_\mathrm{B}^{(i)}$, $i = 1, 2$. Therefore, the convergence of the hydrodynamic forces

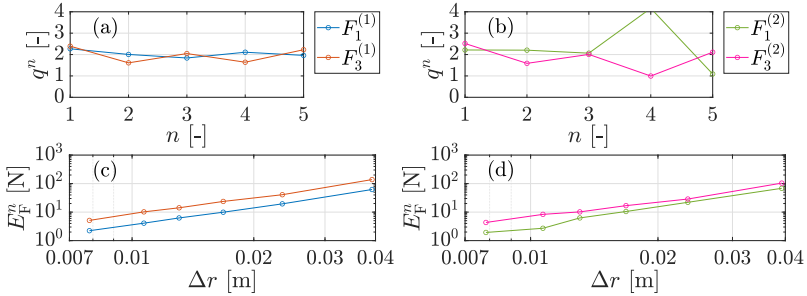

Figure 6.12: Convergence analysis for the hydrodynamic forces acting on the CFB. (a),(b): Empirical order of convergence for the first- and second-order components of the hydrodynamic forces. (c),(d): Corresponding error E_F^n against the step size Δr.

shows that the numerical values for the velocity potentials ${}^{\mathrm{Z}}\phi_{\mathrm{B}}^{(i)}$ also converge. However, to investigate the order of convergence of the velocity potentials ${}^{\mathrm{Z}}\phi_{\mathrm{B}}^{(i)}$, the order of convergence of each Fourier coefficient ${}^{\mathrm{Z}}\widehat{\phi}_{\mathrm{B},m}^{(i)}$ has to be analyzed. In addition, since the Fourier coefficients are space-dependent, it is also necessary to specify the norm that is used in space to calculate the corresponding error of the n-th discretization E^n. All this makes the study of convergence of the velocity potentials ${}^{\mathrm{Z}}\phi_{\mathrm{B}}^{(i)}$ difficult. To make the scope of this convergence analysis not too extensive, the convergence behavior of the corresponding velocity potentials ${}^{\mathrm{Z}}\phi_{\mathrm{B}}^{(i)}$ is not investigated in further detail. But as has been already described, the convergence of the hydrodynamic forces indicates a convergence of the velocity potentials ${}^{\mathrm{Z}}\phi_{\mathrm{B}}^{(i)}$, $i = 1, 2$.

Furthermore, it has to be noted that the hydrodynamic forces acting on the CFB with $R_{\mathrm{S}} = 0$ have not converged with respect to a decreasing step size in time and space, see Fig. 6.11. Therefore, as follows from the previous investigations, replacing the corner of the CFB at $(r, z) = (R, -d)$ by a spherical segment with radius $R_{\mathrm{S}} = 0.2\,\mathrm{m}$ leads to a convergence of the numerical results.

Next, the convergence of the motion of the CFB is studied. Figure 6.13a shows the empirical order of convergence q^n of the first- and second-order components of the displacement ξ. The corresponding errors E_ξ^n, which are defined in Eq. (6.75b), for the first- and second-order component of the displacement ξ are shown against the step size Δr in Fig. 6.13b. It can be seen that both components of the displacement ξ are converging with an empirical order of two.

It can be concluded that the numerical approximations for the unknown hydrodynamic forces and motion of the CFB are converging with order two if the corner of the CFB at $(r, z) = (R, -d)$ is replaced by a spherical segment with radius $R_{\mathrm{S}} = 0.2\,\mathrm{m}$. Together with the results presented in Sect. 6.7.1, this

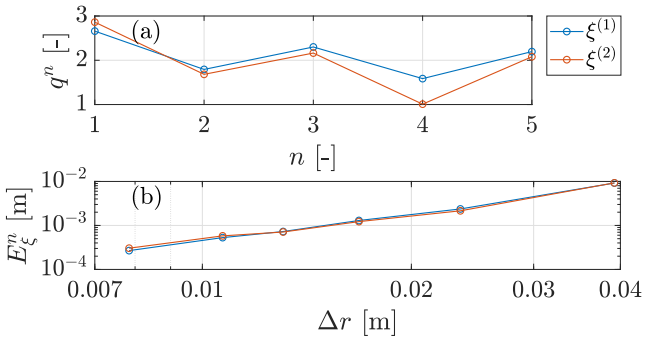

Figure 6.13: Convergence analysis for the displacement of the CFB. (a): Empirical order of convergence of the first- and second-order component of the displacement ξ. (b): Corresponding error E_ξ^n against the step size Δr.

verifies and validates the numerical results calculated by the method presented in this chapter. After introducing a scheme to calculate the FSI numerically and presenting first results for the FSI between the CFB and regular Stokes waves, this method is applied in the next chapter to calculate the FSI between the CFB and water waves corresponding to the NLS.

Analysis of the Fluid-structure Interaction between a Wave Energy Converter and Nonlinear Water Waves

When designing fixed or free-floating structures that are excited by real ocean waves, the hydrodynamic loads acting on the structures and the system response of the structures to the water waves must be estimated. To this end, a method for calculating the nonlinear FSI between a structure and nonlinear water waves has been presented in the previous chapters. Here, it has been shown how the NLS (5.2) can be used to compute the nonlinear FSI between a mechanical structure and nonlinear water waves. The use of the NLS instead of the Stokes waves introduced in Sect. 4.3 to calculate the incoming nonlinear water waves is motivated by the following facts:

- The computation of the incoming nonlinear water waves is computationally less expensive using the NLS. This results from the fact that the nonlinear interactions between regular components must not be explicitly considered using the NLS, see Sect. 5.2.2.
- In different studies, it has been conjectured that the Peregrine breather solution of the NLS, presented in Sect. 5.3.2, is a prototype of rogue waves in the ocean, see e.g. [DystheTrulsen99, ShriraGeogjaev10, DostalEtAl20]. Therefore, using the Peregrine breather solution of the NLS, it can be estimated with low computational effort which hydrodynamic loads a fixed or free-floating structure must withstand in extreme wave events.

In this chapter, the FSI between the WEC introduced in Sect. 3.1 and the incoming water waves corresponding to the NLS is simulated and analyzed. Recall that the WEC introduced in Sect. 3.1 consists of a cylindrical floating body (CFB) moving along a guidance. Only the CFB has contact with the water. Therefore, the FSI between the WEC and water waves can be analyzed by studying the FSI between the CFB and water waves. In the following, the FSI between the CFB of the WEC and nonlinear water waves corresponding to the NLS is simulated and analyzed.
In Sect. 6.7.2, it has been shown that numerical results might not converge if the CFB contains sharp edges or corners, see Fig. 6.11. Therefore, the CFB shown in Fig. 6.1, which contains a semispherical bottom, is used in this chapter. The used system and damping parameters of the CFB are given in Tab. 7.1. Furthermore, the CFB is moving in salt water with density $\rho = 1023\,\mathrm{kg/m^3}$. Only long-crested water waves are considered, which propagate in the x-direction.

Table 7.1: System and damping parameters of the used CFB.

R [m]	R_S [m]	d [m]	$d_\mathrm{lin} + \lambda_{\mathrm{vis},z}$ $\left[\frac{\mathrm{kg}}{\mathrm{s}}\right]$	d_elec $\left[\frac{\mathrm{kg}}{\mathrm{s}}\right]$
1	0.2	1.5	3000	0

In all numerical results presented in this chapter, the CFB is starting from its resting position. The initial values for the Fourier coefficients of the velocity potential corresponding to the body disturbance, ${}^{\mathrm{Z}}\widehat{\phi}^{(i)}_{\mathrm{B},m}$, are set to zero. As in Sect. 6.7, the incident velocity potentials $\phi_0^{(i)}$ of the incoming water waves are multiplied by the factor F_tanh, which is given in Eq. (6.74). Here, the constants a and b are set to $a = 0.4$, $b = 0$.
First, the FSI between the plane-wave solution from Eq. (5.40) of the NLS (5.2) and the CFB is investigated in Sect. 7.1. The corresponding results are compared with those obtained by using regular Stokes waves. Afterward, the Peregrine breather and soliton solutions of the NLS, which are given by Eqs. (5.44) and (5.45), are used in Sect. 7.2 and Sect. 7.3 to compute the respective FSI with the CFB. The corresponding effects of the presence of the CFB on the surrounding water waves are analyzed in Sect. 7.4. Then, the FSI between the CFB and random nonlinear Stokes waves is investigated in Sect. 7.5. This is done to analyze the advantages of exciting the CFB with waves corresponding to solutions of the NLS instead of exciting the CFB with random nonlinear Stokes waves. Finally, this chapter ends with a discussion of the found results in Sect. 7.6.

7.1 Analysis of FSI in Regular Waves

The plane-wave solution from Eq. (5.40) of the NLS (5.2) has been introduced in Sect. 5.3.1 and can be used to describe regular water waves, which fulfill the nonlinear dispersion relation from Eq. (4.8). However, regular water waves can also be described using Stokes waves. The corresponding velocity potential of regular Stokes waves is presented in Sect. 4.3.1.
In this section, the nonlinear FSI between nonlinear regular water waves and the CFB, which has been presented in Fig. 6.1, is investigated. The incoming water waves are described using regular Stokes waves and the plane-wave solution of the NLS, respectively. It is studied whether the use of regular Stokes waves and the plane-wave solution of the NLS leads to the same results for the FSI. Here, the incident velocity potential of the Stokes waves is computed analytically using

the formulas presented in Sect. 4.3.1. On the other side, the wave envelope ψ and the corresponding velocity potential ϕ of the plane-wave solution of the NLS are computed numerically. Here, the wave envelope ψ is computed numerically using the ReSP scheme presented in Sect. 5.4. The first- and second-order component of incident velocity potential ϕ_0, i. e. $\phi_0^{(1)}$ and $\phi_0^{(2)}$, are computed using Eq. (5.27) and the numerical method presented in Sect. 5.5.

It has to be noted that analytical expressions for ψ and ϕ corresponding to the plane-wave solution of the NLS have been given in Eqs. (5.40) and (5.41b). However, numerical values for ψ and ϕ are used in this section, since only numerical solutions for ψ and ϕ can be used in the following sections to compute the corresponding results for the FSI. Therefore, the investigations presented in this section also serve to analyze how the numerical errors occurring in the calculation of the wave envelop ψ and velocity potential ϕ corresponding to the NLS affect the FSI results.

In the following, Stokes waves are considered with amplitude $A = 0.2\,\mathrm{m}$ and wave number $k = 0.5\,\mathrm{m}^{-1}$ in a sea with depth $h = 7\,\mathrm{m}$. Using these parameters, the resulting waves have a steepness of $Ak = 0.1$. Furthermore, the condition for deep water is fulfilled, i. e. $h \geq \frac{1}{2}\lambda = \frac{\pi}{k} = 2\pi$. The corresponding wave frequency ω of the Stokes waves can be calculated using the dispersion relation from Eq. (2.16).

Moreover, water waves are considered, which correspond to the plane-wave solution of the NLS. Here, the wave envelope ψ is computed numerically using the ReSP scheme presented in Sect. 5.4. The necessary initial condition at time $t = 0$ is determined using the analytical plane-wave solution from Eq. (5.40) with $\psi_0 = 2\,\mathrm{m}$, $k_0 = 0.5\,\mathrm{m}^{-1}$, $\varepsilon = 0.1$, $X_\mathrm{s} = 0$, and $k_\mathrm{pw} = 0$. The corresponding carrier wave frequency ω_0 is given by $\omega_0 = \sqrt{k_0 g}$. The resulting wave envelope ψ and sea surface displacement η of the analytical plane-wave solution have been presented in Fig. 5.3. Using the stated values for ψ_0, k_0, and ε, it holds $A = \varepsilon\psi_0$, $k = k_0$ and $\varepsilon = Ak$. In this way, the waves corresponding to the plane-wave solution of the NLS have the same amplitude, wave number, and steepness as the considered Stokes waves.

In order to compute the incident velocity potential ϕ_0 corresponding to the NLS, the NLS is solved on the spatial domain $X \in [-120\,\mathrm{m}, 120\,\mathrm{m}]$ using $J = 2^{11} + 1$ spatial points and time domain $T \in [0, 40\,\mathrm{s}]$ using $N + 1 = 8001$ temporal grid points. This results in the step sizes $\Delta X = 240\,\mathrm{m}/2^{11} = 0.117\,\mathrm{m}$ and $\Delta T = 40\,\mathrm{s}/8000 = 0.005\,\mathrm{s}$. To calculate the velocity potential ϕ_0 corresponding to the plane-wave solution of the NLS, the auxiliary variable $\widetilde{\psi}$ is computed numerically. Here, the complex transport equation (5.11) is solved numerically using the scheme introduced in Eq. (5.64), which is applied on the spatial domain $Z \in [-0.7\,\mathrm{m}, 0]$ using $N + 1 = 29$ spatial grid points. This leads to a step size of $\Delta Z = -0.7\,\mathrm{m}/28 = -0.025\,\mathrm{m}$ in Z-direction.

It has to be noted that T, X, and Z denote the slow temporal and spatial coordinates. These coordinates can be computed from t, x, z by $T = \varepsilon t$, $X = \varepsilon x$, and $Z = \varepsilon z$, see Eqs. (5.1) and (5.9). Therefore, since $\varepsilon = 0.1$ is used in this

section, the velocity potential ϕ_0 corresponding to the plane-wave solution of the NLS is computed on the spatial domain $x \in [-1200\,\mathrm{m}, 1200\,\mathrm{m}]$, $z \in [-7\,\mathrm{m}, 0]$ and the time domain $t \in [0, 400\,\mathrm{s}]$.
All corresponding results for the FSI are computed using $N_\mathrm{F} = 16$ Fourier modes. Absorbing BCs are implemented using the damping μ from Eq. (6.7) and the settings used in [ShaoFaltinsen13]. Since the wavelength of the incoming waves is given by $\lambda = 2\pi/k = 12.56\,\mathrm{m}$, the length of the inner layer R_i and the length of the damping layer L are set to $R_\mathrm{i} = 13\,\mathrm{m}$ and $L = 26\,\mathrm{m}$, respectively. The computational domain $\bar{\Omega}_2$ from Eq. (6.35) is discretized using the spatial step sizes $\Delta r = \Delta z = 0.04\,\mathrm{m}$. Finally, all corresponding numerical results for the FSI are computed on the time domain $t \in [0, 400\,\mathrm{s}]$, which is discretized using a temporal step size of $\Delta t = 0.05\,\mathrm{s}$.
In the following, the hydrodynamic forces acting on the CFB are investigated. Excited by the hydrodynamic forces, the CFB can perform translational motion in the vertical direction. Figure 7.1 shows the hydrodynamic forces resulting from the use of Stokes waves and the waves corresponding to the NLS, respectively. Here, Figs. 7.1a and 7.1b show the respective first- and second-order component of the force acting in the vertical direction, i. e. , $\varepsilon F_3^{(1)}$ and $\varepsilon^2 F_3^{(2)}$. The system is considered in its steady state. In order to visualize the differences in the oscillation periods, the results for the hydrodynamic forces are shifted in time so that the forces have a maximum at time $t = 0$. Due to the small scale of $\varepsilon^2 F_3^{(2)}$, the total force $F_3 = \varepsilon F_3^{(1)} + \varepsilon^2 F_3^{(2)}$ is not shown in Fig. 7.1.
It can be seen that the calculated hydrodynamic forces differ slightly in their oscillation periods and their heights. Compared to the forces, which result from regular Stokes waves, the use of the NLS results in forces $\varepsilon F_3^{(1)}$ and $\varepsilon^2 F_3^{(2)}$ with a higher frequency. The relative difference between the heights of corresponding forces $\varepsilon F_3^{(1)}$ is 1.64%. For $\varepsilon^2 F_3^{(2)}$, the relative difference between the heights of the corresponding forces is given by 2.95%.
The difference in the oscillation periods results from the fact that the Stokes waves include only nonlinear wave effects resulting from the use of a second-order nonlinear wave theory. However, the NLS includes nonlinear wave effects resulting from the use of a third-order nonlinear wave theory. In particular, this means that the plane-wave solution of the NLS satisfies the nonlinear dispersion relation from Eq. (5.42) and the Stokes waves satisfy the linear dispersion relation from Eq. (2.16). Therefore, the regular waves corresponding to the plane-wave solution of the NLS oscillate in time with frequency $\omega_\mathrm{NLS} > \omega_0$, whereby ω_NLS depends on the wave amplitude. On the other side, the Stokes waves oscillate in time with frequency ω. Using the dispersion relation from Eq. (2.16), $\omega_0 = \sqrt{k_0 g}$, and $k_0 = k$, it follows that ω and ω_0 are related by $\omega = \sqrt{kg\tanh(kh)} = \omega_0\sqrt{\tanh(kh)}$. Since h fulfills the deep water condition, it holds $\tanh(kh) \approx 1$ and $\omega \approx \omega_0 \leq \omega_\mathrm{NLS}$. This shows that the waves corresponding to the plane-wave solution of the NLS have a smaller oscillation frequency than the considered Stokes waves. Furthermore, this explains the difference in the oscillation periods presented in Fig. 7.1.

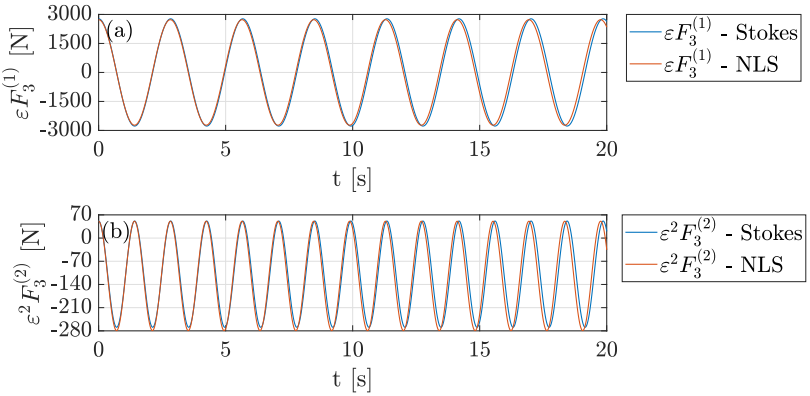

Figure 7.1: (a) First- and (b) second-order component of the hydrodynamic force acting on the CFB in the vertical direction. The CFB is excited by Stokes waves and waves corresponding to the plane-wave solution of the NLS.

It has to be noted that the amplitude of the hydrodynamic forces acting on the CFB and the motion of the CFB are frequency-dependent. For linear waves, this has been shown in Sect. 3.2.3, where the RAO has been introduced. However, the question arises whether the difference in the heights of the forces presented in Fig. 7.1 only results from the different frequencies of the incoming water waves. In order to answer this questions, additional Stokes waves have been considered, which oscillate in time with the frequency ω_{NLS}. In this way, the relative difference between the heights of acting hydrodynamic forces $F_3^{(1)}$, which results from the Stokes waves with frequency ω_{NLS} and the waves corresponding to the plane-wave solution of the NLS, have been reduced from 1.64% to 0.38%. For $\varepsilon^2 F_3^{(2)}$, the relative difference has been reduced from 2.95% to 0.23%. These differences can be even further reduced by increasing the water depth h. Here, it has to be noted that the NLS is only valid for $h \to \infty$. Additional simulations have shown that increasing the water depth from $h = 7\,\mathrm{m}$ to $h = 10\,\mathrm{m}$ reduces the difference between the heights of the forces $\varepsilon F_3^{(1)}$ from 0.38% to 0.04%. For $\varepsilon^2 F_3^{(2)}$, the relative difference is reduced from 0.23% to 0.01%.
Therefore, it has been shown that the different behaviors of the hydrodynamic forces presented in Fig. 6.1 result from the different frequencies of the incoming waves and the use of a too small water depth h. As a result, it is also shown that the numerical schemes presented in Sect. 5.4 and Sect. 5.5.2, which are utilized to compute the incident velocity potential ϕ_0 corresponding to solutions of the NLS, can be used to calculate the FSI in regular waves accurately. The instability, which is analyzed in Sect. 5.5.2 and occurs when the complex transport equation (5.11) is solved numerically, has a negligible influence on the presented numerical results. This validates the use of the NLS to compute the results for the FSI.

7.2 Interaction with the Peregrine Breather Solution

Next, the FSI is investigated, which results when the CFB is exited by waves corresponding to the Peregrine breather solution of the NLS. The influence of an initial perturbation of the Peregrine breather solution on the FSI is also studied. First, the interaction between the CFB and the waves corresponding to the unperturbed Peregrine breather solution of the NLS is considered. Afterward, the effects of an initial perturbation of the Peregrine breather solution on the FSI are studied.

7.2.1 FSI with the Unperturbed Peregrine Breather Solution

Before the FSI can be investigated, the wave envelope ψ of Peregrine breather solution has to be computed. This is done numerically using the ReSP scheme, which has been introduced in Sect. 5.4. To apply the ReSP scheme, an IC has to be specified. The IC is computed using the analytical Peregrine breather solution from Eq. (5.44) at time $T = -20\,\mathrm{s}$ with $k_0 = 0.5\,\mathrm{m}^{-1}$, $\psi_0 = 1.5\,\mathrm{m}$, $\varepsilon = 0.1$, and $X_\mathrm{s} = 44.29\,\mathrm{m}$. The corresponding carrier wave frequency is given by $\omega_0 = \sqrt{k_0 g} = 2.21\,\mathrm{rad/s}$. Here, X_s has been chosen so that the IC has its peak amplitude at $x = 0$. The corresponding analytical solution of the wave envelope ψ has been presented in Fig. 5.4.
In order to compute the incident velocity potential ϕ_0 of the incoming water waves, the NLS is solved on the spatial domain $X \in [-120\,\mathrm{m}, 120\,\mathrm{m}]$ using $J = 2^{11} + 1$ spatial points and time domain $T \in [-20\,\mathrm{s}, 20\,\mathrm{s}]$ using $N + 1 = 8001$ temporal grid points. This results in the step sizes $\Delta X = 240\,\mathrm{m}/2^{11} = 0.117\,\mathrm{m}$ and $\Delta T = 40\,\mathrm{s}/8000 = 0.005\,\mathrm{s}$. To calculate the velocity potential ϕ_0 corresponding to the Peregrine breather solution of the NLS, the auxiliary variable $\widetilde{\psi}$ is computed numerically. Here, the complex transport equation (5.11) is solved numerically using the scheme introduced in Eq. (5.64), which is applied on the spatial domain $Z \in [-0.7\,\mathrm{m}, 0]$ using $N + 1 = 29$ spatial grid points. This leads a step size of $\Delta Z = -0.7\,\mathrm{m}/28 = -0.025\,\mathrm{m}$ in Z-direction.
The corresponding numerical results for the FSI are computed for $h = 7\,\mathrm{m}$. Furthermore, the same domain $\bar{\Omega}$ and step sizes Δr, Δz, and Δt are used as specified in the Sect. 7.1. The FSI is computed on the time domain $t \in [-200\,\mathrm{s}, 200\,\mathrm{s}]$.
For the results presented in this section, the CFB is located at the position $x = X_\mathrm{s}/\varepsilon = 442.94\,\mathrm{m}$. In this way, the waves corresponding to the peak amplitude of the analytical Peregrine breather solution reach the CFB at $t = 0\,\mathrm{s}$.
Figure 7.2a shows the sea surface displacements $\varepsilon\eta^{(1)}_\mathrm{inc}$ and $\varepsilon^2\eta^{(2)}_\mathrm{inc}$ of the incoming water waves of first- and second-order. These are the waves which would be measured in the absence of the CFB. They are measured at the location of

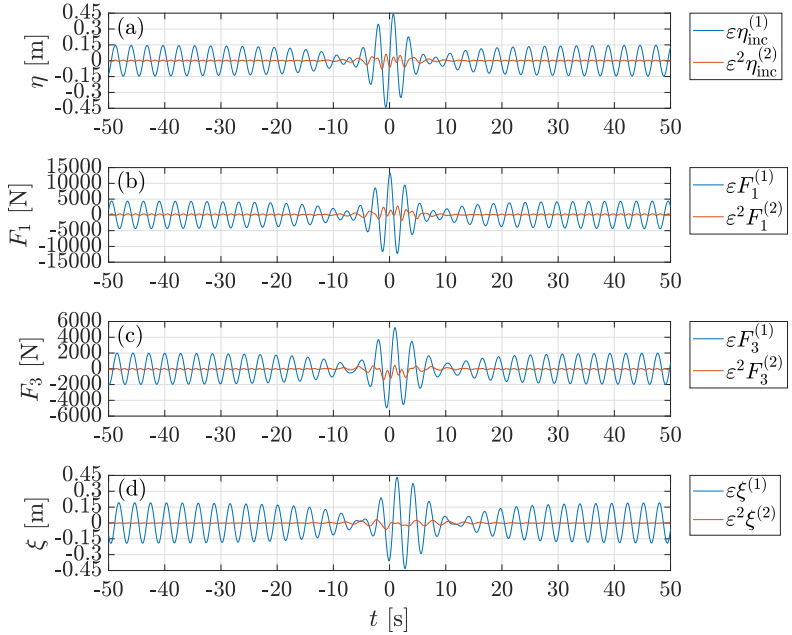

Figure 7.2: FSI between the CFB and waves corresponding to the unperturbed Peregrine breather solution of the NLS. It is shown the first- and second-order components of (a) the incoming water waves, the hydrodynamic forces acting in the (b) horizontal and (c) vertical direction, and (d) the displacement of the CFB.

the center of the CFB. Given the incident velocity potentials $\phi_0^{(1)}$ and $\phi_0^{(2)}$ from Eq. (5.27), $\eta_{\text{inc}}^{(1)}$ and $\eta_{\text{inc}}^{(2)}$ are computed using Eq. (4.19a) and Eq. (4.19b), respectively. The values of $\varepsilon\eta_{\text{inc}}^{(1)}$ and $\varepsilon^2\eta_{\text{inc}}^{(2)}$ are presented in Fig. 7.2a to better understand the corresponding results for the hydrodynamic forces acting on the CFB and the displacement of the CFB. As the wave envelope ψ of the Peregrine breather solution has its peak amplitude at $t = 0$, the time series of the incoming water waves $\eta_{\text{inc}}^{(1)}$ and $\eta_{\text{inc}}^{(2)}$ also have their peak amplitude around $t = 0$.
The corresponding first- and second-order components of the hydrodynamic forces, which act on the CFB in the horizontal and vertical direction, are presented in Figs. 7.2b and 7.2c, respectively. Here, it has to be noted that the presence of the CFB also disturbs the surrounding water waves, which in turn leads to additional hydrodynamic forces acting on the CFB. The hydrodynamic forces presented in Figs. 7.2b and 7.2c do not only contain the forces resulting from an excitation of the incoming water waves $\varepsilon\eta_{\text{inc}}^{(1)}$ and $\varepsilon^2\eta_{\text{inc}}^{(2)}$ presented in Figs. 7.2a. However, the presented forces also include the hydrodynamic forces resulting

from the disturbance of the water waves through the presence of the CFB. This is done by computing the hydrodynamic forces acting on the CFB using the velocity potentials $\phi^{(i)} = \phi_0^{(i)} + \phi_B^{(i)}$ and Eq. (4.29).
Finally, Fig. 7.2d shows the resulting first- and second-order components of the displacement of the CFB. It has to be noted that all results have been calculated over the time period $[-200\,\mathrm{s}, 200\,\mathrm{s}]$. However, to show the effect of the peak amplitude of the Peregrine breather solution on the FSI in a better way, all results are only depicted over the time period $[-50\,\mathrm{s}, 50\,\mathrm{s}]$.
Furthermore, it has to be noted that the CFB can only perform translatory motion in the vertical direction. Therefore, the forces $\varepsilon F_1^{(1)}$ and $\varepsilon^2 F_1^{(2)}$, which act on the CFB in the horizontal direction, do not influence the dynamics of the CFB. However, in order to investigate the loads that the CFBs have to withstand in the open sea, these forces are also presented in Fig. 7.2.
Considering Fig. 7.2a, it can be seen that the sea surface displacements $\varepsilon\eta_{\mathrm{inc}}^{(1)}$ and $\varepsilon^2\eta_{\mathrm{inc}}^{(2)}$ oscillate in time, whereby the oscillation frequency of $\varepsilon^2\eta_{\mathrm{inc}}^{(2)}$ is higher than the oscillation frequency of $\varepsilon\eta_{\mathrm{inc}}^{(1)}$. This result has also been found in Chap. 5. Here, it has been presented in Eqs. (5.35) and (5.37) that $\varepsilon\eta_{\mathrm{inc}}^{(1)}$ oscillates in time with a frequency around ω_0, while $\varepsilon^2\eta_{\mathrm{inc}}^{(2)}$ includes contributions oscillating in time with frequencies around ω_0 and $2\omega_0$. It has to be noted the different contributions of $\varepsilon\eta_{\mathrm{inc}}^{(1)}$ and $\varepsilon\eta_{\mathrm{inc}}^{(2)}$ are not oscillating in time exactly with frequencies ω_0 and $2\omega_0$, since all contributions are multiplied in Eqs. (5.35) and (5.37) with the complex-valued wave envelope ψ. The multiplication with ψ can lead to time-dependent phase shifts of the sea surface displacements $\varepsilon\eta_{\mathrm{inc}}^{(1)}$ and $\varepsilon^2\eta_{\mathrm{inc}}^{(2)}$.
In the following, the magnitude of the second-order component of the incoming water wave, $\varepsilon^2\eta_{\mathrm{inc}}^{(2)}$, is compared to the corresponding magnitude of the first-order component of the incoming water wave, $\varepsilon\eta_{\mathrm{inc}}^{(1)}$. For this, the corresponding wave heights of $\varepsilon\eta_{\mathrm{inc}}^{(1)}$ and $\varepsilon^2\eta_{\mathrm{inc}}^{(2)}$ are computed and compared. Let $|\eta|_{\mathrm{H}}$ denote the time-dependent wave height of the sea surface displacement η. For some given timepoint t, $|\eta|_{\mathrm{H}}$ is defined as the difference between the next maximal and minimal value, which η takes on around the timepoint t. For example, considering the wave height $|\varepsilon\eta_{\mathrm{inc}}^{(1)}|_{\mathrm{H}}$ of the sea surface displacement $\varepsilon\eta_{\mathrm{inc}}^{(1)}$ presented in Fig. 7.2a around $t = 30\,\mathrm{s}$, it is shown that $\varepsilon\eta_{\mathrm{inc}}^{(1)}$ has a maximum of $0.1395\,\mathrm{m}$ at $t = 30.45\,\mathrm{s}$ and a minimum of $-0.1384\,\mathrm{m}$ at $t = 29\,\mathrm{s}$. Therefore, $\varepsilon\eta_{\mathrm{inc}}^{(1)}$ has a wave height of $|\varepsilon\eta_{\mathrm{inc}}^{(1)}|_{\mathrm{H}} = 0.1395\,\mathrm{m} + 0.1384\,\mathrm{m} = 0.2779\,\mathrm{m}$ around $t = 30\,\mathrm{s}$. Similar to the definition of the height $|\eta|_{\mathrm{H}}$ of the sea surface displacement η around a given timepoint t, the height of some acting force F and the displacement of the CFB ξ are defined in the same way and are denoted by $|F|_{\mathrm{H}}$ and $|\xi|_{\mathrm{H}}$, respectively.
Outside the time period $[-30\,\mathrm{s}, 30\,\mathrm{s}]$, the sea surface displacements $\varepsilon\eta_{\mathrm{inc}}^{(1)}$ and $\varepsilon^2\eta_{\mathrm{inc}}^{(2)}$ behave regularly. For $t \notin [-30\,\mathrm{s}, 30\,\mathrm{s}]$, the quotient of the wave heights of $\varepsilon\eta_{\mathrm{inc}}^{(1)}$ and $\varepsilon^2\eta_{\mathrm{inc}}^{(2)}$ is about 3.7%, i. e. $|\varepsilon^2\eta_{\mathrm{inc}}^{(2)}|_{\mathrm{H}}/|\varepsilon\eta_{\mathrm{inc}}^{(1)}|_{\mathrm{H}} = 3.7\%$. This means that the wave height of the second-order component $\varepsilon^2\eta_{\mathrm{inc}}^{(2)}$ is only about 3.7% of the wave height of the first-order component $\varepsilon\eta_{\mathrm{inc}}^{(1)}$. However, considering the wave height of

the incoming water waves around $t = 0$, it results $|\varepsilon^2 \eta_{\mathrm{inc}}^{(2)}|_{\mathrm{H}} / |\varepsilon \eta_{\mathrm{inc}}^{(1)}|_{\mathrm{H}} = 14\%$. This means that the influence of the nonlinear second-order component $\varepsilon^2 \eta_{\mathrm{inc}}^{(2)}$ on the total sea surface displacement $\eta_{\mathrm{inc}} = \varepsilon \eta_{\mathrm{inc}}^{(1)} + \varepsilon^2 \eta_{\mathrm{inc}}^{(2)}$ increases significantly during the peak of the Peregrine breather solution around $t = 0$. This results directly from the fact that the wave envelope ψ of the Peregrine breather solution becomes higher and steeper around its peak amplitude. Recall that $\varepsilon \eta_{\mathrm{inc}}^{(1)}$ depends linearly on ψ, while $\varepsilon^2 \eta_{\mathrm{inc}}^{(2)}$ depends quadratically on ψ, see Eqs. (5.35) and (5.37). Therefore, once again, it is shown that the influence of nonlinear wave effects on the overall behavior of water waves becomes larger for higher and steeper water waves.

The results for the sea surface displacements $\varepsilon \eta_{\mathrm{inc}}^{(1)}$ and $\varepsilon^2 \eta_{\mathrm{inc}}^{(2)}$ can be directly transferred to the results for the acting hydrodynamic forces and the displacement of the CFB. Outside the time period $[-30\,\mathrm{s}, 30\,\mathrm{s}]$, Figs. 7.2b-7.2d show that the effect of the second-order components of the forces and displacement is small compared to the corresponding first-order results. However, the effect of the corresponding second-order components becomes significant during the developing of the peak amplitude of the Peregrine breather solution in the time period $[-30\,\mathrm{s}, 30\,\mathrm{s}]$.

Qualitatively, it can be observed that the first-order quantities $\varepsilon F_1^{(1)}$, $\varepsilon F_3^{(1)}$, and $\varepsilon \xi^{(1)}$ presented in Figs. 7.2b-7.2d are all oscillating around zero outside the time period $[-30\,\mathrm{s}, 30\,\mathrm{s}]$. However, it can also be observed that the second-order quantities $\varepsilon^2 F_1^{(2)}$ and $\varepsilon^2 F_3^{(2)}$ include non-zero mean values in the time period $[-30\,\mathrm{s}, 30\,\mathrm{s}]$. This shows that $\varepsilon^2 F_1^{(2)}$ and $\varepsilon^2 F_3^{(2)}$ include drift forces. For regular waves, such drift forces have already been observed in the results presented in Sect. 6.7.1. Further analyses show that the second-order forces $\varepsilon^2 F_1^{(2)}$ and $\varepsilon^2 F_3^{(2)}$ also include non-zero mean values outside the time period $[-30\,\mathrm{s}, 30\,\mathrm{s}]$, but these are very small. Also the second-order displacement $\varepsilon^2 \xi^{(2)}$ includes a non-zero mean value over the whole time domain, but this mean value is also very small.

Comparing the forces acting in the horizontal and vertical direction with each other, it can be seen that the forces acting in the horizontal direction are much larger than those acting in the vertical direction. This means that the dynamics of the CFB can strongly be increased if the CFB is not moving in the vertical direction but in a plane inclined by some angle α. This effect has already been presented in Chap. 3, where an inclined WEC is investigated. Looking at the harvested energy of the WEC presented in Chap. 3, this also means that the second-order components of the hydrodynamic forces and displacement of the inclined WEC can also significantly affect the amount of harvested energy.

In Sect. 5.3.2, it is noted that the Peregrine breather solution of the NLS is conjectured in different studies to be a prototype of rogue waves in the ocean. Therefore, Fig. 7.2 shows that nonlinear wave effects can contribute significantly to the corresponding FSI during extreme wave events. As a result, the scheme presented in this thesis can be used to estimate the linear and nonlinear hydrodynamic loads acting on structures during extreme wave events. These loads must

be known to make, for example, mechanical structures resistant to rogue waves.

7.2.2 FSI with the Perturbed Peregrine Breather Solution

To compute the wave envelope ψ of the Peregrine breather solution, which is initially perturbed by an irregular sea surface, the IC used in Sect. 7.2.1 is perturbed using the approach presented in Eq. (5.80). The corresponding sea surface displacement $\eta_{\mathrm{LC}}(x,t)$ from Eq. (5.79) of a long-crested random water wave, which is needed to compute the perturbed IC, is calculated using the Pierson-Moskowitz spectrum S_{PM} from Eq. (2.23) with peak frequency $\omega_{\mathrm{p}} = 0.25\,\mathrm{rad/s}$ and different significant wave heights H_{s}. The numerical solution for the wave envelope ψ, the corresponding incident velocity potential ϕ_0, and the corresponding numerical results for the FSI are computed using the same spatial and time domains and discretizations as specified in Sect. 7.2.1.
First, the Peregrine breather solution is initially perturbed by an irregular sea surface with significant wave height $H_{\mathrm{s}} = 1.5\,\mathrm{m}$. Using this value for H_{s}, the perturbing irregular sea surface has the same significant wave height H_{s} as the amplitude $\psi_0 = 1.5\,\mathrm{m}$ of the background wave envelope of the Peregrine breather solution. The corresponding wave envelope ψ of the perturbed Peregrine breather solution has been presented in Fig. 5.14e.
In the following, the FSI is investigated, which occurs between the CFB and waves corresponding to the perturbed Peregrine breather solution presented in Fig. 5.14e. The corresponding results for the FSI are presented in Fig. 7.3. Here, Fig. 7.3a shows the sea surface displacements $\varepsilon\eta_{\mathrm{inc}}^{(1)}$ and $\varepsilon^2\eta_{\mathrm{inc}}^{(2)}$ of the incoming water waves of first- and second-order, which are measured at the position of the center of the CFB. The corresponding hydrodynamic forces of first- and second-order, which are acting on the CFB in the horizontal and vertical direction, are presented in Figs. 7.3b and 7.3c, respectively. Finally, Fig. 7.3d shows the first- and second-order components of the displacement of the CFB.
Compared to the results from Fig. 7.2 for the FSI with the unperturbed Peregrine breather solution, it can be seen that the initial perturbation of the Peregrine breather solution has only an influence on the amplitude of the results for η, F_1, F_3, and ξ, but not on the frequency. This is due to the fact that the considered initial perturbation only changes the amplitude of the IC, see Eq. (5.81). However, it can again be seen that the effect of the second-order components of the forces and displacement becomes significant during the evolution of the peak amplitude of the Peregrine breather solution in the time interval $[-30\,\mathrm{s}, 30\,\mathrm{s}]$. However, the second-order components of the forces and displacement become small outside the time interval $[-30\,\mathrm{s}, 30\,\mathrm{s}]$. This was also the case for the FSI between the CFB and the water waves corresponding to the unperturbed Peregrine breather solution, see Fig. 7.2.
Knowing that the considered perturbation only influences the amplitude of the displacements and hydrodynamic forces acting on the CFB but not the frequency,

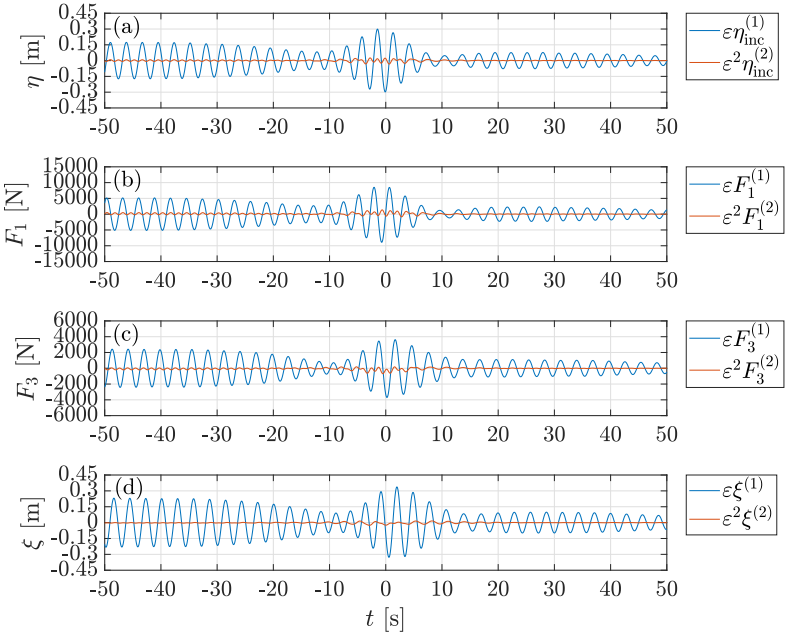

Figure 7.3: FSI between the CFB and waves corresponding to the Peregrine breather solution of the NLS, which is initially perturbed by an irregular sea surface with significant wave height $H_{\mathrm{s}} = 1.5\,\mathrm{m}$. It is shown the first- and second-order components of (a) the incoming water waves, the hydrodynamic forces acting in the (b) horizontal and (c) vertical direction, and (d) the displacement of the CFB.

only the amplitude of the displacements and forces are investigated in more detail in the following. Here, the peak envelopes of the displacements and hydrodynamic forces are considered. The peak envelope of a function f can be computed by connecting all maxima or minima of f. Connecting all maxima results in the upper peak envelope (UPE), connecting all minima results in the lower peak envelope (LPE). To show this in a better way, Fig. 7.4 presents the values of the upper and lower peak envelope for some hydrodynamic force $\varepsilon F_3^{(1)} + \varepsilon^2 F_3^{(2)}$ acting on the CFB in the vertical direction.

In the following, the effect of an initial perturbation of the Peregrine breather solution on the FSI with the CFB is investigated for different significant wave heights H_{s}. Recall that the significant wave height H_{s} describes the average value of the highest third of the waves in an irregular sea. Therefore, the amplitudes of the initial perturbation of the Peregrine breather solution become larger for larger significant wave heights H_{s}. The investigation is performed by studying the value of the upper peak envelope for the total hydrodynamic forces acting

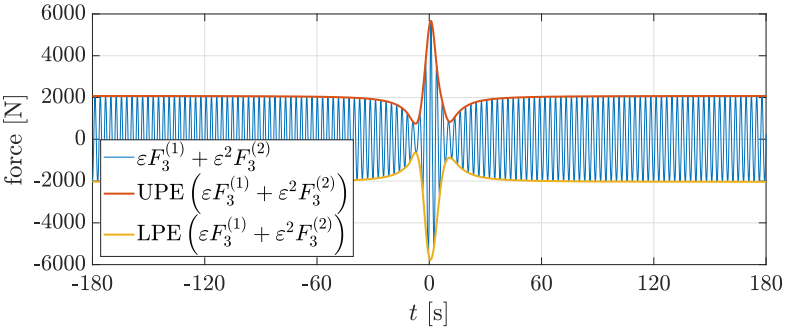

Figure 7.4: Example for the upper and lower peak envelope.

in the horizontal and vertical direction and the total displacement of the CFB. Let F_1, F_3, and ξ denote the total hydrodynamic forces acting in the horizontal and vertical direction and the total displacement of the CFB, respectively. Using the Stokes perturbation expansions from Eqs. (4.13b), (4.28), and (4.34), and considering only the terms of first- and second-order, it results

$$F_1 = \varepsilon F_1^{(1)} + \varepsilon^2 F_1^{(2)}, \quad F_3 = \varepsilon F_3^{(1)} + \varepsilon^2 F_3^{(2)}, \quad \text{and} \quad \xi = \varepsilon \xi^{(1)} + \varepsilon^2 \xi^{(2)}. \tag{7.1}$$

The values of the upper peak envelopes of F_1, F_3 and ξ are presented in Fig. 7.5 for different significant wave heights H_s. Here, the wave envelopes ψ of the perturbed Peregrine breather solutions shown in Figs. 5.12 and 5.14 have been used to compute the corresponding incident velocity potential ϕ_0 of the incoming water waves. The result with $H_s = 0$ represent the results for the Peregrine breather solution without any initial perturbation.

Figure 7.5 shows that the perturbation of the Peregrine breather solution strongly affects the corresponding FSI with the CFB. The higher the value of the significant wave height H_s, the more the results for F_1, F_3 and ξ differ from the corresponding result with $H_s = 0$. For example, it can be seen that the upper peak envelopes of F_1, F_3 and ξ strongly decrease at time point $t = 0$ for $H_s = 1.5\,\text{m}$ and $H_s = 2\,\text{m}$ compared to the corresponding values for $H_s = 0$.

For $H_s = 2\,\text{m}$, Fig. 7.5 also shows that the upper peak envelopes of F_1, F_3 and ξ has higher values at timepoint $t = 120\,\text{s}$ than at $t = 0$. This means that the perturbation of the Peregrine breather solution can also lead to high hydrodynamic forces and displacements outside the time period $[-30\,\text{s}, 30\,\text{s}]$, where the unperturbed Peregrine breather solution reaches its peak amplitude. Furthermore, this means that nonlinear wave effects can largely affect the FSI over the whole simulation time and not only in the time period $[-30\,\text{s}, 30\,\text{s}]$. To present this in a better way, Fig. 7.6 shows the time series of the first- and second-order components of the hydrodynamic forces acting on the CFB in the vertical direction for $H_s = 2\,\text{m}$ and $t \in [-180\,\text{s}, 180\,\text{s}]$. Here, it is shown that the

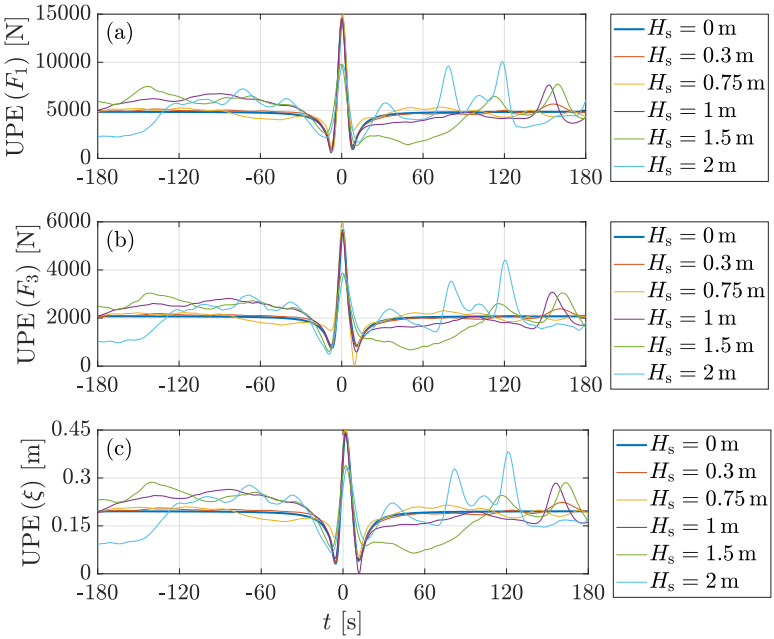

Figure 7.5: Upper peak envelopes for the FSI between the CFB and water waves corresponding to the Peregrine breather solution, which is initially perturbed by irregular sea surfaces with different significant wave heights H_s. Shown are the upper peak envelopes of (a) F_1, (b) F_3, and (c) ξ.

force $\varepsilon^2 F_3^{(2)}$ can contribute significantly to the total hydrodynamic force F_3 over the whole simulation time.

It can be concluded that an initial perturbation can strongly affect the behavior of the Peregrine breather solution. Furthermore, nonlinear wave effects can contribute significantly to the corresponding FSI over the whole simulation time. Compared to the FSI between the CFB and waves corresponding to the unperturbed Peregrine breather solution, an initial perturbation considerably affects the water waves and the resulting FSI.

It has to be noted that all results presented in this section have only been computed for one realization of the stochastic perturbation for each value of H_s. A stochastic analysis should be performed using many given realizations of the stochastic processes to better analyze the effect of an increasing significant wave height H_s on the corresponding FSI. However, to make the scope of this thesis not too extensive, a corresponding study is not shown here.

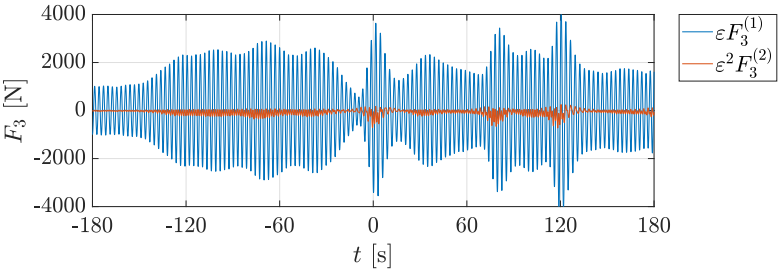

Figure 7.6: Hydrodynamic forces acting on the CFB, which result from waves corresponding to the Peregrine breather solution that is initially perturbed by an irregular sea surface with significant wave height $H_s = 2\,\mathrm{m}$.

7.3 Interaction with the Soliton Solution

Next, the FSI between the CFB and the waves corresponding to the soliton solution of the NLS is considered. The influence of an initial perturbation of the soliton solution on the FSI is also investigated here. Again, all results are computed numerically.

7.3.1 FSI with the Unperturbed Soliton Solution

First, results are presented for the FSI between the CFB and water waves corresponding to the unperturbed soliton solution of the NLS. The initial condition for the ReSP scheme, which is described in Sect. 5.4, is computed using the soliton solution from Eq. (5.45) at time $T = 0$ with $k_0 = 0.5\,\mathrm{m}^{-1}$, $\psi_0 = 1.5\,\mathrm{m}$, $\varepsilon = 0.1$, and $X_s = 0$. In Sect. 5.3.3, the wave envelope ψ and sea surface displacement η of the corresponding analytical soliton solution are shown in Fig. 5.5.
The numerical solution of the NLS and the corresponding incident velocity potential ϕ_0 are computed using the same spatial domain and corresponding step sizes ΔX and ΔZ as specified in Sect. 7.2.1. Furthermore, the numerical solution of the NLS and the corresponding incident velocity potential ϕ_0 are computed on the time domain $T \in [0, 40\,\mathrm{s}]$ using a temporal step size of $\Delta T = 0.005\,\mathrm{s}$. The corresponding numerical results for the FSI are computed using the same spatial domain $\bar{\Omega}$ and water depth h as specified in Sect. 7.2.1. In addition, the same step sizes Δr and Δz are used as in section 7.2.1. The numerical results for the FSI are computed on the time domain $t \in [0\,\mathrm{s}, 400\,\mathrm{s}]$ using a temporal step size of $\Delta t = 0.05\,\mathrm{s}$.
To compute the corresponding FSI with the CFB, the CFB is placed at location $x = 442.9\,\mathrm{m}$. In this way, the peak amplitude of the unperturbed soliton

solution reaches the CFB at time $t = 200\,\mathrm{s}$.
Figure 7.7a shows the sea surface displacements $\varepsilon\eta_{\mathrm{inc}}^{(1)}$ and $\varepsilon^2\eta_{\mathrm{inc}}^{(2)}$ of the incoming water waves of first- and second-order, which are measured at the position of the center of the CFB. The first- and second-order components of the hydrodynamic forces, which act on the CFB in the horizontal and vertical direction, are presented in Figs. 7.7b and 7.7c, respectively. Finally, Fig. 7.7d shows the resulting first- and second-order components of the displacement of the CFB. It has to be noted that the sea surface displacements $\varepsilon\eta_{\mathrm{inc}}^{(1)}$ and $\varepsilon^2\eta_{\mathrm{inc}}^{(2)}$ of the incoming water waves become significantly small outside the time domain $[150\,\mathrm{s}, 250\,\mathrm{s}]$. Therefore, the corresponding FSI with the CFB is shown in Fig. 7.7 only for the time domain $t \in [150\,\mathrm{s}, 250\,\mathrm{s}]$.
First, the heights of the first- and second-order quantities shown in Figs. 7.7a-7.7c are compared with each other. Here, it can be observed that the quotient of $|\varepsilon\eta_{\mathrm{inc}}^{(1)}|_{\mathrm{H}}$ and $|\varepsilon^2\eta_{\mathrm{inc}}^{(2)}|_{\mathrm{H}}$ at time $t = 200\,\mathrm{s}$ is about 4%, i. e. $|\varepsilon^2\eta_{\mathrm{inc}}^{(2)}|_{\mathrm{H}}/|\varepsilon\eta_{\mathrm{inc}}^{(1)}|_{\mathrm{H}} = 4\%$. Similar results are observed for the corresponding forces acting on the CFB. At

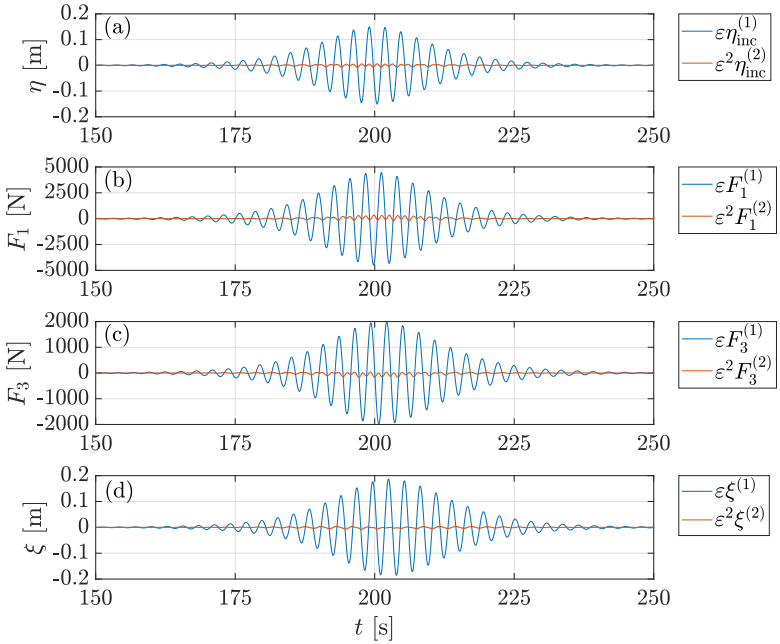

Figure 7.7: FSI between the CFB and waves corresponding to the unperturbed soliton solution of the NLS. It is shown the first- and second-order components of (a) the incoming water waves, the hydrodynamic forces acting in the (b) horizontal and (c) vertical direction, and (d) the displacement of the CFB.

time $t = 200\,\mathrm{s}$, it holds $|\varepsilon^2 F_1^{(2)}|_\mathrm{H}/|\varepsilon F_1^{(1)}|_\mathrm{H} = 5.4\%$ and $|\varepsilon^2 F_3^{(2)}|_\mathrm{H}/|\varepsilon F_3^{(1)}|_\mathrm{H} = 5.2\%$. Therefore, it is observed that the second-order quantities $\varepsilon^2\eta_\mathrm{inc}^{(2)}$, $\varepsilon^2 F_1^{(2)}$ and $\varepsilon^2 F_3^{(2)}$ presented in Figs. 7.7a-7.7c do not contribute as much to the total quantities η, F_1 and F_3 as it has been the case during the peak amplitude of the unperturbed Peregrine breather solution, see Fig. 7.2. However, the nonlinear effects coming from the force components of second-order are small, but not negligible. Therefore, they should still be considered for constructing cylindrical offshore structures, like jacket structures and piles, operating in real ocean waves.
Finally, the displacements $\varepsilon\xi^{(1)}$ and $\varepsilon^2\xi^{(2)}$ of the CFB are investigated. First, Fig. 7.7d shows that the incoming sea surface displacement of first-order, $\varepsilon\eta_\mathrm{inc}^{(1)}$, becomes maximal at time $t = 199\,\mathrm{s}$. In contrast, the displacement $\varepsilon\xi^{(1)}$ becomes maximal at time $t = 202.5\,\mathrm{s}$. This shift in time results from the inertia effects of the CFB. Considering the displacement $\varepsilon^2\xi^{(2)}$, it can be observed that $\varepsilon^2\xi^{(2)}$ becomes small at time $t = 202.5\,\mathrm{s}$. However, in the time periods $[150\,\mathrm{s}, 200\,\mathrm{s}]$ and $[205\,\mathrm{s}, 250\,\mathrm{s}]$, where the respective amplitude of $\varepsilon\xi^{(1)}$ increases and decreases, the displacement $\varepsilon^2\xi^{(2)}$ reaches its highest amplitudes. Here, the quotient of the heights of the displacements $\varepsilon\xi^{(1)}$ and $\varepsilon^2\xi^{(2)}$ reaches values up to 4%, i. e. $|\varepsilon^2\xi^{(2)}|_\mathrm{H}/|\varepsilon\xi^{(1)}|_\mathrm{H} = 4\%$. Therefore, also considering the displacement of the CFB, it can be concluded that the nonlinear effects appearing in the FSI should be considered for the construction of cylindrical offshore structures operating in real ocean waves.

7.3.2 FSI with the Perturbed Soliton Solution

To compute the wave envelope ψ of the soliton solution, which is initially perturbed by an irregular sea surface, the IC used in Sect. 7.3.1 is perturbed using the approach presented Eq. (5.80). The corresponding sea surface displacement $\eta_\mathrm{LC}(x,t)$ from Eq. (5.79) of a long-crested random water wave, which is needed to compute the perturbed IC, is calculated using the Pierson-Moskowitz spectrum S_PM from Eq. (2.23) with peak frequency $\omega_\mathrm{p} = 0.25\,\mathrm{rad/s}$ and different significant wave heights H_s. The numerical solution for the wave envelope ψ, the corresponding incident velocity potential ϕ_0, and the corresponding numerical results for the FSI are computed using the same spatial and time domains and discretizations as specified in Sect. 7.3.1.
First, the soliton solution is initially perturbed by an irregular sea surface with significant wave height $H_\mathrm{s} = 1.5\,\mathrm{m}$. The corresponding wave envelope ψ of the perturbed soliton solution has been presented in Fig. 5.17e.
In the following, the FSI is investigated, which occurs between the CFB and the perturbed soliton solution presented in Fig. 5.17e. The corresponding results for the FSI are presented in Fig. 7.8. Here, Fig. 7.8a shows the sea surface displacements $\varepsilon\eta_\mathrm{inc}^{(1)}$ and $\varepsilon^2\eta_\mathrm{inc}^{(2)}$ of the incoming water waves of first- and second- order, which are measured at the position of the center of the CFB. The corresponding

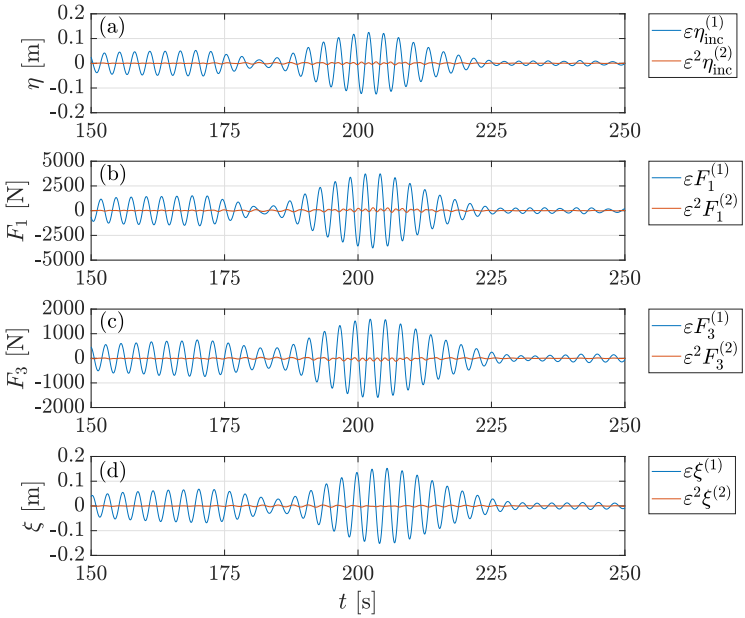

Figure 7.8: FSI between the CFB and waves corresponding to the soliton solution of the NLS, which is initially perturbed by an irregular sea surface with significant wave height $H_s = 1.5\,\mathrm{m}$. It is shown the first- and second-order components of (a) the incoming water waves, the hydrodynamic forces acting in the (b) horizontal and (c) vertical direction, and (d) the displacement of the CFB.

forces of first- and second- order, which are acting on the CFB in the horizontal and vertical direction, are presented in Figs. 7.8b and 7.8c, respectively. Finally, Fig. 7.8d shows the first- and second-order components of the displacement of the CFB.

In contrast to the results shown in Fig. 7.7 for the soliton solution without any initial perturbation, it can be seen that the incoming water waves shown in Fig. 7.8a are exciting the CFB over the whole presented time domain, see e.g. Figs. 7.8b-7.8d for $t \leq 180\,\mathrm{s}$. Therefore, also the walls of the CFB have to resist the acting hydrodynamic forces over the whole time domain. Regarding the WEC, which has been introduced in Chap. 3, this means that energy can be harvested over the whole time domain. This would not be the case, if the WEC is excited by the waves corresponding to the unperturbed soliton solution, since the CFB would only move during a short time period, see Fig. 7.7d.

Investigating the results presented in Figs. 7.8b and 7.8c, it can be seen that the largest amplitude of the first-order components of the hydrodynamic forces are acting on the CFB during the peak amplitude of the perturbed soliton solution

at $t \approx 200\,\mathrm{s}$. Therefore, also the first-order components of the displacement of the CFB reach their highest amplitudes around $t \approx 200\,\mathrm{s}$. However, compared to the results presented in Fig. 7.7 for the unperturbed soliton solution, it can be seen that the peak amplitudes of $\varepsilon\eta_{\mathrm{inc}}^{(1)}$, $\varepsilon F_1^{(1)}$, $\varepsilon F_3^{(1)}$, and $\varepsilon\xi^{(1)}$ are shifted in time. Therefore, an initial perturbation of the soliton solution does not only affect the amplitudes of $\varepsilon F_1^{(1)}$, $\varepsilon F_3^{(1)}$, and $\varepsilon\xi^{(1)}$, but also the locations of the corresponding maximal amplitudes in time.
Considering the second-order quantities $\varepsilon^2 F_1^{(2)}$, $\varepsilon^2 F_3^{(2)}$, and $\varepsilon^2\xi^{(2)}$, Figs. 7.8b-7.8d show that the amplitudes of these quantities become relatively large in the time around $t = 200\,\mathrm{s}$, where also the unperturbed soliton solution has its peak amplitude. However, Figs. 7.8b-7.8d also show that $\varepsilon^2 F_1^{(2)}$, $\varepsilon^2 F_3^{(2)}$, and $\varepsilon^2\xi^{(2)}$ have large amplitudes at time $t = 185\,\mathrm{s}$, where the corresponding first-order quantities have low amplitudes. In order to show this is a better way, Fig. 7.9 shows a zoom into the results presented in Figs. 7.8b-7.8d around $t = 185\,\mathrm{s}$. Therefore, if the soliton solution is initially perturbed by an irregular sea surface, it is observed that the contribution of the second-order quantities to the overall results for the FSI can become significant for short time periods.
Next, the influence of different significant wave heights H_{s} on the results for the FSI is investigated. Again, this is done by considering the upper peak envelopes of F_1, F_3, and ξ. The values of the upper peak envelopes of F_1, F_3 and ξ are presented in Fig. 7.10 for different values of H_{s} over the time period $[20\,\mathrm{s}, 380\,\mathrm{s}]$. Here, the corresponding wave envelopes ψ of the initially perturbed soliton solutions shown in Figs. 5.15 and 5.17 are used to compute the corresponding incident velocity potential ϕ_0 of the incoming water waves. The results for $H_{\mathrm{s}} = 0$ represent the results for the unperturbed soliton solution.
Figure 7.10 shows that an initial perturbation of the soliton solution strongly affects the corresponding FSI with the CFB. Hydrodynamic forces are not only acting on the CFB in the time period $[150\,\mathrm{s}, 250\,\mathrm{s}]$, where water waves corresponding to the unperturbed soliton solution act on the CFB, but over the

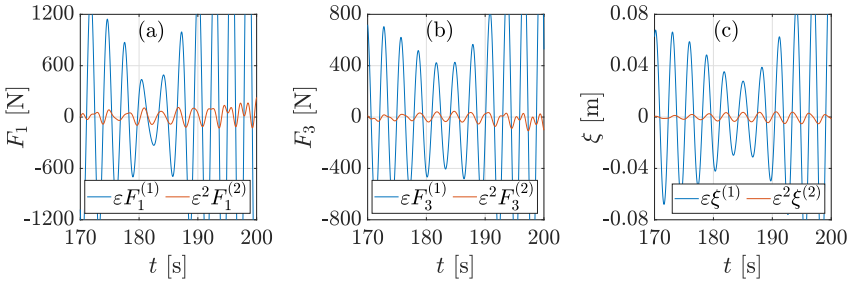

Figure 7.9: Zoom into the results presented in Figs. 7.8b-7.8d around $t = 185\,\mathrm{s}$. It is shown the first- and second-order components of the hydrodynamic forces acting in the (a) horizontal and (b) vertical direction, and (c) the displacement of the CFB.

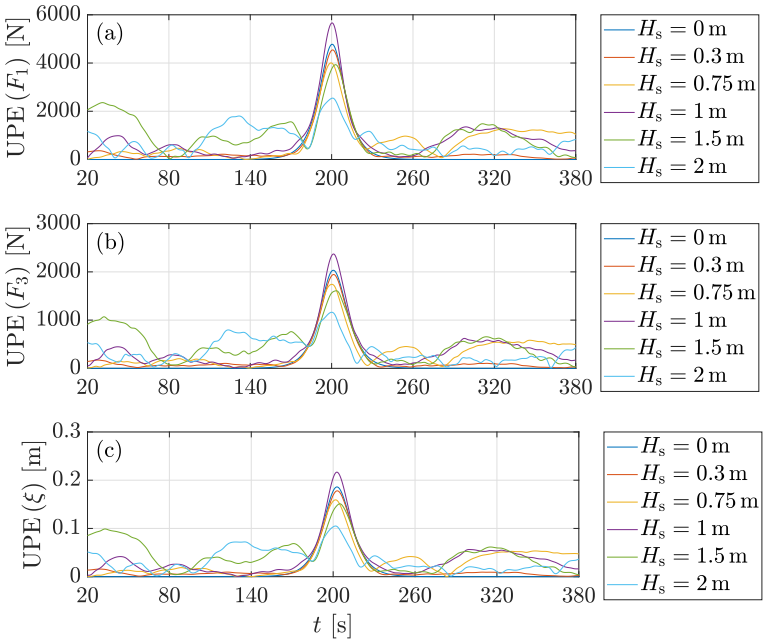

Figure 7.10: Upper peak envelopes for the FSI between the CFB and water waves corresponding to the soliton solution, which is initially perturbed by irregular sea surfaces with different significant wave heights H_s. Shown are the upper peak envelopes of (a) F_1, (b) F_3, and (c) ξ.

whole time domain. Therefore, the CFB also performs translational motion over the whole time domain.

Considering the maximal amplitudes of the upper peak envelopes of F_1, F_3, and ξ around $t = 200\,\mathrm{s}$, it can be seen that the initial perturbation of the soliton solution by an irregular sea surface can lead to a small shift of the corresponding maximal amplitudes in time. For example, the maximal amplitude of the upper peak envelopes of F_1 for $H_s = 0.75\,\mathrm{m}$ and $H_s = 1.5\,\mathrm{m}$ are shifted against each other by about 3 s. Such a shift in time has already been observed in the results presented in Fig. 7.7. Furthermore, Fig. 7.10 shows that the perturbation of the soliton solution has a significant effect on the maximal amplitude of the upper peak envelopes of F_1, F_3, and ξ. For example, it can be seen that the maximal value of UPE(F_3) around $t = 200\,\mathrm{s}$ changes between 1163 N for $H_s = 2\,\mathrm{m}$ and 2370 N for $H_s = 1\,\mathrm{m}$.

It has to be noted that all results presented in this section have only been computed for one realization of the stochastic perturbation for each value of H_s.

Therefore, considering different stochastic perturbations with the same significant wave heights H_s might even lead to larger maximal values of UPE(F_1), UPE(F_3), and UPE(ξ). To make the scope of this thesis not too extensive, a corresponding stochastical analysis about the range of the maximal values of UPE(F_1), UPE(F_3), and UPE(ξ) for other realizations of the stochastic perturbations is not shown here. However, it has been shown that an initial perturbation can strongly affect the behavior of the soliton solution and the corresponding FSI with a cylindrical structure.

7.4 Influence of the Presence of the Body on Nonlinear Water Waves

In the previous sections, the influence of the water waves on the motion of the CFB has been investigated. However, the presence the CFB also disturbs the incoming water waves. In Sect. 4.1.4, the velocity potential ϕ corresponding to the water waves, which are perturbed by the presence of the CFB, has been separated into the velocity potentials ϕ_0 and ϕ_B, see Eq. (4.21). Here, ϕ_0 is the velocity potential of the incoming water waves, and ϕ_B is the velocity potential corresponding to the body disturbance.
In this section, the influence of the CFB on the surrounding water waves is studied. Such an investigation is interesting, for example, if a second structure is moving next to the CFB considered in this chapter. In this case, the water waves are disturbed by the presence of the CFB, whereby the disturbance can lead to hydrodynamic forces acting on the second structure and vice versa. Investigating the influence of the CFB on the incoming water waves, it can be analyzed whether these hydrodynamic interaction forces between the two structures can be neglected in the computation of the corresponding motion of each structure or not.
In the following, the influence of the CFB on the surrounding water waves is investigated by studying the frequency spectrum of the sea surface displacement. Here, the spectrum of the incoming water waves η_{inc}, which are not disturbed by the presence of the CFB, are compared with the spectrum of the water waves η_{total}, which are disturbed by the presence of the CFB. First, the FSI between the incoming water waves and the CFB is computed over a time period of length 400 s. This includes the calculation of η_{total}. Afterward, the time series of η_{inc} and η_{total} at a given spatial position are considered. Physically, this corresponds to a sensor that measures the sea surface displacement at a given spatial position. In this section, the sensor is placed 1 m away from the CFB.

Based on the direction of the incoming long-crested water waves, the sensor is located exactly behind the cylinder. Figure 7.11 depicts the position of the used sensor. It has to be noted that the computed frequency spectra depend on the location of the sensor. However, to make the study not too extensive, only one sensor location is considered in this section.
In the following, the frequency spectra of the first- and second-order component of η_{inc} and η_{total}, which are given by $\varepsilon\eta_{\text{inc}}^{(1)}$, $\varepsilon^2\eta_{\text{inc}}^{(2)}$, $\varepsilon\eta_{\text{total}}^{(1)}$, and $\varepsilon^2\eta_{\text{total}}^{(2)}$, are compared with each other. After calculating the time series of $\varepsilon\eta_{\text{inc}}^{(1)}$, $\varepsilon^2\eta_{\text{inc}}^{(2)}$, $\varepsilon\eta_{\text{total}}^{(1)}$, and $\varepsilon^2\eta_{\text{total}}^{(2)}$ at the given spatial position, the corresponding frequency spectra are calculated using a discrete Fourier transform. To eliminate the influence of the transition phase of the CFB motion on $\varepsilon\eta_{\text{total}}^{(1)}$ and $\varepsilon^2\eta_{\text{total}}^{(2)}$, the time series of $\varepsilon\eta_{\text{inc}}^{(1)}$, $\varepsilon^2\eta_{\text{inc}}^{(2)}$, $\varepsilon\eta_{\text{total}}^{(1)}$, and $\varepsilon^2\eta_{\text{total}}^{(2)}$ are only considered during the steady state of the CFB. In addition, all considered time series have been truncated so that they start and end with a maximum. However, since the considered time series are not periodic, the corresponding time series are also windowed using a Hann filter.
Since the resulting frequency spectra are complex-valued, only the amplitudes of the spectra are considered. Denoting the frequency spectra by $P = P(\omega)$, the values of $|P(\omega)|$ corresponding to $\varepsilon\eta_{\text{inc}}^{(1)}$, $\varepsilon^2\eta_{\text{inc}}^{(2)}$, $\varepsilon\eta_{\text{total}}^{(1)}$, and $\varepsilon^2\eta_{\text{total}}^{(2)}$ are investigated in this section.
The described investigations are performed for the case that the CFB is excited by waves corresponding to Peregrine breather and soliton solution of the NLS, respectively. The solutions of the NLS are considered without and with an initial perturbation by an irregular sea surface with peak frequency $\omega_{\text{p}} = 0.25\,\text{rad/s}$ and significant wave height $H_{\text{s}} = 1.5\,\text{m}$. All numerical results are calculated using the same wave parameters, time domains, spatial domains, and step sizes as specified in Sect. 7.2 and Sect. 7.3, respectively.

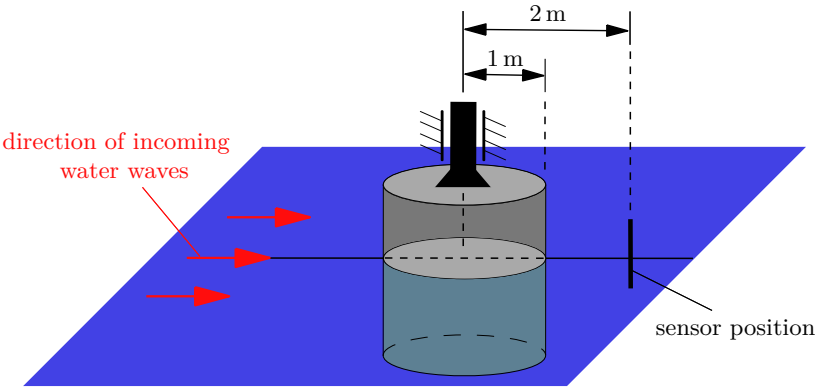

Figure 7.11: Position of sensor, which measures the sea surface displacements.

7.4.1 Influence of the Peregrine Breather Solution

First, the effect of the presence of the CFB on the waves corresponding to the unperturbed Peregrine breather solution of the NLS is investigated. The time series of $\varepsilon\eta^{(1)}_{\mathrm{inc}}$ and $\varepsilon^2\eta^{(2)}_{\mathrm{inc}}$, which are analyzed in the following, are the same as presented in Fig. 7.2a. The corresponding frequency spectra of $\varepsilon\eta^{(1)}_{\mathrm{inc}}$, $\varepsilon^2\eta^{(2)}_{\mathrm{inc}}$, $\varepsilon\eta^{(1)}_{\mathrm{total}}$, and $\varepsilon^2\eta^{(2)}_{\mathrm{total}}$ are presented in Fig. 7.12. Here, Fig. 7.12a and Fig. 7.12b show the same frequency spectra using a linear and logarithmic vertical axis scale, respectively.

Figure 7.12 shows that the frequency spectrum of the first component of the incoming undisturbed water waves, $\varepsilon\eta^{(1)}_{\mathrm{inc}}$, has a high peak around $\omega = 2.2\,\mathrm{rad/s}$. This peak corresponds to the carrier wave frequency $\omega_0 = \sqrt{k_0 g} = 2.2147\,\mathrm{rad/s}$, with which the background wave of the undisturbed Peregrine breather solution oscillates in time. This background wave can also be seen in Fig. 7.2a outside the time period $[-30\,\mathrm{s}, 30\,\mathrm{s}]$. The remaining components of the frequency spectrum of $\varepsilon\eta^{(1)}_{\mathrm{inc}}$ result from the rise of $\varepsilon\eta^{(1)}_{\mathrm{inc}}$ during the peak amplitude of the Peregrine breather solution in the time period $[-30\,\mathrm{s}, 30\,\mathrm{s}]$.

Considering the spectrum of the second component of the incoming undisturbed water waves, $\varepsilon^2\eta^{(2)}_{\mathrm{inc}}$, it can be seen that the spectrum has a high peak around $\omega = 4.4\,\mathrm{rad/s}$. This indicates that the corresponding sea surfce displacement $\varepsilon^2\eta^{(2)}_{\mathrm{inc}}$ oscillates in time with frequency $\omega = 2\omega_0$. This has also been observed in the analysis of the results presented in Fig. 7.2a. However, the spectrum of $\varepsilon^2\eta^{(2)}_{\mathrm{inc}}$ also includes components around ω_0. These components have already been observed in the general formula for $\varepsilon^2\eta^{(2)}_{\mathrm{inc}}$ presented in Eq. (5.37). However, instead of containing only a single frequency component at $\omega = \omega_0$, the spectrum of $\varepsilon^2\eta^{(2)}_{\mathrm{inc}}$ contains many frequency components around ω_0. This results from the rise of $\varepsilon^2\eta^{(2)}_{\mathrm{inc}}$ during the peak amplitude of the Peregrine breather solution in the time period $[-30\,\mathrm{s}, 30\,\mathrm{s}]$.

Comparing the frequency spectra of the incoming water waves with the corresponding frequency spectra of the waves disturbed by the presence of the CFB, it can be seen that the spectra of $\varepsilon\eta^{(1)}_{\mathrm{inc}}$ and $\varepsilon\eta^{(1)}_{\mathrm{total}}$ only differ slightly from each other. For $\omega < \omega_0$, both spectra are approximately the same. For $\omega \geq \omega_0$, only a small change in the frequency spectra can be observed. This means that the CFB has only a minor influence on the higher frequency components of the first-order components of the surrounding water waves.

However, comparing the spectra of $\varepsilon^2\eta^{(2)}_{\mathrm{inc}}$ and $\varepsilon^2\eta^{(2)}_{\mathrm{total}}$ with each other, it can be seen that the CFB significantly affects the amplitude of the spectrum of the second-order components of the surrounding water waves. It is shown that the presence of the CFB does not introduce new components in the frequency spectrum, but the amplitudes of the frequency components around $\omega = 2\omega_0$ are significantly increased. Furthermore, it can be seen that the presence of the CFB does not change the frequency components around $\omega = \omega_0$. The frequency components around $\omega < 1\,\mathrm{rad/s}$ are changed, but the corresponding amplitudes

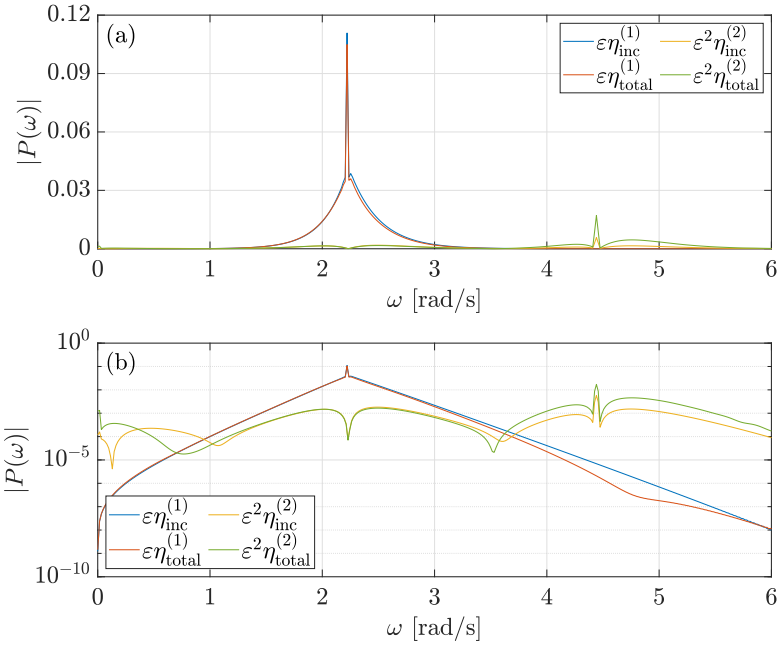

Figure 7.12: Frequency spectra of water waves measured at the position of the sensor, which correspond to the unperturbed Peregrine breather solution of the NLS. The spectra are shown using a (a) linear and (b) logarithmic vertical axis scale.

are small. Moreover, a nonzero component at $\omega = 0$ is introduced, which indicates that $\varepsilon^2\eta^{(2)}_{\text{total}}$ includes a constant shift in time. Therefore, it can be concluded that the presence of the CFB has only a small effect on the spectrum of the first-order components of the surrounding water waves but a significant effect on the spectrum of the corresponding second-order components.
Next, the frequency spectra of $\varepsilon\eta^{(1)}_{\text{inc}}$, $\varepsilon^2\eta^{(2)}_{\text{inc}}$, $\varepsilon\eta^{(1)}_{\text{total}}$, and $\varepsilon^2\eta^{(2)}_{\text{total}}$ are investigated for the case that the CFB is excited by waves corresponding to the Peregrine breather solution of the NLS, which has been initially perturbed by an irregular sea surface with significant wave height $H_{\text{s}} = 1.5\,\text{m}$. The corresponding results are presented in Fig. 7.13. Again, all results are shown using a linear and logarithmic vertical axis scale. The time series of $\varepsilon\eta^{(1)}_{\text{inc}}$ and $\varepsilon^2\eta^{(2)}_{\text{inc}}$, which are analyzed in the following, are the same as presented in Fig. 7.3a.
Compared to the the frequency spectra presented in Fig. 7.12, it can be seen that a perturbation of the Peregrine breather solution does not change the described qualitative behavior of the frequency spectra of $\varepsilon\eta^{(1)}_{\text{inc}}$, $\varepsilon^2\eta^{(2)}_{\text{inc}}$, $\varepsilon\eta^{(1)}_{\text{total}}$, and $\varepsilon^2\eta^{(2)}_{\text{total}}$. Again, the frequency spectra of $\varepsilon\eta^{(1)}_{\text{inc}}$ and $\varepsilon^2\eta^{(2)}_{\text{inc}}$, which are presented in Fig. 7.13,

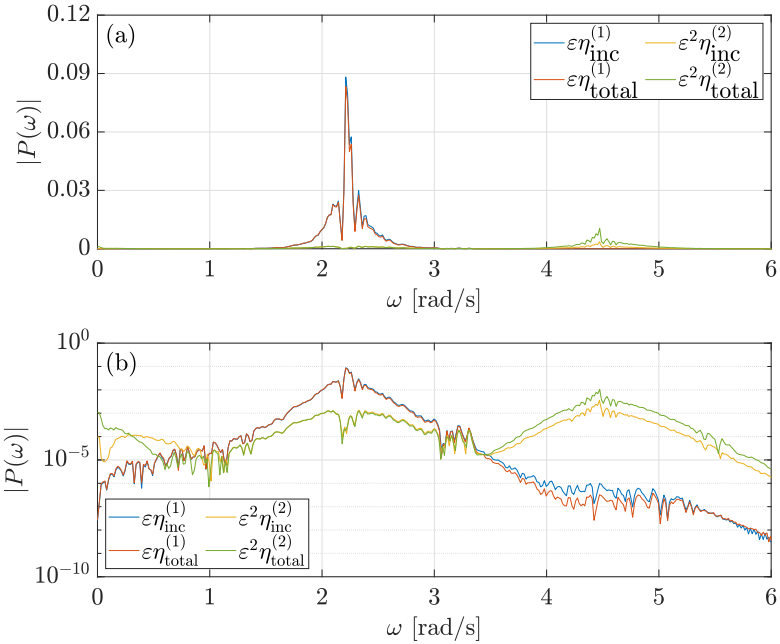

Figure 7.13: Frequency spectra of water waves measured at the position of the sensor, which correspond to the Peregrine breather solution of the NLS initially perturbed by an irregular sea surface with significant wave height $H_s = 1.5\,\text{m}$. The spectra are shown using a (a) linear and (b) logarithmic vertical axis scale.

contain components around $\omega = \omega_0$ and $\omega = 2\omega_0$, respectively. Going from $\varepsilon\eta^{(1)}_{\text{inc}}$ to $\varepsilon^2\eta^{(1)}_{\text{total}}$ and from $\varepsilon^2\eta^{(2)}_{\text{inc}}$ to $\varepsilon^2\eta^{(2)}_{\text{total}}$, it can be seen that the presence of the CFB only slightly changes the spectrum of the first-order components of the surrounding waves, but has a considerable influence on the corresponding second-order components.

Figure 7.13 also shows large noise in all presented frequency spectra. This noise result from the initial perturbation of the Peregrine breather solution, but also from the windowing of the corresponding time series by the Hann filter.

It can be concluded that the presence of the CFB does not significantly affect the frequency spectra of first-order components of the surrounding water waves, but the frequency spectra of the corresponding second-order components. Therefore, for the considered wave and system parameters, when analyzing the motion of two structures moving side by side in the ocean, the corresponding hydrodynamic interaction forces between the two bodies can become small if a linear FSI is considered. However, they can become significant if a nonlinear FSI is considered.

7.4.2 Influence of the Soliton Solution

In this section, the effect of the presence of the CFB on the waves corresponding to the soliton solution of the NLS is investigated. Again, the frequency spectra of $\varepsilon\eta^{(1)}_{\text{inc}}$, $\varepsilon^2\eta^{(2)}_{\text{inc}}$, $\varepsilon\eta^{(1)}_{\text{total}}$, and $\varepsilon^2\eta^{(2)}_{\text{total}}$ are compared with each other. Considering the interaction with the CFB and the unperturbed soliton solution, the corresponding frequency spectra are presented in Fig. 7.14. The time series of $\varepsilon\eta^{(1)}_{\text{inc}}$ and $\varepsilon^2\eta^{(2)}_{\text{inc}}$, which are analyzed in the following, are the same as presented in Fig. 7.7a.
The same qualitative behavior of the frequency spectra of $\varepsilon\eta^{(1)}_{\text{inc}}$, $\varepsilon^2\eta^{(2)}_{\text{inc}}$, $\varepsilon\eta^{(1)}_{\text{total}}$, and $\varepsilon^2\eta^{(2)}_{\text{total}}$ can be observed as has been presented in Fig. 7.12 for the unperturbed Peregrine breather solution. For example, the frequency spectra of $\varepsilon\eta^{(1)}_{\text{inc}}$ and $\varepsilon^2\eta^{(2)}_{\text{inc}}$ shown in Fig. 7.14 contain components around $\omega = \omega_0 = 2.2147\,\text{rad/s}$ and $\omega = 2\omega_0$, respectively. By comparing the frequency spectra of $\varepsilon\eta^{(1)}_{\text{inc}}$ and $\varepsilon\eta^{(1)}_{\text{total}}$ with each other, it can be seen that the presence of the CFB only slightly changes the amplitude of the spectrum of the first-order components of the surrounding water waves. In contrast, the presence of the CFB significantly affects the spec-

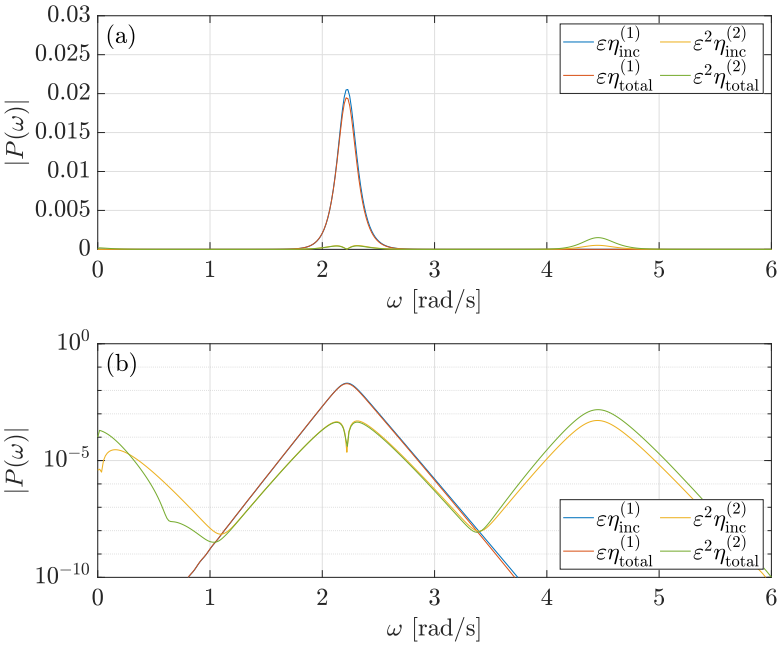

Figure 7.14: Frequency spectra of water waves measured at the position of the sensor, which correspond to the unperturbed soliton solution of the NLS. The spectra are shown using a (a) linear and (b) logarithmic vertical axis scale.

trum of the corresponding second-order components. Considering the frequency spectra of $\varepsilon^2\eta_{\mathrm{inc}}^{(2)}$ and $\varepsilon^2\eta_{\mathrm{total}}^{(2)}$, it can be seen that the presence of the CFB changes the amplitude of the frequency components around $\omega = 2\omega_0$ and $\omega \leq 1.2\,\mathrm{rad/s}$. Compared to the corresponding results for the unperturbed Peregrine breather solution presented in Fig. 7.12, it has to be noted that the frequency spectra shown in Fig. 7.14 do not have high single peaks at $\omega = \omega_0$ and $\omega = 2\omega_0$. This results from the fact that the incoming water waves corresponding to the soliton solution do not propagate on a background wave with frequency ω_0, see Fig. 7.7a.
For the sake of completeness, the frequency spectra of $\varepsilon\eta_{\mathrm{inc}}^{(1)}$, $\varepsilon^2\eta_{\mathrm{inc}}^{(2)}$, $\varepsilon\eta_{\mathrm{total}}^{(1)}$, and $\varepsilon^2\eta_{\mathrm{total}}^{(2)}$ are investigated next for the case that the CFB is excited by waves corresponding to the soliton solution of the NLS, which has been initially perturbed by an irregular sea surface with significant wave height $H_{\mathrm{s}} = 1.5\,\mathrm{m}$. The corresponding results are presented in Fig. 7.15. Again, all results are shown using a linear and logarithmic vertical axis scale. The time series of $\varepsilon\eta_{\mathrm{inc}}^{(1)}$ and $\varepsilon^2\eta_{\mathrm{inc}}^{(2)}$, which are analyzed in the following, are the same as presented in Fig. 7.8a. Compared to the results presented in Fig. 7.14, it can be seen that a perturbation of the soliton solution does not change the described qualitative behavior of the frequency spectra of $\varepsilon\eta_{\mathrm{inc}}^{(1)}$, $\varepsilon^2\eta_{\mathrm{inc}}^{(2)}$, $\varepsilon\eta_{\mathrm{total}}^{(1)}$, and $\varepsilon^2\eta_{\mathrm{total}}^{(2)}$. Again, as it has been the case going from the unperturbed to the perturbed Peregrine breather solution of the NLS, the perturbation of the soliton solution only introduces large noise in all presented frequency spectra. This noise result from the perturbation of the soliton solution but also from the windowing of the corresponding time series by the Hann filter.
Again, it can be concluded that the presence of the CFB does not significantly affect the frequency spectra of the first-order components of the surrounding water waves, but the frequency spectra of the corresponding second-order components. This can again be important when the motion of two structures, which are moving side by side in the ocean, is analyzed considering a nonlinear FSI.

7.5 Interaction with Random Nonlinear Stokes Waves

In the previous sections, the FSI between the CFB and water waves corresponding to solutions of the NLS has been investigated. Here, the influence of the water waves on the dynamics of the CFB has been studied. In addition, the influence of the presence of the CFB on the surrounding water waves has been analyzed. In this section, corresponding results are presented for the FSI between the CFB and the random nonlinear Stokes waves introduced in Sect. 4.3.2. Afterward, the

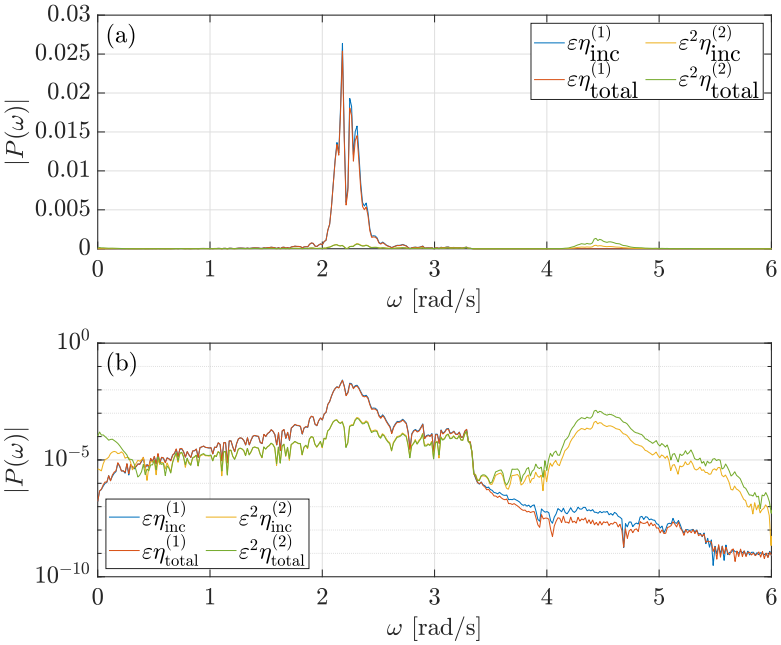

Figure 7.15: Frequency spectra of water waves measured at the position of the sensor, which correspond to the soliton solution of the NLS initially perturbed by an irregular sea surface with significant wave height $H_\text{s} = 1.5\,\text{m}$. The spectra are shown using a (a) linear and (b) logarithmic vertical axis scale.

obtained results are compared with those presented in the previous sections. In this way, the similarities and differences between the FSI with random nonlinear Stokes waves and waves corresponding to the NLS can be investigated.

The first-order component of the used long-crested incoming random water waves, $\varepsilon\eta^{(1)}_{\text{inc}}$, is computed using Eq. (2.28) with $\chi_0 = 0$. The amplitude of $\varepsilon\eta^{(1)}_{\text{inc}}$ is described using the PM-spectrum S_{PM} from Eq. (2.23) with peak frequency $\omega_\text{p} = \frac{2\pi}{3}\,\text{rad/s}$ and significant wave height $H_\text{s} = 0.7\,\text{m}$. Using this peak frequency, the corresponding random water waves have a peak period of $2\pi/\omega_\text{p} = 3\,\text{s}$. The PM-spectrum S_{PM} is discretized in $M_\omega = 120$ parts with respective widths $\Delta\omega_m$ and frequencies $\omega_m \in [\omega_{\min}, \omega_{\max}] = [0, 10\,\text{rad/s}]$.

The corresponding first- and second-order components of the incident velocity potential of the incoming water waves, $\varepsilon\phi^{(1)}_0$ and $\varepsilon^2\phi^{(2)}_0$, are computed using Eqs. (4.45) and (4.47), respectively. The corresponding numerical results for the FSI are computed for $h = 7\,\text{m}$. Furthermore, the same domain $\bar{\Omega}$ and step sizes Δr, Δz, and Δt are used as specified in the Sect. 7.2.1. All numerical results are computed for the time domain $t \in [0\,\text{s}, 400\,\text{s}]$.

First, the FSI between the CFB and the random nonlinear Stokes waves of second order is investigated. Corresponding results for the FSI are presented in Fig. 7.16. Here, Fig. 7.16a shows the sea surface displacements $\varepsilon\eta_{\mathrm{inc}}^{(1)}$ and $\varepsilon^2\eta_{\mathrm{inc}}^{(2)}$ of the incoming water waves of first- and second-order, which are measured at the position of the center of the CFB. It is shown that $\varepsilon^2\eta_{\mathrm{inc}}^{(2)}$ contributes largely to the overall incoming water waves over the whole time domain. Compared to $\varepsilon\eta_{\mathrm{inc}}^{(1)}$, the amplitude of $\varepsilon^2\eta_{\mathrm{inc}}^{(2)}$ can become relatively large. For example, at $t = 55\,\mathrm{s}$, the quotient of the wave heights of $\varepsilon\eta_{\mathrm{inc}}^{(1)}$ and $\varepsilon^2\eta_{\mathrm{inc}}^{(2)}$ is about 41%, i. e. $|\varepsilon^2\eta_{\mathrm{inc}}^{(2)}|_{\mathrm{H}}/|\varepsilon\eta_{\mathrm{inc}}^{(1)}|_{\mathrm{H}} = 41\%$. Furthermore, it can be observed that $\varepsilon^2\eta_{\mathrm{inc}}^{(2)}$ is oscillating with a higher mean frequency than $\varepsilon\eta_{\mathrm{inc}}^{(1)}$. Therefore, for the used wave parameters, a linear wave theory is not sufficient to compute the temporal behavior of the incoming water waves. A nonlinear wave theory must be used here to accurately simulate the temporal behavior of the incoming water waves.
Figures 7.16b and 7.16c present the hydrodynamic forces of first- and second-order,

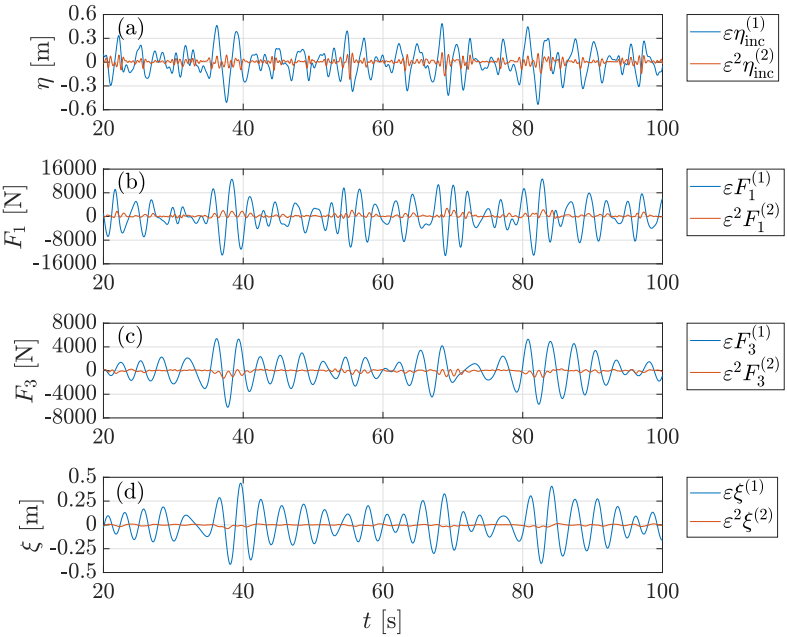

Figure 7.16: FSI between the CFB and random nonlinear Stokes waves, which are described using the PM-spectrum with peak frequency $\omega_{\mathrm{p}} = \frac{2\pi}{3}$ rad/s and significant wave height $H_{\mathrm{s}} = 0.7\,\mathrm{m}$. Shown are the first- and second-order components of (a) the incoming water waves, the hydrodynamic forces acting in the (b) horizontal and (c) vertical direction, and (d) the displacement of the CFB.

which act on the CFB in the horizontal and vertical direction, respectively. It can be seen that the second-order components of the corresponding hydrodynamic forces contribute largely to the overall forces over the whole time domain. This means that the amplitudes of $\varepsilon^2 F_1^{(2)}$ and $\varepsilon^2 F_3^{(2)}$ can become relatively high compared to the amplitudes of $\varepsilon F_1^{(1)}$ and $\varepsilon F_3^{(1)}$. Moreover, it can be seen that $\varepsilon^2 F_1^{(2)}$ and $\varepsilon^2 F_3^{(2)}$ are oscillating with a higher frequency than $\varepsilon F_1^{(1)}$ and $\varepsilon F_3^{(1)}$. The hydrodynamic forces $\varepsilon^2 F_1^{(2)}$ and $\varepsilon^2 F_3^{(2)}$ are also not oscillating around zero, but they contain positive and negative shifts, respectively. The higher oscillation frequencies and shifts have already been observed in the results presented in Sect. 7.2 and 7.3, where the CFB has been excited by waves corresponding to solutions of the NLS.

Finally, Fig. 7.16d shows the first- and second-order components of the displacement of the CFB. Here, it can be seen that $\varepsilon^2 \xi^{(2)}$ contributes to the total displacement of the CFB over the whole simulation time. However, this contribution is small compared to the contribution of the forces $\varepsilon^2 F_1^{(2)}$ and $\varepsilon^2 F_3^{(2)}$ to the total acting hydrodynamic forces. For the amount of harvested energy of the point absorber presented in Chap. 3, this means that the second-order component of the displacement of the WEC, $\varepsilon^2 \xi^{(2)}$, would not significantly affect the amount of harvested energy. However, this is only the case for the considered system and wave parameters. For different water waves, $\varepsilon^2 \xi^{(2)}$ can largely affect the amount of harvested energy. This has been shown, for example, in Fig. 7.2d, where the response of the CFB excited by waves corresponding to the unperturbed Peregrine breather solution of the NLS is presented. Here, it has been presented that $\varepsilon^2 \xi^{(2)}$ has a significant contribution to the overall displacement during the time period $[-30\,\mathrm{s}, 30\,\mathrm{s}]$.

Next, the influence of the CFB on the surrounding random nonlinear Stokes waves is investigated. Again, this is done by comparing the frequency spectra of $\varepsilon\eta_{\mathrm{inc}}^{(1)}$, $\varepsilon^2\eta_{\mathrm{inc}}^{(2)}$, $\varepsilon\eta_{\mathrm{total}}^{(1)}$, and $\varepsilon^2\eta_{\mathrm{total}}^{(2)}$ with each other. The CFB is excited by the incoming water waves $\varepsilon\eta_{\mathrm{inc}}^{(1)}$ and $\varepsilon^2\eta_{\mathrm{inc}}^{(2)}$ presented in Fig. 7.16. The corresponding frequency spectra of $\varepsilon\eta_{\mathrm{inc}}^{(1)}$, $\varepsilon^2\eta_{\mathrm{inc}}^{(2)}$, $\varepsilon\eta_{\mathrm{total}}^{(1)}$, and $\varepsilon^2\eta_{\mathrm{total}}^{(2)}$ are presented in Fig. 7.17. Again, all results are shown using a linear and logarithmic vertical axis scale.

Considering Fig. 7.17, it can be observed that the frequency spectrum of $\varepsilon\eta_{\mathrm{inc}}^{(1)}$ consists of many larger peaks in the domain $\omega \in [0, 10\,\mathrm{rad/s}]$. Between these peaks, the frequency components of $\varepsilon\eta_{\mathrm{inc}}^{(1)}$ have small amplitudes. This is due to the fact that $\varepsilon\eta_{\mathrm{inc}}^{(1)}$ has been computed using the superposition of $M_\omega = 120$ regular water waves with wave frequencies $\omega \in [0, 10\,\mathrm{rad/s}]$, see Eq. (2.28) with $\chi_0 = 0$. Using the PM-spectrum S_{PM}, the amplitudes of the peaks of the frequency components of $\varepsilon\eta_{\mathrm{inc}}^{(1)}$ are given by $\sqrt{2S_{\mathrm{PM}}(\omega)\Delta\omega}$. This can also be seen in Fig. 7.17, where the amplitude function $f(\omega) = \sqrt{2S_{\mathrm{PM}}(\omega)\Delta\omega}$ is presented for $\omega \in [0, 10\,\mathrm{rad/s}]$. It has to be noted that the amplitudes of the frequency components of $\varepsilon\eta_{\mathrm{inc}}^{(1)}$ shown in Fig. 7.17 are not exactly given by $\sqrt{2S_{\mathrm{PM}}(\omega)\Delta\omega}$. This is due to the fact that the frequency spectrum has been discretized too roughly. This can be

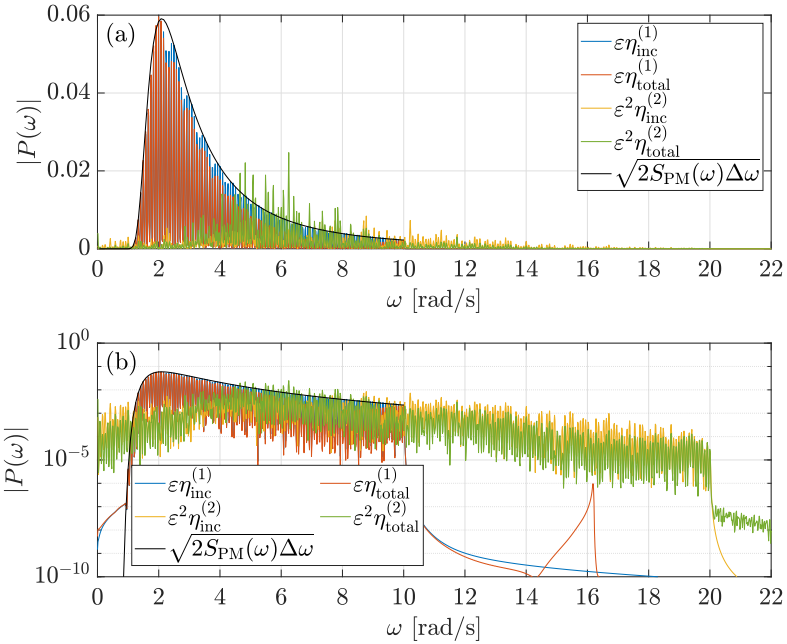

Figure 7.17: Frequency spectra of random nonlinear Stokes waves measured at the position of the sensor. The spectra are shown using a (a) linear and (b) logarithmic vertical axis scale.

fixed by simulating $\varepsilon\eta^{(1)}_{\mathrm{inc}}$ over a longer simulation time. For the results presented in Fig. 7.17, $\varepsilon\eta^{(1)}_{\mathrm{inc}}$ has been simulated over a simulation time of 400 s.
Considering the second-order component of the incoming water waves, it can be observed that the frequency spectrum of $\varepsilon^2\eta^{(2)}_{\mathrm{inc}}$ contains components with $\omega \in [0, 20\,\mathrm{rad/s}]$. This results from the fact that $\varepsilon^2\eta^{(2)}_{\mathrm{inc}}$ contains interactions between the frequency components of the incoming water waves of first order. This has also been described in Sect. 4.3.2, where the nonlinear incident velocity potential of random water waves has been discussed. Therefore, since the spectrum of $\varepsilon\eta^{(1)}_{\mathrm{inc}}$ contains wave components with frequencies $\omega \in [0, 10\,\mathrm{rad/s}]$, the spectrum of $\varepsilon^2\eta^{(2)}_{\mathrm{inc}}$ contains wave components with frequencies $\omega \in [0, 20\,\mathrm{rad/s}]$. Here, the frequency components of $\varepsilon^2\eta^{(2)}_{\mathrm{inc}}$ with frequencies $\omega \in [4\,\mathrm{rad/s}, 11\,\mathrm{rad/s}]$ have the highest amplitudes.
Next, the effect of the presence of the CFB on the surrounding water waves is investigated. Comparing the frequency spectra of $\varepsilon\eta^{(1)}_{\mathrm{inc}}$ and $\varepsilon\eta^{(1)}_{\mathrm{total}}$ with each other, it is observed that the presence of the CFB only affects the frequency components of the surrounding water waves with frequencies $\omega > \omega_{\mathrm{p}}$, whereby

the peak frequency ω_p is given by $\omega_\mathrm{p} = \frac{2\pi}{3}\,\mathrm{rad/s} = 2.09\,\mathrm{rad/s}$. However, the effect of the CFB on the corresponding amplitudes is small. In contrast, by comparing the frequency spectra of $\varepsilon^2\eta^{(2)}_\mathrm{inc}$ and $\varepsilon^2\eta^{(2)}_\mathrm{total}$ with each other, it can be seen that the CFB significantly affects the amplitude of the frequency spectrum of the second-order components over the whole frequency domain, i. e. for all $\omega \in [0, 20\,\mathrm{rad/s}]$. Especially for $\omega \in [4\,\mathrm{rad/s}, 8\,\mathrm{rad/s}]$, the presence of the CFB strongly increases the amplitude of the corresponding frequency components. This shows that the presence of the CFB only slightly affects the first-order components of the surrounding water waves but largely affects the corresponding second-order components.

It has to be noted that the presence of the CFB does not introduce additional frequency components of large amplitude in the first-order component of the surrounding water waves. This means that the amplitudes of the spectrum of $\varepsilon\eta^{(1)}_\mathrm{total}$ decays significantly for frequencies $\omega > 10\,\mathrm{rad/s}$. However, Fig. 7.17b shows that the CFB introduces frequency components in the spectrum of $\varepsilon\eta^{(1)}_\mathrm{total}$ around $\omega \approx 16\,\mathrm{rad/s}$. However, these introduced frequency components have very small amplitudes. They are related to the eigenfrequency of the considered mechanical system. Using the system parameters of the CFB summarized in Tab. 7.1, the resulting CFB has a mass of 4768 kg and an eigenfrequency of 16.04 rad/s. Recall that also the motion of the CFB disturbs the incoming water waves. Therefore, Fig. 7.17b shows that the motion of the CFB introduces frequency components in the spectrum of $\varepsilon\eta^{(1)}_\mathrm{total}$, which are oscillating in time with the eigenfrequency of the CFB. However, these frequency components have only a small effect on the motion of $\varepsilon\eta^{(1)}_\mathrm{total}$.

Similar to the results presented in Fig. 7.17b, it has to be noted that frequency components around $\omega \approx 16\,\mathrm{rad/s}$ can be observed in the frequency spectra of the waves corresponding to the NLS, which are disturbed by the presence of the CFB. However, because their effect on the motion of $\varepsilon\eta^{(1)}_\mathrm{total}$ is small, these frequency components have not been presented in Figs. 7.12-7.15.

The introduction of components in the wave spectrum, which have frequencies around the eigenfrequency of the CFB, can also be very important for the motion of two structures moving next to each other. If both structures have similar eigenfrequencies, which also lie in the range of the frequency components of the incoming water waves, the hydrodynamic interaction forces between these two structures can significantly affect the motion of the structures. This must be considered when analyzing the motion of two structures moving side by side in the ocean.

7.6 Discussion

In the previous sections, the FSI between the CFB and different incoming water waves has been investigated. In Sect. 7.2 and Sect. 7.3, it was shown that the interaction between the CFB and unperturbed solutions of the NLS leads to large nonlinear components in the acting hydrodynamic forces and the displacement of the CFB. However, for the used wave parameters, these nonlinear components only contribute significantly to the total hydrodynamic forces and displacement during a short time period, see Figs. 7.2 and 7.7.
This changes when solutions of the NLS are initially perturbed by irregular sea surfaces. Here, it has been shown that the considered initial perturbations can strongly affect the behavior of the Peregrine breather and soliton solution. Furthermore, nonlinear effects can contribute significantly to the corresponding FSI. Recall that the Peregrine breather solution of the NLS has been conjectured in different studies as a prototype of rogue waves in the ocean, see e.g. [DystheTrulsen99, ShriraGeogjaev10, DostalEtAl20]. Therefore, it has also been shown that nonlinear effects can contribute significantly to the corresponding FSI during extreme wave events. As a result, the proposed scheme presented in this thesis can be used to estimate the linear and nonlinear hydrodynamic loads acting on mechanical structures during extreme wave events. These loads must be known to make, for example, mechanical structures resistant to rogue waves.
In Sect. 7.5, the interaction between the CFB and random nonlinear Stokes waves has been computed. For the used wave parameters, it was shown that the nonlinear components of the incoming water waves and hydrodynamic forces largely affect the corresponding total quantities over the whole time dome. This shows that random nonlinear Stokes waves can be used to simulate the motion of floating bodies in irregular seas and that the results for the FSI can change significantly if nonlinear effects are considered.
Studying the FSI between the CFB and incoming water waves, the effect of the presence of the CFB on the incoming water waves has also been investigated. Excited by random nonlinear Stokes waves and waves corresponding to solutions of the NLS, it has been shown that the presence of the CFB has only a minor effect on the first-order components of the surrounding waves but a large effect on the corresponding second-order components. This can become important, for example, when analyzing the motion of two bodies moving side by side in the ocean.
However, although the frequency spectra of random nonlinear Stokes waves and waves corresponding to the NLS show some similarities, there are also differences. Considering the frequency spectra corresponding to the excitation of random nonlinear Stokes waves, Fig. 7.17 has shown that the frequency spectra of all considered sea surface displacements contain components over a wide frequency range. This is because the corresponding incoming water waves are calculated

by superimposing many regular waves with frequencies over a wide frequency range. On the other side, Figs. 7.12-7.15 show the frequency spectra of waves corresponding to solutions of the NLS. Here, it is presented that the corresponding spectra only contain frequency components in a small range around ω_0 and $2\omega_0$. The corresponding frequency spectra are narrow-banded. This also does not change if the corresponding solutions of the NLS are initially perturbed by irregular sea surfaces. Therefore, water waves corresponding to solutions of the NLS cannot be used to compute the temporal behavior of random water waves occurring in the ocean, which have a broad-banded frequency spectrum. For this case, random nonlinear Stokes waves have to be used to calculate the temporal behavior of broad-banded incoming water waves. Furthermore, random nonlinear Stokes waves have to be used to compute the corresponding FSI between a structure and broad-banded nonlinear water waves.

Finally, it has to be noted that the computations of the FSI with different water waves also differ in their computational effort. In Sect. 4.3.2, it has been shown that the computation of random nonlinear Stokes waves needs the calculation of wave-wave interactions between regular wave components. For the results, which have been presented in Sect. 7.5, this means that the computation of the random nonlinear Stokes waves needs the calculation of $M_\omega = 120$ linear wave components and $M_\omega^2 = 14400$ nonlinear wave interaction. On the other side, when calculating water waves using the NLS, the calculation of the nonlinear wave interactions is not required, see Sect. 5.2.2. As a result, the calculation of the FSI between a mechanical structure and waves corresponding to solutions of the NLS needs less computation time than the calculation of the FSI between a mechanical structure and random nonlinear Stokes waves. In this way, the calculation of the results presented in Sect. 7.2 and Sect. 7.3, where the FSI between the CFB and waves corresponding to solutions of the NLS is analyzed, took about 8.5 h each. In contrast, the calculation of the results, which have been presented in Sect. 7.5 for the FSI between the CFB and random nonlinear Stokes waves, took about 100 h. The stated computation times include the calculation of the incoming water waves and the calculation of the corresponding FSIs. All calculations were performed in Matlab. No parallel computing was used.

Compared to the computation times mentioned above, the computation of the FSI between the CFB and incoming regular waves, which was presented in Sect. 7.1 for a water of depth of $h = 7$ m, took about 5.5 h. Therefore, the computation of the FSI with waves corresponding to the NLS is slower than the computation of the FSI with nonlinear regular waves. However, it is much faster than the computation of the FSI with random nonlinear Stokes waves.

It can be concluded that Stokes waves and waves corresponding to the NLS can both be used to compute the FSI between floating structures and nonlinear water waves. It has been shown that Stokes waves can be used to investigate the motion of a floating structure in irregular nonlinear seas. Moreover, it has been shown that the NLS can be used to simulate the motion of a floating structure in ocean waves with narrow spectral bandwidth and in rogue waves.

Here, the investigations show that the NLS approach is much more efficient for the considered scenarios. In addition, the presented approach to initially perturb a solution of the NLS offers a possibility to model water waves with the NLS, which are irregular in their amplitude. Therefore, it is found that the NLS offers an interesting possibility to efficiently investigate the behavior of structures excited by random nonlinear ocean waves.

Conclusion

An efficient computation of the FSI between mechanical structures and ocean waves is an important topic in many ocean engineering and naval architecture applications. For example, the form and parameters of WECs should be optimized to harvest a large amount of energy in ocean waves. To this end, the corresponding hydrodynamic forces acting on the WECs must be computed for many designs. In addition, nonlinear wave effects must be considered to model the temporal behavior of larger or faster waves. This is, for example, interesting when ships are excited by rogue waves and the corresponding hydrodynamic forces acting on the hull of a ship should be calculated.

This work presents a new computational method for the FSI in nonlinear water waves using the NLS. To this end, the application areas, accuracy, stability, and computational efficiency of this method are analyzed in a comprehensive manner. The individual chapters are summarized in the following, and contributions are pointed out.

First, Chap. 2 introduces the nonlinear governing equations of fluid motion. Here, the behavior of homogeneous, incompressible, and non-viscous fluids is considered, whereby surface tension effects are neglected. The fluid behavior is modeled using potential flow theory. Since nonlinear BCs at the unknown location of the free sea surface make the computation of solutions of the nonlinear governing equations of fluid motion complicated, the corresponding linearized equations are considered. Various solutions of the linearized equations are presented in the absence of mechanical structures. Furthermore, the effects of the presence and motion of a mechanical structure on the fluid dynamics of the surrounding water waves are discussed.

Afterward, the dynamics of a WEC for harvesting wave energy is investigated in the framework of linear wave theory in Chap. 3 using simulation and experimental results. Based on the corresponding results, it is found that using an inclined WEC, the averaged energy harvesting output can be increased up to a factor of about 4.52 compared to the corresponding standard vertically heaving WEC. Furthermore, a simple control strategy is proposed, where the inclination angle is adjusted according to the frequency of the incoming water waves. Compared to the standard vertical point absorber, using such a control strategy leads to an even higher increase in the energy harvesting output by a factor of about 6.05.

However, using the linearized wave theory, nonlinear wave effects are neglected,

which can significantly influence the wave motion for higher or faster waves. The question is how the dynamic behavior of the WEC and the average harvested energy output change when moving from linear to nonlinear wave theory. Chapter 4 shows how the nonlinear FSI between a structure and nonlinear water waves can be calculated. Here, Stokes perturbation expansions of the velocity potential and sea surface displacement with respect to the wave steepness are used. In this way, the nonlinear governing equations of fluid motion are transformed into a sequence of linear equations that have to be solved. Solutions of the sequence of linear equations are presented for incoming regular and random water waves. These are the so-called Stokes waves of higher order. Here, it is shown that nonlinear wave-wave interactions between the regular wave components of an irregular sea state have to be computed when considering random nonlinear water waves. This can be time-consuming.

As an alternative to computing the FSI using Stokes waves, Chap. 5 introduces the NLS to compute the nonlinear FSI between a structure and deep water waves. The NLS consists of a partial differential equation for the wave envelope. Compared to the nonlinear governing equations of fluid motion, which contain nonlinear BCs at the unknown location of the sea surface, the NLS can be solved much more efficiently. Based on solutions of the NLS, it is presented how the velocity potential of the corresponding incoming water waves can be computed numerically. This velocity potential is needed to compute the FSI between the corresponding incoming water waves and a mechanical structure. Here, it is shown that the corresponding FSI can be modeled up to an error of third-order in the wave steepness of the incoming water waves. Nonlinear wave-wave interaction between regular wave components of an irregular sea state must not be computed to consider random nonlinear water waves. This makes this approach more efficient than the computation of random nonlinear Stokes waves.

Furthermore, Chap. 5 shows how random nonlinear water waves can be generated by initially perturbing analytical solutions of the NLS. The effects of the initial irregular perturbation on the fluid dynamics of the incoming water waves are investigated. Here, it is shown that the initial irregular perturbation of the water waves significantly affects the temporal behavior of the water particles during the propagation of the corresponding waves.

A numerical method for the computation of the nonlinear FSI for given nonlinear water waves is presented in Chap. 6. The computation of the FSI includes the numerical calculation of the velocity potentials disturbed by the presence of the structure, the hydrodynamic forces acting on the structure, and the dynamics of the structure. Absorbing BCs are introduced to prevent the reflections from waves at the outer boundary to the inside of the computational domain. Corresponding numerical results are analyzed for the WEC presented in Chap. 3. A comparison with the results presented in Chap. 3 and found in literature shows good agreement. Furthermore, in the absence of sharp corners and edges, all numerical approximations for the hydrodynamic forces and motion of the WEC converge with an empirical order of two.

The nonlinear FSI between a WEC and nonlinear water waves is investigated in Chap. 7. Furthermore, the similarities and differences between the FSI with random nonlinear Stokes waves and waves corresponding to the NLS are studied. Here, the first- and second-order components of the hydrodynamic forces and the displacement of the WEC are investigated. Furthermore, the effects of the presence of the WEC on the surrounding water waves are studied. It is found that nonlinear effects can contribute significantly to the corresponding FSI using both Stokes waves and waves corresponding to the NLS. Furthermore, it has been shown that Stokes waves and waves corresponding to the NLS lead approximately to the same results for incoming regular water waves. The corresponding differences result from the fact that the NLS assumes an infinite water depth and includes nonlinear wave effects coming from the use of a third-order nonlinear wave theory, which affect the corresponding dispersion relation.
The computation of the FSI using Stokes waves and waves corresponding to the NLS show differences in the areas of application and in the computation times. Stokes waves can be used to simulate general random nonlinear ocean waves. However, nonlinear interactions between regular wave components must be computed, which is very time-consuming. On the other hand, the NLS can be used to simulate ocean waves with a narrow spectral bandwidth and moderate wave steepness. Considering the presented method of perturbing analytical solutions of the NLS by irregular sea surfaces, water waves with a narrow spectral bandwidth and moderate wave steepness can be simulated, which show a random perturbation in their amplitude. For these waves, the investigations show that the NLS approach is significantly faster by a factor of up to ten when computing the FSI for the considered scenarios.
From the above contributions, the following conclusions can be drawn. In addition to Stokes waves, the NLS offers an interesting possibility to compute the FSI with nonlinear water waves. Using the NLS, nonlinear wave-wave interactions between regular wave components must not be computed to calculate nonlinear irregular seas. Also, nonlinear wave effects are directly considered in the FSI using the NLS.
However, there are some restrictions and challenges that need to be considered. First of all, it is shown in Chap. 5 that different instabilities appear in the computation of the velocity potential corresponding to solutions of the NLS. These instabilities depend on the considered solution of the NLS and on the numerical scheme, which is used to compute the corresponding velocity potential below the sea surface. Due to these instabilities, the corresponding velocity potential can only be computed accurately up to a finite depth. However, the value of this finite depth can change significantly for different wave parameters and step sizes of the used numerical scheme. Here, it has to be noted that it is often not even necessary to determine the velocity potential down to the sea bottom. This is the case, for example, for mechanical structures floating on the sea surface, which have a small draft. Since the velocity potential corresponding to the incident water waves must only be known on the sea surface and the

surface of the floating structure, an instability of the velocity potentials of the NLS in large depths does not affect the FSI.
Secondly, the NLS can only accurately describe the behavior of ocean waves with a narrow spectral bandwidth and a small wave steepness. Random waves with a broad spectral bandwidth and a large wave steepness cannot be described using the NLS. However, it is shown that the nonlinear FSI can be simulated very efficiently using the NLS. Therefore, the NLS could be used, for example, to study the behavior of a mechanical system in nonlinear water waves with a narrow spectral bandwidth efficiently. In this way, in a first step, it can also be estimated efficiently whether nonlinear wave effects significantly affect the motion of the considered system. If the corresponding nonlinear wave effects cannot be neglected, Stokes waves can be used in a second step to calculate the motion of the structure in random nonlinear waves with a broader spectral bandwidth. Furthermore, specific analytical solutions of the NLS, like the Peregrine breather solution, have been conjectured in different studies as a prototype of rogue waves in the ocean. By computing the FSI with waves corresponding to the Peregrine breather solution, it can be estimated with a low computational effort which hydrodynamic loads a fixed or free-floating structure must withstand in extreme wave events.
Due to its efficiency, it is found that the NLS offers an interesting possibility to investigate the behavior of structures excited by nonlinear ocean waves. In addition, the presented approach of initially perturbing analytical solutions of the NLS provides a way to model water waves with the NLS, which are random in their amplitude. In future studies, it would be interesting to extend the presented approach to random nonlinear water waves, which can have a larger wave steepness or a broader spectral bandwidth. This could be done using an extended version of the NLS, with which such water waves can be simulated very well. Corresponding extended versions of the NLS, which can consider waves with a larger wave steepness or a broader spectral bandwidth, can be found, for example, in [Dysthe79, TrulsenDysthe96, ToffoliEtAl10, AdcockTaylor16]. After computing the velocity potential corresponding to an extended version of the NLS, the approach presented in this work could be very promising to efficiently simulate the FSI in nonlinear random waves with a larger wave steepness or broader spectral bandwidth.
Additionally, based on the approach presented in this thesis, it would be interesting to consider the effects of stochastic wind excitation on the motion of the water waves. Using a corresponding extended version of the NLS, waves excited by a stochastic wind excitation could be simulated, and the corresponding FSI with a given structure could be investigated efficiently. Therefore, the approach presented in this work, which is based on the NLS, offers interesting possibilities to efficiently investigate the temporal behavior of nonlinear water waves and the corresponding FSI with mechanical structures.

Bibliography

[AdcockEtAl11] Adcock, T.A.A.; Taylor, P.H.; Yan, S.; Ma, Q.W.; Janssen, P.A.E.M.: Did the Draupner wave occur in a crossing sea? *Proceedings of the Royal Society A: Mathematical, Physical and Engineering Sciences*, Vol. 467, No. 2134, pp. 3004–3021, 2011. DOI:10.1098/RSPA.2011.0049.

[AdcockTaylor16] Adcock, T.A.A.; Taylor, P.H.: Non-linear evolution of unidirectional focussed wave-groups on a deep water: A comparison of models. *Applied Ocean Research*, Vol. 59, pp. 147–152, 2016. DOI:10.1016/J.APOR.2016.05.012.

[Akers15] Akers, B.F.: Modulational instabilities of periodic traveling waves in deep water. *Physica D: Nonlinear Phenomena*, Vol. 300, pp. 26–33, 2015. DOI:10.1016/J.PHYSD.2015.02.005.

[AntoineDuboscq15] Antoine, X.; Duboscq, R.: GPELab, a Matlab toolbox to solve Gross–Pitaevskii equations II: Dynamics and stochastic simulations. *Computer Physics Communications*, Vol. 193, pp. 95–117, 2015. DOI:10.1016/J.CPC.2015.03.012.

[BaiEatock Taylor09] Bai, W.; Eatock Taylor, R.: Fully nonlinear simulation of wave interaction with fixed and floating flared structures. *Ocean Engineering*, Vol. 36, No. 3-4, pp. 223–236, 2009. DOI:10.1016/J.OCEANENG.2008.11.003.

[BaiTeng13] Bai, W.; Teng, B.: Simulation of second-order wave interaction with fixed and floating structures in time domain. *Ocean Engineering*, Vol. 74, pp. 168–177, 2013. DOI:10.1016/J.OCEANENG.2013.07.014.

[BeattyEtAl15] Beatty, S.J.; Hall, M.; Buckham, B.J.; Wild, P.; Bocking, B.: Experimental and numerical comparisons of self-reacting point absorber wave energy converters in regular waves. *Ocean Engineering*, Vol. 104, pp. 370–386, 2015. DOI:10.1016/J.OCEANENG.2015.05.027.

[BenjaminFeir67] Benjamin, T.B.; Feir, J.E.: The disintegration of wave trains on deep water Part 1. Theory. *Journal of Fluid Mechanics*, Vol. 27, No. 3, pp. 417–430, 1967. DOI:10.1017/S002211206700045X.

[BinghamZhang07] Bingham, H.B.; Zhang, H.: On the accuracy of finite-difference solutions for nonlinear water waves. *Journal of Engineering Mathematics*, Vol. 58, pp. 211–228, 2007. DOI:10.1007/s10665-006-9108-4.

[BludovEtAl09] Bludov, Y.V.; Konotop, V.; Akhmediev, N.: Matter rogue waves. *Physical Review A*, Vol. 80, No. 3, p. 033610, 2009. DOI:10.1103/PhysRevA.80.033610.

[BSH] BSH: Sea state statistics. `https://www.bsh.de/DE/DATEN/Klima-und-Meer/Seegang/Seegangsstatistiken/seegangsstatistiken_node.html`. Accessed on 20. January 2023.

[BüchmannEtAl98] Büchmann, B.; Skourup, J.; Cheung, K.F.: Run-up on a structure due to second-order waves and a current in a numerical wave tank. *Applied Ocean Research*, Vol. 20, No. 5, pp. 297–308, 1998. DOI:10.1016/S0141-1187(98)00022-4.

[BudarFalnes75] Budar, K.; Falnes, J.: A resonant point absorber of ocean-wave power. *Nature*, Vol. 256, pp. 478–479, 1975. DOI:10.1038/256478a0.

[CaoEtAl93] Cao, Y.; Beck, R.F.; Schultz, W.W.: An absorbing beach for numerical simulations of nonlinear waves in a wave tank. In Proceedings of 8th International Workshop on Water Waves and Floating Bodies, pp. 17–20, 1993.

[CarterEtAl20] Carter, J.D.; Curtis, C.W.; Kalisch, H.: Particle trajectories in nonlinear Schrödinger models. *Water Waves*, Vol. 2, pp. 31–57, 2020. DOI:10.1007/s42286-019-00008-7.

[Chabchoub13] Chabchoub, A.: *An experimental study on breathers in water waves*. Ph.D. thesis, Hamburg University of Technology, 2013.

[ChabchoubEtAl12] Chabchoub, A.; Akhmediev, N.; Hoffmann, N.P.: Experimental study of spatiotemporally localized surface gravity water waves. *Physical Review E*, Vol. 86, No. 1, p. 016311, 2012. DOI:10.1103/PhysRevE.86.016311.

[ChandrasekaranRaghavi15] Chandrasekaran, S.; Raghavi, B.: Design, development and experimentation of deep ocean wave energy converter system. *Energy Procedia*, Vol. 79, pp. 634–640, 2015. DOI:10.1016/j.egypro.2015.11.545.

[Chen06] Chen, X.B.: The set-down in the second-order Stokes' waves. In Proceedings of the International Conference on Hydrodynamics, Italy, pp. 179–185, 2006.

[ChenEtAl95] Chen, X.B.; Molin, B.; Petitjean, F.: Numerical evaluation of the springing loads on tension leg platforms. *Marine Structures*, Vol. 8, No. 5, pp. 501–524, 1995. DOI:10.1016/0951-8339(95)97306-S.

[ClaussEtAl88] Clauss, G.; Lehmann, E.; Östergaard, C.: *Meerestechnische Konstruktionen*. Berlin, Heidelberg: Springer, 1. Edn., 1988.

[Clément96] Clément, A.: Coupling of two absorbing boundary conditions for 2D time-domain simulations of free surface gravity waves. *Journal of Computational Physics*, Vol. 126, No. 1, pp. 139–151, 1996. DOI:10.1006/JCPH.1996.0126.

[CocoRusso13] Coco, A.; Russo, G.: Finite-difference ghost-point multigrid methods on Cartesian grids for elliptic problems in arbitrary domains. *Journal of Computational Physics*, Vol. 241, pp. 464–501, 2013. DOI:10.1016/J.JCP.2012.11.047.

[CongEtAl21] Cong, P.; Teng, B.; Bai, W.: Second-order wave run-up on a vertical cylinder adjacent to a plane wall based on the application of quadratic transfer function in bi-directional waves. *Marine Structures*, Vol. 76, p. 102879, 2021. DOI:10.1016/J.MARSTRUC.2020.102879.

[CooleyTukey65] Cooley, J.W.; Tukey, J.W.: An algorithm for the machine calculation of complex Fourier series. *Mathematics of Computation*, Vol. 19, No. 90, pp. 297–301, 1965. DOI:10.2307/2003354.

[CorbellaStretch14] Corbella, S.; Stretch, D.D.: Directional wave spectra on the east coast of South Africa. *Journal of the South African Institution of Civil Engineering= Joernaal van die Suid-Afrikaanse Instituut van Siviele Ingenieurswese*, Vol. 56, No. 3, pp. 53–64, 2014. DOI:10520/EJC161372.

[DeconinckOliveras11] Deconinck, B.; Oliveras, K.: The instability of periodic surface gravity waves. *Journal of Fluid Mechanics*, Vol. 675, pp. 141–167, 2011. DOI:10.1017/S0022112011000073.

[DostalEtAl20] Dostal, L.; Hollm, M.; Kreuzer, E.: Study on the behavior of weakly nonlinear water waves in the presence of random wind forcing. *Nonlinear Dynamics*, Vol. 99, No. 3, pp. 2319–2338, 2020. DOI:10.1007/S11071-019-05416-5.

[DostalEtAl23] Dostal, L.; Hollm, M.; Maki, A.: First passage times for nonlinear ship dynamics using Gaussian random fields and effective waves. *Ocean Engineering*, Vol. 281, p. 114751, 2023. DOI:10.1016/J.OCEANENG.2023.114751.

[DostalPick19] Dostal, L.; Pick, M.A.: Theoretical and experimental study of a pendulum excited by random loads. *European Journal of Applied Mathematics*, Vol. 30, No. 5, pp. 912–927, 2019. DOI:10.1017/S0956792518000529.

[DrewEtAl09] Drew, B.; Plummer, A.R.; Sahinkaya, M.N.: A review of wave energy converter technology. *Proceedings of the Institution of Mechanical Engineers, Part A: Journal of Power and Energy*, Vol. 223, No. 8, pp. 887–902, 2009. DOI:10.1243/09576509JPE782.

[DucrozetEtAl14] Ducrozet, G.; Engsig-Karup, A.P.; Bingham, H.B.; Ferrant, P.: A non-linear wave decomposition model for efficient wave–structure interaction. Part A: Formulation, validations and analysis. *Journal of Computational Physics*, Vol. 257, pp. 863–883, 2014. DOI:10.1016/J.JCP.2013.09.017.

[DudleyEtAl14] Dudley, J.M.; Dias, F.; Erkintalo, M.; Genty, G.: Instabilities, breathers and rogue waves in optics. *Nature Photonics*, Vol. 8, pp. 755–764, 2014. DOI:10.1038/NPHOTON.2014.220.

[Dysthe79] Dysthe, K.B.: Note on a modification to the nonlinear Schrödinger equation for application to deep water waves. *Proceedings of the Royal Society A: Mathematical, Physical and Engineering Sciences*, Vol. 369, pp. 105–114, 1979. DOI:10.1098/RSPA.1979.0154.

[DystheTrulsen99] Dysthe, K.B.; Trulsen, K.: Note on breather type solutions of the NLS as models for freak-waves. *Physica Scripta*, Vol. T82, pp. 48–52, 1999. DOI:10.1238/PHYSICA.TOPICAL.082A00048.

[Eatock TaylorHung87] Eatock Taylor, R.; Hung, S.M.: Second order diffraction forces on a vertical cylinder in regular waves. *Applied Ocean Research*, Vol. 9, No. 1, pp. 19–30, 1987. DOI:10.1016/0141-1187(87)90028-9.

[El-TantawyEtAl22] El-Tantawy, S.A.; Salas, A.H.; Alyousef, H.A.; Alharthi, M.R.: Novel approximations to a nonplanar nonlinear Schrödinger equation and modeling nonplanar rogue waves/breathers in a complex plasma. *Chaos, Solitons & Fractals*, Vol. 163, p. 112612, 2022. DOI:10.1016/J.CHAOS.2022.112612.

[ErikssonEtAl05] Eriksson, M.; Isberg, J.; Leijon, M.: Hydrodynamic modelling of a direct drive wave energy converter. *International Journal of Engineering Science*, Vol. 43, No. 17-18, pp. 1377–1387, 2005. DOI:10.1016/J.IJENGSCI.2005.05.014.

[Evans10] Evans, L.C.: *Partial differential equations*. Providence, RI: American Mathematical Society, 2. Edn., 2010. DOI:10.1090/GSM/019.

[Faltinsen93] Faltinsen, O.M.: *Sea loads on ships and offshore structures*. Cambridge: Cambridge University Press, 1993.

[FaltinsenLøken79] Faltinsen, O.M.; Løken, A.E.: Slow drift oscillations of a ship in irregular waves. *Applied Ocean Research*, Vol. 1, No. 1, pp. 21–31, 1979. DOI:10.1016/0141-1187(79)90005-1.

[FermiEtAl55] Fermi, E.; Pasta, J.; Ulam, S.; Tsingou, M.: Studies of the nonlinear problems. Tech. rep., Los Alamos Scientific Laboratory of the University of Carlifornia, 1955. Report No.: LA-1940.

[FerrantEtAl03] Ferrant, P.; Touzé, D.L.; Pelletier, K.: Non-linear time-domain models for irregular wave diffraction about offshore structures. *International Journal for Numerical Methods in Fluids*, Vol. 43, No. 10-11, pp. 1257–1277, 2003. DOI:10.1002/FLD.506.

[Garrett71] Garrett, C.J.R.: Wave forces on a circular dock. *Journal of Fluid Mechanics*, Vol. 46, No. 1, pp. 129–139, 1971. DOI:10.1017/S0022112071000430.

[Givoli91] Givoli, D.: Non-reflecting boundary conditions. *Journal of Computational Physics*, Vol. 94, No. 1, pp. 1–29, 1991. DOI:10.1016/0021-9991(91)90135-8.

[GraingerEtAl21] Grainger, J.P.; Sykulski, A.M.; Jonathan, P.; Ewans, K.: Estimating the parameters of ocean wave spectra. *Ocean Engineering*, Vol. 229, p. 108934, 2021. DOI:10.1016/J.OCEANENG.2021.108934.

[GreavesIglesias18] Greaves, D.; Iglesias, G.: *Wave and tidal energy*. Hoboken, NY: John Wiley & Sons, 2018. DOI:10.1002/9781119014492.

[GrossmannEtAl07] Grossmann, C.; Roos, H.G.; Stynes, M.: *Numerical treatment of partial differential equations*. Berlin, Heidelberg: Springer-Verlag Berlin Heidelberg, 2007. DOI:10.1007/978-3-540-71584-9.

[GrueBiberg93] Grue, J.; Biberg, D.: Wave forces on marine structures with small speed in water of restricted depth. *Applied Ocean Research*, Vol. 15, No. 3, pp. 121–135, 1993. DOI:10.1016/0141-1187(93)90036-W.

[HadiEtAl20] Hadi, E.S.; Iqbal, M.; Wibawa, A.; Kurdi, O.; Karnoto, K.: Experimental studies of interaction forces that affect the position of vertical plates on oscillating heave plates with cylindrical bodies in regular waves. *International Journal of Renewable Energy Development*, Vol. 9, No. 1, pp. 77–84, 2020. DOI:10.14710/IJRED.9.1.77-84.

[HanssenEtAl18] Hanssen, F.C.; Bardazzi, A.; Lugni, C.; Greco, M.: Free-surface tracking in 2D with the harmonic polynomial cell method: Two alternative

strategies. *International Journal for Numerical Methods in Engineering*, Vol. 113, No. 2, pp. 311–351, 2018. DOI:10.1002/NME.5615.

[HarmsEtAl22] Harms, J.; Hollm, M.; Dostal, L.; Kern, T.A.; Seifried, R.: Design and optimization of a wave energy converter for drifting sensor platforms in realistic ocean waves. *Applied Energy*, Vol. 321, p. 119303, 2022. DOI:10.1016/J.APENERGY.2022.119303.

[HinzeEtAl09] Hinze, M.; Pinnau, R.; Ulbrich, M.; Ulbrich, S.: *Optimization with PDE constraints*. Dordrecht: Springer, 2009. DOI:10.1007/978-1-4020-8839-1.

[HollmEtAl21] Hollm, M.; Dostal, L.; Fischer, H.; Seifried, R.: Study on the interaction of nonlinear water waves considering random seas. *Proceedings in Applied Mathematics and Mechanics*, Vol. 20, No. 1, p. e202000307, 2021. DOI:10.1002/PAMM.202000307.

[HollmEtAl22a] Hollm, M.; Dostal, L.; Höhne, J.; Yurchenko, D.; Seifried, R.: Investigation of the dynamics of a multibody wave energy converter excited by regular and irregular waves. *Ocean Engineering*, Vol. 265, p. 112570, 2022. DOI:10.1016/J.OCEANENG.2022.112570.

[HollmEtAl22b] Hollm, M.; Dostal, L.; Seifried, R.: Hydrodynamic forces acting on cylindrical piles subjected to wind-forced random nonlinear water waves. In W. Lacarbonara; B. Balachandran; M.J. Leamy; J. Ma; J.A. Tenreiro Machado; G. Stepan (Eds.) Advances in Nonlinear Dynamics, pp. 95–105, Cham: Springer International Publishing, 2022.

[HollmEtAl22c] Hollm, M.; Dostal, L.; Yurchenko, D.; Seifried, R.: Performance increase of wave energy harvesting of a guided point absorber. *The European Physical Journal Special Topics*, Vol. 231, No. 8, pp. 1465–1473, 2022. DOI:10.1140/EPJS/S11734-022-00497-7.

[HollmEtAl24] Hollm, M.; Dostal, L.; Carter, J.D.; Seifried, R.: Determination of particle paths and hydrodynamic forces of random wind forced nonlinear ocean waves. *Proceedings of the Institution of Mechanical Engineers, Part M: Journal of Engineering for the Maritime Environment*, Vol. 238, No. 2, pp. 406–416, 2024. DOI:10.1177/14750902231196812.

[HollmSeifried23] Hollm, M.; Seifried, R.: Hydrodynamic forces acting on mechanical systems in linear and nonlinear ocean waves. *Proceedings in Applied Mathematics and Mechanics*, Vol. 23, No. 2, p. e202300141, 2023. DOI:10.1002/PAMM.202300141.

[Hughes85] Hughes, S.A.: Directional wave spectra using cosine-squared and cosine 2s spreading functions. *Coastal Engineering Technical Note. Coastal Engineering Research Center, Coastal and Hydraulics Laboratary, Vicksburg, Mississippi*, 1985.

[IsraeliOrszag81] Israeli, M.; Orszag, S.A.: Approximation of radiation boundary conditions. *Journal of Computational Physics*, Vol. 41, No. 1, pp. 115–135, 1981. DOI:10.1016/0021-9991(81)90082-6.

[Jagannathan88] Jagannathan, S.: Non-linear free surface flows and an application of the Orlanski boundary condition. *International Journal for Numerical Methods in Fluids*, Vol. 8, No. 9, pp. 1051–1070, 1988. DOI:10.1002/FLD.1650080907.

[Jost13] Jost, J.: *Partial differential equations*. New York: Springer-Verlag New York, 3. Edn., 2013. DOI:10.1007/978-1-4614-4809-9.

[KinoshitaBao00] Kinoshita, T.; Bao, W.: Third-order wave diffraction by a truncated circular cylinder. *Proceedings of the Institution of Mechanical Engineers, Part C: Journal of Mechanical Engineering Science*, Vol. 214, No. 6, pp. 789–800, 2000. DOI:10.1243/0954406001523786.

[KnabnerAngermann03] Knabner, P.; Angermann, L.: *Numerical methods for elliptic and parabolic partial differential equations*. New York: Springer, 2003. DOI:DOI.ORG/10.1007/B97419.

[LaiEtAl02] Lai, M.C.; Lin, W.W.; Wang, W.: A fast spectral/difference method without pole conditions for poisson-type equations in cylindrical and spherical geometries. *IMA Journal of Numerical Analysis*, Vol. 22, No. 4, pp. 537–548, 2002. DOI:10.1093/IMANUM/22.4.537.

[Langtangen03] Langtangen, H.P.: *Computational partial differential equations: numerical methods and diffpack programming*. Berlin, Heidelberg: Springer, 2. Edn., 2003. DOI:10.1007/978-3-642-55769-9.

[Le Méhauté76] Le Méhauté, B.: *An introduction to hydrodynamics and water waves*. New York: Springer, 1976. DOI:10.1007/978-3-642-85567-2.

[LeeEtAl22] Lee, U.J.; Jeong, W.M.; Cho, H.Y.: Estimation and analysis of JONSWAP spectrum parameter using observed data around Korean coast. *Journal of Marine Science and Engineering*, Vol. 10, No. 5, p. 578, 2022. DOI:10.3390/JMSE10050578.

[LejerskogEtAl15] Lejerskog, E.; Boström, C.; Hai, L.; Waters, R.; Leijon, M.: Experimental results on power absorption from a wave energy converter at the Lysekil wave energy research site. *Renewable Energy*, Vol. 77, pp. 9–14, 2015. DOI:10.1016/J.RENENE.2014.11.050.

[LeVeque92] LeVeque, R.J.: *Numerical methods for conservation laws*. Basel: Birkhäuser, 2. Edn., 1992. DOI:10.1007/978-3-0348-8629-1.

[LiangZuo17] Liang, C.; Zuo, L.: On the dynamics and design of a two-body wave energy converter. *Renewable Energy*, Vol. 101, pp. 265–274, 2017. DOI:10.1016/J.RENENE.2016.08.059.

[Lin08] Lin, P.: *Numerical modeling of water waves*. London, New York: Taylor & Francis, 2008.

[LiuAbbaspour82] Liu, P.L.F.; Abbaspour, M.: An integral equation method for the diffraction of oblique waves by an infinite cylinder. *International Journal for Numerical Methods in Engineering*, Vol. 18, No. 10, pp. 1497–1504, 1982. DOI:10.1002/NME.1620181005.

[Lloyd89] Lloyd, A.R.J.M.: *Seakeeping: ship behaviour in rough weather*. Chichester: Ellis Horwood Ltd, 1989.

[Logan14] Logan, J.D.: *Applied partial differential equations*. Cham: Springer, 3. Edn., 2014. DOI:10.1007/978-3-319-12493-3.

[LoMei85] Lo, E.; Mei, C.C.: A numerical study of water-wave modulation based on a higher-order nonlinear Schrödinger equation. *Journal of Fluid Mechanics*, Vol. 150, pp. 395–416, 1985. DOI:10.1017/S0022112085000180.

[MalenicaEtAl95] Malenica, Š.; Clark, P.J.; Molin, B.: Wave and current forces on a vertical cylinder free to surge and sway. *Applied Ocean Research*, Vol. 17, No. 2, pp. 79–90, 1995. DOI:10.1016/0141-1187(95)00002-I.

[MalenicaMolin95] Malenica, Š.; Molin, B.: Third-harmonic wave diffraction by a vertical cylinder. *Journal of Fluid Mechanics*, Vol. 302, pp. 203–229, 1995. DOI:10.1017/S0022112095004071.

[Marsal76] Marsal, D.: *Die numerische Lösung partieller Differentialgleichungen in Wissenschaft und Technik*. Mannheim, Wien, Zürich: Bibliographisches Institut, 1976.

[MaYan06] Ma, Q.W.; Yan, S.: Quasi ALE finite element method for nonlinear water waves. *Journal of Computational Physics*, Vol. 212, No. 1, pp. 52–72, 2006. DOI:10.1016/J.JCP.2005.06.014.

[McCormick13] McCormick, M.E.: *Ocean wave energy conversion*. Mineola, NY: Courier Dover Publications, 2013.

[Mei83] Mei, C.C.: *The applied dynamics of ocean surface waves*. New York: John Wiley & Sons, 1983.

[Miche44] Miche, M.: Mouvements ondulatoires de la mer en profondeur constante ou décroissante. *Annales de Ponts et Chaussées*, pp. 26–78, 131–164, 270–292, 369–406, 1944.

[MitsuyasuEtAl75] Mitsuyasu, H.; Tasai, F.; Suhara, T.; Mizuno, S.; Okhuso, M.; Honda, T.; Rikiishi, K.: Observation of the directional spectrum of ocean waves using a cloverleaf buoy. *Journal of Physical Oceanography*, Vol. 5, No. 4, pp. 750–760, 1975. DOI:10.1175/1520-0485(1975)005<0750:OOTDSO>2.0.CO;2.

[Molin79] Molin, B.: Second-order diffraction loads upon three-dimensional bodies. *Applied Ocean Research*, Vol. 1, No. 4, pp. 197–202, 1979. DOI:10.1016/0141-1187(79)90027-0.

[Newman18] Newman, J.N.: *Marine hydrodynamics*. Cambridge: The MIT press, 2018.

[Ogilvie83] Ogilvie, T.F.: Second-order hydrodynamic effects on ocean platforms. In R.W. Yeung (Ed.) Proceedings of the International Workshop on Ship and Platform Motions, University of California, Berkeley, pp. 205–265, 1983.

[OlayaEtAl14] Olaya, S.; Bourgeot, J.M.; Benbouzid, M.: Modelling and preliminary studies for a self-reacting point absorber WEC. In 2014 First International Conference on Green Energy ICGE 2014, pp. 14–19, IEEE, 2014. DOI:10.1109/ICGE.2014.6835390.

[OnoratoEtAl01] Onorato, M.; Osborne, A.R.; Serio, M.; Bertone, S.: Freak waves in random oceanic sea states. *Physical Review Letters*, Vol. 86, No. 25, pp. 5831–5834, 2001. DOI:10.1103/PhysRevLett.86.5831.

[OnoratoEtAl04] Onorato, M.; Osborne, A.R.; Serio, M.; Cavaleri, L.; Brandini, C.; Stansberg, C.T.: Observation of strongly non-Gaussian statistics for random sea surface gravity waves in wave flume experiments. *Physical Review E*, Vol. 70, No. 6, p. 067302, 2004. DOI:10.1103/PhysRevE.70.067302.

[OnoratoEtAl06] Onorato, M.; Osborne, A.R.; Serio, M.; Cavaleri, L.; Brandini, C.; Stansberg, C.T.: Extreme waves, modulational instability and second order theory: wave flume experiments on irregular waves. *European Journal of Mechanics-B/Fluids*, Vol. 25, No. 5, pp. 586–601, 2006. DOI:10.1016/j.euromechflu.2006.01.002.

[OnoratoEtAl13] Onorato, M.; Residori, S.; Bortolozzo, U.; Montina, A.; Arecchi, F.T.: Rogue waves and their generating mechanisms in different physical contexts. *Physics Reports*, Vol. 528, No. 2, pp. 47–89, 2013. DOI:10.1016/j.physrep.2013.03.001.

[OpenStreetMap] OpenStreetMap: Map data. `https://www.openstreetmap.org`. Accessed on 11. December 2024. Data is available under the Open Database License, see `https://www.openstreetmap.org/copyright`.

[Orlanski76] Orlanski, I.: A simple boundary condition for unbounded hyperbolic flows. *Journal of Computational Physics*, Vol. 21, No. 3, pp. 251–269, 1976. DOI:10.1016/0021-9991(76)90023-1.

[Osborne10] Osborne, A.R.: *Nonlinear Ocean Waves and the Inverse Scattering Transform*. Amsterdam: Academic Press, 1. Edn., 2010.

[Pearson74] Pearson, R.A.: Consistent boundary conditions for numerical models of systems that admit dispersive waves. *Journal of Atmospheric Sciences*, Vol. 31, No. 6, pp. 1481–1489, 1974. DOI:10.1175/1520-0469(1974)031<1481:CBCFNM>2.0.CO;2.

[Peregrine83] Peregrine, D.H.: Water waves, nonlinear Schrödinger equations and their solutions. *The Journal of the Australian Mathematical Society Series B Applied Mathematics*, Vol. 25, No. 1, pp. 16–43, 1983. DOI:10.1017/S0334270000003891.

[PolinderEtAl04] Polinder, H.; Damen, M.E.C.; Gardner, F.: Linear PM generator system for wave energy conversion in the AWS. *IEEE Transactions on Energy Conversion*, Vol. 19, No. 3, pp. 583–589, 2004. DOI:10.1109/TEC.2004.827717.

[PrudellEtAl10] Prudell, J.; Stoddard, M.; Amon, E.; Brekken, T.K.A.; von Jouanne, A.: A permanent-magnet tubular linear generator for ocean wave energy conversion. *IEEE Transactions on Industry Applications*, Vol. 46, No. 6, pp. 2392–2400, 2010. DOI:10.1109/TIA.2010.2073433.

[RahmanEtAl99] Rahman, M.; Bora, S.N.; Satish, M.G.: A note on second-order wave forces on a circular cylinder in finite water depth. *Applied Mathematics Letters*, Vol. 12, No. 1, pp. 63–70, 1999. DOI:10.1016/S0893-9659(98)00128-1.

[Romate92] Romate, J.E.: Absorbing boundary conditions for free surface waves. *Journal of Computational Physics*, Vol. 99, No. 1, pp. 135–145, 1992. DOI:10.1016/0021-9991(92)90281-3.

[RyabkovaEtAl19] Ryabkova, M.; Karaev, V.; Guo, J.; Titchenko, Y.: A review of wave spectrum models as applied to the problem of radar probing of the sea surface. *Journal of Geophysical Research: Oceans*, Vol. 124, No. 10, pp. 7104–7134, 2019. DOI:10.1029/2018JC014804.

[ShaoEtAl22] Shao, Y.; Zheng, Z.; Liang, H.; Chen, J.: A consistent second-order hydrodynamic model in the time domain for floating structures with large horizontal motions. *Computer-Aided Civil and Infrastructure Engineering*, Vol. 37, No. 7, pp. 894–914, 2022. DOI:10.1111/MICE.12782.

[ShaoFaltinsen13] Shao, Y.L.; Faltinsen, O.M.: Second-order diffraction and radiation of a floating body with small forward speed. *Journal of Offshore Mechanics and Arctic Engineering*, Vol. 135, No. 1, p. 011301, 2013. DOI:10.1115/1.4006929.

[SharmaDean79] Sharma, J.N.; Dean, R.G.: *Development and Evaluation of a Procedure for Simulating a Random Directional Second-Order Sea Surface and Associated Wave Forces.* Ocean Engineering Report 20, University of Delaware, Newark, 1979.

[ShemerDorfman08] Shemer, L.; Dorfman, B.: Experimental and numerical study of spatial and temporal evolution of nonlinear wave groups. *Nonlinear Processes in Geophysics*, Vol. 15, No. 6, pp. 931–942, 2008. DOI:10.5194/npg-15-931-2008.

[ShriraGeogjaev10] Shrira, V.I.; Geogjaev, V.V.: What makes the Peregrine soliton so special as a prototype of freak waves? *Journal of Engineering Mathematics*, Vol. 67, pp. 11–22, 2010. DOI:10.1007/s10665-009-9347-2.

[Sichermann09] Sichermann, W.: *Zur Simulation und Vorhersage extremer Schiffsbewegungen im natürlichen Seegang.* Ph.D. thesis, Hamburg University of Technology, Hamburg, Germany, 2009.

[SkourupEtAl00] Skourup, J.; Cheung, K.F.; Bingham, H.B.; Büchmann, B.: Loads on a 3D body due to second-order waves and a current. *Ocean Engineering*, Vol. 27, No. 7, pp. 707–727, 2000. DOI:10.1016/S0029-8018(99)00013-X.

[SlunyaevEtAl13a] Slunyaev, A.; Clauss, G.F.; Klein, M.; Onorato, M.: Simulations and experiments of short intense envelope solitons of surface water waves. *Physics of Fluids*, Vol. 25, No. 6, p. 067105, 2013. DOI:10.1063/1.4811493.

[SlunyaevEtAl13b] Slunyaev, A.; Pelinovsky, E.; Sergeeva, A.; Chabchoub, A.; Hoffmann, N.; Onorato, M.; Akhmediev, N.: Super-rogue waves in simulations based on weakly nonlinear and fully nonlinear hydrodynamic equations. *Physical Review E*, Vol. 88, No. 1, p. 012909, 2013. DOI:10.1103/PhysRevE.88.012909.

[SlunyaevEtAl14] Slunyaev, A.; Pelinovsky, E.; Guedes Soares, C.: Reconstruction of extreme events through numerical simulations. *Journal of Offshore Mechanics and Arctic Engineering*, Vol. 136, No. 1, p. 011302, 2014. DOI:10.1115/1.4025545.

[Stoker57] Stoker, J.J.: *Water waves: The mathematical theory with applications.* New York: Interscience Publishers, 1957. DOI:10.1002/9781118033159.

[Stokes47] Stokes, G.G.: On the theory of oscillatory waves. *Transactions of the Cambridge Philosophical Society*, Vol. 8, pp. 441–455, 1847.

[SunEtAl15] Sun, J.L.; Wang, C.Z.; Wu, G.X.; Khoo, B.C.: Fully nonlinear simulations of interactions between solitary waves and structures based on the finite element method. *Ocean Engineering*, Vol. 108, pp. 202–215, 2015. DOI:10.1016/J.OCEANENG.2015.08.007.

[ToffoliEtAl10] Toffoli, A.; Gramstad, O.; Trulsen, K.; Monbaliu, J.; Bitner-Gregersen, E.; Onorato, M.: Evolution of weakly nonlinear random directional waves: laboratory experiments and numerical simulations. *Journal of Fluid Mechanics*, Vol. 664, pp. 313–336, 2010. DOI:10.1017/S002211201000385X.

[TomYeung13] Tom, N.; Yeung, R.W.: Performance enhancements and validations of a generic ocean-wave energy extractor. *Journal of Offshore Mechanics and Arctic Engineering*, Vol. 135, No. 4, p. 041101, 2013. DOI:10.1115/1.4024150.

[TongEtAl21] Tong, C.; Shao, Y.; Bingham, H.B.; Hanssen, F.C.W.: An adaptive harmonic polynomial cell method with immersed boundaries: Accuracy, stability, and applications. *International Journal for Numerical Methods in Engineering*, Vol. 122, No. 12, pp. 2945–2980, 2021. DOI:10.1002/NME.6648.

[TrulsenDysthe96] Trulsen, K.; Dysthe, K.B.: A modified nonlinear Schrödinger equation for broader bandwidth gravity waves on deep water. *Wave Motion*, Vol. 24, No. 3, pp. 281–289, 1996. DOI:10.1016/S0165-2125(96)00020-0.

[TrulsenEtAl00] Trulsen, K.; Kliakhandler, I.; Dysthe, K.B.; Velarde, M.G.: On weakly nonlinear modulation of waves on deep water. *Physics of Fluids*, Vol. 12, No. 10, pp. 2432–2437, 2000. DOI:10.1063/1.1287856.

[TsayLiu83] Tsay, T.K.; Liu, P.L.F.: A finite element model for wave refraction and diffraction. *Applied Ocean Research*, Vol. 5, No. 1, pp. 30–37, 1983. DOI:10.1016/0141-1187(83)90055-X.

[TsuchiyaYasuda81] Tsuchiya, Y.; Yasuda, T.: A new approach to Stokes wave theory. *Bulletin of the Disaster Prevention Research Institute*, Vol. 31, No. 1, pp. 17–34, 1981.

[TulinWaseda99] Tulin, M.P.; Waseda, T.: Laboratory observations of wave group evolution, including breaking effects. *Journal of Fluid Mechanics*, Vol. 378, pp. 197–232, 1999. DOI:10.1017/S0022112098003255.

[TveitoWinther98] Tveito, A.; Winther, R.: *Introduction to partial differential equations: a computational approach*. New York: Springer, 1998. DOI:10.1007/B98967.

[VaziriEtAl14] Vaziri, V.; Najdecka, A.; Wiercigroch, M.: Experimental control for initiating and maintaining rotation of parametric pendulum. *The European Physical Journal Special Topics*, Vol. 223, pp. 795–812, 2014. DOI:10.1140/EPJST/E2014-02141-Y.

[VermaakKamper12] Vermaak, R.; Kamper, M.J.: Design aspects of a novel topology air-cored permanent magnet linear generator for direct drive wave energy converters. *IEEE Transactions on Industrial Electronics*, Vol. 59, No. 5, pp. 2104–2115, 2012. DOI:10.1109/TIE.2011.2162215.

[WangWu06] Wang, C.Z.; Wu, G.X.: An unstructured-mesh-based finite element simulation of wave interactions with non-wall-sided bodies. *Journal of Fluids and Structures*, Vol. 22, No. 4, pp. 441–461, 2006. DOI:10.1016/J.JFLUIDSTRUCTS.2005.12.005.

[WangWu07] Wang, C.Z.; Wu, G.X.: Time domain analysis of second-order wave diffraction by an array of vertical cylinders. *Journal of Fluids and Structures*, Vol. 23, No. 4, pp. 605–631, 2007. DOI:10.1016/J.JFLUIDSTRUCTS.2006.10.008.

[WatersEtAl07] Waters, R.; Stålberg, M.; Danielsson, O.; Svensson, O.; Gustafsson, S.; Strömstedt, E.; Eriksson, M.; Sundberg, J.; Leijon, M.: Experimental results from sea trials of an offshore wave energy system. *Applied Physics Letters*, Vol. 90, No. 3, p. 034105, 2007. DOI:10.1063/1.2432168.

[Wehausen71] Wehausen, J.V.: The motion of floating bodies. *Annual Review of Fluid Mechanics*, Vol. 3, pp. 237–268, 1971. DOI:10.1146/ANNUREV.FL.03.010171.001321.

[Whitham99] Whitham, G.B.: *Linear and nonlinear waves*. New York: John Wiley & Sons, 1999. DOI:10.1002/9781118032954.

[Witt19] Witt, A.: *Inducing predefined nonlinear rogue waves on basis of breather solutions*. Ph.D. thesis, Hamburg University of Technology, 2019. DOI:10.15480/882.2224.

[WuEtAl14] Wu, B.; Wang, X.; Diao, X.; Peng, W.; Zhang, Y.: Response and conversion efficiency of two degrees of freedom wave energy device. *Ocean Engineering*, Vol. 76, pp. 10–20, 2014. DOI:10.1016/J.OCEANENG.2013.11.001.

[Yeung81] Yeung, R.W.: Added mass and damping of a vertical cylinder in finite-depth waters. *Applied Ocean Research*, Vol. 3, No. 3, pp. 119–133, 1981. DOI:10.1016/0141-1187(81)90101-2.

[YeungEtAl12] Yeung, R.W.; Peiffer, A.; Tom, N.; Matlak, T.: Design, analysis, and evaluation of the UC-Berkeley wave-energy extractor. *Journal of Offshore Mechanics and Arctic Engineering*, Vol. 134, No. 2, p. 021902, 2012. DOI:10.1115/1.4004518.

[YuenLake80] Yuen, H.C.; Lake, B.M.: Instabilities of waves on deep water. *Annual Review of Fluid Mechanics*, Vol. 12, pp. 303–334, 1980. DOI:10.1146/ANNUREV.FL.12.010180.001511.

[YuenLake82] Yuen, H.C.; Lake, B.M.: Nonlinear dynamics of deep-water gravity waves. *Advances in Applied Mechanics*, Vol. 22, pp. 67–229, 1982. DOI:10.1016/S0065-2156(08)70066-8.

[YurchenkoAlevras18] Yurchenko, D.; Alevras, P.: Parametric pendulum based wave energy converter. *Mechanical Systems and Signal Processing*, Vol. 99, pp. 504–515, 2018. DOI:10.1016/J.YMSSP.2017.06.026.

[Zakharov68] Zakharov, V.E.: Stability of periodic waves of finite amplitude on the surface of a deep fluid. *Journal of Applied Mechanics and Technical Physics*, Vol. 9, No. 2, pp. 190–194, 1968. DOI:10.1007/BF00913182.

[ZhangTeng21] Zhang, Y.; Teng, B.: A nonlinear potential flow model for higher-harmonic wave loads and ringing response of a monopile. *Ocean Engineering*, Vol. 222, p. 108574, 2021. DOI:10.1016/J.OCEANENG.2021.108574.